


Summer 2011

Ultrafast Electron Diffraction Study of the Dynamics of Antimony Thin Films and Nanoparticles

Mahmoud Abdel-Fattah
Old Dominion University

Follow this and additional works at: https://digitalcommons.odu.edu/ece_etds

 Part of the [Electrical and Computer Engineering Commons](#), [Materials Science and Engineering Commons](#), and the [Nanoscience and Nanotechnology Commons](#)

Recommended Citation

Abdel-Fattah, Mahmoud. "Ultrafast Electron Diffraction Study of the Dynamics of Antimony Thin Films and Nanoparticles" (2011). Doctor of Philosophy (PhD), dissertation, Electrical/Computer Engineering, Old Dominion University, DOI: 10.25777/8w6j-aq95 https://digitalcommons.odu.edu/ece_etds/53

This Dissertation is brought to you for free and open access by the Electrical & Computer Engineering at ODU Digital Commons. It has been accepted for inclusion in Electrical & Computer Engineering Theses & Dissertations by an authorized administrator of ODU Digital Commons. For more information, please contact digitalcommons@odu.edu.

**ULTRAFAST ELECTRON DIFFRACTION STUDY OF THE
DYNAMICS OF ANTIMONY THIN FILMS AND NANOPARTICLES**

by

Mahmoud Abdel-Fattah
B.Sc. May 1991, Cairo University
M.S. May 1998, Cairo University

A Dissertation Submitted to the Faculty of Old Dominion University in
Partial Fulfillment of the Requirement for the Degree of

DOCTOR OF PHILOSOPHY

ELECTRICAL ENGINEERING

OLD DOMINION UNIVERSITY

August 2011

Approved by:

Hani Elsayéd-Ali (Director)

Aleksey Bugayev (Member)

Helmut Baumgart (Member)

Gón Namkoong (Member)

ABSTRACT

ULTRAFAST ELECTRON DIFFRACTION STUDY OF THE DYNAMICS OF ANTIMONY THIN FILMS AND NANOPARTICLES

Mahmoud Abdel-Fattah
Old Dominion University, 2011
Director: Dr. Hani Elsayed-Ali

The ultrafast fast phenomena that take place following the application of a 120 fs laser pulse on 20 nm antimony thin films and 40 nm nanoparticles were studied using time-resolved electron diffraction. Samples are prepared by thermal evaporation, at small thickness (< 10 nm) antimony nanoparticles form while at larger thicknesses we get continuous thin films.

The samples are annealed and studied by static heating to determine their Debye temperatures, which were considerably less than the standard value. The thermal expansion under static heating also yielded the expansion coefficient of the sample material. Nanoparticle samples gave a very accurate thermal expansion coefficient ($11 \times 10^{-6} \text{ K}^{-1}$).

Ultrafast time resolved electron diffraction studies with ~1.5 ps resolution are performed for both kinds of samples to determine the lattice thermalization time and study the difference in relaxation time between the thin films and nanoparticles.

Knowing the Debye temperature from the static heating experiment (144 K for nanoparticles and 148 K for 20 nm thin films), we could measure the temperature rise due to the laser pulse. The thermal pressure and acoustic lattice oscillations are also studied.

There was a noticeable delay of 6 ps between the onset of the drop of intensity and the onset of the drop in diffraction ring size, which indicates the propagation of a thermal stress front in the film.

This dissertation is dedicated to my parents, my wife, and my children.

ACKNOWLEDGMENTS

I am grateful to my advisor, Dr. Hani Elsayed-Ali, for his support, guidance, and continued funding for my research. I would also like to thank my committee members for their time and input.

I would like to thank my dear colleague Ahmad Esmail for all of his support, especially for letting me use his electron diffraction system. I am also thankful for my dear colleagues Ibrahim El-Kholy, Mohamed Hafez, Mohammed Hegazy, and Wei Cao for their support.

TABLE OF CONTENTS

	Page
LIST OF FIGURES	ix
CHAPTER I. INTRODUCTION.....	1
I.1. Antimony	1
I.2. The structure of nanoparticles	4
I.3. Time-resolved electron diffraction studies	5
I.4. Previous studies on antimony nanoparticles.....	5
I.5. Dynamic vibrational properties	8
I.6. Photoinduced electrons as probe	8
I.7. Previous work on group V semimetals.....	9
CHAPTER II. THEORY	12
II.1. Electron pulse broadening.....	12
II.2. Hot carrier dynamics	16
II.3. Two-temperature model	18
II.4. Debye-Waller factor	21
II.5. Two-temperature model (TTM) simulation	22
CHAPTER III. EXPERIMENTAL SETUP	25
III.1 Sample preparation	25
III.2 Electron gun	28
III.3 Sample holder/heater	31
III.4 Diffraction pattern imaging.....	32
III.5 Optical and experimental setup.....	34
III.6 Data analysis	37
CHAPTER IV. RESULTS AND DISCUSSION.....	40
IV.1. Interpretation of the electron diffraction pattern	41
IV.2. Thin film growth modes of antimony	47
IV.3. Static heating of Sb thin films and nanoparticles	58
IV.3.1. Calculation of Debye temperature for nanoparticles and thin films	61
IV.3.2. Calculating the expansion coefficient using thin film diffraction ring size	63
IV.4. Time-resolved studies of Sb thin films and nanoparticles.....	67
IV.4.1. Time-resolved scan on Al thin film	67
IV.4.2. Temperature rise after thermal equilibrium for 20 nm Sb thin film	69

	Page
IV.4.3. The effect of the pump fluence on the decay constant for the 20 nm Sb film.....	71
IV.4.4. Delayed lattice expansion.....	78
IV.4.5. Decay constant comparison between the Sb nanoparticles and 20 nm thin film.....	80
IV.4.6. Temperature increase in the Sb nanoparticles and 20 nm thin film.....	82
IV.4.7. Inhomogeneous lattice spacing.....	84
IV.4.8. Harmonic lattice oscillations	86
CHAPTER V. SUMMARY.....	88
BIBLIOGRAPHY.....	90
APPENDICES	98
VITA	160

LIST OF FIGURES

Figure	Page
1.1 Starting from the NaCl structure we can derive the A7 Peierls distorted structure of Sb by motion of atomic planes normal to the (111) axis in alternative direction, as indicated in the figure.....	2
1.2 The antimony A7 hexagonal unit cell with the rhombohedral one inside it.....	3
1.3 The construction of the A7 structure from the simple cubic one.....	4
1.4 Diffraction patterns of Sb nanoparticles.....	6
1.5 Diffraction patterns of Sb clusters.....	7
1.6 Diffraction pattern for antimony nanoparticles with the background removed due to the cooling gas removed	7
1.7 Integrated Bragg peak correlated to the lattice planes that produce it.....	9
2.1 An electron pulse disk simulating a drifting femtosecond photoelectron pulse	13
2.2 (a) The electron pulse broadening Δt as a function of EP drift	15
2.3 Stages of the electron distribution following optical excitation	17
2.4 The temporal profile of 100 nm films of Au and Ni irradiated by a 200 fs laser pulse of 400 nm wavelength.....	21
2.5 TTM simulation of Sb thin film 20 nm thick.....	23
3.1 The tungsten filament that we used for depositing Sb thin films and nanoparticles	27
3.2 The configuration of the photoactivated electron gun	30
3.3 Schematic of the sample holder/heater	32
3.4 MCP detector/signal amplifier	33
3.5 The beam profile of the pump laser at the target equivalent plane	35
3.6 The optical setup layout of the UED system	36

Figure	Page
3.7	The image processing flow chart39
4.1	Thin film electron diffraction patterns for gold (a) and aluminum (b) taken for the simplicity of their fcc structure for the sole purpose of calibrating the imaging system41
4.2	A quadrant of the electron diffraction pattern of antimony nanoparticles.....45
4.3	Two types of samples are used in this study: continuous thin film (a) and scattered nanoparticles (b)46
4.4	All the recorded diffraction peaks for Sb nanoparticles are plotted against the corresponding scattering parameter47
4.5	TEM image of Sb nanoparticles with an effective thickness of 5 nm48
4.6	TEM image of Sb nanoparticles with an effective thickness of 10 nm49
4.7	TEM image of Sb nanoparticles with an effective thickness of 10 nm49
4.8	(a) TEM image of Sb nanoparticles with an effective thickness of 50 Å on both sides of the TEM grid50
4.9	TEM image of Sb nanoparticles with an effective thickness of 50 Å on both sides of the TEM grid51
4.10	TEM image of Sb thin film with thickness 20 nm.....52
4.11	TEM image of Sb thin film with thickness 20 nm.....52
4.12	HRTEM image of Sb thin film with thickness 200 Å53
4.13	HRTEM image of Sb thin film with thickness 200 Å53
4.14	TEM image of Sb nanoparticles of a distribution with effective thickness 50 Å.....54
4.15	TEM image of Sb nanoparticles of a distribution with effective thickness 50 Å.....55
4.16	TEM image of Sb nanoparticles with an effective thickness of 50 Å56
4.17	Size distribution for the nanoparticles in Fig. 4.16 that are annealed to 220 °C56
4.18	TEM image of Sb nanoparticles with a film thickness of 50 Å.....57

Figure	Page
4.19 Size distribution for the nanoparticles in Fig. 4.18 that are annealed to 350 °C	57
4.20 The diffraction intensity amplitude of Sb film of thickness 200 Å that is directly heated through the heating stage.....	59
4.21 The diffraction intensity amplitude of Sb nanoparticles of effective thickness 50 Å that is directly heated through the heating stage	60
4.22 Natural logarithm of the intensity ratio of antimony nanoparticles as a function of $(\sin \theta/\lambda)^2$	62
4.23 Natural logarithm of the intensity ratio of antimony 20 nm thin film as a function of $(\sin \theta/\lambda)^2$	63
4.24 The diffraction ring radius of Sb nanoparticles of effective thickness 50 Å that is directly heated through the heating stage	64
4.25 The diffraction ring radius of Sb nanoparticles of effective thickness 50 Å that is directly heated through the heating stage	66
4.26 Al thin film diffraction has a decay constant of 1.72 ps	68
4.27 Diffraction intensity of the 20 nm thin film under a fluence of 5.3 mJ/cm ²	69
4.28 Diffraction intensity of the 20 nm thin film under a fluence of 7.3 mJ/cm ²	70
4.29 Diffraction rings (232), (312), (122), (042), (410) of the 20 nm thin film under laser fluence 2.9 mJ/cm ²	72
4.30 Diffraction rings (232), (312), (122), (042), (410) of the 20 nm thin film under laser fluence 6.0 mJ/cm ²	73
4.31 Diffraction rings (300), (220), (312), (042), (232), and (410) of the 20 nm thin film under laser fluence 3.3 mJ/cm ²	74
4.32 Diffraction rings (300), (220), (312), (042), (232), and (410) of the 20 nm thin film under laser fluence 7.3 mJ/cm ²	75
4.33 Diffraction rings (112), (300), (220), (312), (134), (042), (232), and (410) of the 20 nm thin film under laser fluence 2.7 mJ/cm ²	76
4.34 Diffraction rings (112), (300), (220), (312), (134), (042), (232), and (410) of the 20 nm thin film under laser fluence 5.3 mJ/cm ²	77

Figure	Page
4.35 The intensity drop is plotted with the diffraction ring size in the same scale ($\times 330$).....	79
4.36 Time-resolved scan of the 50 Å thick nanoparticles. Data is fit to an exponential decay function	80
4.37 Time-resolved scan of the 200 Å film. Data is fit to an exponential decay function	81
4.38 The diffraction intensity of time-resolved scan of the 50 Å effective thickness nanoparticles.	83
4.39 Time-resolved scan of the 20 nm film	85
4.40 Diffraction ring (300) of the 34 nm film.....	85
4.41 Time-resolved scan of the 23 nm film	86
4.42 Time-resolved scan of the 23 nm film	87

CHAPTER I

INTRODUCTION

The application of an ultrafast laser pulse in the range of 100 fs on a crystalline sample leads to structural changes that can lead to melting. The energy of the laser pulse energizes the electrons that in turn transfer their excitation energy to the lattice through collisions. The lattice oscillations result in a loss in the crystallization order which we can see as a reduction in the diffraction pattern. Studying the electron diffraction pattern gives us qualitative and quantitative information about lattice temperature, lattice expansion, optical and acoustical phonons, electron-phonon coupling, Debye temperature, phase change, and size effects.

I.1. Antimony

Antimony is a member of group V_B semimetals which received much attention and was heavily investigated for potential applications in electronic technology. All three members of that group, namely, arsenic, antimony, and bismuth, are characterized by the A7 crystal structure that can be constructed by slightly modifying the NaCl cubic structure. The antimony lattice is the rhombohedral A7 structure with $a = 0.45067$ nm and $\alpha = 57.1075^\circ$. The simplest way to visualize the A7 structure, which is shared with bismuth and arsenic, is to start with a sodium chloride (NaCl) crystal and replace both the sodium and chlorine atoms with antimony atoms. Next, stretch the lattice along the body diagonal until the rhombohedral angle α is reduced from its cubic value of 60° . Lastly, every other sublattice along the diagonal is removed. A simpler way to describe the process is to also start with an NaCl structure and move the (111) planes towards and

away from each other in an alternative order. This process is illustrated in Fig. 1.1. The rhombohedral unit cell has two atoms, with the center of inversion symmetry right in the middle of them; this point is considered the origin of the unit cell. The distortion parameter for antimony is $u = 0.23349$ under the rhombohedral structure, instead of 0.25 in the cubic structure.²⁴

Antimony was primarily chosen for this thesis due to its ability to form well isolated nanoparticles by the method of thermal evaporation in vacuum. The physical properties of antimony are summed up as follows: it is a brittle, silvery metal whose solid-state density is 6.68 gm/cm^3 . The melting point of Sb is $630.6 \text{ }^\circ\text{C}$ and the boiling point is $1587 \text{ }^\circ\text{C}$. Sb has a relatively high vapor pressure of $7.5 \times 10^{-2} \text{ Torr}$ at $603 \text{ }^\circ\text{C}$.²⁵

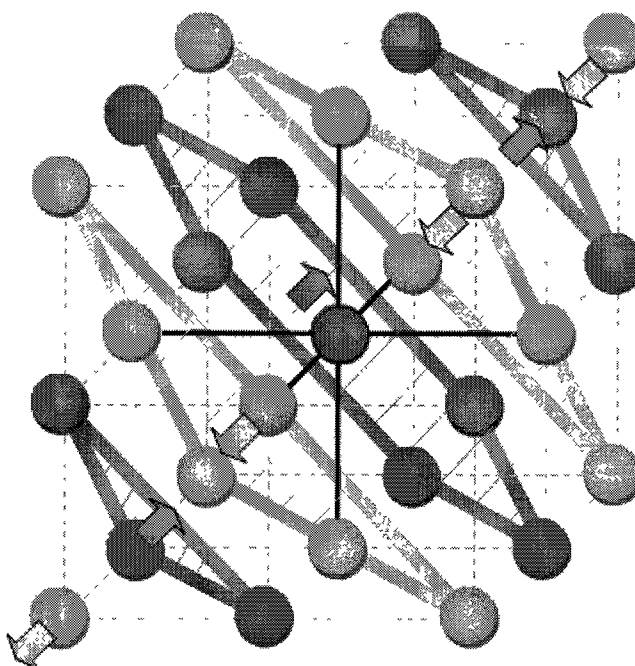


FIG. 1.1. Starting from the NaCl structure we can derive the A7 Peierls distorted structure of Sb by motion of atomic planes normal to the (111) axis in alternative direction, as indicated in the figure.²⁷

Throughout this dissertation I adopt the hexagonal system to represent diffraction patterns. The details and conversion between the rhombohedral and hexagonal representations will be given in Chapter 4. The hexagonal unit cell with the rhombohedral one is shown in Fig. 1.2, where atoms from the other sublattice are omitted except the one in the center, shown as an open circle.

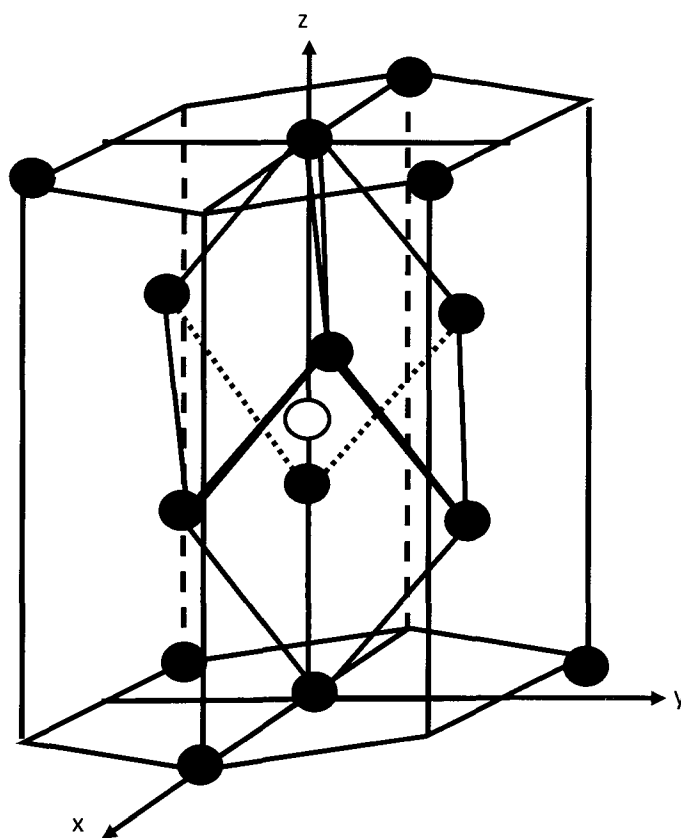


FIG. 1.2. The antimony A7 hexagonal unit cell with the rhombohedral one inside it. Atoms from the second sublattice are omitted for clarity.

Another way to describe the A7 structure is to start with a cubic structure (Fig. 1.3) where the (111) planes have an alternating displacement along the $[111]$ direction. Fig. 1.3 also shows the two vibration modes, A_{1g} and E_g . A_{1g} corresponds to a modulation of the (111) spacing, and E_g represents a sliding to the (111) planes.

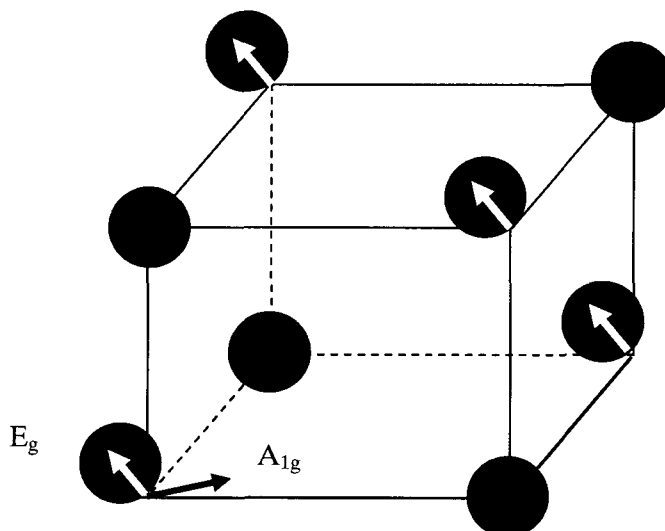


FIG. 1.3. The construction of the A7 structure from the simple cubic one. The A_{1g} and E_g phonon directions are indicated.²⁶

I.2. The structure of nanoparticles

Nanoparticles are of high interest to researchers in both basic science and applied fields. The small size that is between molecular and bulk ones, as well as the high surface-to-bulk ratios, drives interesting physical properties. Heat capacity, electron-phonon coupling, melting point, and nonlinear optical response are some examples for the properties that behave differently in the case of nanoparticles than that of a bulk. The geometry of nanoparticles allows for more complex phonon modes than that of a thin film where simple one-dimensional treatment is appropriate. Optical pump probe studies performed on tin and gallium nanoparticles showed acoustic phonon oscillations with a period of about 20 ps observable only in the case of larger size nanoparticles (220-250 Å).¹ Interesting phenomena associated with nanosize could be found but not necessarily anticipated; e.g., superheating of tin nanocrystals at 50 °C above the bulk's melting point was reported.⁶

I.3. Time-resolved electron diffraction studies

The application of an ultrafast laser pulse to the surface of a bulk metal or a thin film or nanoparticles brings about a number of interesting phenomena. The absorption of the pulse fluence is carried out by the electrons due to their large scattering cross-section. According to the two-temperature model (TTM), the electrons thermalize quickly (\leq hundred femtoseconds), then transfer their excitation energy to the lattice. The solid may undergo thermal or nonthermal melting, superheating, phase change ...etc. The transient phenomena following the absorbance of an ultrafast laser pulse take the order of a few hundred femtoseconds (photon-electron and electron-electron interactions) to several picoseconds (electron-lattice phonon interactions) and need to be studied with a fast probe that directly probes the lattice. Using an optical effect (reflection, refraction or transmission) to monitor the laser-induced phenomena will be greatly affected by the electron cloud rather than the lattice. The largest scattering cross-section for the lattice is achieved with the use of either X-ray or an electron pulse.

I.4. Previous studies on antimony nanoparticles

Electron diffraction studies on antimony nanoparticles are not abundant; we found three publications about the preparation conditions and the resulting diffraction patterns. The first of these three studies was done by Stein et al.² The electron diffraction patterns that were recorded are represented in Fig. 1.4. Pattern (1) was recorded in the presence of 1 Torr Ar gas for cooling, pattern (2) was taken without cooling gas, and pattern (3) was taken for a polycrystalline antimony thin film, for the sake of comparison. The first pattern shows small peaks that happen to match the position of those of the bulk's

diffraction pattern. No useful information can be extracted about the particle size or the exact structure due to the low level of the peaks. The second pattern has three broad peaks, or rather plateaus, that can be attributed to the amorphous structure of the nanoparticles.

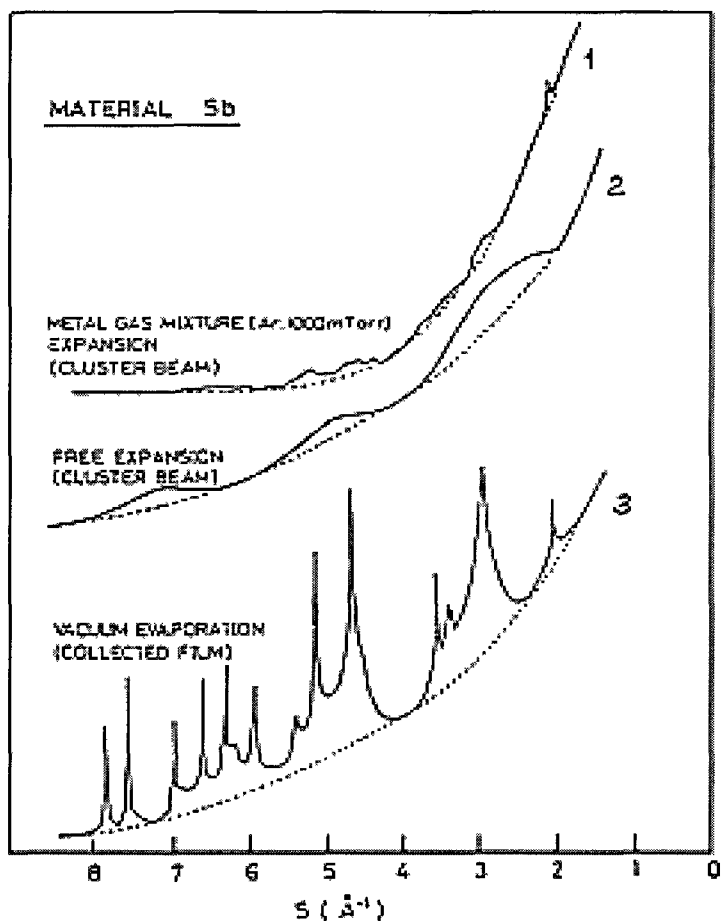


FIG. 1.4. Diffraction patterns of Sb nanoparticles.⁴

The second study was undertaken by Sun et al.³ who used He as a cooling gas instead of Ar. By increasing the He pressure to 1.3×10^{-3} Torr and keeping the source temperature at 1100 °C, they obtained three diffraction patterns that are almost identical.

The three diffraction patterns have three broad peaks whose amplitudes got larger with increasing He pressure (Fig. 1.5).

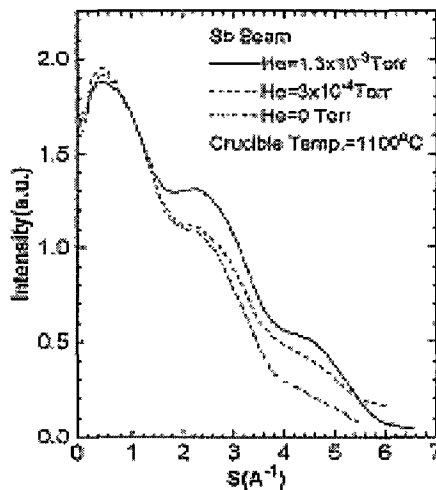


FIG. 1.5. Diffraction patterns of Sb clusters. The effect of the ambient gas is shown in the figure.³

In the third study, M. Kaufmann *et al.* studied Sb nanoclusters with mean size range of 20-40 nm prepared under an ambient inner gas. Their study found a phase change between crystalline and amorphous phases and particles composed of Sb₄ tetramers. Fig. 1.6 shows the diffraction pattern with background removed.

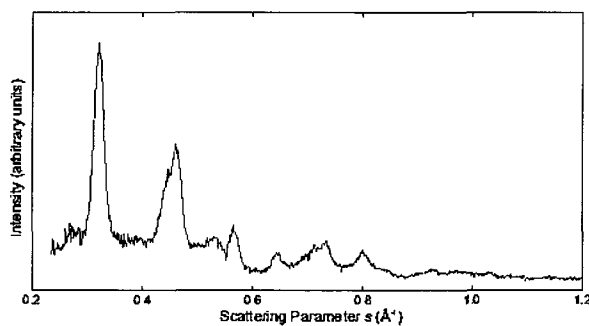


FIG. 1.6. Diffraction pattern for antimony nanoparticles with the background due to the cooling gas removed⁴.

I.5. Dynamic vibrational properties

Ultrafast optical excitation of nanoparticles and thin films will transfer some of the laser pump energy to the electrons. Electrons achieve internal thermal equilibrium through e-e collisions within about a hundred femtoseconds⁵ to a few picoseconds.⁶ For very thin films and small-sized nanoparticles, the electrons can be considered to be at thermal equilibrium even within the duration of the laser pulse. The excited electrons collide both with other electrons and with the lattice; but due to the huge difference between the masses of an electron and that of an atom, it takes much longer to reach thermal equilibrium between the electrons and the lattice. As electrons relax to an equilibrium Fermi-Dirac distribution, they are at a significantly higher effective temperature than that of the lattice. At this time the electrons transfer their excess energy to the lattice, resulting in exciting phonons which could be coherent in nature.⁷ Those coherent phonons are standing waves for a period dependent on the film thickness or the nanoparticles' dimensions. Optical pump probe experiments indicate that the electrons' pressure might play a role in generating the acoustic phonons.⁸

I.6. Photoinduced electrons as probe

The probing techniques for monitoring laser-induced ultrafast phenomena in nanoparticles, thin films and various targets are optical probes, laser-induced X-ray or photoinduced Ultrafast Electron Diffraction (UED). Optical probes deal mainly with the electrons, give no clear insight about the lattice, and are insufficient for studying phonons. Laser-induced x-ray probes are effective in monitoring the lattice and lattice phonons but their low signal-to-noise ratio²⁸ leaves a lot to be desired. In this work, UED

is the technique of choice. UED provides a means to study ultrafast structural dynamics with picosecond resolution and sufficiently high signal and signal-to-noise ratio. Fig. 1.7 shows the interpretation of an electron diffraction peak after performing radial integration.

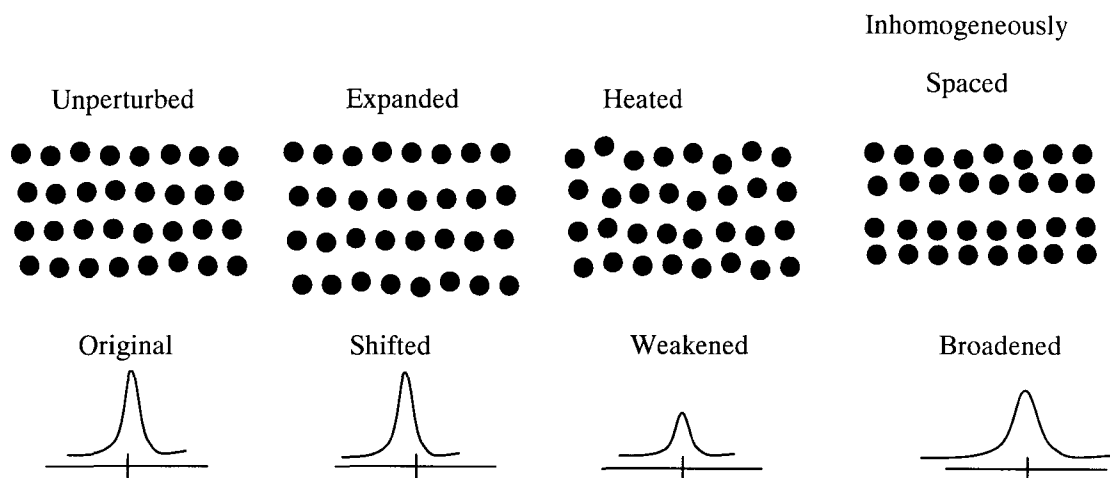


FIG. 1.7. Integrated Bragg peak correlated to the lattice planes that produce it²⁹

The UED method has a drawback, though, in that the electron pulse suffers broadening due to the electronic charge. The electrons' pack disperses in all directions as the pulse propagates, leading to a longer probe pulse. To keep the electron pulse as short as possible, it is necessary to shorten the propagating length and increase the acceleration energy. The details of this effect will be discussed later in the dissertation.

I.7. Previous work on group V semimetals

Studying the dynamics of the optical phonons (A_{1g} , E_g) of arsenic structure, semimetals became an attractive research topic in the past decade and is still under intensive investigation due to the availability of ultrafast lasers, time-resolved electron

diffraction, and time-resolved x-ray diffraction technologies. The frequencies of these two phonons at room temperature were determined by spontaneous Raman scattering to be 4.5 and 3.5 THz for antimony, and 2.9 and 2.2 THz for bismuth.^{9,10} Only fully symmetrical phonons (A_{1g}) were observed in early studies,^{11,12} which draws interest to the generation mechanisms. A Displacive Excitation of Coherent Phonons (DECP) mechanism was developed¹³ in which the atoms suffer an abrupt displacement from their equilibrium positions under the effect of the hot charge carriers and start oscillating about the new, temporary equilibrium positions. This mechanism was able to explain fully symmetric modes only, which alienated it from Raman scattering. Later studies were able to detect non-fully symmetrical modes of Sb, Bi, and Te.¹⁴⁻¹⁶ Theoretical studies proposed that DECP can be considered to be a special case of resonant Raman scattering in which both displacive and impulsive components exist.¹⁷

Bismuth drew the most attention, followed by antimony and tellurium, which is not from the arsenic group. Sokolowski-Tinten et al.¹⁸ pioneered the x-ray diffraction study of coherent optical phonons on bismuth. Bismuth attracted attention despite drawbacks such as the difficulty of producing single crystals of high quality and the localized generation of photoexcited photons at very shallow depths. On the other hand, bismuth has the advantages of generating high-amplitude, coherent, optical phonons with relatively low frequency and very strong phonon spectrum softening.^{19,20} Also, group V semimetals have a very strong electron-phonon coupling.

The A_{1g} phonon of bismuth was found to undergo frequency chirping.²¹ Phonon chirping is also called anharmonicity in the form of amplitude-dependent frequency. Double-pulse excitation experiments and theoretical calculation based on density

functional theory concluded that electronic softening of optical phonons and electron-hole plasma are responsible for the chirp.²¹ Further study of the electron-hole plasma effect at an excitation level of 1% of the valence electrons to the conduction band showed optical phonon softening over the entire frequency spectrum.²¹

Results for the A_{1g} phonon using ultrafast X-ray diffraction to measure the bond-softening induced quasi-equilibrium positions were confirmed. Calculations assumed that an electron-hole pair is generated for each absorbed photon.²¹ Since the electron-hole recombination time is generally much longer than the phonon period, the charge carriers establish Fermi-Dirac distribution in each band. The chemical potential sets different values for the conduction bands than the valence bands.

Depth-resolved studies concluded that the two-chemical potential model held only for the length of one phonon oscillation cycle followed by a transition to a single-chemical potential model.²² At strong photoexcitation it was found that the thermalization time for the photoexcited carriers is between 2-3 ps, which indicates rapid energy transfer from the charge carriers to the lattice.²³

CHAPTER II

THEORY

This chapter covers the physical models and mathematical treatments related to the different processes involved in our pump probe experiment. These processes include the electron-probe pulse broadening, the laser-pump beam interaction with the lattice through the electronic medium in what is known as the two-temperature model, and the Debye-Waller effect, which explains the drop in the diffraction intensity.

The effect of ultrafast laser excitation, even at low energy, on the electrons of a semimetal has a tremendous influence on the interatomic forces. Ultrafast laser pulses shorter than the energy-relaxation mechanisms in the lattice trigger lattice oscillations due to the alteration of binding forces. The generation of the coherent optical phonon (A_{1g}) can be explained by Impulsive Stimulated Raman Scattering (ISRS) and another mechanism through a sudden change in the equilibrium interatomic distance which is the bond-softening-induced weakening of the Peierls distortion. Therefore, it is also called Displacive Excitation of Coherent Phonons (DECP).

II.1. Electron pulse broadening

The probing technique in our work is an electron pulse generated by the frequency-tripled laser pulse. The electron pulse does not maintain the same pulse length as the laser pulse. The photoelectron pulse suffers broadening upon its release off the photocathode surface. The broadening begins in the acceleration region of the electron gun, followed by the most-effective broadening mechanism in the drift region.

The electrons of the photoelectron pulse interact among themselves in a way that broadens the pulse. Such an effect is called a space-charge effect. A mathematical treatment of the space-charge broadening is performed using one-dimensional and two-dimensional models. In the two-dimensional approach, the expression^{30,31}

$$V(z) = \frac{Ne}{2\epsilon_0\pi r_b^2} \left[\sqrt{z^2 + r_b^2} - z \right], \quad (2.1)$$

describes the on-axis potential distribution of an electron disk with radius r_b and length l , as shown in Fig. 2.1. The center of the electron disk is at $z = 0$. In Eq. (1), N is the total number of electrons in the electron pulse, e is the electron charge, and ϵ_0 is the vacuum permittivity.

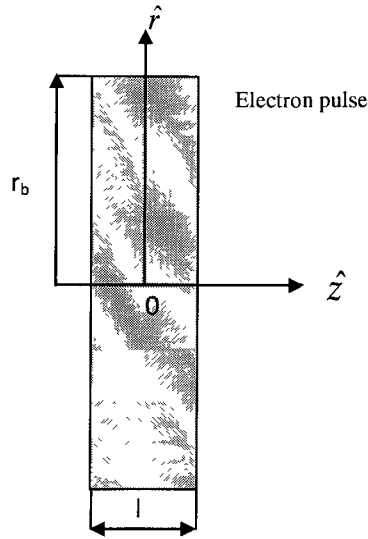


FIG. 2.1 An electron pulse disk simulating a drifting femtosecond photoelectron pulse.³⁰

The Poisson equation for the problem of Fig. 2.1 can be written as

$$\frac{1}{r} \frac{\partial}{\partial r} \left(r \frac{\partial \phi}{\partial r} \right) + \frac{1}{r^2} \frac{\partial^2 \phi}{\partial \theta^2} + \frac{\partial^2 \phi}{\partial z^2} = \frac{en(r, \theta, z)}{\epsilon_0}, \quad (2.2)$$

where $\phi \equiv \phi(r,t,z)$ is the potential distribution in free space and $n \equiv n(r,\theta,z)$ is the electron density. In order to solve Eq. (2.2), one can use the Green's function

$$G(r, r', \theta, \theta', z, z') = \frac{1}{\sqrt{r^2 + r'^2 - 2rr' \cos(\theta - \theta') + (z - z')^2}}, \quad (2.3)$$

satisfying,

$$\frac{1}{r} \frac{\partial}{\partial r} \left(r \frac{\partial G}{\partial r} \right) + \frac{\partial^2 G}{\partial z^2} = -\frac{4\pi}{r} \delta(r - r') \delta(\theta - \theta') \delta(z - z'). \quad (2.4)$$

The details of the solution can be found at Ref.(30). The solution to the propagation model is presented in Fig. 2.2, which also shows a comparison between the developed two-dimensional model and the one-dimensional fluid model. Fig. 2.2(a) shows the electron pulse broadening $\Delta t = l/v_b$ (where v_b is electron pulse velocity) as a function of electron pulse drift time t for initial electron pulse duration of $T = 50$ fs, electron initial energy of 30 keV, $r_b = 0.4$ mm, and $N = 1000$. Fig. 2.2(b) shows the electron energy spread ΔE as a function of electron pulse drift time t for initial electron pulse duration of $T = 1000$ fs, electron initial energy of 30 keV, $r_b = 0.1$ mm, and $N = 5000$. Fig. 2.2(c) shows the electron pulse broadening Δt as a function of electron pulse drift time t for initial electron pulse duration of $T = 1000$ fs, electron initial energy of 30 keV, $r_b = 0.1$ mm, and $N = 5000$. Fig. 2.2(d) shows the electron energy spread ΔE as a function of electron pulse drift time t for initial electron pulse duration of $T = 3000$ fs, electron initial energy of 30 keV, $r_b = 0.4$ mm, and $N = 3000$ in the cases of one- and two-dimensional models.

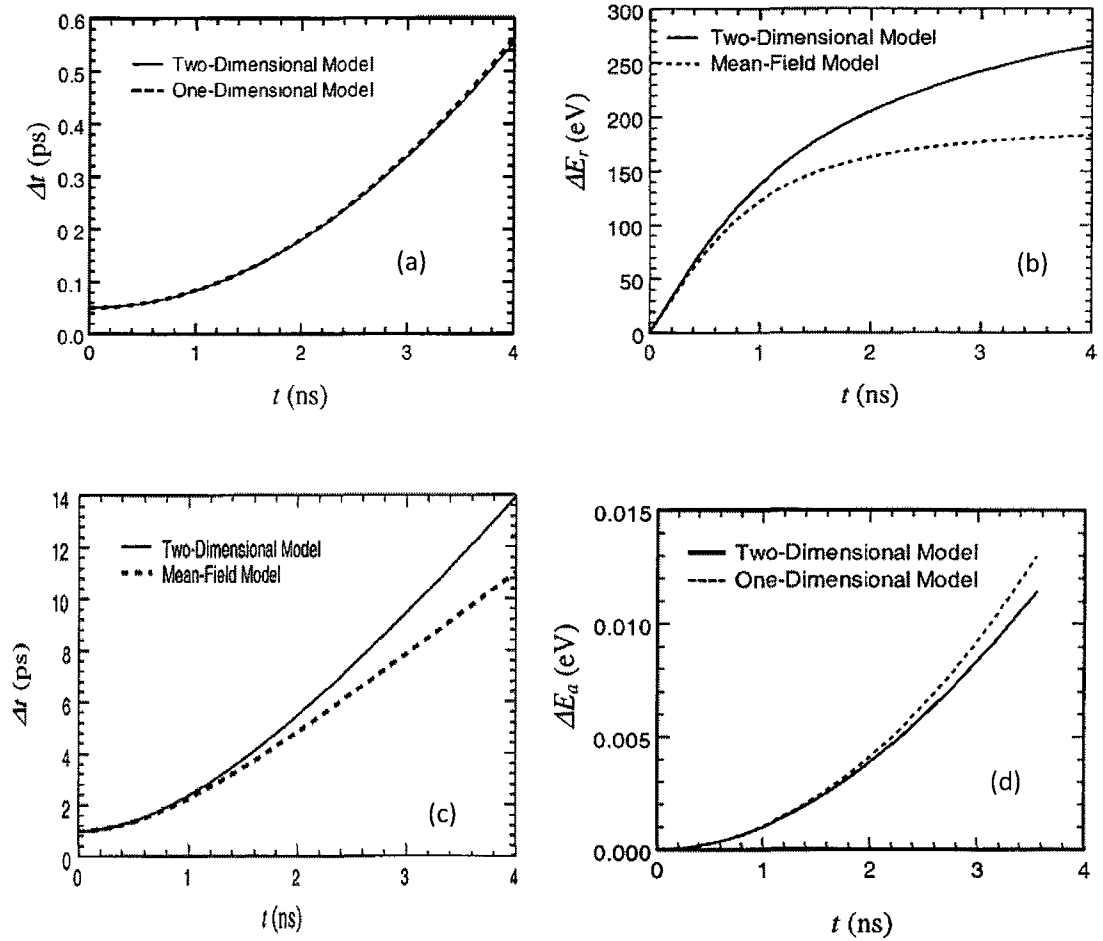


FIG. 2.2 (a) The electron pulse broadening Δt as a function of EP drift time t for initial EP duration of 50 fs, electron initial energy of 30 keV, $r_b = 50.4 \mu\text{m}$, and $N = 1000$. (b) shows the electron energy spread ΔE as a function of electron pulse drift time t for initial electron pulse duration of $T = 1000$ fs, electron initial energy of 30 keV, $r_b = 0.1$ mm, and $N = 5000$. (c) shows the electron pulse broadening Δt as a function of electron pulse drift time t for initial electron pulse duration of $T = 1000$ fs, electron initial energy of 30 keV, $r_b = 0.1$ mm, and $N = 5000$. (d) shows the electron energy spread ΔE as a function of electron pulse drift time t for initial electron pulse duration of $T = 3000$ fs, electron initial energy of 30 keV, $r_b = 0.4$ mm, and $N = 3000$ in the cases of 1D and 2D models.³⁰

As can be seen from Fig. 2.2(a), the results of both the one- and two-dimensional models almost coincide because the parameters satisfy the condition of one-dimensional model limit $l/r_b \ll 1$.

Due to the one-dimensional limit, the one-dimensional model is suitable for analyzing femtosecond photoelectron guns, but it becomes inaccurate when the electron

pulse duration develops into the picosecond regime, especially for the smaller electron-beam radius.³⁰

II.2. Hot carrier dynamics

The femtosecond laser pulse triggers a burst of hot electrons of energy up to $h\nu_0$ above Fermi level, where $h\nu_0$ is the photon energy. Depending on the pumping strength, the excited, nonequilibrium electrons travel through the material with ballistic speeds prior to establishing an electron temperature. The ballistic range is expected to cover the entire length of our samples, both thin films and nanoparticles. For example, in the case of Au,³⁸ the speed of the ballistic electrons is in the range of 10^6 m/s, which means that the ballistic range can reach 100 nm for 100 fs laser pulse. Following the photon-electron interaction is an electron-relaxation process dominated by electron-electron collisions. The duration of this stage is determined by the density of states at the Fermi level. The duration of this stage is typically in the range of 10^{-14} s, thus the electronic system is considered to be at equilibrium during the lifetime of the laser pulse. Having established Fermi-Dirac distribution, the electronic collisions with the lattice transfer the excess thermal energy of the electrons that are now at much higher temperature than the lattice to the crystal until thermal equilibrium is achieved. Fig. 2.3 shows the phases of the electron dynamics following the laser pulse.

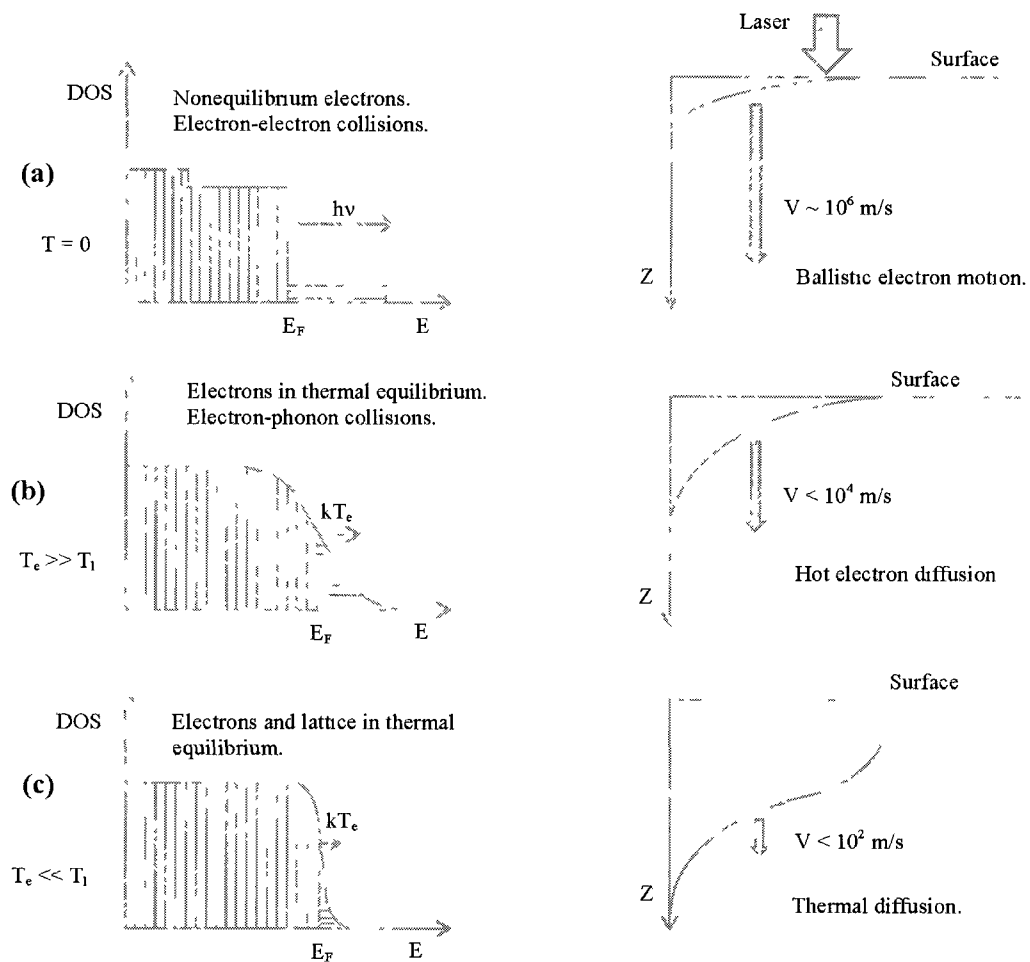


FIG. 2.3 Stages of the electron distribution following optical excitation. (a) High nonequilibrium in the electron distribution. (b) Electrons at equilibrium at a much higher temperature than the lattice. (c) Electrons and lattice at thermal equilibrium.³¹

Following the electron-electron thermalization, the hot electrons establish a Fermi-Dirac distribution and the use of the term “temperature” becomes justified. Following the thermalization of electrons, electron-phonon collisions become predominant until both the electronic system and the lattice are at thermal equilibrium. The next section gives a detailed treatment of this process.

II.3. Two-temperature model (TTM)^{31-32,40}

The most acceptable scenario is that laser energy is absorbed into the sample via photon-electron interactions, and the electrons are driven to a highly excited state of nonequilibrium but only for a few tens of femtoseconds. Electrons regain an equilibrium Fermi distribution within a few hundreds femtoseconds that they can be considered to be at equilibrium during or shortly after the interaction with the laser pulse. While the laser pulse and electron-electron collisions are of comparable durations, the energy transfer from the electrons to the lattice phonons takes many collisions due to the small mass of an electron in comparison to a lattice constituent. The time it takes the electrons to reach thermal equilibrium with the lattice phonons is termed thermalization time.

For the sake of this mathematical analysis, it is practical to consider the laser beam diameter to be much larger than both the optical and electron penetration depths, hence the one-dimensional treatment is justified.

$$C_e \frac{\partial T_e}{\partial t} = \nabla (K_e \nabla T_e) - G(T_e - T_l) + S(z, t) \quad (2.5a)$$

$$C_l \frac{\partial T_l}{\partial t} = G(T_e - T_l) \quad (2.5b)$$

where C_e is the electronic heat capacity, C_l is the lattice heat capacity, T_e is the electron temperature, T_l is the lattice temperature, K_e is the electrons thermal conductivity, and G is the electron-lattice coupling coefficient.

The first equation represents the increase in the electron temperature due to the external source (laser). The second step is the heating of the lattice by means of the hot electrons.

Equations (2.5a) and (2.5b) provide two equations for two unknowns, the electron-gas temperature T_e and the metal-lattice temperature T_l . They can be solved in a coupled manner, or they can be combined to give a single-energy equation describing heat transport through phonon-electron interaction.

The complexity of solving Eqs. (2.5a) and (2.5b) lies in the temperature-dependent heat capacity of the electron gas, i.e., $C_e \equiv C_e(T_e)$. For an electron-gas temperature lower than the Fermi temperature, the electrons' heat capacity is proportional to the electron temperature. Such temperature dependence makes Eqs. (2.5a) and (2.5b) nonlinear. The electron-phonon coupling coefficient characterizes the energy exchange and is given by

$$G = \frac{\pi^2}{6} \frac{m_e n_e v_s^2}{\tau_e T_e}, \quad (2.6)$$

for $T_e \gg T_l$, where m_e is the electron mass, n_e is the electron density and v_s

is the speed of sound, where

$$v_s = \frac{k_B}{2\pi\hbar} (6\pi^2 n_a)^{\frac{1}{3}} \theta_D. \quad (2.7)$$

Then, the coupling coefficient can be written as

$$G = \frac{\pi^4}{18} \frac{(n_e v_s k_B)^2}{K}. \quad (2.8)$$

It is clear that G shows a dependence on the thermal conductivity, K ; the atomic number density, n_a ; and the Debye temperature, θ_D . To obtain the single-energy equation governing either the lattice or the electron temperature, one can proceed by assuming all thermal properties, including heat capacities of the electron gas and the metal lattice as

well as the thermal conductivity, to be temperature-independent. Then, by obtaining the electron temperature, T_e , as a function of the lattice temperature T_l , from Eq. (2.5b) and substituting in Eq. (2.5a), we get

$$T_e = T_l + \frac{C_l}{G} \frac{\partial T_l}{\partial t}, \quad (2.9)$$

$$\nabla^2 T_l + \left(\frac{C_l}{G} \right) \frac{\partial}{\partial t} \nabla^2 T_l = \left(\frac{C_l + C_e}{K} \right) \frac{\partial T_l}{\partial t} + \left(\frac{C_l C_e}{KG} \right) \frac{\partial^2 T_l}{\partial t^2}. \quad (2.10)$$

A similar equation describing the electron temperature can be obtained in the same manner by using

$$T_l = T_e - \frac{K}{G} \nabla^2 T_e + \frac{C_e}{G} \frac{\partial T_e}{\partial t}. \quad (2.11)$$

Heat conduction through the metal lattice is neglected in Eq. (2.5b). However, when the transient time lengthens or the physical domain becomes too thick, heat conduction may become appreciable and should be included. Thus, the second coupled equation becomes

$$C_l \frac{\partial T_l}{\partial t} = K_l \nabla^2 T_l + G(T_e - T_l), \quad (2.12)$$

where K_l is the thermal conductivity of the metal lattice.

Fig. 2.4 illustrates an application of the TTM for Au and Ni 100 nm films with an applied 200 fs laser pulse with wavelength 400 nm and fluence of 23 mJ/cm².

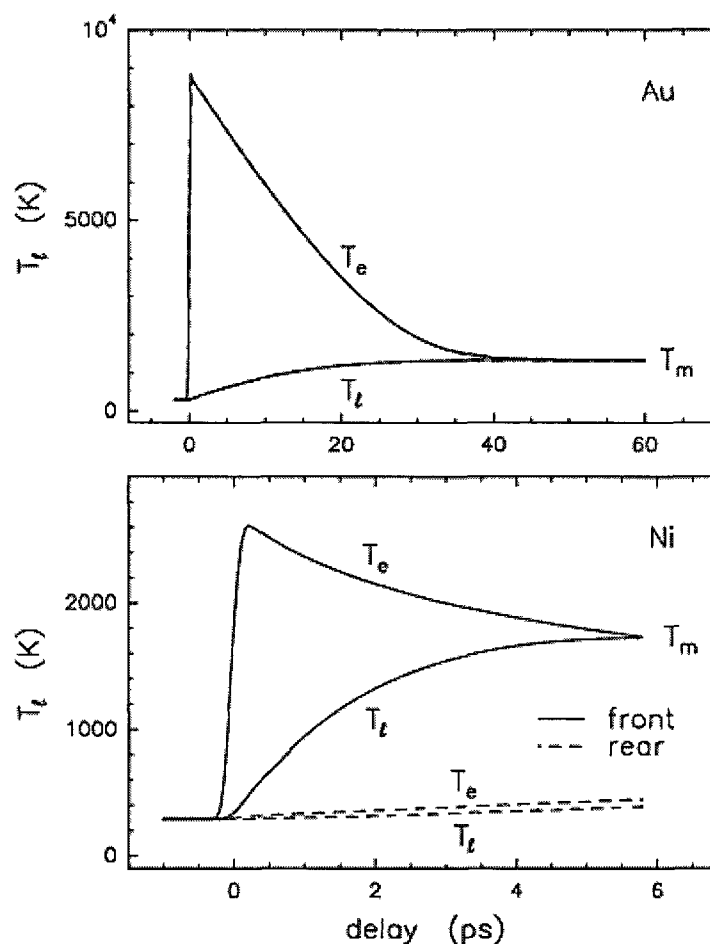


FIG. 2.4 The temporal profile of 100 nm films of Au and Ni irradiated by a 200 fs laser pulse of 400 nm wavelength. The TTM is used for a laser fluence of 23 mJ/cm^2 . The dashed line is used to show the back of the film; for Au the front and rear surfaces follow perfectly.³¹

II.4. Debye-Waller factor

The Debye-Waller effect is the attenuation of Bragg peaks as the temperature of the lattice rises. As the temperature of the lattice increases, the mean vibrational amplitude of the lattice atoms also increases, causing a reduction in the diffraction intensity. Thermal energy increases the temperature of the crystal and fuels inharmonic,

thermal atomic vibrations. The attenuation due to the Debye-Waller effect is expressed as³³⁻³⁴

$$I(Q, T) \propto \exp(-2M), \text{ i.e.,}$$

$$I(Q, T) = I_0(Q, T_0) \exp(-2M), \quad (2.13)$$

where $\mathbf{Q} \equiv \hbar(\mathbf{k}_f - \mathbf{k}_i)$ is the momentum transfer vector of the scattered electrons, and $2M$ is the Debye-Waller factor along the direction of \mathbf{Q} . The Debye-Waller factor could be expressed as

$$2M = \langle u_Q^2 \rangle Q^2, \quad (2.14)$$

where $\langle u_Q^2 \rangle$ is the mean square atomic deviation in the direction of \mathbf{Q} .

For cubic basis crystals, $\langle u_Q^2 \rangle$ will be simplified to $\langle u^2 \rangle$ due to isotropy. The mean square elastic deviations $\langle u^2 \rangle$ is related to the diffraction intensity, so measuring the integrated intensity of an elastic scattering over small temperature increments ΔT , $\langle u^2 \rangle$ could be measured through the expression

$$\Delta \langle u^2 \rangle \approx Q^{-2} \Delta \ln [I(Q, T)]. \quad (2.15)$$

A measurement at a given temperature should be taken as a reference, and then the variations from that point could be calculated with the help of the previous equation.

II.5. Two-temperature model (TTM) simulation

Ultrafast laser heating of metals has distinctive mechanisms of energy transfer due to temporal pulse width and physical dimensions of the metal film. Classical large

scale models lose their fidelity when the metal film dimensions are of the same order as the electron mean free path or when the laser pulse width is less than the electron-phonon interaction time. Those models, namely, Fourier heat conduction law and parabolic one-step model, are unable to reliably describe the energy transfer in the case of ultrafast laser heating of metal thin films. As an upper limit, when the film thickness becomes of the same order of magnitude as the mean free path of energy carriers, the physical foundation of the Fourier model loses its ground. This is due to the collapse of the concept of temperature gradient because of the lack of sufficient carriers within the film. Therefore, defining the heat flow vector in the conventional way becomes invalid.

Since an analytical solution for Eqs. 2.5(a, b) is unavailable, we resort to numerical solution methods. Several groups^{6,7} have developed their own numerical techniques or used existing options in some complex software libraries in order to solve that set of coupled equations. In our case we decided to use FlexPDE[®] for its ease of use and flexibility. Figure 2.5 shows the TTM simulation for a 20 nm Sb film.

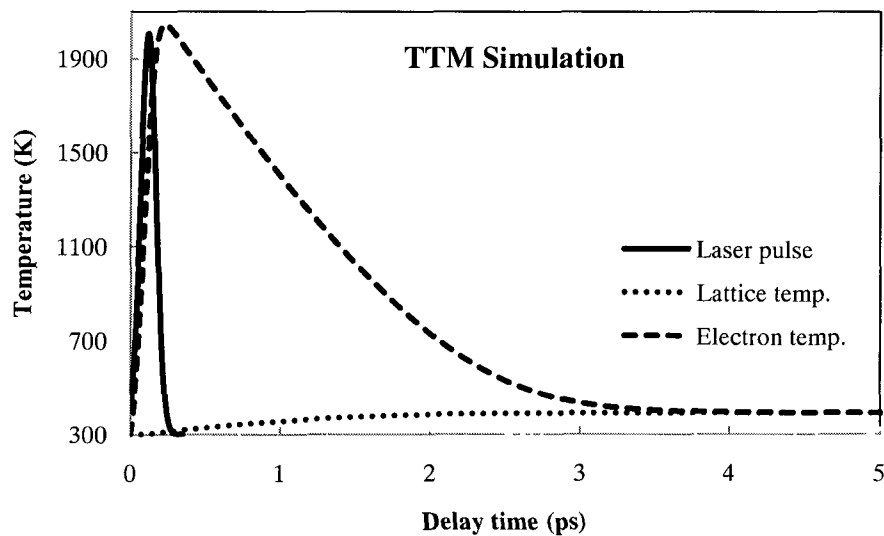


FIG. 2.5 TTM simulation of Sb thin film 20 nm thick. The code is run in FlexPDE[®].

Thermal-insulation boundary conditions were used so as to constrain the sides of the sample to the ambient temperature and neglect any heat losses from the back surface. The electron and lattice temperature were used as the two variables for which the equations are to be solved. The initial conditions for the electron and the lattice systems were chosen as $T_e = T_l = T_a = 300$ K. All the details of the application of this numerical solution and code algorithm can be found in Ref. (37).

CHAPTER III

EXPERIMENTAL SETUP

III.1 Sample preparation

The method of choice for our sample preparation is thermal deposition in a high vacuum chamber. The vacuum chamber is pumped down using a turbomolecular pump to the 10^{-6} torr range. After the vacuum is appropriate for the process of thermal deposition, the tungsten filament that is used to host the deposition material is heated until the deposition starts. Tungsten is suitable because of its high melting point and low vapor pressure. The filament is heated using resistive heating in the following manner. A Variac is plugged into a 110 V outlet with the output connected to a 10:1 step-down transformer. The output of the transformer goes through a high-current feedthrough to the filament. In our lab setting, the voltage value at the Variac is about 12 V for the antimony deposition, and it varies significantly for different materials, with gold, chromium and platinum requiring the maximum output level of power our system can deliver.

The produced vapor condenses on the inside walls of the chamber including the substrate. In the case of antimony nanoparticles, the substrate is a thin graphite film (< 10 nm) on top of a 400 mesh grid (400 holes per inch). The thin carbon film is almost transparent for our electron beam and the 400 mesh grid has a transmission of 35%. A crystal thickness monitor is used to monitor the deposition progress. To produce well-dispersed nanoparticles with decent coverage (for practical electron diffraction pattern intensity), we found that a mean thickness of 5 nm is ideal. Crossing to, or exceeding, 10 nm will produce a continuous film rather than nanoparticles.

To increase the diffraction intensity without the risk of increasing the mean thickness that would produce a continuous film, we found it worthwhile to prepare one film on each side of the carbon film, thus doubling the diffraction intensity without changing the morphology of the sample. The tungsten filament is loaded with a few small pieces with a total weight of about a gram. After the deposition process had ended, the antimony pieces are found to be without any significant change in shape, which indicates that antimony has a very high vapor pressure and tends to sublime rather than melt and/or boil for the vapor pressure to be significant. In metals with low-vapor pressure, like aluminum, the loaded material has to melt and reach the boiling point for the deposition to start.

Several samples were investigated while the system was still being improved for reliable data collection. Those samples included aluminum, silver, gold, and bismuth. The samples were in the form of free-standing or deposited on a thin carbon support film. In the early stages of the experimentation, films of thickness varying between 20 to 40 nm and from polycrystalline to singly crystalline of the above-mentioned elements were prepared and studied briefly before attention was directed to antimony nanoparticles and 20 nm thin films. The antimony samples (Alfa Aesar[®], 99.999% 1-4 mm pieces, stock # 11676) were loaded into the tungsten filament, Fig. 3.1.

Some of the solids we tried showed a better ability to form well-isolated nanoparticles than others. In this experiment, we found that antimony produced the best-quality nanoparticles compared to the others that we tried. The other materials that we tried tended to form more flattened and continuous thin films. There is a trade-off; nevertheless, in this thickness range the diffraction intensity is directly proportional to the

film thickness.

Because they are grown on an amorphous carbon substrate film, the resulting nanoparticles do not have a preferred growth direction; and they are grown amorphous, as shown by the TEM images in the following chapter. After the samples have been mounted in the electron diffraction vacuum chamber, we heat them slowly to a 200 °C temperature. After the annealing process is over, the isolated nanoparticles become crystalline with no collective alignment or any kind of correlation between each other. The resulting electron diffraction pattern is, therefore, that of a polycrystalline film, i.e., concentric rings.

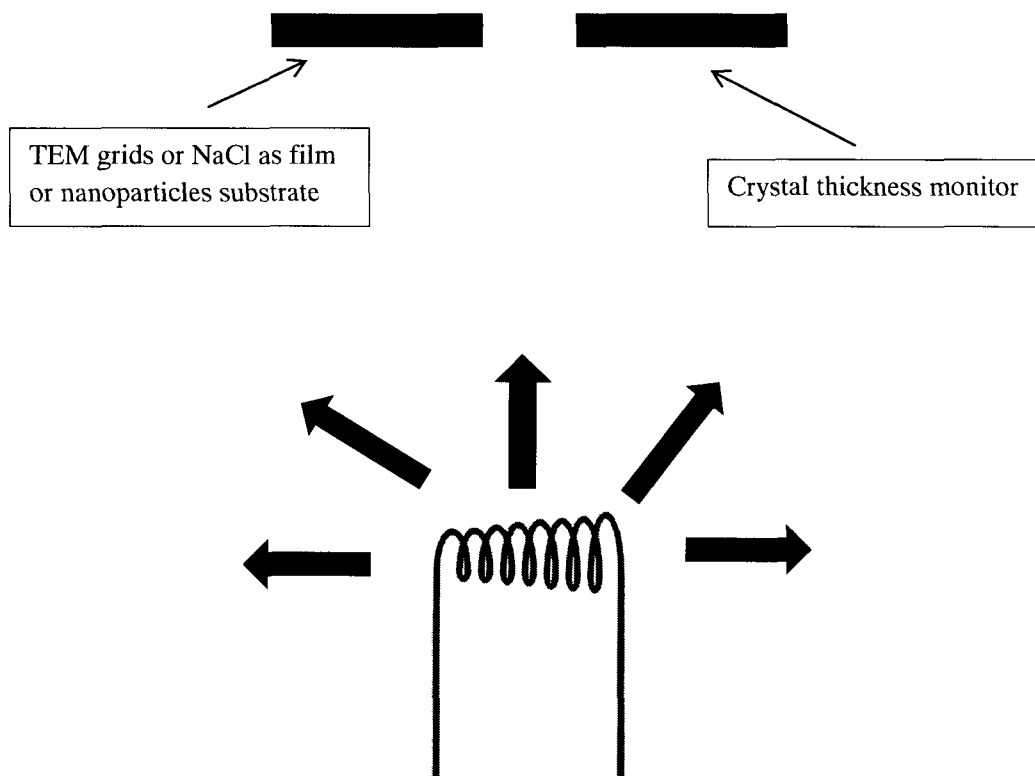


FIG. 3.1 The tungsten filament that we used for depositing Sb thin films and nanoparticles

The variation of the intensity of the diffracted pattern, as a function of probe delay, probes the lattice dynamics on the atomic level. Among the applications of the electron diffraction patterns, the Debye-Waller effect can give the temperature rise due to a given drop in the diffraction pattern intensity. The diffraction pattern rings shrink in size as the lattice expands with the rising temperature. The thickness of the rings may indicate anharmonicity in lattice spacings. These are examples of the physical parameters characteristic of the transient nature following the effect of a pump pulse that we can extract from a time-resolved scan. The TEM grids that we used are (Pacific Grid Tech.) 400 Mesh Cu pre-coated with thin carbon film. The carbon film thickness is < 10 nm, per the manufacturer's specifications.

III.2 Electron gun

The electron gun is the heart of Ultrafast Electron Diffraction (UED) time-resolved pump-probe scans. Part of the laser beam is utilized to generate an electron pulse which is energized to 35 keV and focused onto a microchannel plate (MCP) detector, followed by a phosphorous screen. There are three main techniques used to probe the lattice in a time-resolved scan. Low-energy lasers are used mainly to monitor the change in reflectivity following the application of a strong laser-pump pulse; such technique is desired for the experimental simplicity and non-broadening of the pulse width. A major drawback for this technique is the interference of the electronic cloud with the lattice signal. X-ray is another probe that was successfully used to probe ultrafast phenomena in solids. While pulse broadening is not a threat here either, the signal-to-noise ratio is very low and the experimental complexity is the highest.

The choice of the probe makes for the centerpiece of any time-resolved experiment. As we have seen, there are optical, x-ray, and electron beam probes. In choosing any of these, we need to fulfill a number of conditions. A good probe must have a large cross-section for elastic scattering with the lattice, i.e., diffraction, no or minimal interaction with the electron cloud of the sample, decent signal-to-noise ratio, minimal experimental complexity, minimal pulse width broadening, stability, reproducibility, minimal effect on the sample, and probe size at the sample must be smaller than that of the pump.

With these conditions in mind, we chose to go with the electron beam. There are no commercially available photo-activated electron guns, so we had to design and build our own. The structure of the electron gun is shown in Fig. 3.2. The photocathode is a 25 nm silver thin film deposited on a sapphire window. The work function of silver is 4 eV, so the 800 nm (1.55 eV) laser wavelength is tripled before it hits the photocathode. The photoelectrons are accelerated normally to the surface due to the applied -35 kV on the photocathode. The photoelectron beam goes through a grounded mesh followed by a 200 μm pinhole.

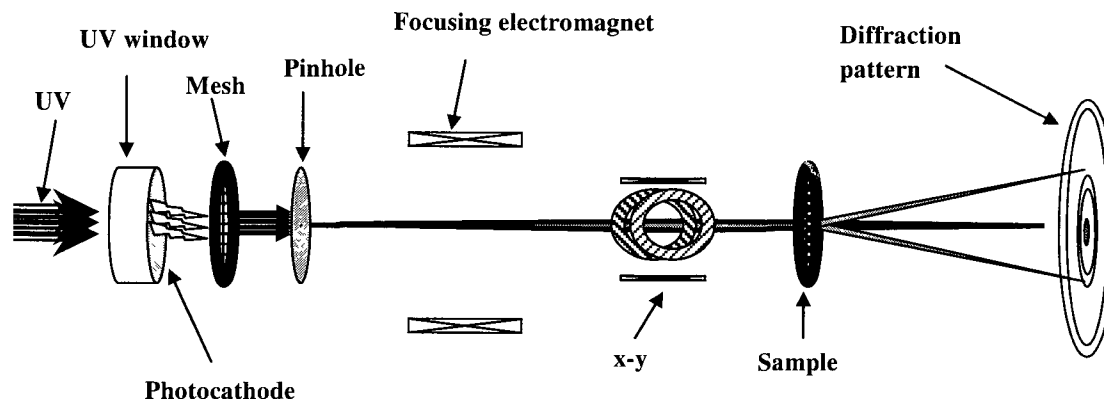


FIG. 3.2 The configuration of the photoactivated electron gun. The frequency tripled laser beam hits the Ag thin film deposited on a sapphire window and generates an electron pulse. The photoelectrons accelerate due to the biasing of the photocathode (~ 35 keV) to the grounded mesh. A $150\text{-}200\ \mu\text{m}$ pinhole follows the mesh; then the electrons drift freely to the sample. An external electromagnet is used to focus the e-beam and two smaller pairs of electromagnets are used to direct the e-beam in the x-y directions.

After leaving the pinhole, the electrons drift through the field-free region towards the sample. The electron beam leaves the pinhole and drifts towards the target with some divergence due to the Coulomb's repulsion between the electrons. The focusing of the e-beam is done by applying a magnetic field which is generated by an external electromagnet. The electromagnet consists of a wrapped copper wire (~ 200 turns) wound around the external of the nipple just past the pinhole. A DC current (~ 4 A) was found to be sufficient to focus the laser beam on the MCP to a minimal spot size (~ 0.4 mm). The e-beam is manipulated in the (x) and (y) directions with 2 pairs of smaller electromagnets placed just past the focusing electromagnet.

The e-beam pulse stretches as it propagates in the chamber due to the Coulomb repulsion between the electrons, an effect that is called space-charge effect. Reducing the distance between the e-gun and the sample helps in reducing the space-charge effect; also

reducing the number of electrons per pulse helps reduce the pulse stretching. The details of the pulse broadening were given in the previous chapter.

The distance between the photocathode and the mesh is 3.7 mm, resulting in a field strength 9.8 kV/mm. Such high field strength can give rise to a major problem that we faced in operating our high-voltage e-gun; that is, the discharge that can happen in various parts of the e-gun either glow (constant) or arc (pulsing) discharge. To minimize the occurrence of any discharge, the e-gun metal components were polished to a near-mirror finish and the machinable ceramic (Macor[®]) was neatly handled and rigorously cleaned.

III.3 Sample holder/heater

Just as the e-gun was home-designed and built, the sample holder was also designed and built in the same fashion. Once the samples are prepared they must be moved quickly into vacuum to reduce the chance of oxidization. The sample holder was built with the capacity to hold 10 TEM grids. The sample holder is mounted on an x-y-z-rotatable manipulator to place the samples in the pump-probe beams intersection point. Once we have the samples inside the vacuum chamber, we need to be able to heat them to a certain temperature either for sample annealing or temperature scans, so we designed the sample holder to also be a heater. That was done by using resistive heating by means of running a molybdenum wire through ceramic rods inserted in the heater body. A thermocouple is placed in contact with the heater surface to monitor the temperatures of the heaters and samples.

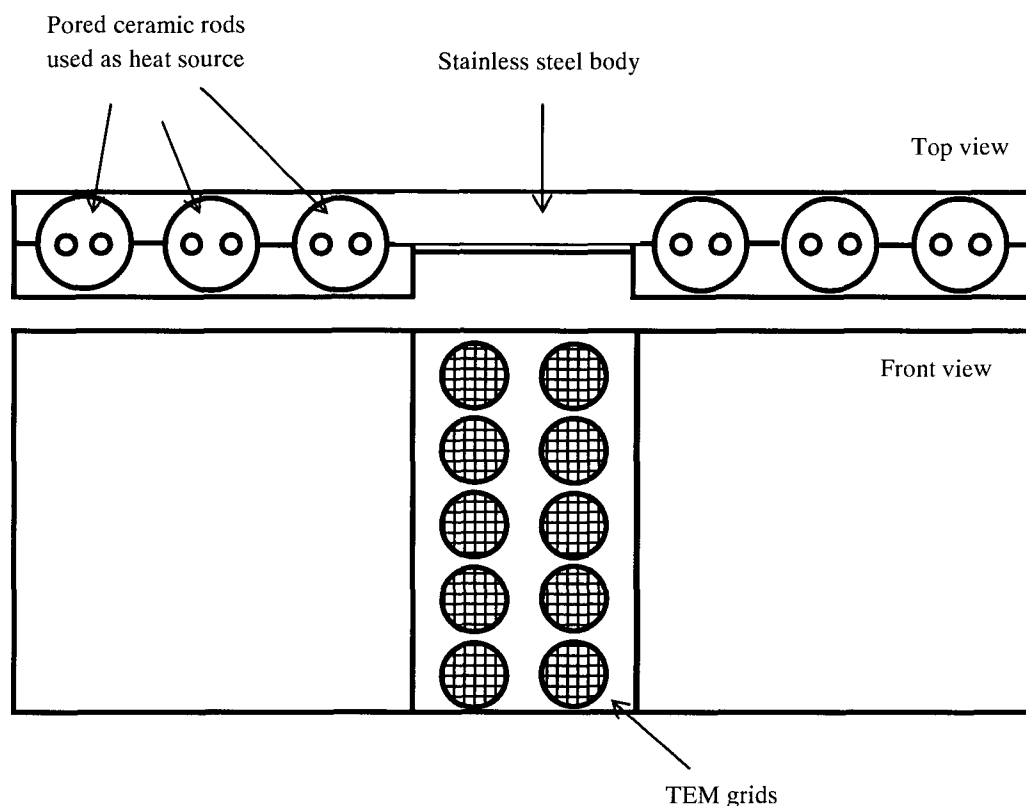


FIG. 3.3 Schematic of the sample holder/heater. The sample holder is made from stainless steel and can hold up to 10 samples. There is a thermocouple placed near the samples and connected to a temperature controller for sample heating.

III.4 Diffraction pattern imaging

The diffracted beam is very weak and needs to be amplified before it can form a tangible pattern on the phosphor screen. We used a Chevron (Burle Industries, Inc.) configuration of Multi-Channel Plates (MCP) to amplify the pattern by about a million times followed by a phosphorus screen that is deposited on a one-to-one fiber optic faceplate. The image that is formed on the phosphorus screen is then acquired by an electrically cooled CCD camera. The details of MCP design and functionality are given in Fig. 3.4.

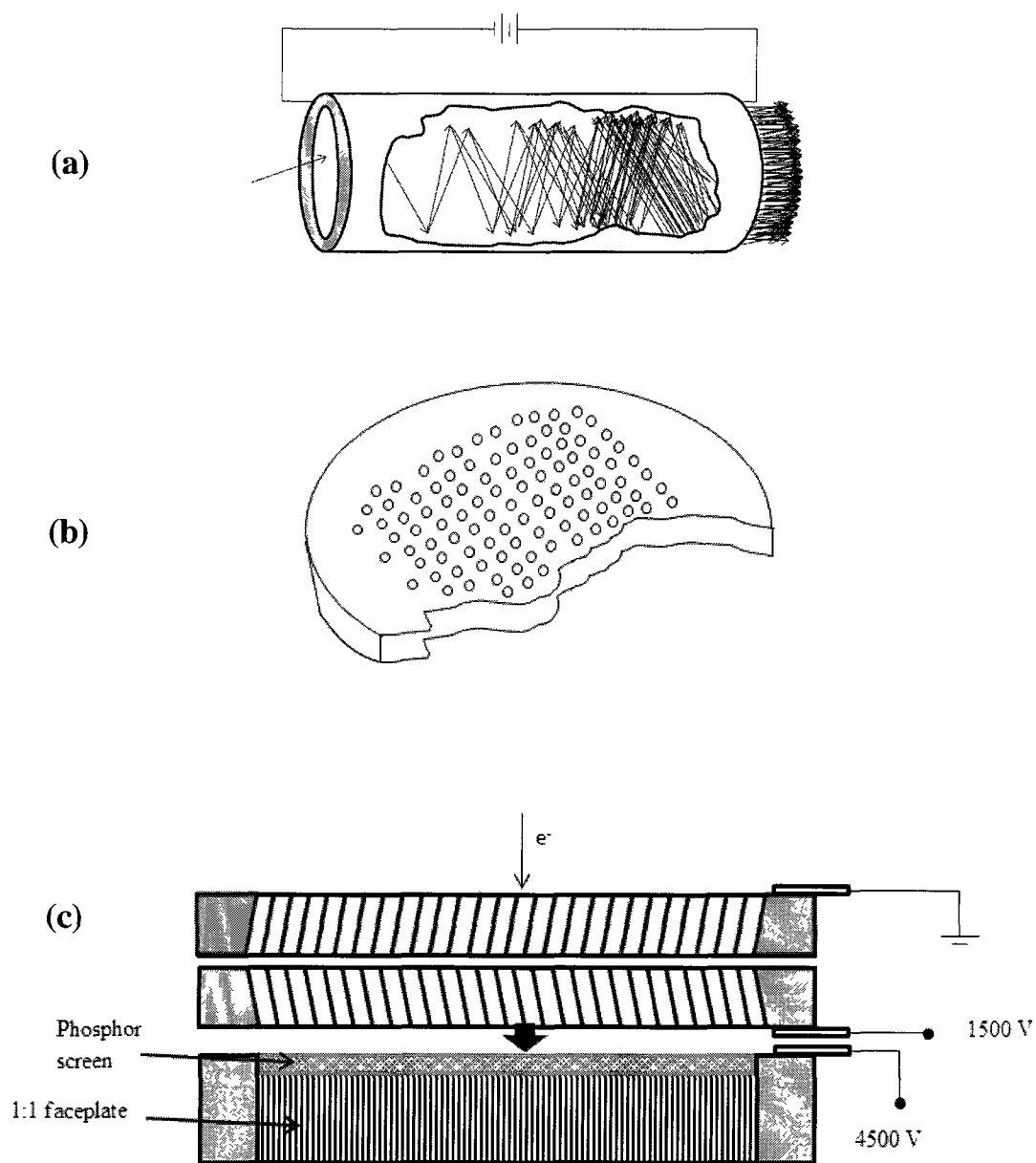


FIG. 3.4 MCP detector/signal amplifier. a) amplification of a single channel, b) a single MCP, c) Chevron configuration with biasing coupled to a phosphorus screen faceplate.

III.5 Optical and experimental setup

The laser system is the most essential component in our experimental setup. The long- and short-term stability and the beam profile quality are very important to be reliable. There are four optical components to the laser; namely, the oscillator, the oscillator pump laser, the regenerative/multipass amplifier, and the amplifier pump laser. There are also electronic controls and environmental conditions to manage when running the laser. The oscillator is a Spectra physics Tsunami laser pumped with a diode-pumped Nd:YLF Spectra physics Millennia laser that provides 5 W of 527 nm CW laser. Details of the self-mode locking and chirped pulse amplification cannot be hosted here. More information can be found at the manufacturer's website.

The optical-setup part of the system is illustrated in Fig. 3.6. The laser output is split 50:50 and one part is directed towards a half wave plate – polarizing beam splitter combination to control the pulse energy that we apply to the sample. Following the polarizing beam splitter, the laser beam goes through a Galilean beam reducer to a beam diameter of ~2 mm at the sample location. The input window reflects 8% of the input and the laser beam hits the sample with 45° angle. We measure the beam size at the target equivalent plane by placing a mirror after the beam reducer and perform a knife-edge x-y scan to the laser beam. The result of the profile scan is shown in Fig. 3.5; for the horizontal scan, the diameter for Gaussian beams is measured at 90% - 10% of the energy. The beam area is 2 mm^2 ($2 \cdot \sqrt{2} = 2.83 \text{ mm}^2$ corrected for the 45% angle of incidence).

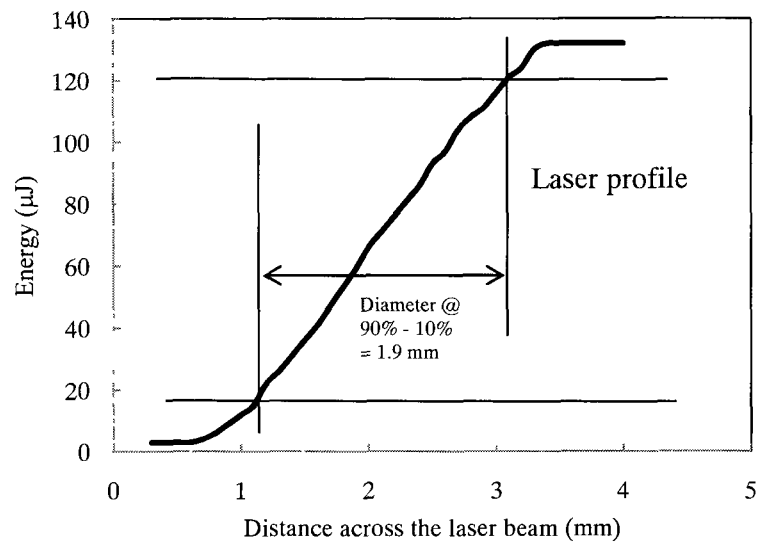


FIG. 3.5 The beam profile of the pump laser at the target equivalent plane. The area is 2 mm^2 .

The other half of the laser beam that gets reflected off the surface of the beam splitter is directed towards the delay stage; then the frequency tripling BBO crystal set. The three frequencies that leave the BBO crystals are reflected by two narrow-band dielectric mirrors for Nd:YAG fourth harmonic (264 nm), which is suitable for 3ω of the 800 nm (266 nm) wavelength. The residual first and second harmonics that reach the fused silica window are too weak to have an effect on the photocathode of the e-gun. The frequency tripled laser is lightly focused before it hits the photocathode. The number of electrons per pulse is measured using a Faraday cup and found to be ~ 4000 electrons. From the previous chapter we estimate that this number of electrons corresponds to a pulse length ~ 1.7 ps.

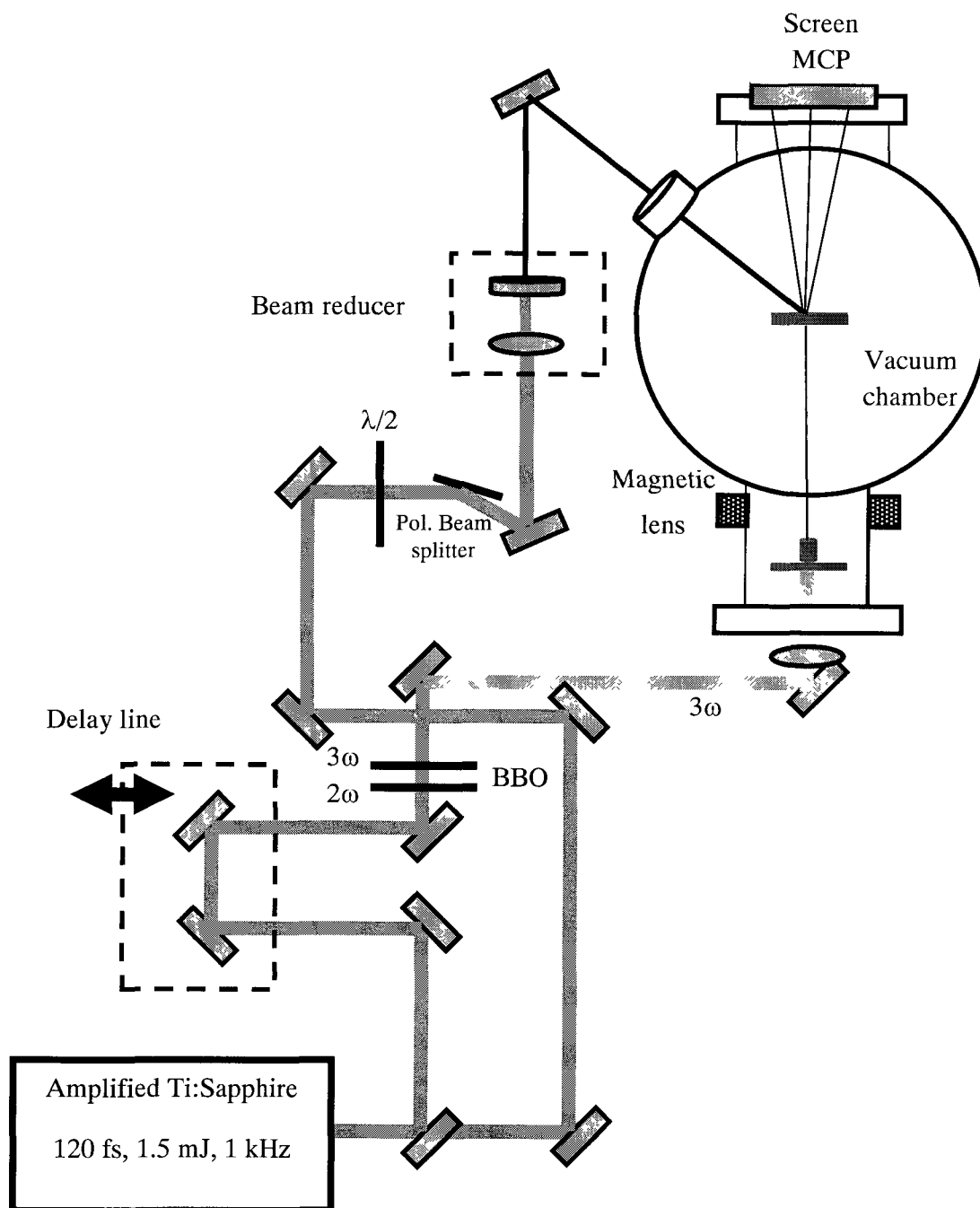


FIG. 3.6 The optical setup of the UED system. The laser beam is split into a pump and probe. The probe beam is frequency tripled after the delay stage.

The spatial overlap between the pump laser beam and the electron beam is achieved by loading a TEM grid with 300-600 μm pinhole and we make sure both beams are centered at the pinhole. The sample holder, which is perpendicular to the e-beams, is moved only in that plane to study different samples, so the spatial overlap is always guaranteed. The pump laser diameter at the sample was kept at ~ 2 mm while the electron beam size is ~ 700 μm .

For the temporal overlapping, we start by measuring the optical paths for both beams and compensating for the e-beam, which is traveling at one-third of the speed of light. After the rough measurement is done, we confirm the temporal overlapping by running a pump-probe experiment on a sample like Al thin film and we assign the point where the drop in diffraction intensity begins as (t_0). The vacuum chamber is pumped down with an ion pump to a pressure $< 10^{-9}$ torr so that the current of the ion pump components is < 50 μA , which I found to have tolerable or no background illumination on the MCP detector.

III.6 Data analysis

The image of the diffraction pattern forms on the phosphorus screen following the MCP amplification of the image's electrons. An electrically cooled camera is lens-coupled to the external flange of the MCP-phosphorus screen system, and we make sure to collect as much emission off the screen as possible. The image acquisition time ranges from a few seconds to a minute, depending on the camera saturation. The camera has a dynamic range of 16-bit, which enables the accumulation of many images.

The strength of the diffraction pattern depends on the status of the sample. Nanoparticles give weak patterns, as well as thin films that are not properly annealed. Well-annealed thin films of thickness 20-25 nm give the strongest diffraction patterns.

The images are collected and saved in the .spe format, which is the trademark for Roper Scientific's Winview[®] camera control and acquisition software. The concentric rings of the diffraction patterns are analyzed by using the open source ImageJ software, which was our best choice for radial integration. The radial integration yields a number of peaks superimposed on a background. We next take those images to Peak fit[®] to separate the peaks and run peak fitting where we import information like the peak intensity, peak position, and peak width.

The details of the image processing are shown in Fig. 3.7. We start with the raw image, followed by the radial integration, the background subtraction, and finally the individual peak separation and fitting. After all the processing is done, the diffraction peaks information is processed using a spreadsheet application to present the various physical processes we can learn from our experiments.

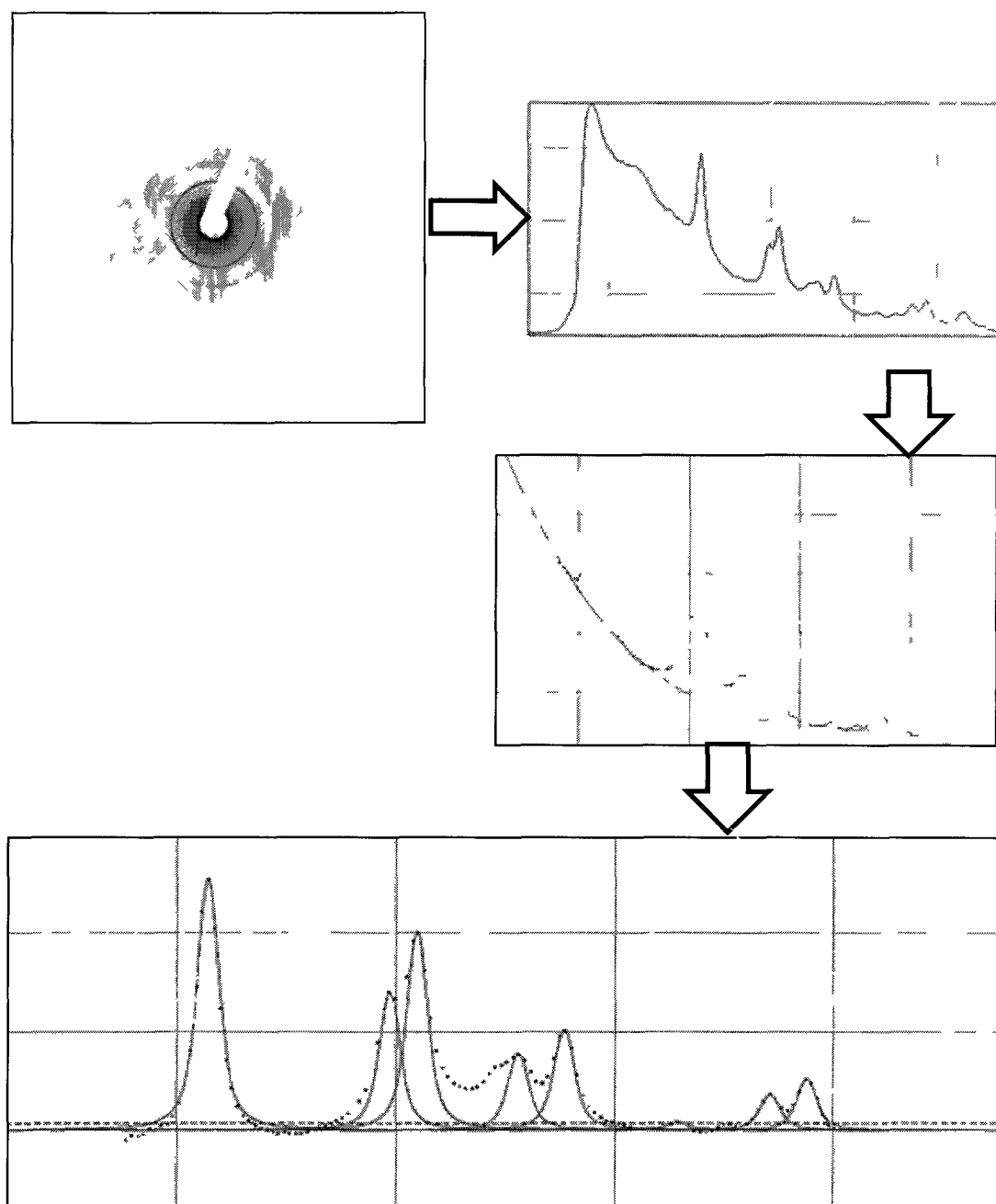


FIG. 3.7 The image processing flow chart. The raw image (shown in inverse colors) is radially averaged; then the background is removed, and the individual peaks are fitted.

CHAPTER IV

RESULTS AND DISCUSSION

This chapter aims to display the results of the static heating and the time-resolved experiments on antimony thin films and nanoparticles and use them together to study the lattice dynamics following the application of a femtosecond laser pump. Increasing the temperature of the sample, either in a static heating manner or an impulsive one, would increase the mean square vibration amplitude $\langle u^2 \rangle$. That added agitation will reduce the lattice order, which is observed as a decrease in the intensity of the diffraction pattern. A plot of the diffraction intensity of the Debye-Scherrer peaks versus temperature is used to calculate the Debye temperature of the samples and compare that with the bulk's value (200 K).⁴¹

The diffraction peaks' locations versus temperature plot is used to calculate the expansion coefficient and, as a function of delay, can give an insight into coherent lattice vibrations. The Debye-Scherrer peaks are fitted to the Lorentzian peak function in order to measure the widths of these peaks.

The widths of the peaks may indicate a few underlying causes, such as non-uniform heating of the sample, a reduction in the nanoparticles size, and inhomogeneity of the lattice spacings. The latter factor can be visualized by considering the lattice parameter to be varying along the pump beam direction. Next, the uneven spacing results in a spectrum of values for the diffraction angle, which is seen as a width to the diffraction ring.

The time-resolved scans will also be fitted to the Debye-Waller model. The time-

resolved intensity scans will be used to calculate the temperature rise due to the laser pulse by employing the associated Debye temperature. We have also observed a delay between the intensity drop and the ring size drop which we will use to calculate the film thickness.

IV.1. Interpretation of the electron diffraction pattern

Electron diffraction patterns of unknown or non-cubic polycrystalline thin film samples could be difficult to interpret, or the interpretation could carry a degree of uncertainty. To overcome or minimize the uncertainty in the electron diffraction interpretation, we calibrated the system using some known fcc elements such as Au, Ag, and Al. While all of these elements were used in the early stages of the experiment, the diffraction patterns of a gold thin film and an aluminum thin film are shown in Fig. 4.1.

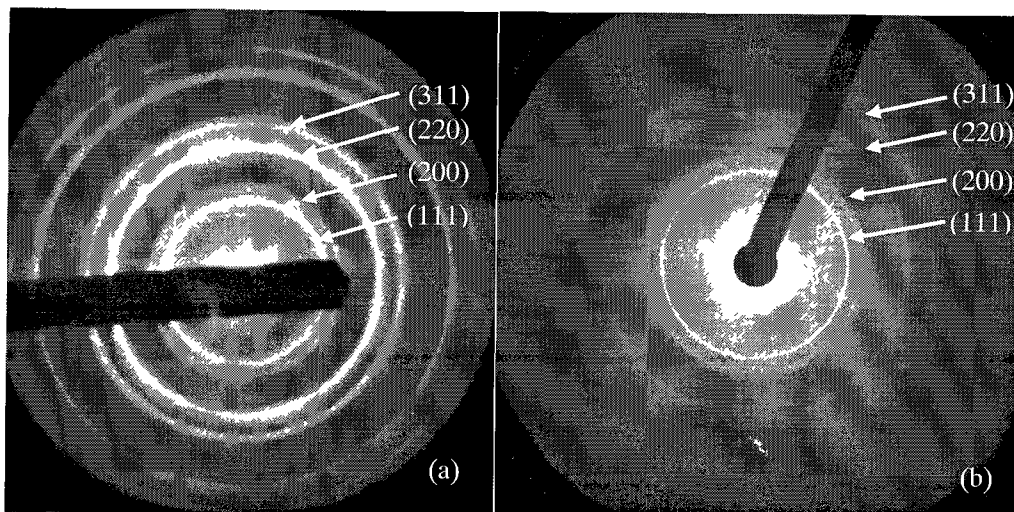


FIG. 4.1. Thin film electron diffraction patterns for gold (a) and aluminum (b) taken for the simplicity of their fcc structure for the sole purpose of calibrating the imaging system.

The interpretation of the diffraction pattern of the calibration gold thin film is quite simple and straightforward. The diffraction data are readily available in numerous records. We prepared several Au and Al thin films to use them to calibrate the electron diffraction system and find the camera length as well as perform a camera calibration.⁵³⁻⁵⁴

By using this modified form of Bragg's condition:

$$Rd = \lambda L, \quad (4.1)$$

where R is the diffraction ring radius (mm), d is the interplanar spacing (\AA), λ is the wavelength of the electron beam (\AA), and L is the camera length (distance from the sample to the inner surface of the MCP (mm)) which is found to be 229.2 mm. Substituting for the first four diffraction rings' spacing and the rings' radii we get the camera constant (λL). Now, we can use the camera constant along with the diffraction ring radius to identify the lattice spacing for any other sample under the conditions of: maintaining the electron beam energy, the distance between sample and MCP, the camera, the camera lens with zoom setting, and the distance between the camera and screen.

The structure of antimony can be described by both rhombohedral and hexagonal geometries, an important constraint for the arsenic (A7) structure that serves as a selection rule for finding possible diffraction planes that participate in the diffraction pattern, especially those that are not listed in X-ray powder diffraction data references. Starting from the hexagonal structure and running all possible (hkl) combinations from 0 to 9 for all three indices, followed by a transformation to the rhombohedral indices, we get only those allowed hexagonal combinations that transform to whole numbers in the rhombohedral system; the results are shown in Table. 4.1. The resulting combinations are

sorted by interplanar distance, giving good match to the published data and agreement to the second order with the observed Debye-Scherrer peaks.

The next step after indexing the diffraction pattern is to prepare it for quantitative analysis. The radial integration of the diffraction pattern rings produces symmetric peaks superimposed on a decaying background. The background is fitted to any of the built-in functions in Peakfit™; see Fig. 4.2. After the background has been removed, some of the peaks are too close and, hence, a deconvolution software (Peakfit™) is used to isolate the Debye-Scherrer peaks. The nonlinear background is a result of inelastic scattering of the probe beam electrons with the sample. The background also increases either slightly or significantly when the pump beam is applied to the sample, depending on the fluence and the sample geometry because the support bars of the TEM grids may reflect the pump laser in a diffuse manner.

The background, due to the application of the laser pump beam, could sometimes saturate the MCP detector to the point of rendering it useless for taking images. To get rid of it, we needed to identify the nature of that radiation, whether it is positively or negatively charged. One way of eliminating the charged background is to install a mesh between the sample and the MCP detector. Different voltages, ranging between positive and negative values, were applied to the mesh ranging. The background was found to diminish at a voltage ~ -100 V, which suggested that the background was not due to positive ions but, indeed, from stray secondary electrons. The source of those stray electrons could be a photoelectric effect through multiphoton absorption, since the 800 nm laser wavelength (1.55 eV) is well below the work function of any of the elements we use, so the classic one photon photoelectric effect is ruled out. The mesh was later

removed and the repelling voltage was, instead, applied to the inner surface of the MCP detector (-90 V).

Table 4.1. Calculated and observed Debye-Scherrer peaks for Sb films and nanoparticles

Calculated d, Å	Hexagonal indices			Rhombohedral indices			Observed d, Å
	H	K	L	h	k	l	
3.7566667	0	0	3	1	1	1	3.77
3.5421471	1	0	1	1	0	0	3.5
3.1110376	0	1	2	1	1	0	3.11
2.2484699	1	0	4	2	1	1	2.25
2.1542269	1	1	0	1	0	-1	2.15
1.8783333	0	0	6	2	2	2	1.87
1.8405673	0	2	1	1	1	-1	1.85
1.7710736	2	0	2	2	0	0	1.77
1.5555188	0	2	4	2	2	0	1.55
1.4157423	1	1	6	3	2	1	1.41
1.3680783	1	2	2	2	1	-1	1.37
1.2522222	0	0	9	3	3	3	1.25
1.2437435	3	0	0	2	-1	-1	1.24
1.0771135	2	2	0	2	0	-2	1.08
1.0178354	3	1	2	3	0	-1	1.02
0.971405	1	3	4	3	2	-1	0.97
0.9343853	2	2	6	4	2	0	0.93
0.9202836	0	4	2	2	2	-2	0.92
0.8855368	4	0	4	4	0	0	0.88
0.8462941	2	3	2	3	1	-2	0.84
0.8142212	4	1	0	3	-1	-2	0.81

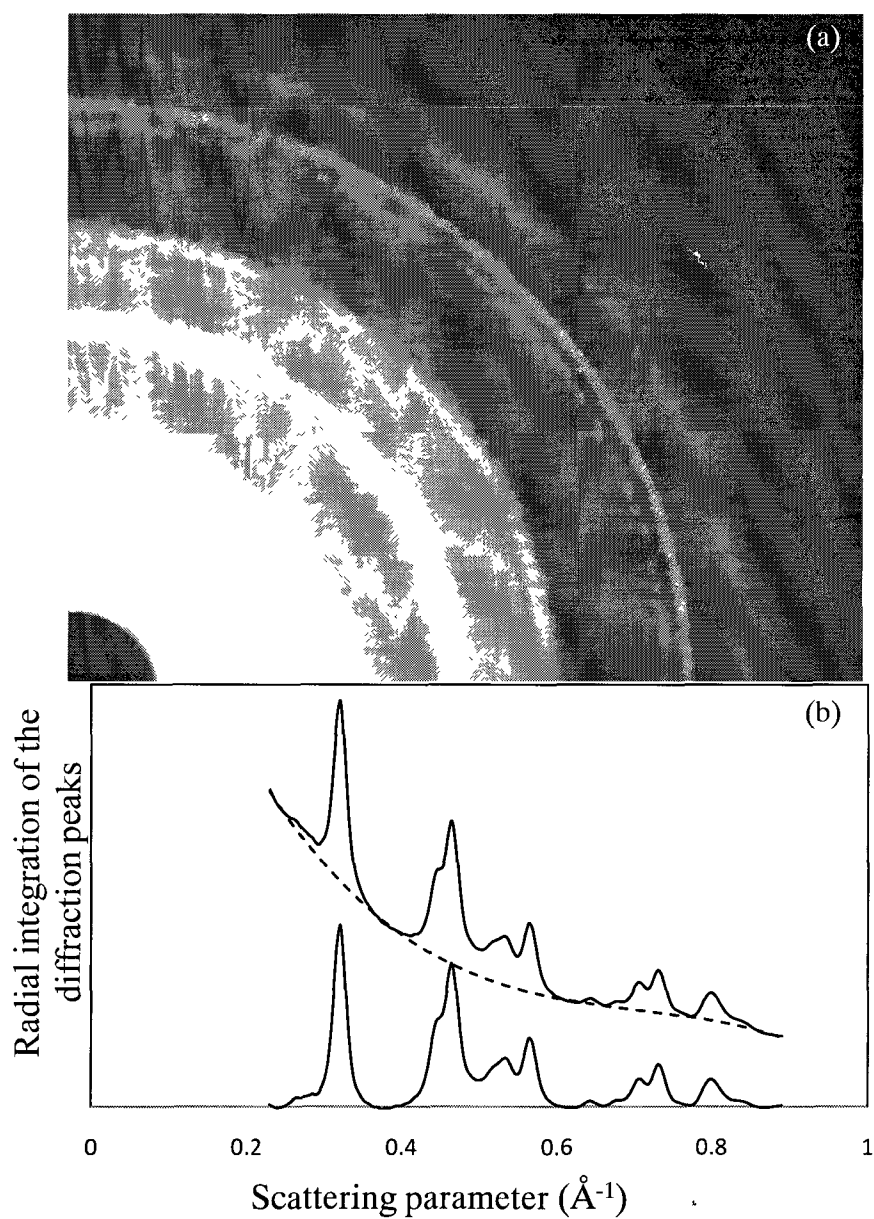


FIG. 4.2. A quadrant of the electron diffraction pattern of antimony nanoparticles (a) and its radial integration (b) superimposed on background (dotted line) and after background removal.

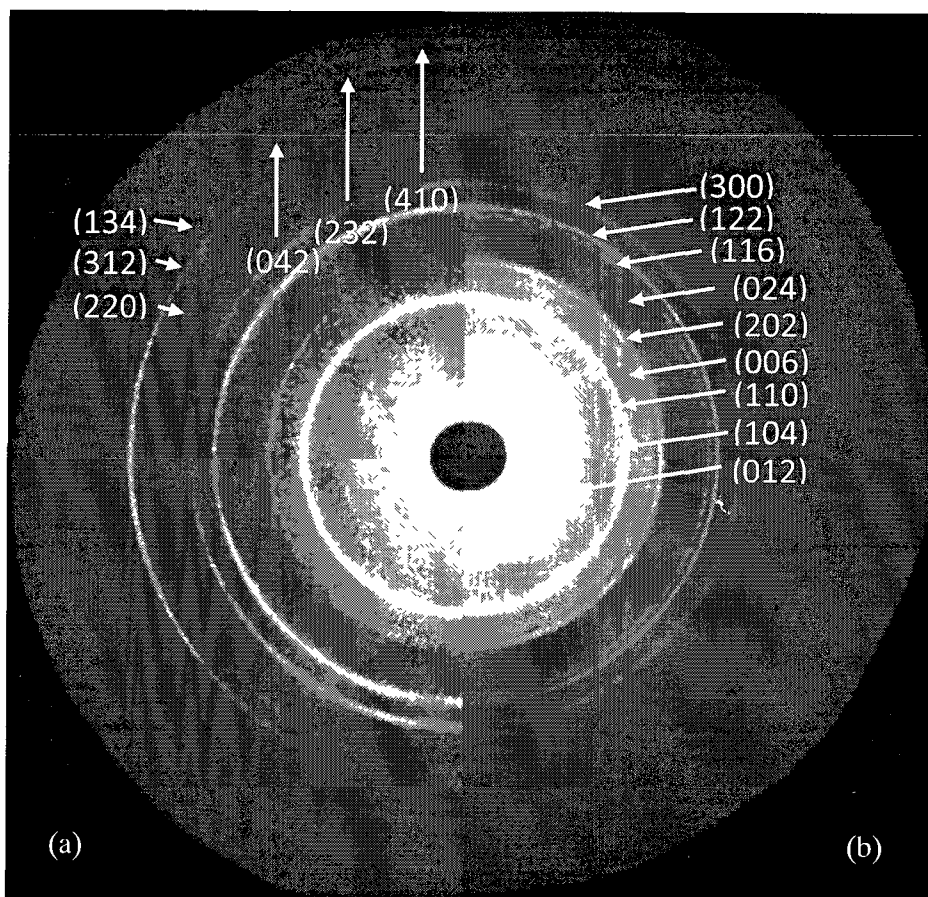


FIG. 4.3. Two types of samples are used in this study: continuous thin film (a) and scattered nanoparticles (b). Both diffraction patterns are indexed using the hexagonal unit cell notations.

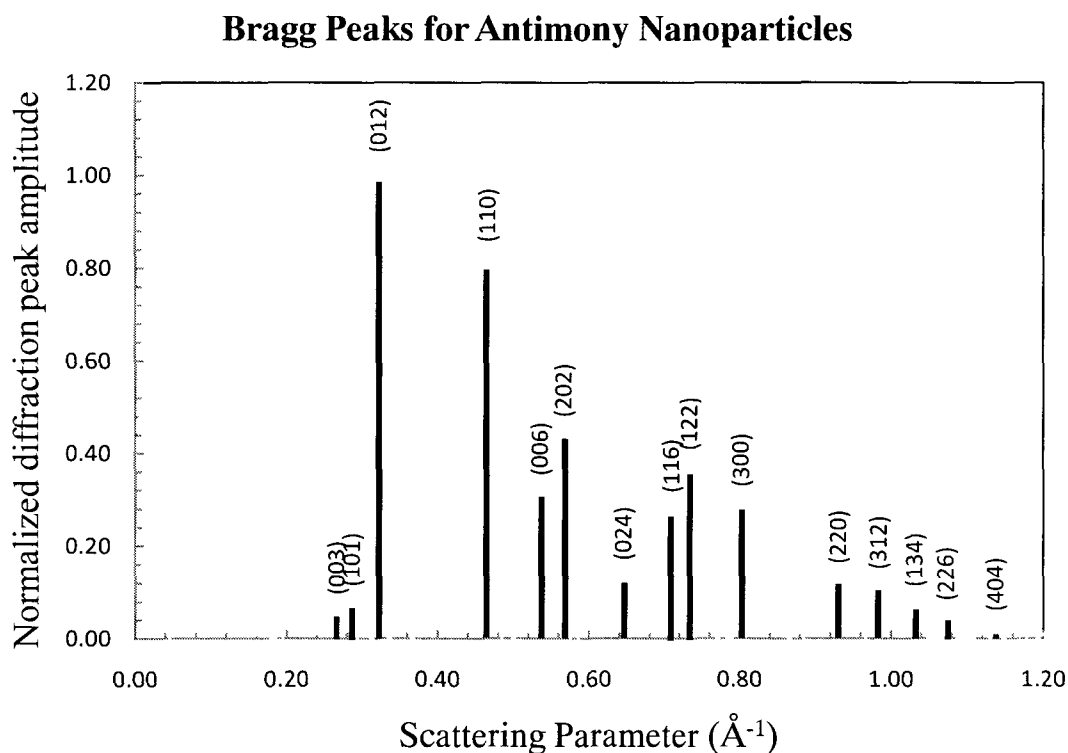


FIG. 4.4. All the recorded electron diffraction peaks for Sb nanoparticles are plotted against the corresponding scattering parameter. The Debye-Scherrer peaks are normalized to the (012) peak.

IV.2. Thin film growth modes of antimony

The preparation of nanoparticles is a very diverse technology. We tried to use commercially available samples (silver nanoparticles) but were unsuccessful in preparing isolated nanoparticles distribution on a carbon TEM grid. They always stuck together to form clusters that are too dense for the e-beam probe to pass through.

Using our expertise in thin film preparation by thermal deposition, we prepared antimony films with different thicknesses and studied them under the TEM. Two thicknesses were tested, 50 \AA and 100 \AA . The 50 \AA average thickness film yielded somewhat uniform, well-scattered distribution of nanoparticles, as seen in Fig. 4.5.

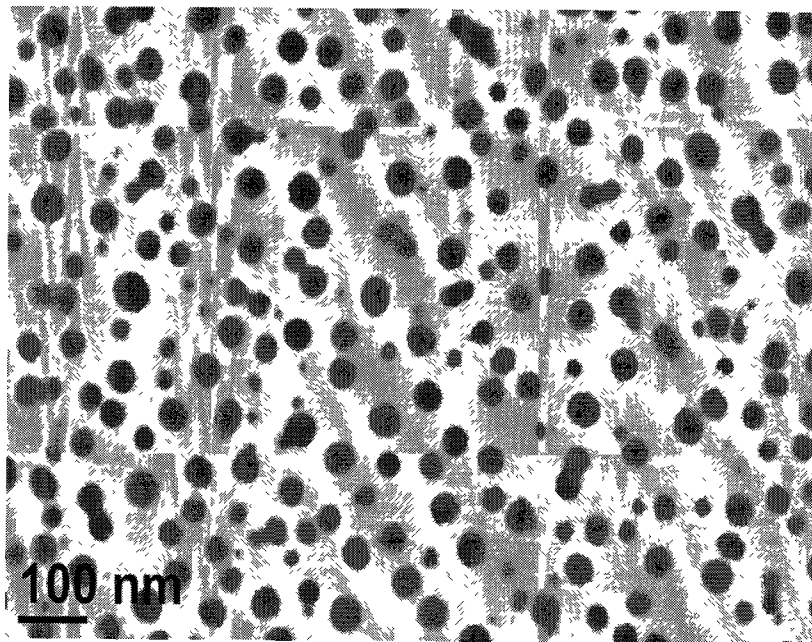


FIG. 4.5. TEM image of Sb nanoparticles with an effective thickness of 5 nm. The nanoparticles are well dispersed.

The 100 Å average thickness thin film (Figs. 4.6 and 4.7) gives clustered nanoparticles that are not suitable for our study but would give a stronger diffraction pattern due to the increased coverage.

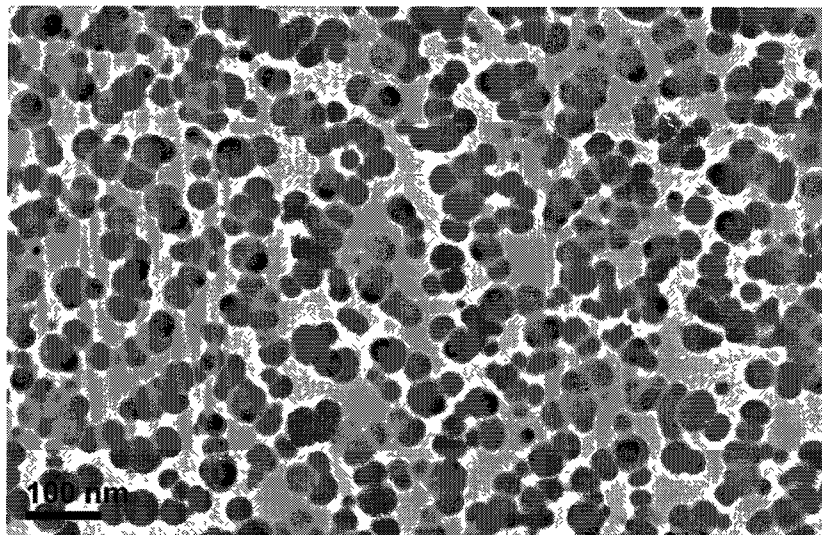


FIG. 4.6. TEM image of Sb nanoparticles with an effective thickness of 10 nm. The nanoparticles did not grow in size but increased in number and started to form clusters.

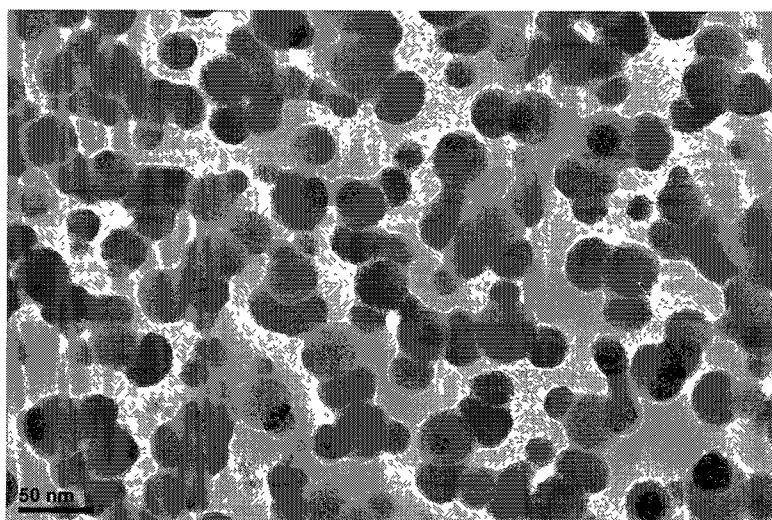


FIG. 4.7. TEM image of Sb nanoparticles with an effective thickness of 10 nm. The nanoparticles did not grow in size but increased in number and started to form clusters. This image is shown at higher magnification than the previous one to show more details.

To get the benefit of the 50 Å nanoparticles isolation and the 100 Å coverage, we resorted to depositing 50 Å on the two sides of the TEM carbon-coated grid (Fig. 4.8). A

closer look at the sample of Fig. 4.8 is shown in Fig. 4.9, where we see two particles on opposite sides of the grid while the equilibrium shape of the annealed nanoparticle is clearly on a hexagonal base, this is not the case for all particles, though.

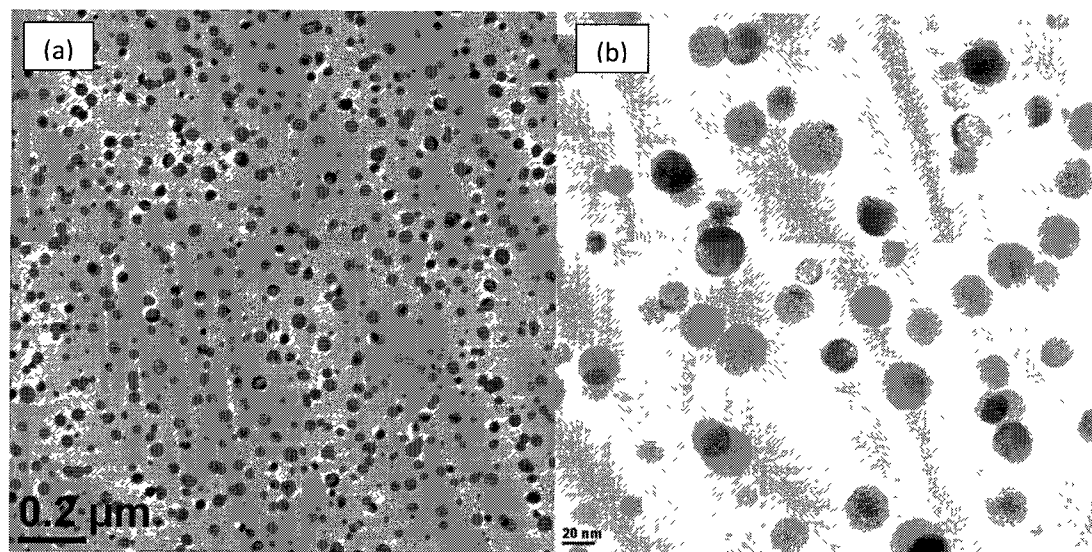


FIG. 4.8. (a) TEM image of Sb nanoparticles with an effective thickness of 50 \AA on both sides of the TEM grid. Using this method gives good coverage without particle clustering; (b) nanoparticles annealed to $220 \text{ }^\circ\text{C}$ reveals that each one is singly crystalline.

When the thickness of the film is increased to 200 \AA , something dramatic happens. At 200 \AA , the as-deposited structure changes from forming particle clusters to forming a continuous, smooth, crystalline film. We will not ponder the details of that transition since it is not the focus of our current study.

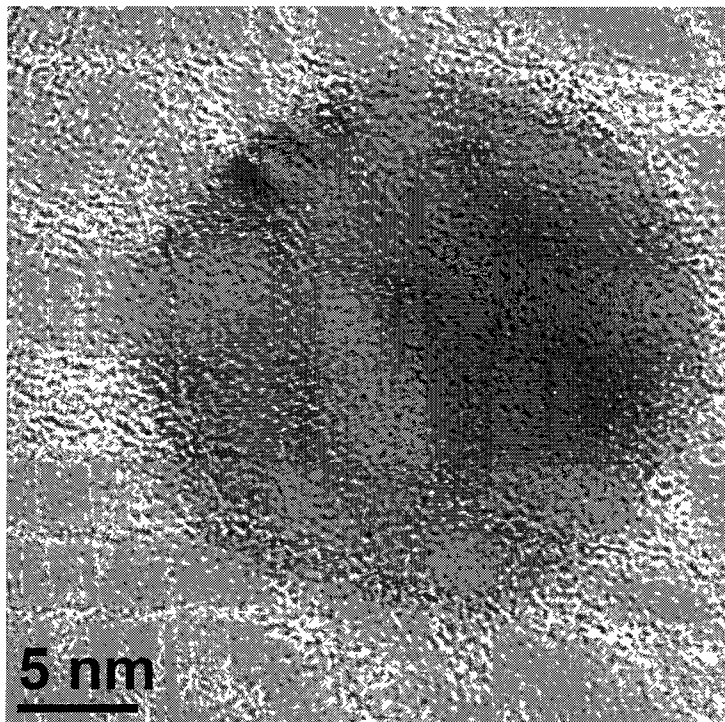


FIG. 4.9. TEM image of Sb nanoparticles with an effective thickness of 50 \AA on both sides of the TEM grid. The equilibrium shape is hexagonal for this annealed nanoparticle.

The as-deposited Sb thin film is very close in morphology (FIGs. 4.10 and 4.11) and crystal structure (FIGs. 4.12 and 4.13) to the one annealed to $200 \text{ }^\circ\text{C}$. So, the film is ready to yield a polycrystalline electron diffraction pattern right out of the evaporator, but this is not the case for nanoparticles. In the case of nanoparticles, the electron diffraction pattern indicates amorphous structure which is characterized by diffuse discs and the absence of sharp rings. The nanoparticles configuration, thus, requires annealing to a temperature around $220 \text{ }^\circ\text{C}$ until the polycrystalline diffraction rings are observed by our camera. Fig. 4.14 shows a TEM image of an as-deposited nanoparticle. It is obvious that the atoms are randomly arranged. Annealing that sample by heating it slowly over a period of about two hours to $220 \text{ }^\circ\text{C}$ transforms the structure to that in Fig. 4.15, a single

crystalline structure for each individual nanoparticle for an overall randomly oriented distribution that is almost equivalent to a polycrystalline film.

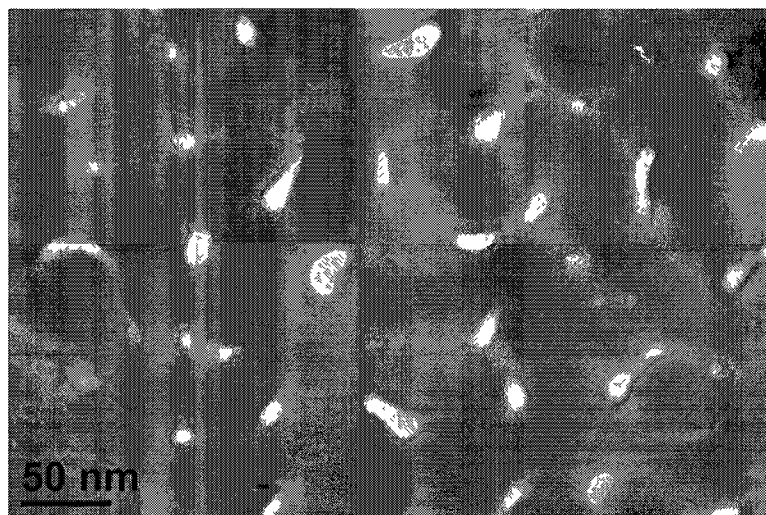


FIG. 4.10. TEM image of Sb thin film with thickness 20 nm. The light-colored patches are voids in the carbon support film. This is an image of an as-deposited film.

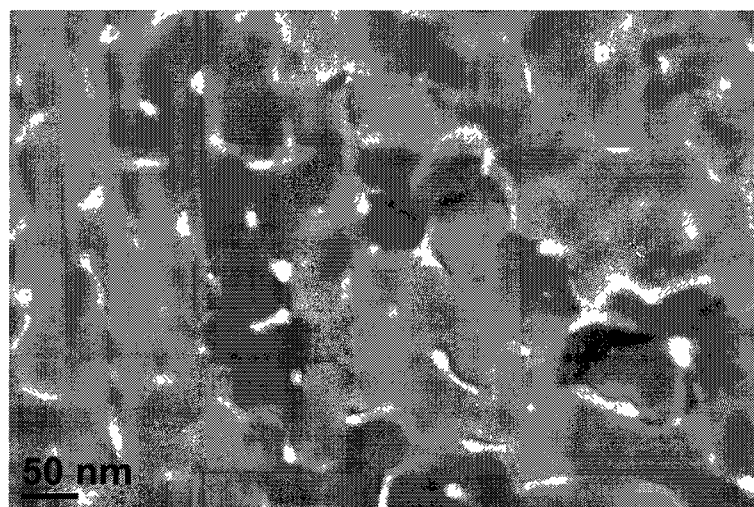


FIG. 4.11. TEM image of Sb thin film with thickness 20 nm. The light-colored patches are voids in the carbon support film. This is an image of an annealed film at a temperature of 220 C.

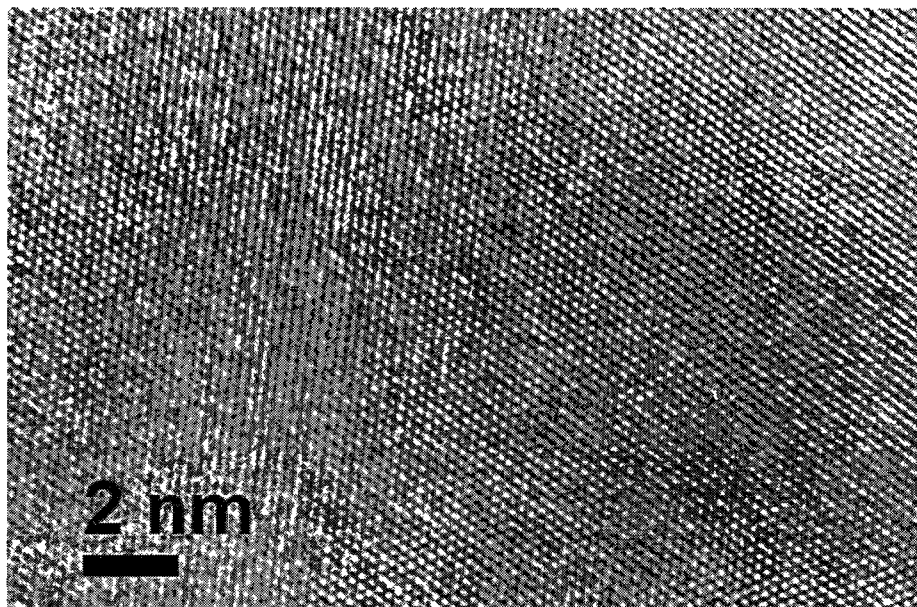


FIG. 4.12. HRTEM image of Sb thin film with thickness 200 Å. This is an image of an as-deposited film where the atoms form a well-defined crystalline structure.

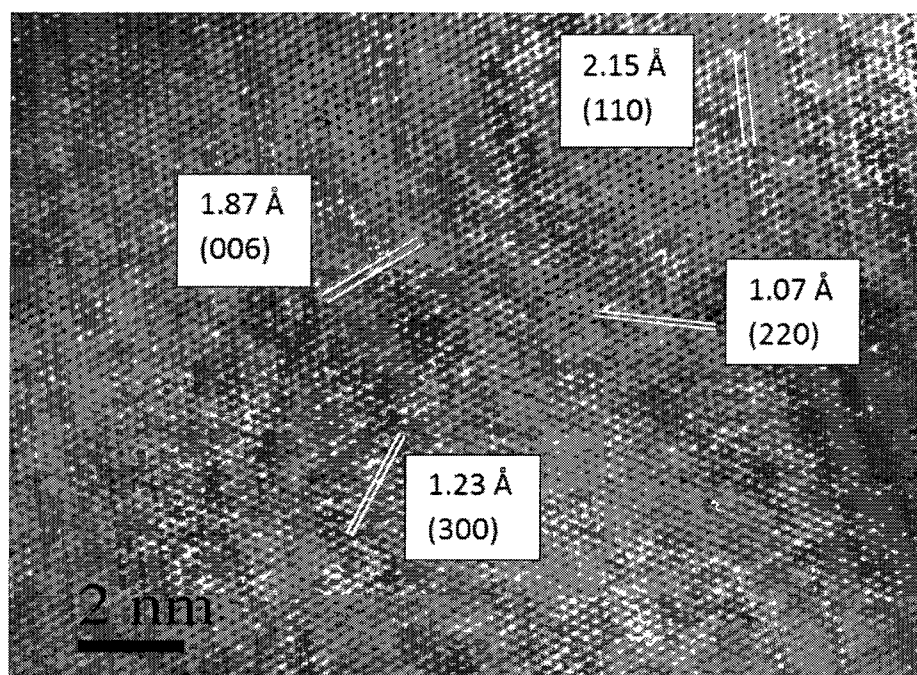


FIG. 4.13. HRTEM image of Sb thin film with thickness 200 Å. This is an image of an annealed film where the structure resembles that of an as-deposited film.

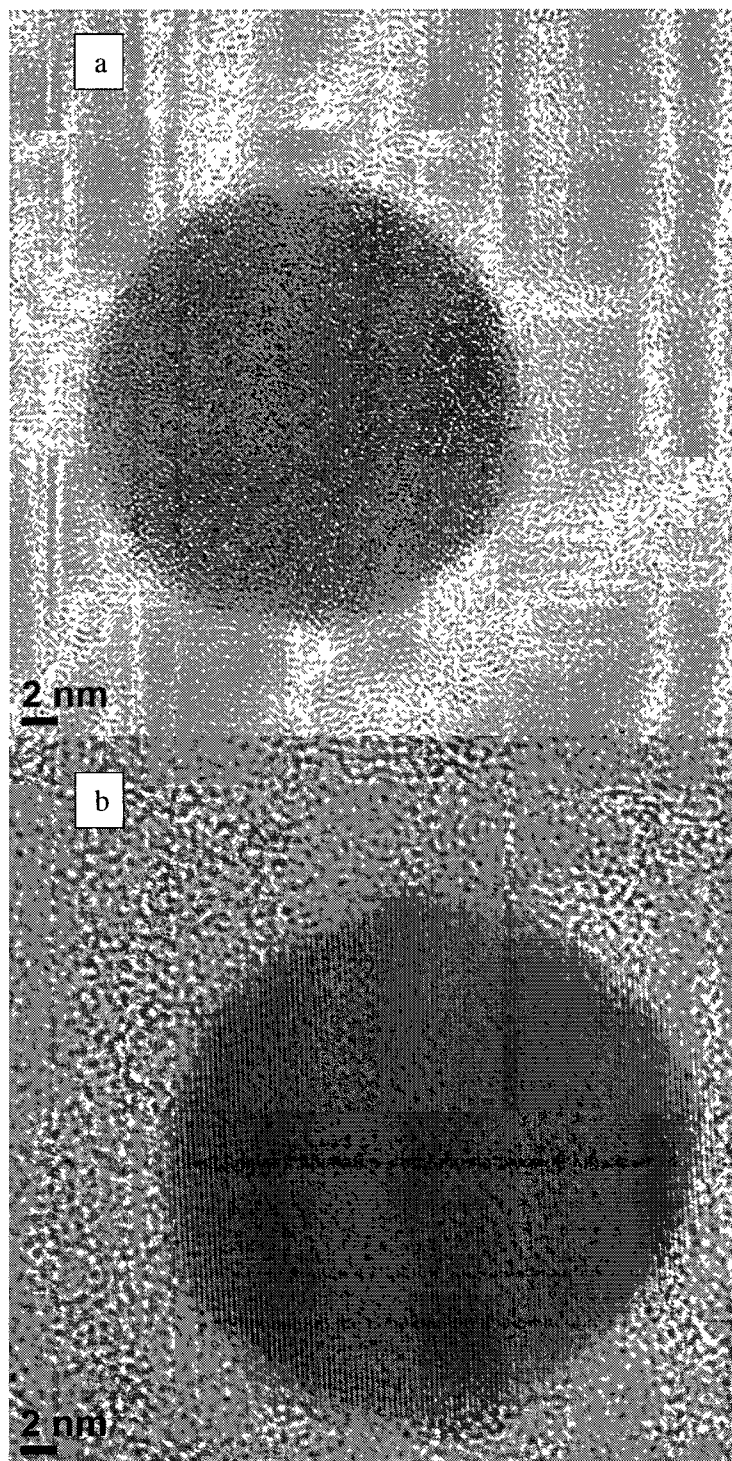


FIG. 4.14. TEM image of an Sb nanoparticle of a distribution with film thickness 50 \AA . There is an image of an as-deposited film (a) that shows the atoms of the nanoparticles as being amorphous, and the singly crystalline one after annealing (b).

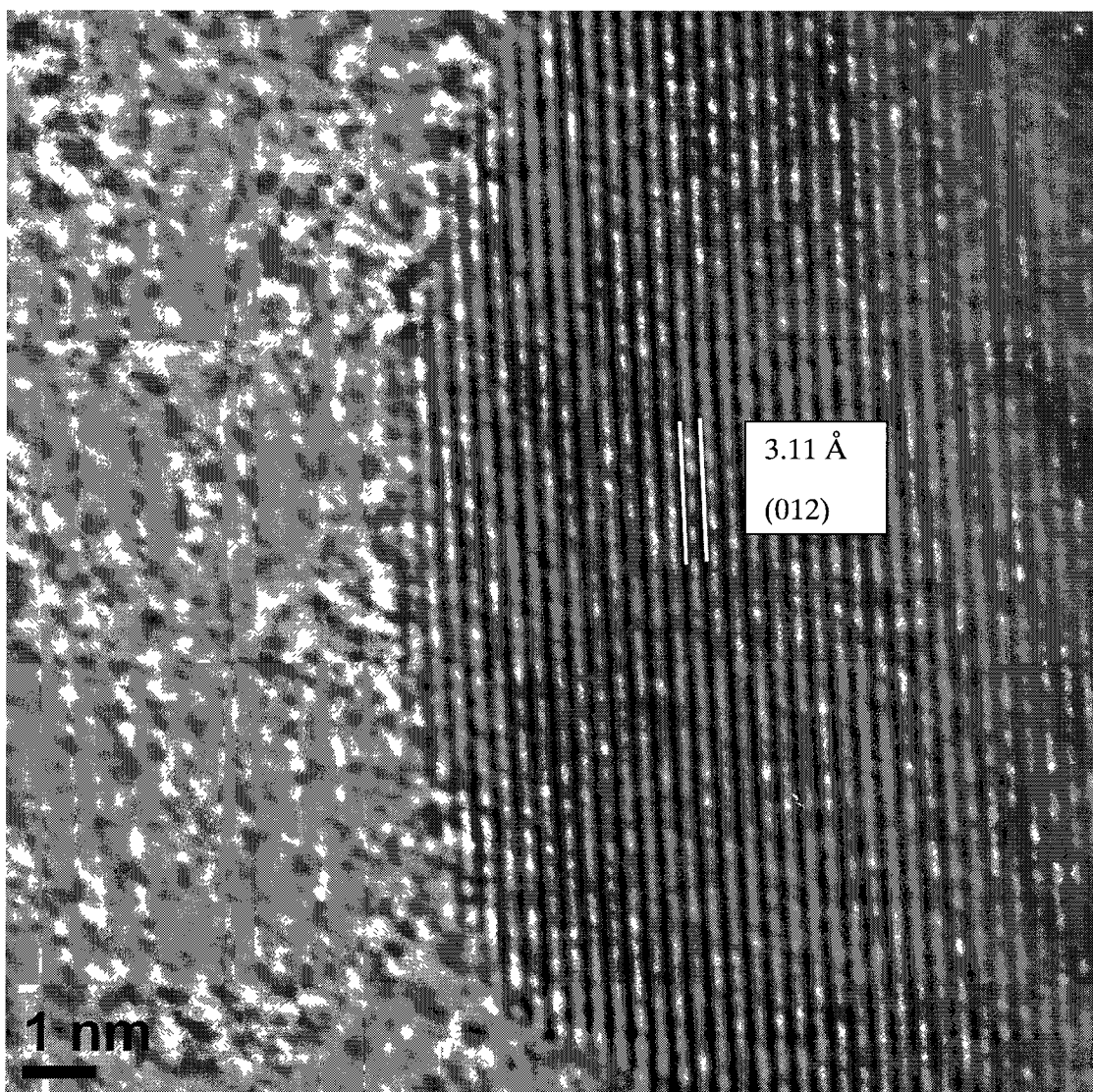


FIG. 4.15. TEM image of an Sb nanoparticle of a distribution with film thickness 50 Å. This is an image of an annealed film that shows the atoms of the nanoparticles as being singly crystalline.

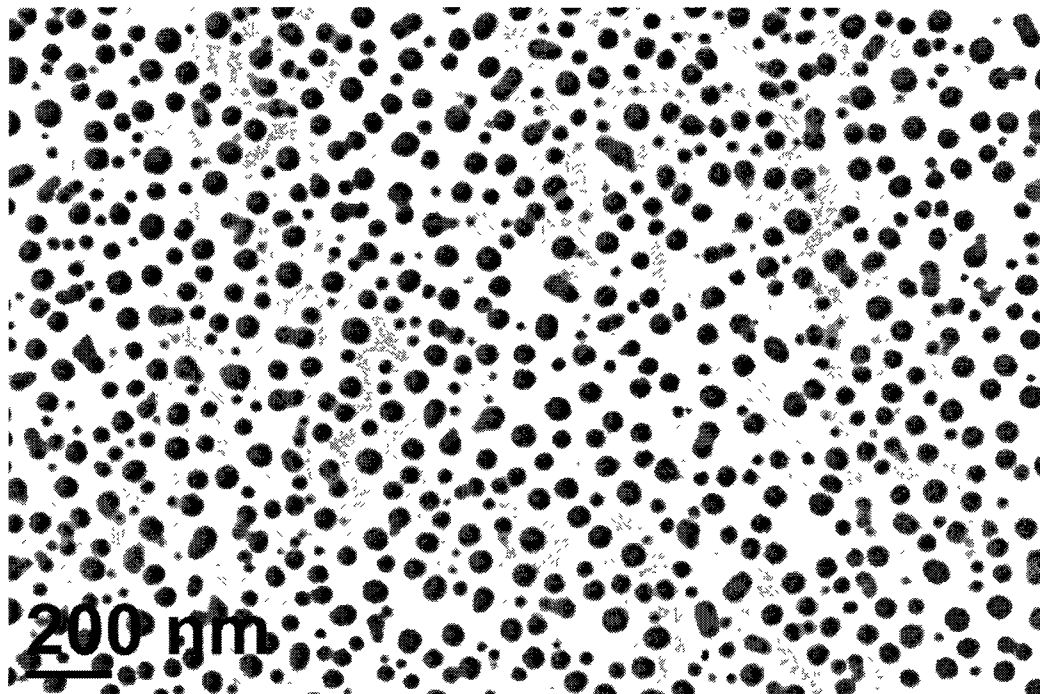


FIG. 4.16. TEM image of Sb nanoparticles with a film thickness of 50 Å. The nanoparticles are annealed to 220 °C.

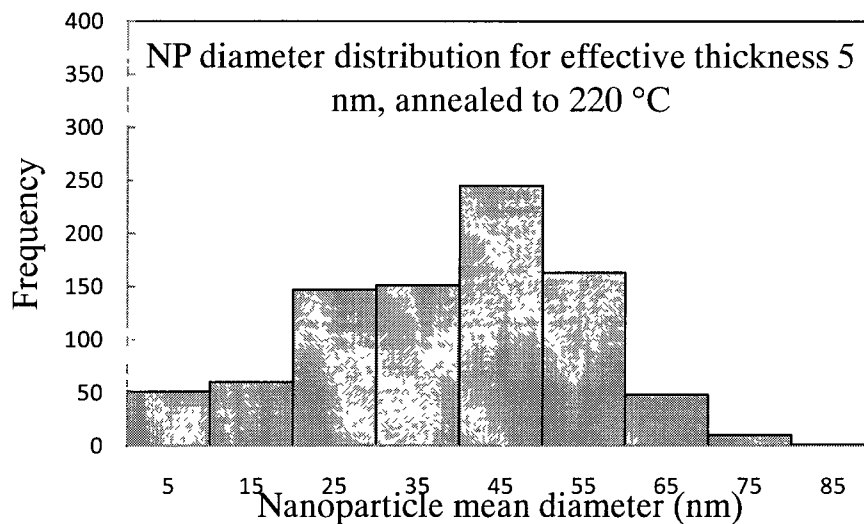


FIG. 4.17. Size distribution for the nanoparticles in Fig. 4.16 that are annealed to 220 °C. The nanoparticles' diameter peaks at around 45 nm. The annealing was performed at 1 K/min rate.

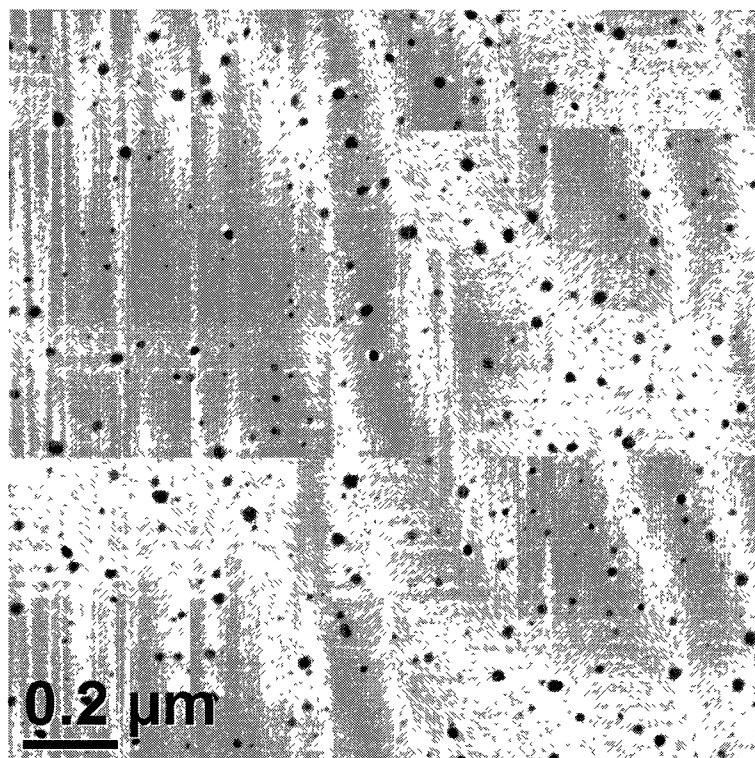


FIG. 4.18. TEM image of Sb nanoparticles with a film thickness of 50 Å. The nanoparticles are annealed to 350 °C.

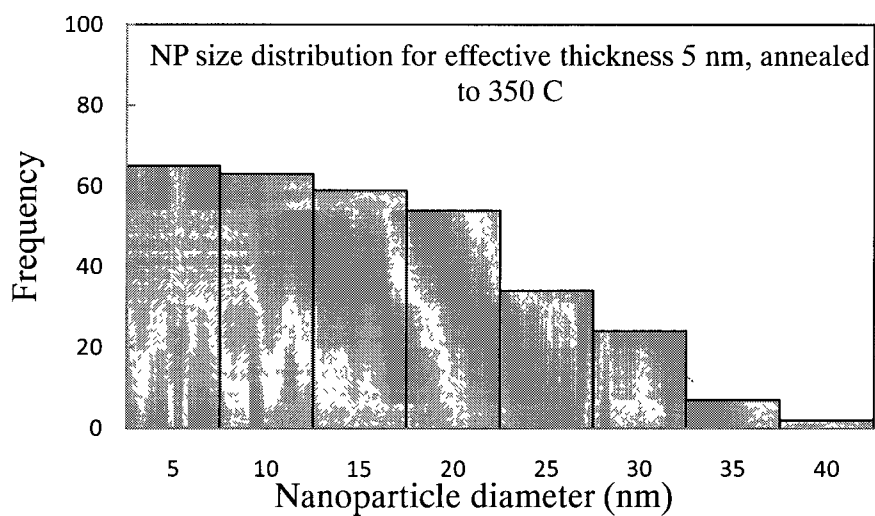


FIG. 4.19. Size distribution for the nanoparticles in Fig. 4.18 that are annealed to 350 °C. The nanoparticles' diameters are much smaller than that in Fig. 4.17 due to evaporation. The annealing was performed at 1 K/min rate and turned off once the desired temperature was reached.

The annealing of the nanoparticles up to 220 °C was found to be sufficient for crystallization. Further heating resulted in loss of the diffraction pattern. As shown in Fig. 4.16, the annealed nanoparticles are distributed in size according to Fig. 4.17. Those that are annealed to 350 °C have lost most of their mass. The melting point of antimony (630 °C) is much higher than the 350 °C at which we notice the transformation of the nanoparticles' properties. This can be explained by the high vapor pressure of antimony. This tendency of antimony to evaporate at low temperatures was experienced during the thermal deposition process of preparing the thin films and nanoparticles. The antimony was found to evaporate at a temperature in the range of 300 - 400 °C; and when the evaporation chamber was opened, we found that the antimony load had sharp corners that indicate sublimations rather than melting.

IV.3. Static heating of Sb thin films and nanoparticles

The Sb thin films and nanoparticles were subjected to the effect of direct heating. The heat is applied through the heating stage to the sample on the TEM grids. As the temperature of the sample rises, the diffraction intensity is attenuated and the diffraction pattern rings reduce in size in accordance with the expansion of the lattice for positive expansion coefficient or increase for negative expansion coefficient. As the Debye temperature of the thin films and nanoparticles is expected to be lower than that of the bulk due to the increased surface-to-bulk ratio, the Debye temperature of the thin films and nanoparticles is also calculated so it can be applied for the calculation of the temperature increase in the case of time-resolved studies. The diffraction rings radii are normalized to that of a lower temperature measurement to calculate the expansion

coefficient.

For 20 nm thin films, the thermally induced attenuation in diffraction intensity is shown in Fig. 4.20, and that of the nanoparticles is shown in Fig. 4.21. For both Figs. 4.20 and 4.21, the data points are fitted to an exponential decay function so we can use the fit to calculate the Debye temperature.

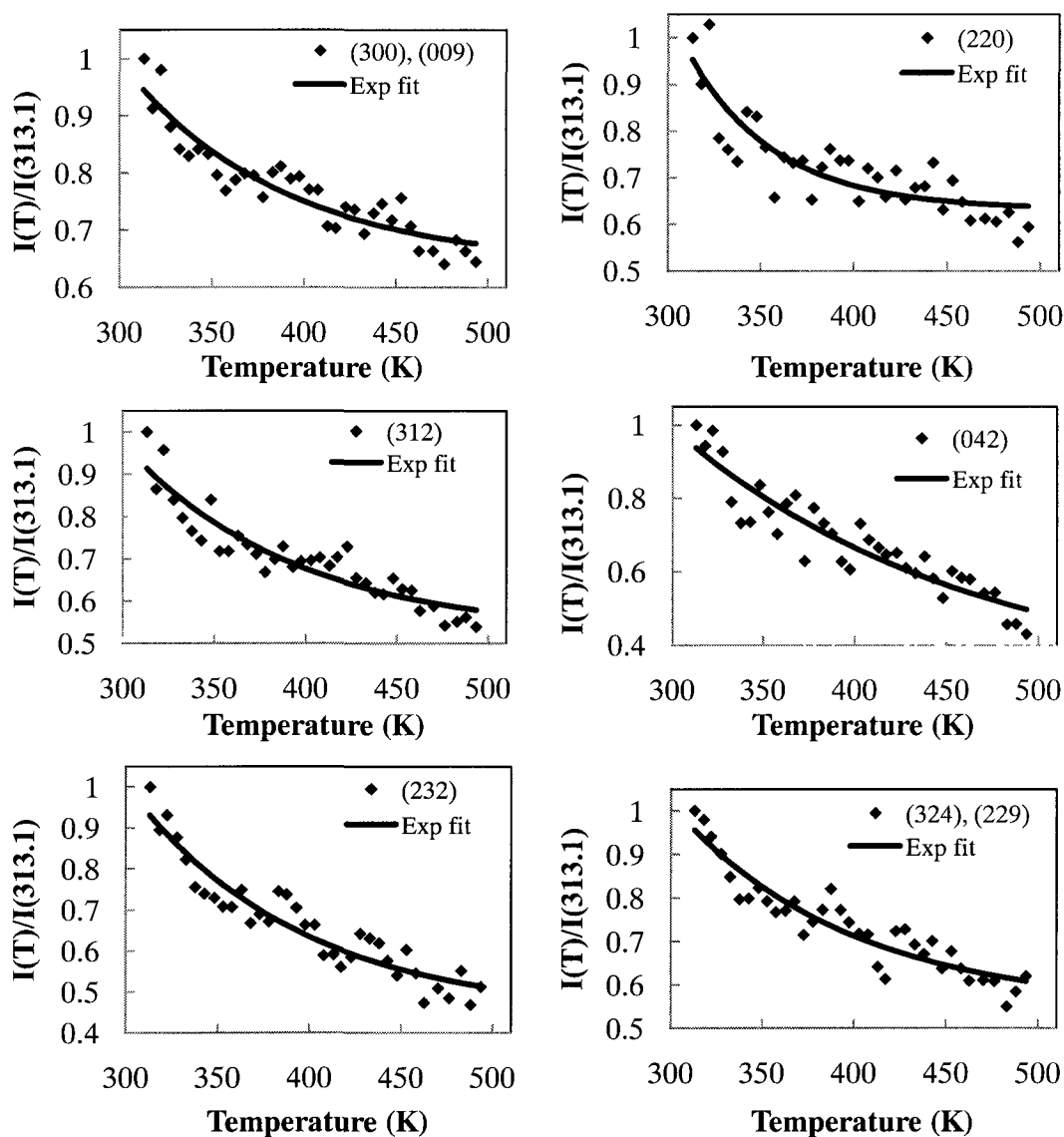


FIG. 4.20. The diffraction intensity amplitude of Sb film of thickness 200 Å that is directly heated through the heating stage. The measured values are normalized to that taken at 313 K. Debye temperature is calculated as 174 K.

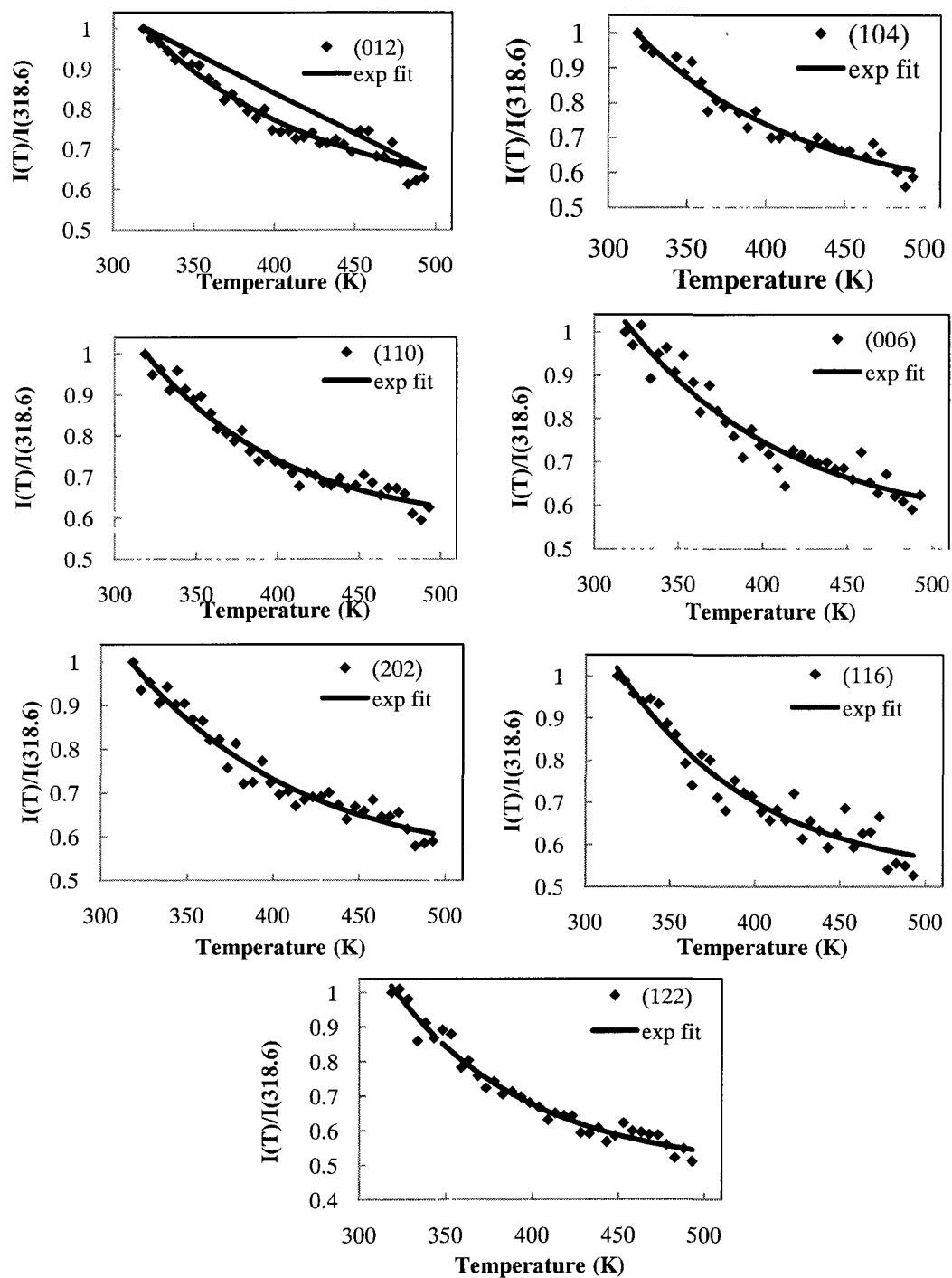


FIG. 4.21. The diffraction intensity amplitude of Sb nanoparticles of film thickness 50 Å that is directly heated through the heating stage. The measured values are normalized to that taken at 313 K. Debye temperature is calculated as 150 K.

IV.3.1. Calculation of Debye temperature for nanoparticles and thin films

The Debye temperature for either one of our samples will be determined using Mastumuro's method.⁴² The integrated electron diffraction intensity of a (hkl) Bragg peak can be written as:

$$I(\text{hkl}) = K P(\theta) A(E) |F(\text{hkl})|^2 \exp(-2M), \quad (4.2)$$

where K is a constant, $P(\theta)$ is the Lorentz polarization factor, $A(E)$ is a function of the electron energy (E), $F(\text{hkl})$ is the structure factor, and $\exp(-2M)$ is the Debye-Waller factor due to thermal displacements in the lattice. The function $A(E)$ describes the dependence on E through the beam intensity, the absorption of the sample, and the sensitivity of the detection and imaging system.

The factor (M) can be written as: $M = B (\sin \theta/\lambda)^2$, where λ is the wavelength corresponding to the electron energy. In an experiment to measure the Debye temperature, two intensity measurements at different temperatures are made and the ratio of the intensities is given by:

$$\ln[I(T_2)/I(T_1)] = -2\Delta B (\sin \theta/\lambda)^2 + C, \quad (4.3)$$

where $C = \ln[P(\theta_2) A(E_2) / P(\theta_1) A(E_1)]$ cancels out. A plot of $\ln[I(T_2)/I(T_1)]$ vs $(\sin \theta/\lambda)^2$ yields a straight line whose slope gives the difference in the Debye-Waller factor ΔB for the two temperatures. The Debye temperature Θ_D is calculated from the Debye theory using the high temperature approximation:

$$\Theta_D^2 = (6h^2 / mk_B)(\Delta T / \Delta B), \quad (4.4)$$

where m is the mass of an atom, h is Planck's constant, k_B is Boltzmann's constant, and ΔT is the temperature difference between the two temperature points.

For the case of nanoparticles, we use the plot in Fig. 4.22 which represents diffraction intensity drop due to temperature increase from 319 K to 493 K. The Bragg peaks represented in the figure are: (012), (104), (110), (006), (202), (116), and (122) from left to right, respectively. From Fig. 4.22, the slope ($-2\Delta B$) of the linear fit is found to be -0.0146 nm^{-2} , the parameters of the calculation are:

$$\Delta B = 0.0073 \text{ nm}^{-2} (0.0073 \times 10^{-18} \text{ m}^{-2}),$$

$$\Delta T = 174 \pm 2 \text{ K},$$

$$h = 6.626 \times 10^{-34} \text{ Js},$$

$$m = 121.76 \times 1.66 \times 10^{-27} \text{ kg},$$

$$k_B = 1.38 \times 10^{-23} \text{ m}^2\text{kgs}^{-2}\text{K}^{-1}.$$

Substituting in Eq. (4.4) we get:

$$\theta_D = \sqrt{\frac{6 \times (6.626 \times 10^{-34})^2 \times 174.4}{121.76 \times 1.66 \times 10^{-27} \times 1.38 \times 10^{-23} \times 0.0073 \times 10^{-18}}} = 150 \pm 2 \text{ K}.$$

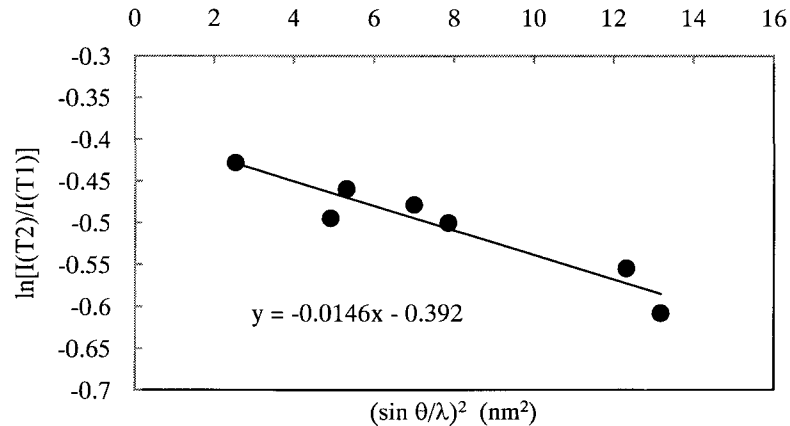


FIG. 4.22. Natural logarithm of the intensity ratio of antimony nanoparticles as a function of $(\sin \theta/\lambda)^2$. The straight line slope gives $\Delta B = 0.0079 \text{ nm}^{-2}$ with $\Delta T = 174 \pm 2 \text{ K}$. The Debye temperature is found to be $150 \pm 2 \text{ K}$. The corresponding diffraction rings are: (012), (104), (110), (006), (202), (116), and (122), respectively.

From Fig. 4.23 we find the slope to be -0.0112 which is equal to $-2\Delta B$. We get:

$$\Delta B = 0.0056 \text{ nm}^{-2} (0.0056 \times 10^{-18} \text{ m}^{-2}),$$

$$\Delta T = 180 \pm 2 \text{ K},$$

Substituting in Eq. (4.4) we get:

$$\theta_D = \sqrt{\frac{6 \times (6.626 \times 10^{-34})^2 \times 180.5}{121.76 \times 1.66 \times 10^{-27} \times 1.38 \times 10^{-23} \times 0.0056 \times 10^{-18}}} = 174 \pm 2 \text{ K}.$$

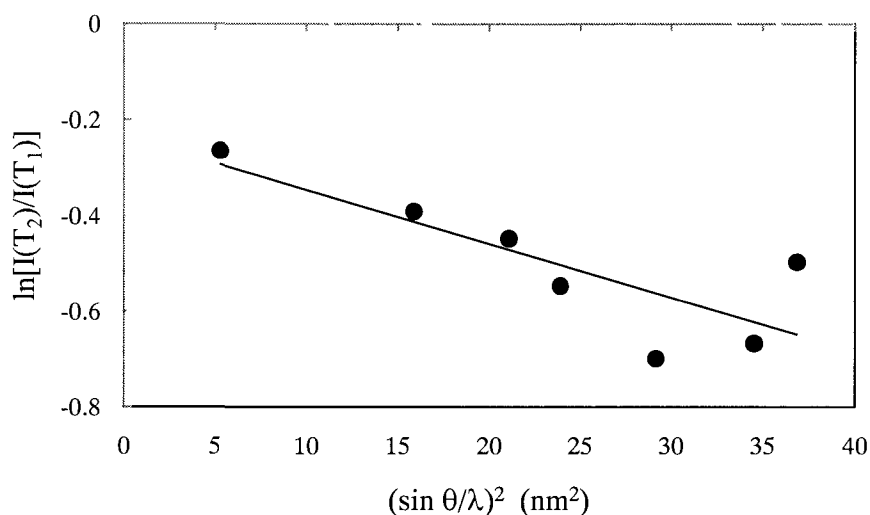


FIG. 4.23. Natural logarithm of the intensity ratio of antimony 20 nm thin film as a function of $(\sin \theta/\lambda)^2$. The straight line slope gives $\Delta B = 0.0056 \text{ nm}^{-2}$ with $\Delta T = 180 \pm 2 \text{ K}$. The Debye temperature is found to be $174 \pm 2 \text{ K}$. The corresponding diffraction rings are: (110), (300), (220), (312), (042), (232), and {(324), (229)}, respectively.

V.3.2. Calculating the expansion coefficient using thin film diffraction ring size

The temperature scan was performed during heating of the samples with a rate of 1 K/sec. Fig. 4.24 is used to determine the coefficient of linear expansion of antimony. By applying a simple linear fit, we get $\alpha = (9 - 20) \times 10^{-6} \text{ K}^{-1}$ for the various peaks. This is in good agreement with the stranded value α_{\perp} and $\alpha_{\parallel} = 8, 20 \times 10^{-6} \text{ K}^{-1}$, respectively.⁴³

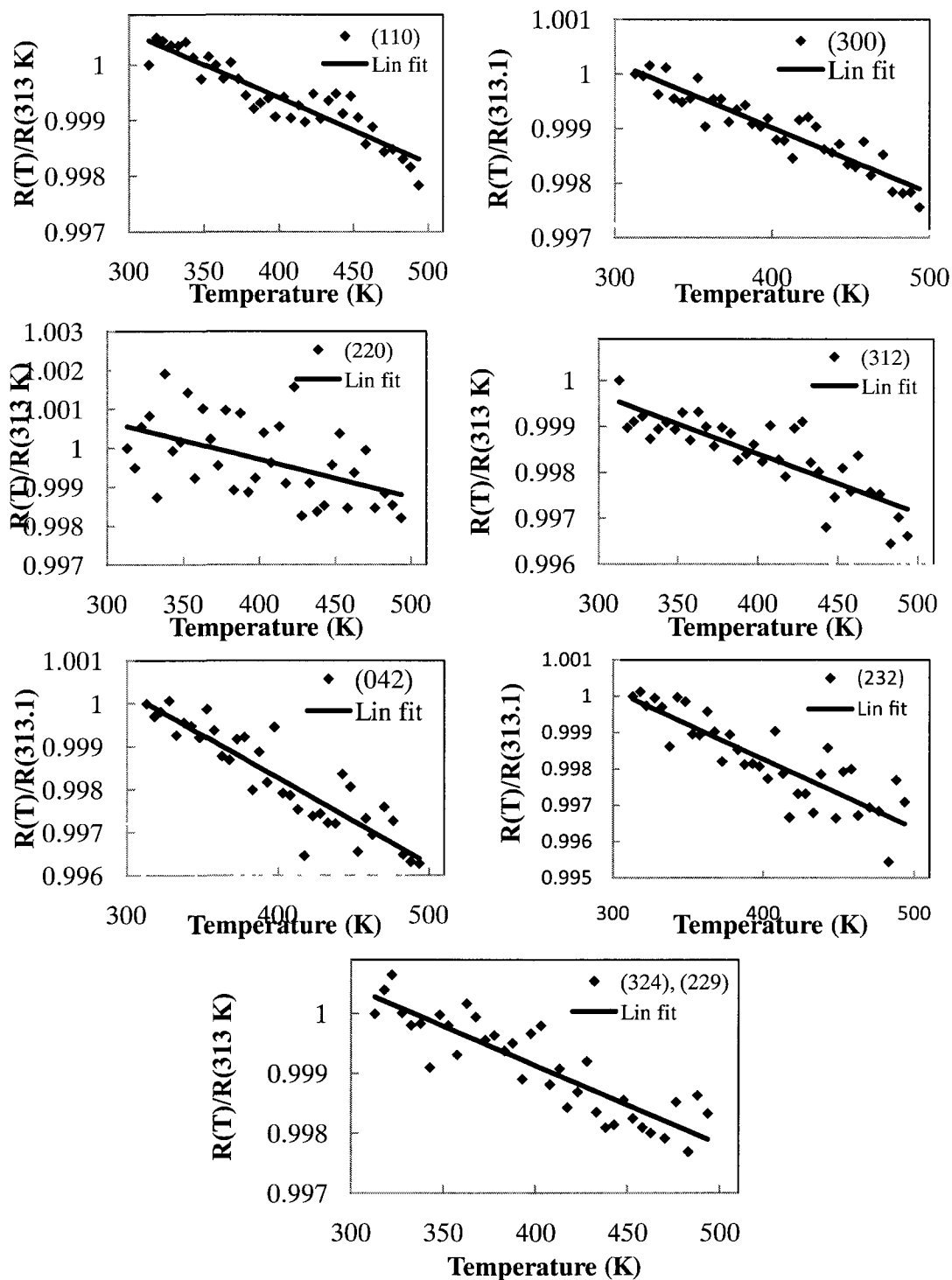


FIG. 4.24. The diffraction ring radius of a 20 nm Sb thin film that is directly heated through the heating stage. The plotted values are normalized to that taken at 313 K. The slope gives the expansion coefficient for each lattice direction; the values range between $9\text{-}20 \times 10^{-6} \text{ K}^{-1}$. This is within the measured values for α_{\perp} and α_{\parallel} .⁴³

In the case of Sb nanoparticles the expansion coefficient takes a wider range of values than in the case of the continuous thin film. As in Fig. 4.25 we can see that the values are 11, 30, -2, 10, 4, 20, and $11 \times 10^{-6} \text{ K}^{-1}$ for the planes (012), (104), (110), (006), (202), (116), and (122), respectively. Note that the (111) plane shows almost no change or a slight contraction rather than expansion with temperature while its nearest plane (104) shows an exceptionally high expansion coefficient.

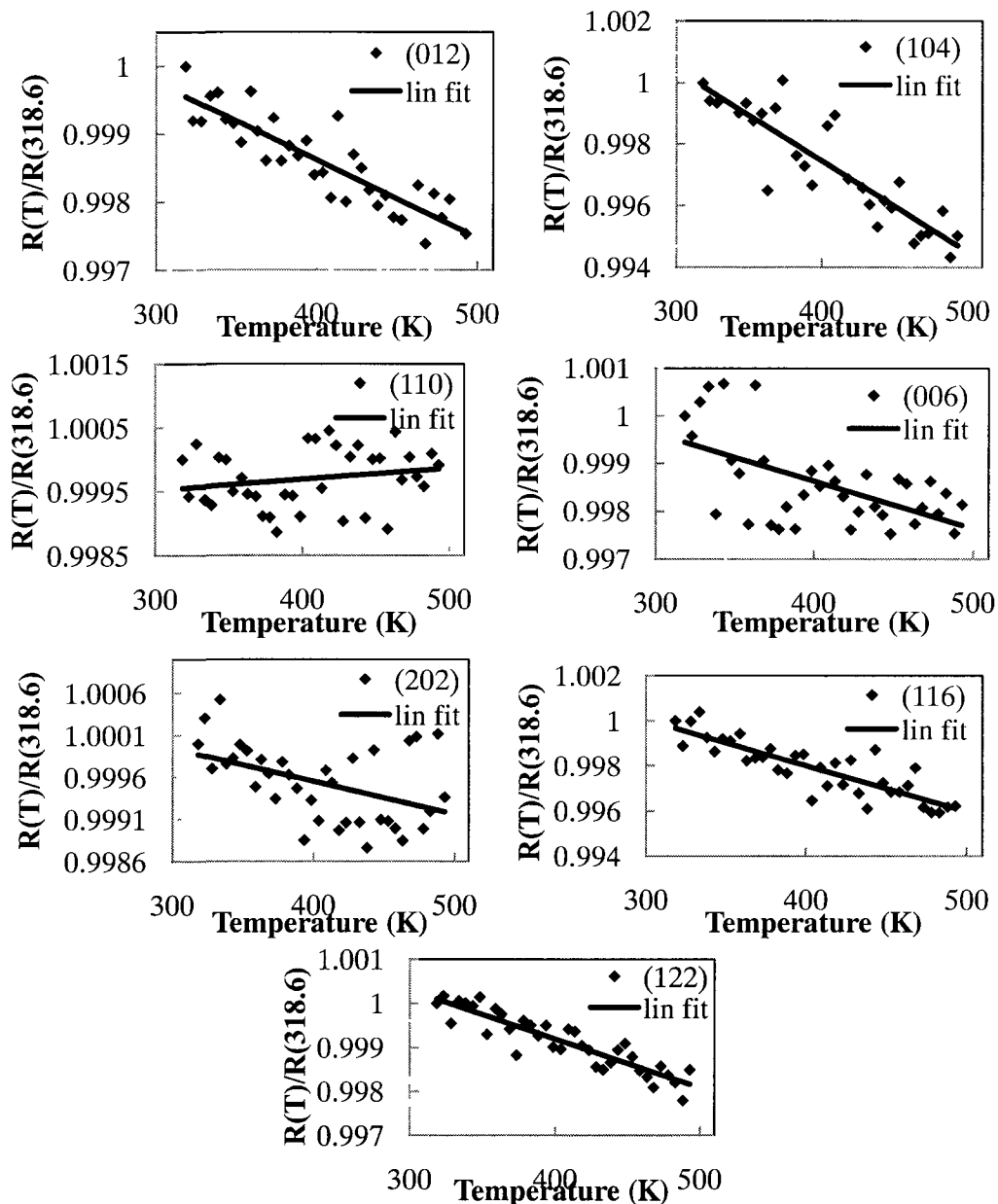


FIG. 4.25. The diffraction ring radius of Sb nanoparticles that is directly heated through the heating stage. The plotted values are normalized to that taken at 313 K. The slope gives the expansion coefficient for each lattice direction; the values are 11 , 30 , -2 , 10 , 4 , 20 , and $11 \times 10^{-6} \text{ K}^{-1}$ for the planes (012), (104), (110), (006), (202), (116), and (122), respectively.

IV.4. Time-resolved studies of Sb thin films and nanoparticles

The following time-resolved studies were performed using an electron-pulse probe whose length is vital when discussing temporal phenomena. The temporal resolution of our system is limited due to the long distance between the photocathode and the sample. The number of electrons per pulse was measured using a Faraday cup and was found to be ~ 4000 . The temporal resolution of our system can be estimated by using an electron packet propagation model.^{44,45} The number of electrons per pulse was measured using a Faraday cup to be 4000 which, according to the model, can be estimated to correspond to a pulse width of 1.2 ps.

IV.4.1. Time-resolved scan on Al thin film

Before we can describe any transient observation using our electron diffraction system, we must have a reliable knowledge of the temporal resolution of the system. We already have an estimate on the electron pulse length from the Faraday cup measurement, but we need to make a more intrusive effort to reaffirm our understanding of the pulse length and the overall system resolution. We prepared a 20 nm Al thin film and transferred it to a TEM grid. We used a fluence of 5.3 mJ/cm^2 to pump the Al film.

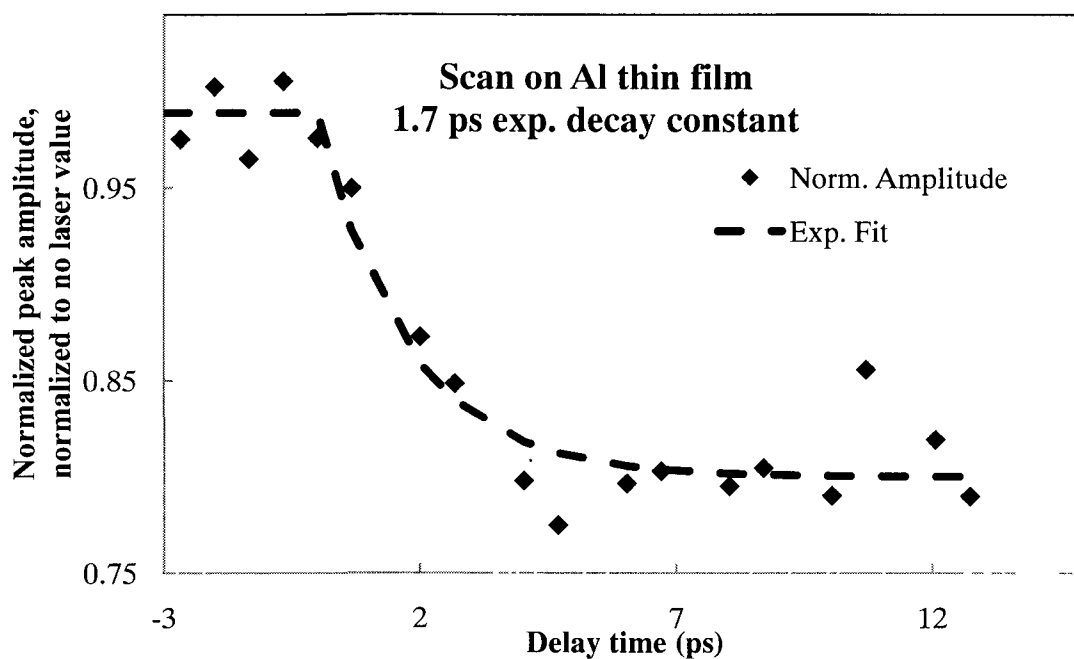


FIG. 4.26 Al thin film diffraction has a decay constant of 1.72 ps. Since Al is known to be faster than this time, we can estimate the temporal resolution of our system to equal this characteristic time.

Aluminum thin films have shown ~ 600 fs relaxation in similar UED experiments.⁶ We used an Al thin film as a sample to determine the decay constant for its time-resolved intensity scan (Fig. 26). The decay constant is 1.7 ps, which will set the temporal resolution for our system.

IV.4.2. Temperature rise after thermal equilibrium for 20 nm Sb thin film

In the following we calculate the temperature rise in the thin film at a delay of 24 ps where the thermal equilibrium is established and the term “temperature” could be defined.

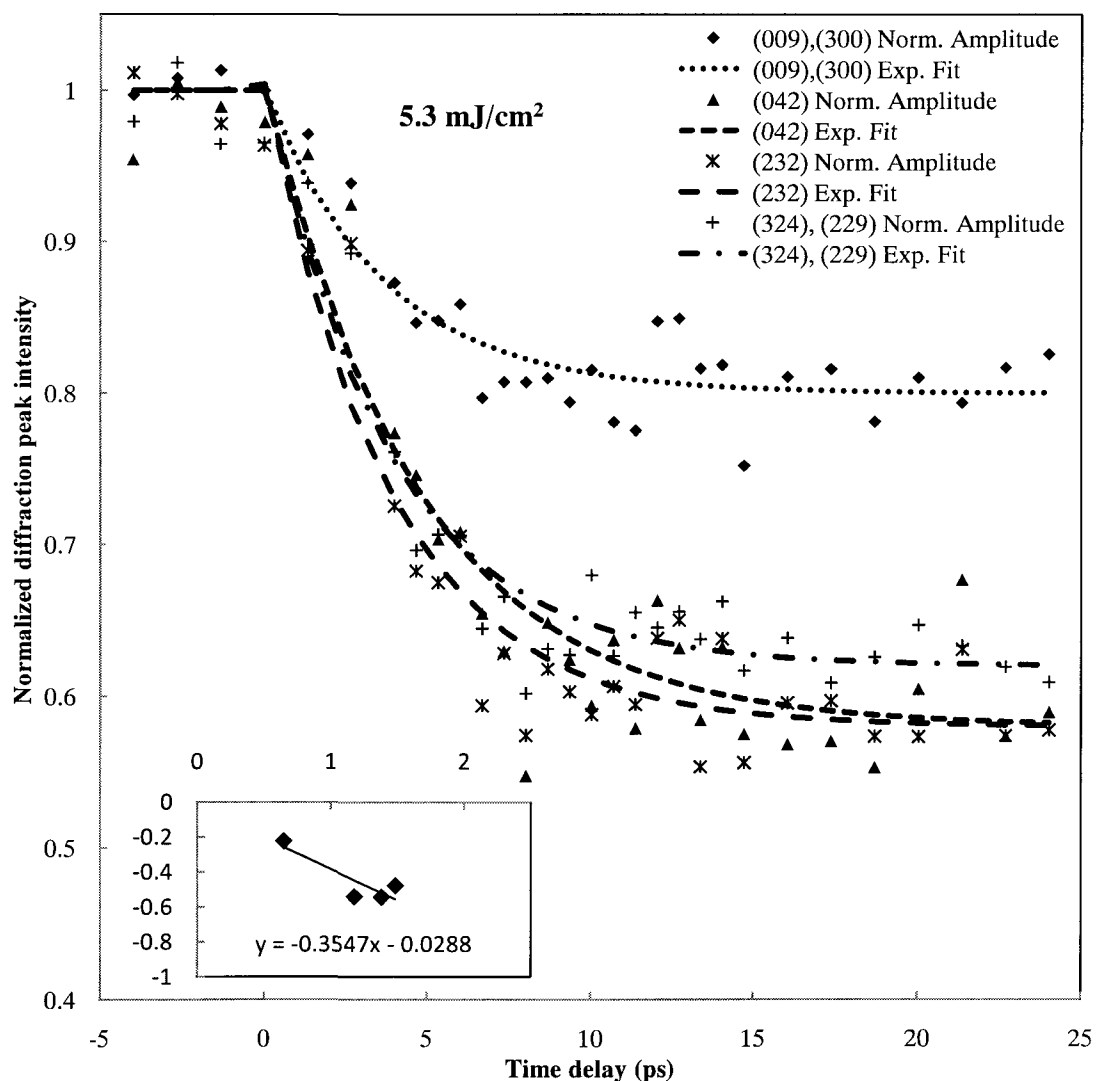


FIG. 4.27 Diffraction intensity of the 20 nm thin film under a fluence of 5.3 mJ/cm². The decay time constant for the four diffraction rings are 3.69, 4.67, 3.86, and 3.78 ps, respectively. The mean value for the decay constant is 4 ps. This intensity drop corresponds to a temperature increase of 228 K, calculated using the previously calculated Debye temperature 174 K. The inset is a plot of $\ln[I(T)/I(t_0)]$ vs d^{-2} .

We use Eq. (4.4) and Figs. 4.27 and 4.28 to calculate the temperature rise, which is found to be 228 K and 296 K for the two fluence levels used, 5.3 and 7.1 mJ/cm², respectively. The exponential decay constant is 4 and 3.62 ps for the fluences 5.3 and 7.1 mJ/cm², respectively.

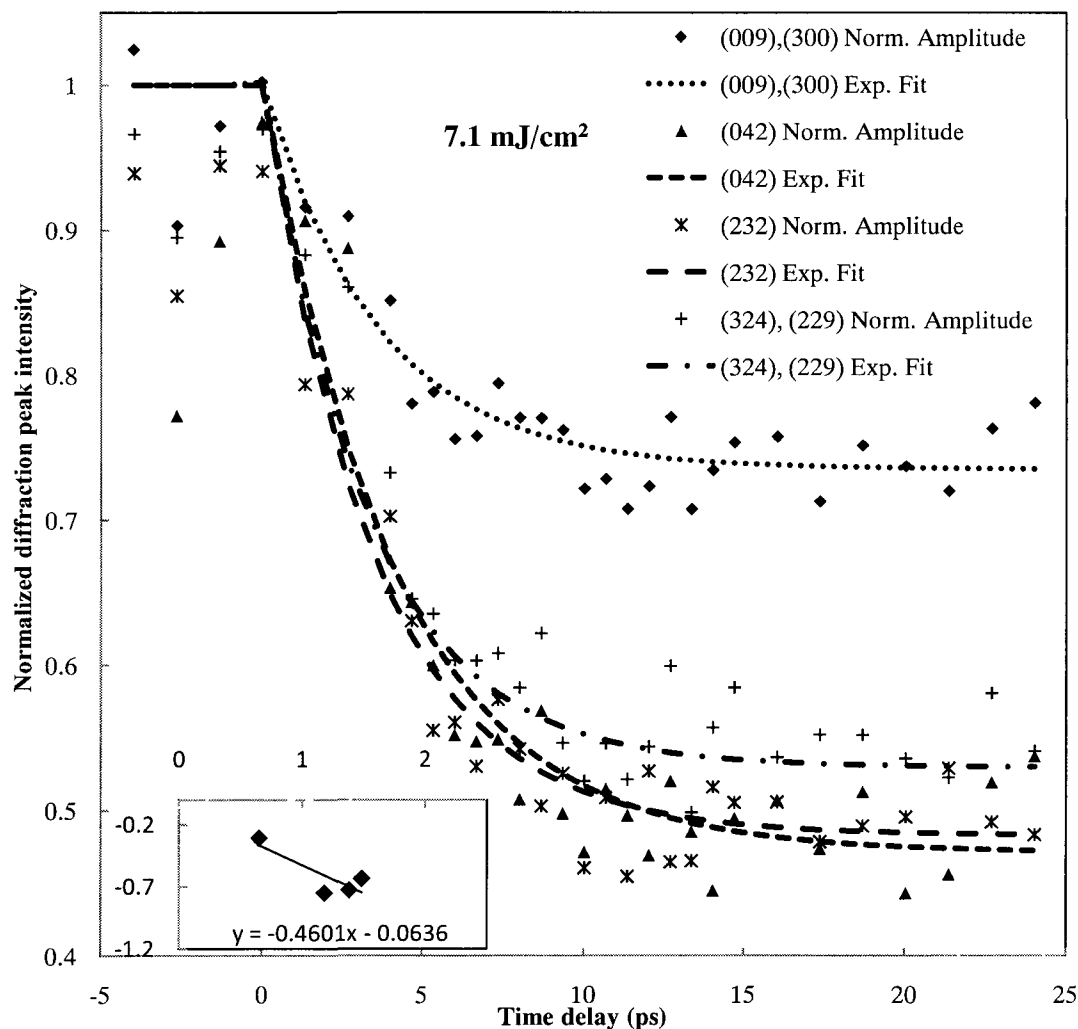


FIG. 4.28 Diffraction intensity of the 20 nm thin film under a fluence of 7.3 mJ/cm². The decay time constant for the four diffraction rings are 3.57, 4.09, 3.52, and 3.3 ps, respectively. The mean value for the decay constant is 3.62 ps. This intensity drop corresponds to a temperature increase of 296 K, calculated using the previously calculated Debye temperature 174 K. The inset is a plot of $\ln[I(T)/I(t_0)]$ vs d^{-2} .

IV.4.3. The effect of the pump fluence on the decay constant for the 20 nm Sb film

The effect of changing the laser fluence may extend beyond heating the sample to a higher temperature. It has been shown that at high fluence the diffracted intensity's decay constant is inversely proportional to the pump laser fluence,²³ which indicates non-thermal melting. The non-thermal melting regime dominates when the fluence is high enough to excite a threshold percentage of the valence band electrons to the non-bonding conduction band. The level of pumping we use here keeps us within the thermal regime.

To our knowledge there has been little work done to investigate the dependence of exponential decay of the diffracted intensity on the pumping fluence in the pumping region under the damage threshold. The studies that were performed at higher fluences could not be simply extrapolated into the lower fluence region due to different factors not applicable in all cases, such as the density of the excited electrons. We have performed three sets of time resolved scans; each scan set consisted of two scans at two pump levels. Each scan set was performed back to back to guarantee similar experimental conditions. By fitting the data using a simple exponential decay function and comparing the results we found that the decay constant for all peaks fell in the range 1.6 – 4.1 ps with absolutely no dependence on the applied fluence. One cannot confirm with certainty that there is no dependence on fluence, because the resolution of our diffraction system is limited to 1.7 ps, but most of the measured values for the decay constant were under our resolution, which gives us a level of assurance about the lack of dependence until a higher resolution experiment is carried out.

The results from the three sets are displayed in the following figures. In Figs. 4.29 through 4.34, we can see no correlation between the decay constant and fluence.

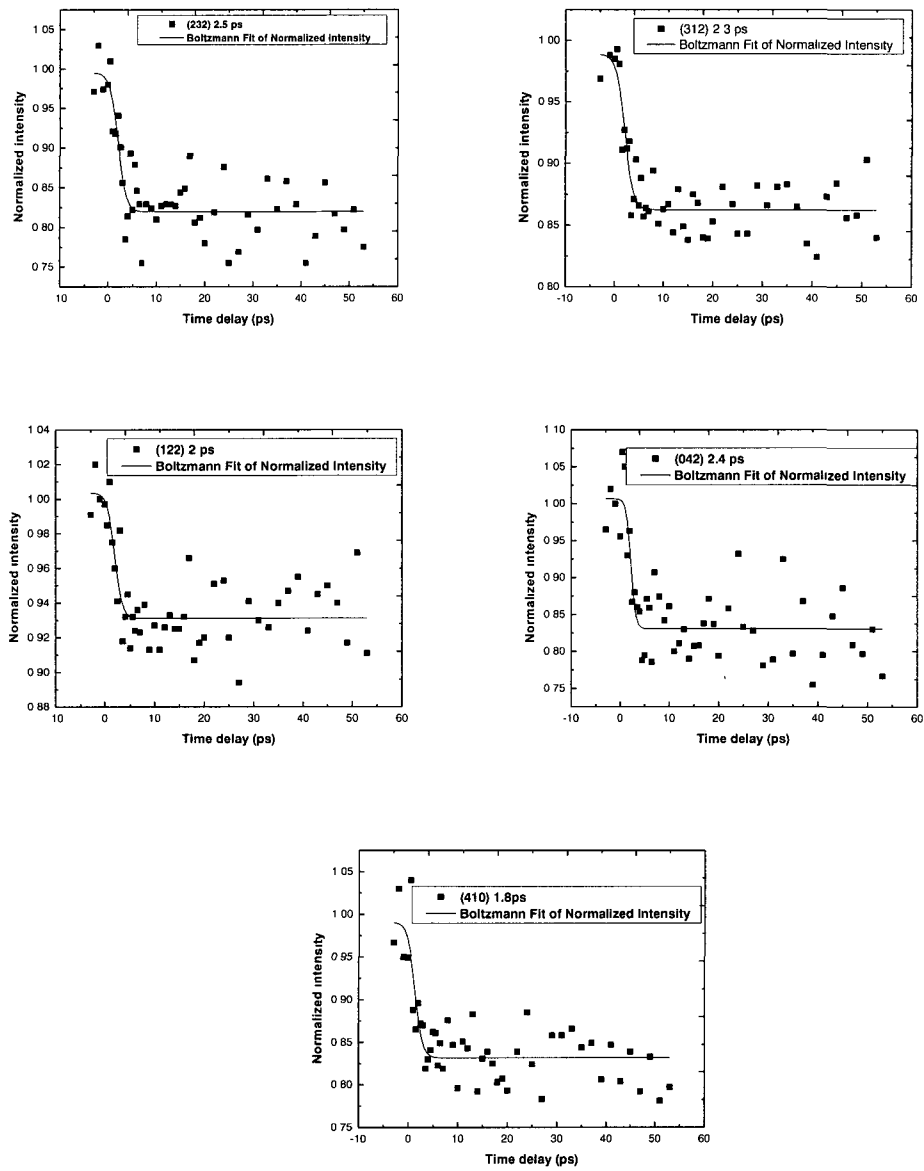


FIG. 4.29 Diffraction rings (232), (312), (122), (042), (410) of the 20 nm thin film under laser fluence 2.9 mJ/cm^2 . The decay time constants for the five rings are 2.5, 2.3, 2.0, 2.4 and 1.8 ps, respectively.

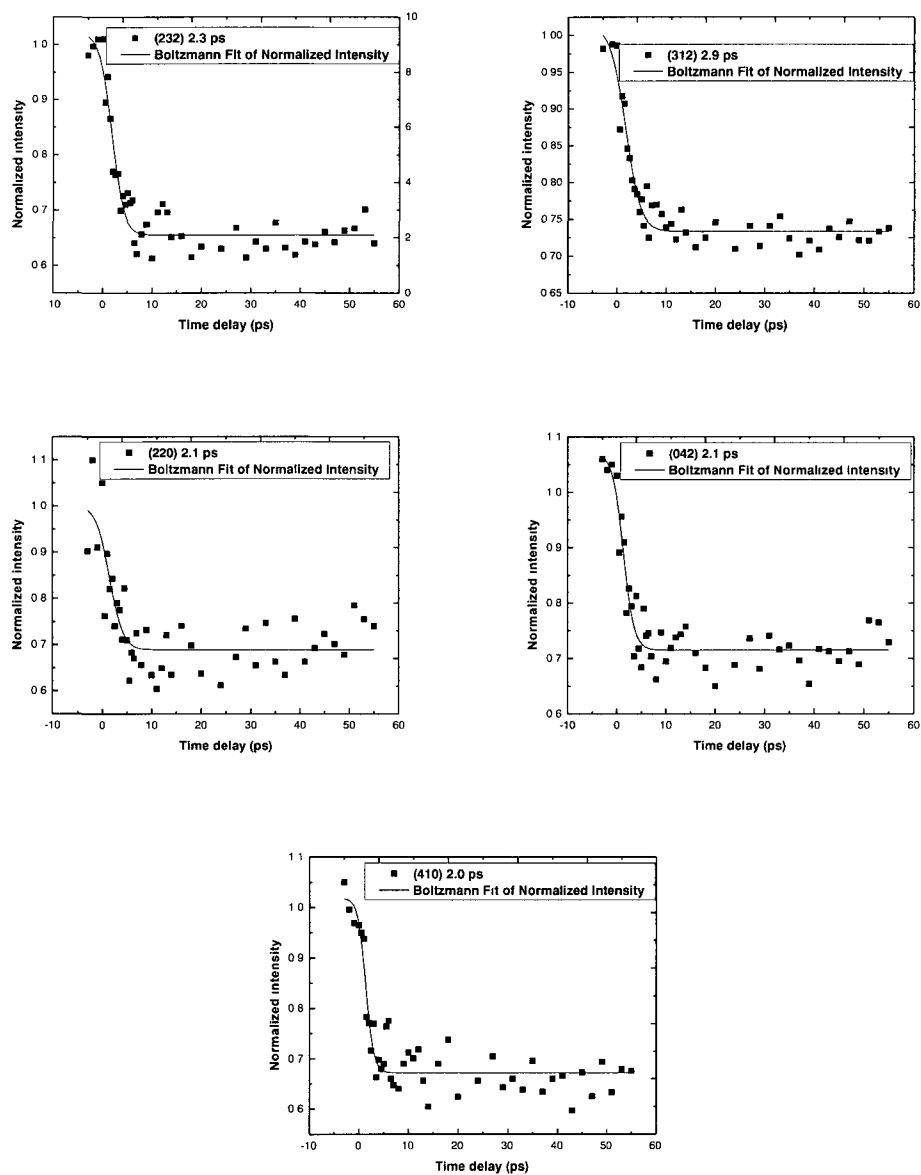


FIG. 4.30 Diffraction rings (232), (312), (122), (042), (410) of the 20 nm thin film under laser fluence 6.0 mJ/cm^2 . The decay time constants for the five rings are 2.3, 2.9, 2.1, 2.1 and 2.0 ps, respectively.

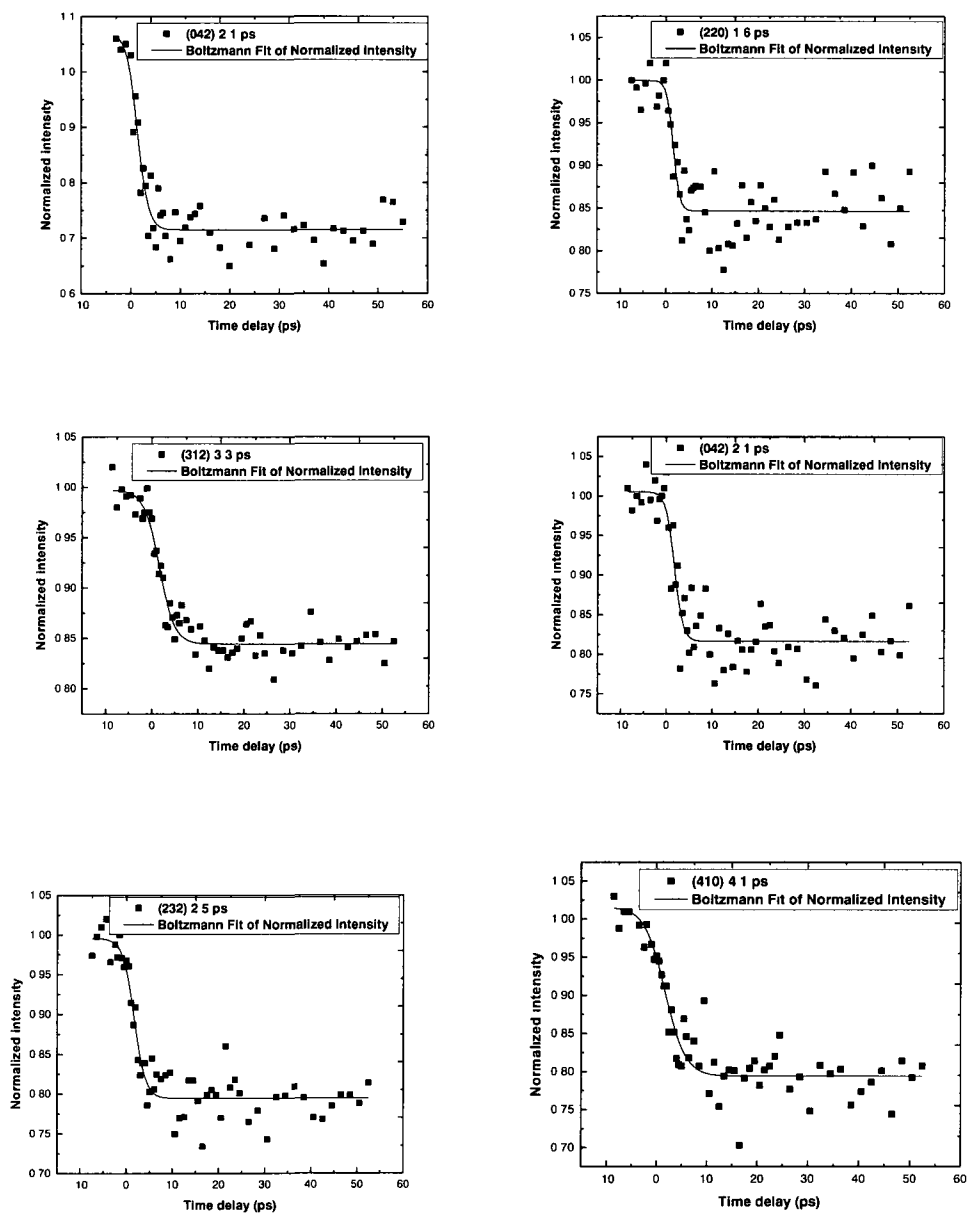


FIG. 4.31 Diffraction rings (300), (220), (312), (042), (232), and (410) of the 20 nm thin film under laser fluence 3.3 mJ/cm^2 . The decay time constants for the six rings are 1.9, 1.6, 3.3, 2.1, 2.5 and 4.1 ps, respectively.

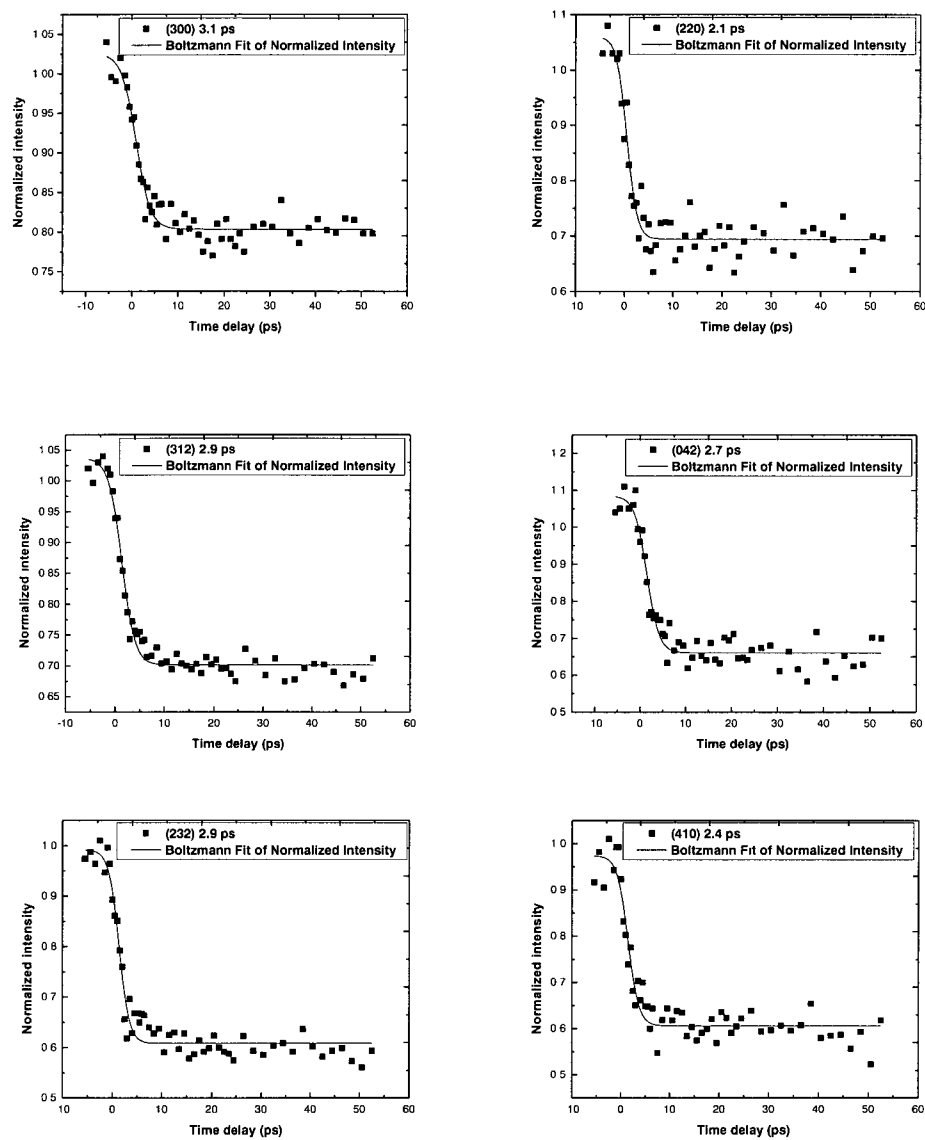


FIG. 4.32 Diffraction rings (300), (220), (312), (042), (232), and (410) of the 20 nm thin film under laser fluence 7.3 mJ/cm^2 . The decay time constants for the six rings are 3.1, 2.1, 2.9, 2.7, 2.9 and 2.4 ps, respectively.

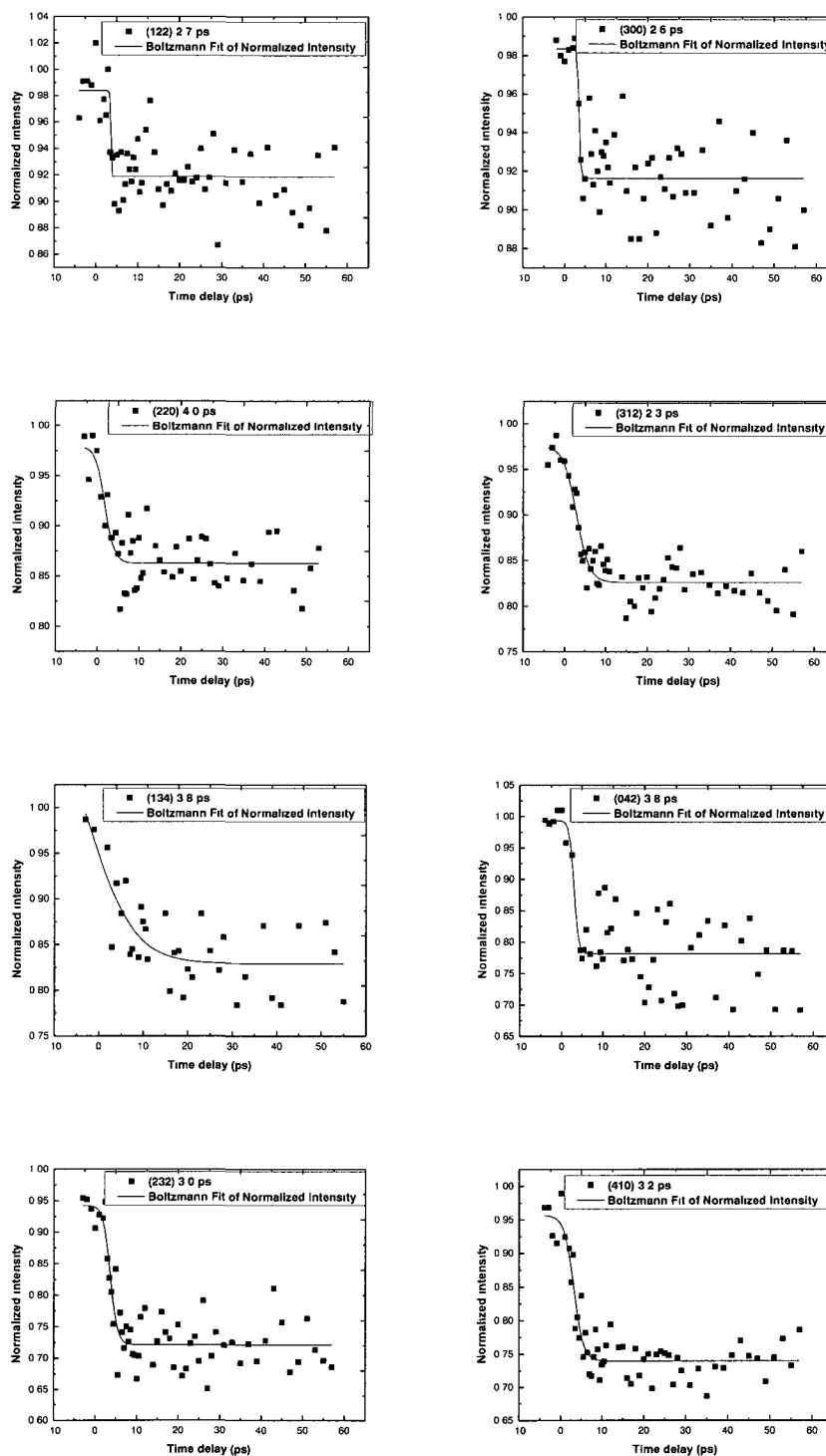


FIG. 4.33 Diffraction rings (112), (300), (220), (312), (134), (042), (232), and (410) of the 20 nm thin film under laser fluence 2.7 mJ/cm^2 . The decay time constants for the eight rings are 2.7, 2.6, 4.0, 2.3, 3.8, 3.8, 3.0 and 3.2 ps, respectively.

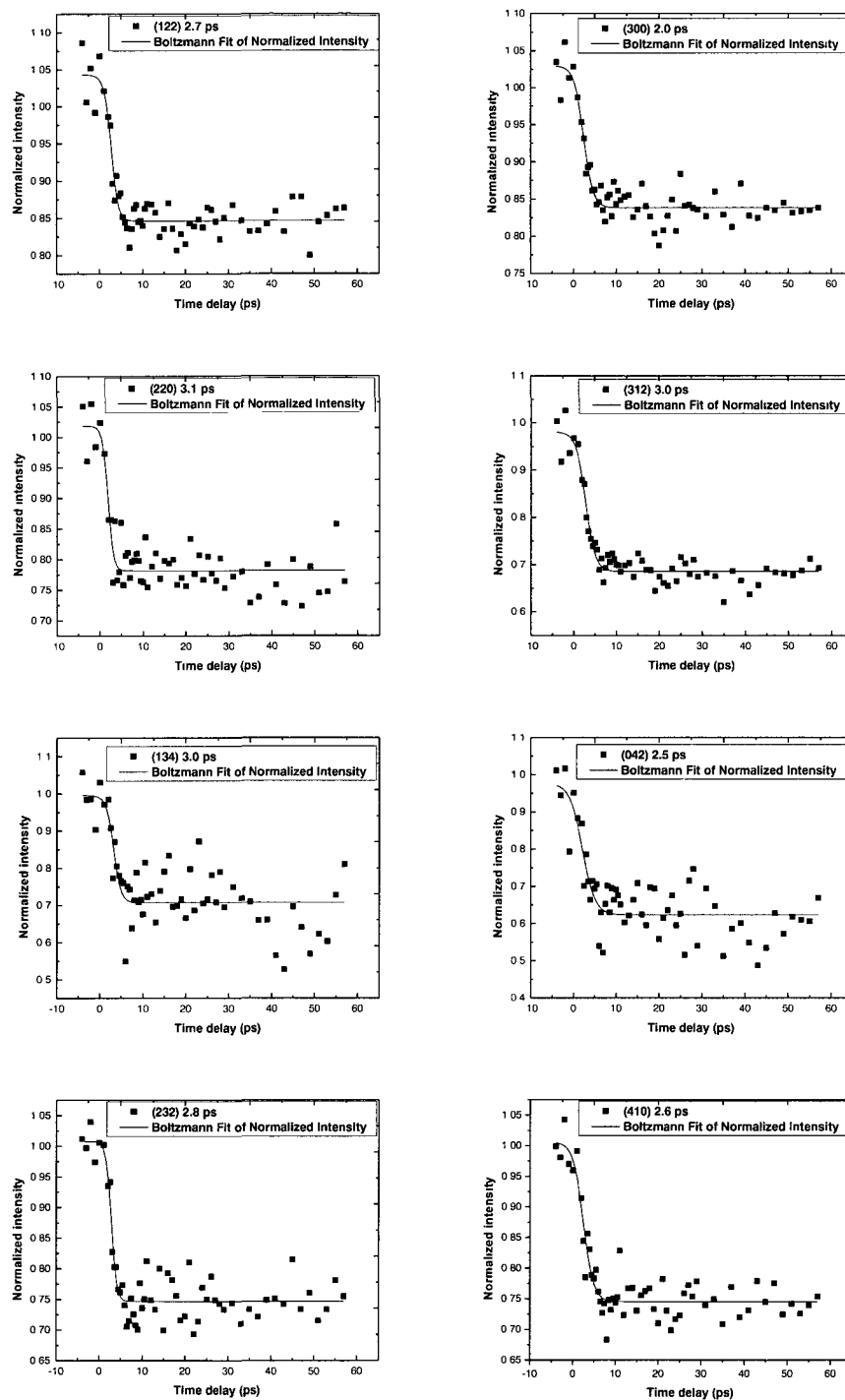


FIG. 4.34 Diffraction rings (112), (300), (220), (312), (134), (042), (232), and (410) of the 20 nm thin film under laser fluence 5.3 mJ/cm^2 . The decay time constants for the eight rings are 2.0, 2.7, 2.0, 3.1, 3.0, 3.0, 2.5 and 2.8 ps, respectively.

IV.4.4. Delayed lattice expansion

The application of laser excitation is almost immediately followed by thermal agitation of the atoms in the lattice. This effect reduces the order of the lattice, resulting in a decrease in the diffraction intensity. In this section we report an observation of a delayed lattice expansion. In our electron-diffraction pattern, we find that the reduction in diffraction rings' radii, indicating a lattice expansion in the Sb thin film, takes place 6 ps after t_0 , which is marked by the initial drop in diffraction intensity. After the hot electrons thermalize with the lattice, there is a stress generated at the surface that travels into the film with the speed of sound in an effort to release the stress through lattice expansion^{47,48,49}. Since the stress wave travels into the film with the speed of sound, we apply the delay value of 6 ps and the speed of sound in antimony 4230 m/s to get a film thickness of 20.5 nm, which is exactly the thickness of our film.

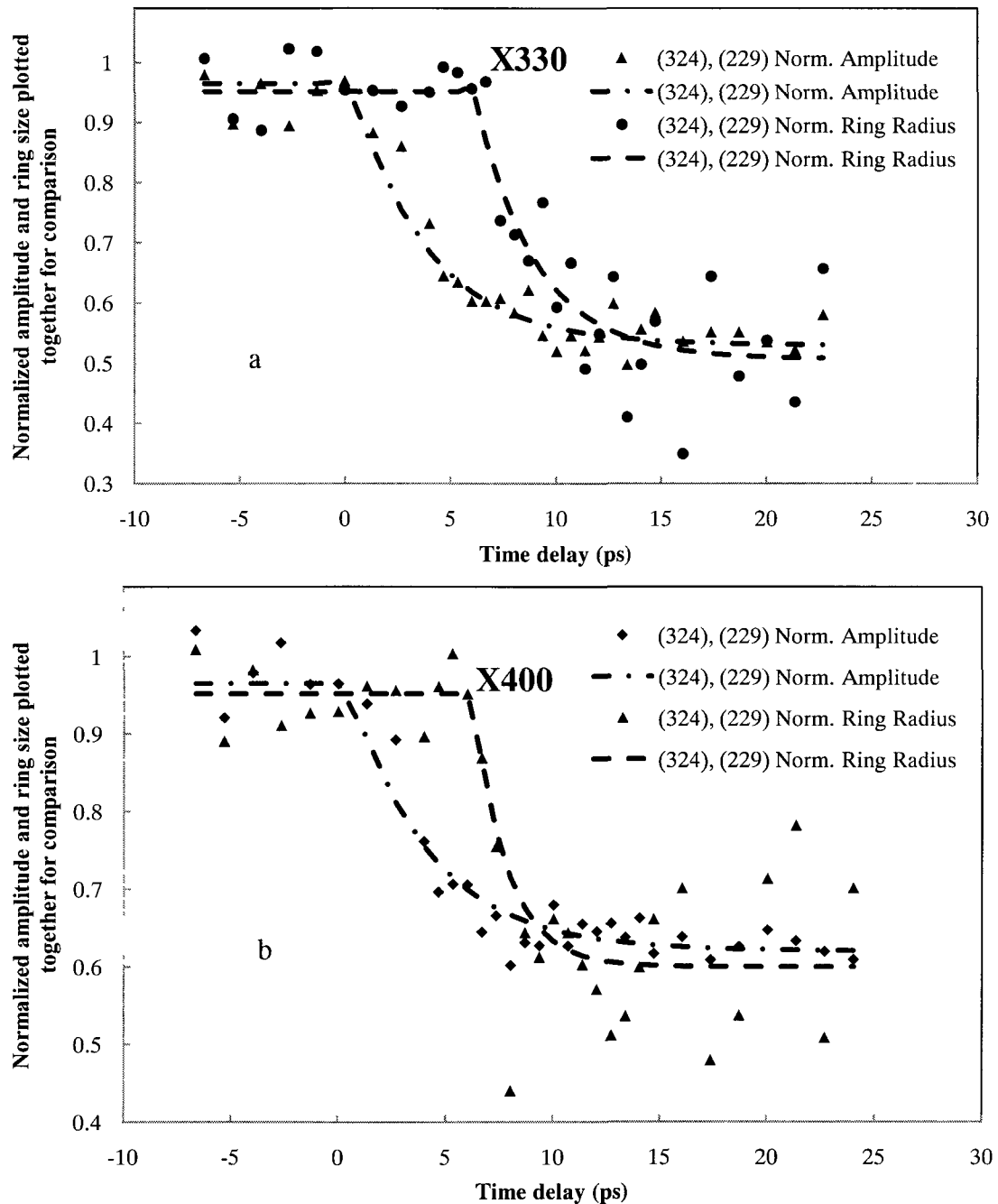


FIG. 4.35 The intensity drop is plotted with the diffraction ring size in the same scale ($\times 330$) and ($\times 400$). The 20 nm Sb film is under a laser fluence 7.1 (a) and 5.3 (b) mJ/cm². There is time delay 6 ps between the initial drop in intensity and the lattice expansion. This time delay corresponds to the propagation of the stress wave inside the film before the stress is relieved through lattice expansion. The propagation time with the speed of sound gives a film thickness 20.5 nm, which corresponds to the film thickness.

IV.4.5. Decay constant comparison between the Sb nanoparticles and 20 nm thin film

This section aims to compare the time-resolved electron-diffraction intensity for antimony nanoparticles and thin films. Both samples were exposed to the same laser fluence and experimental conditions and showed almost-similar exponential decay time constant. The electron-probe pulse was not set to the standard low value that is used in the rest of the time-resolved section of this chapter.

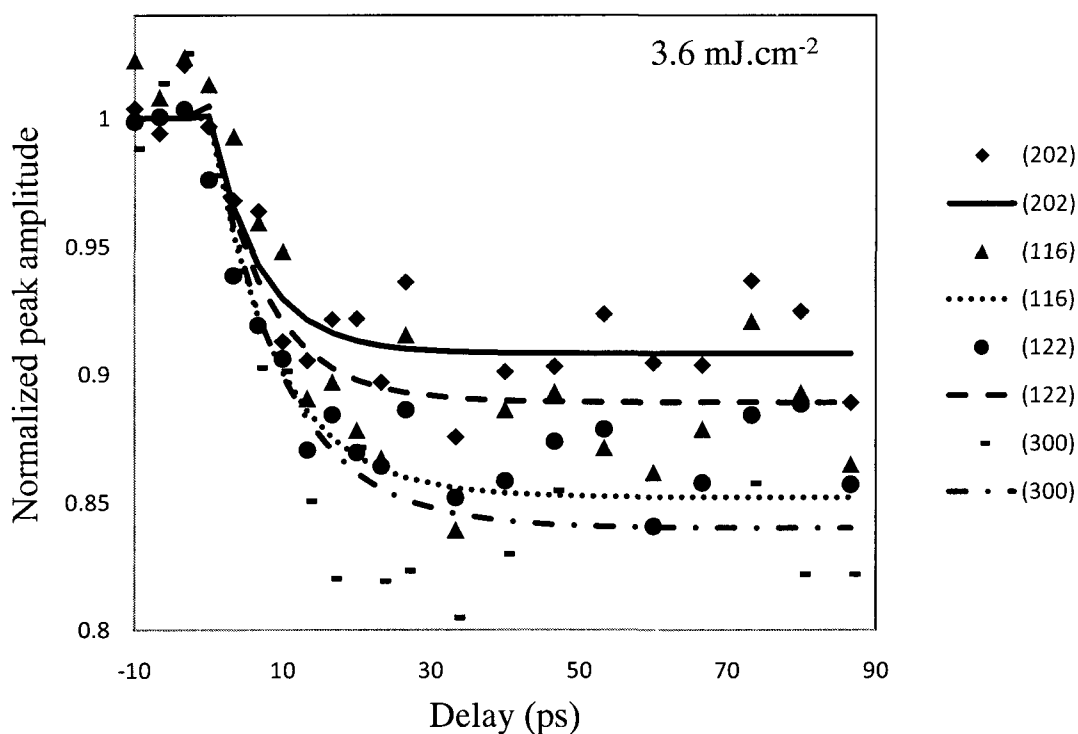


FIG. 4.36 Time-resolved scan of the 50 Å effective thickness nanoparticles. Data is fit to an exponential decay function. The exponential decay constant is 8.3 ± 0.65 ps.

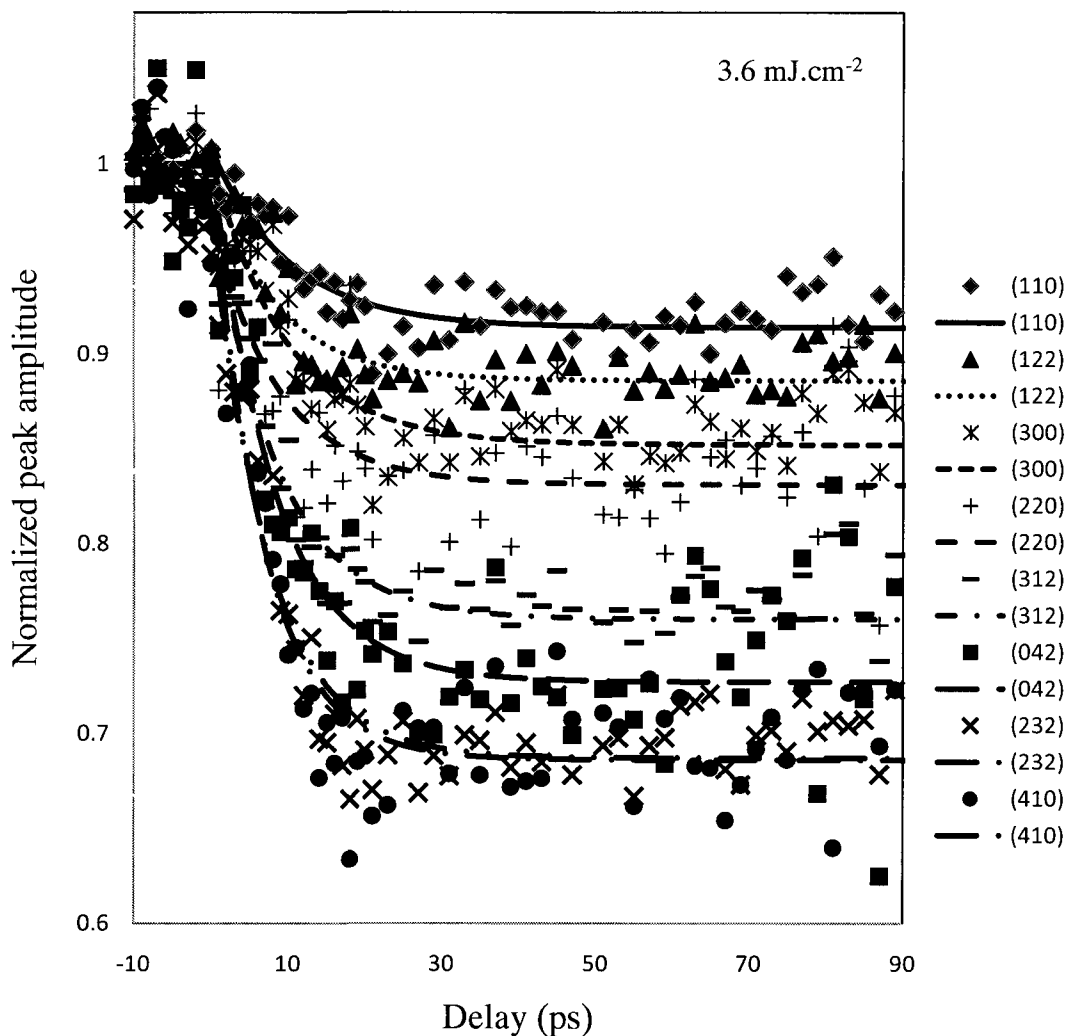


FIG. 4.37 Time-resolved scan of the 300 Å film. Data is fit to an exponential decay function. The exponential decay constant is 8.45 ± 0.38 ps.

The behavior in Figs. 4.36 and 4.37 does not show any dependence on the film geometry. Previous study has shown similar independence of electron-phonon coupling among different size nanoparticles⁵⁰. The effect of the laser pulse on our samples could be thermal or nonthermal. At higher resolution systems, the transient atomic dynamics are directly probed with either an X-ray or an electron beam. Lindenberg et al.⁵¹ reported nonthermal melting in covalently bonded materials due to laser-induced bond softening

using an X-ray probe. According to Rouse et al⁵², nonthermal melting is almost an order of magnitude faster than the thermal one. The work they did on InSb showed that the laser pulse changes the interatomic potential, immediately excites longitudinal optical phonons, and after many cycles the solid liquefies, indicating the existence of an energy barrier before melting. The faster melting at higher laser fluences was explained by lowering the energy barrier and by the stronger flow of energy into the vibrations.

IV.4.6. Temperature increase in the Sb nanoparticles and 20 nm thin film

The figures in the previous section are used to calculate the temperature rise for both the Sb nanoparticles and 20 nm thin films. Eq. 4.4 is rewritten as:

$$\frac{\ln\left\{\frac{I}{I_0}\right\}}{1/d_{(hkl)}^2} = \frac{3h^2\Delta T}{mK_B\theta_D^2}. \quad (4.5)$$

To find the temperature rise for the time-resolved experiments shown in Figs. 4.36 and 4.37, we plotted the natural logarithm of the normalized diffraction intensity ($\ln(I/I_0)$) versus $(1/d_{(hkl)}^2)$ for all possible peaks (Fig. 4.38). The slopes of both plots are used in Eq. 4.5 to find the asymptotic temperature rise for both samples. The significance of the observed time-resolved integrated intensity is that we are actually monitoring the heating of the lattice during electron-phonon energy transfer.

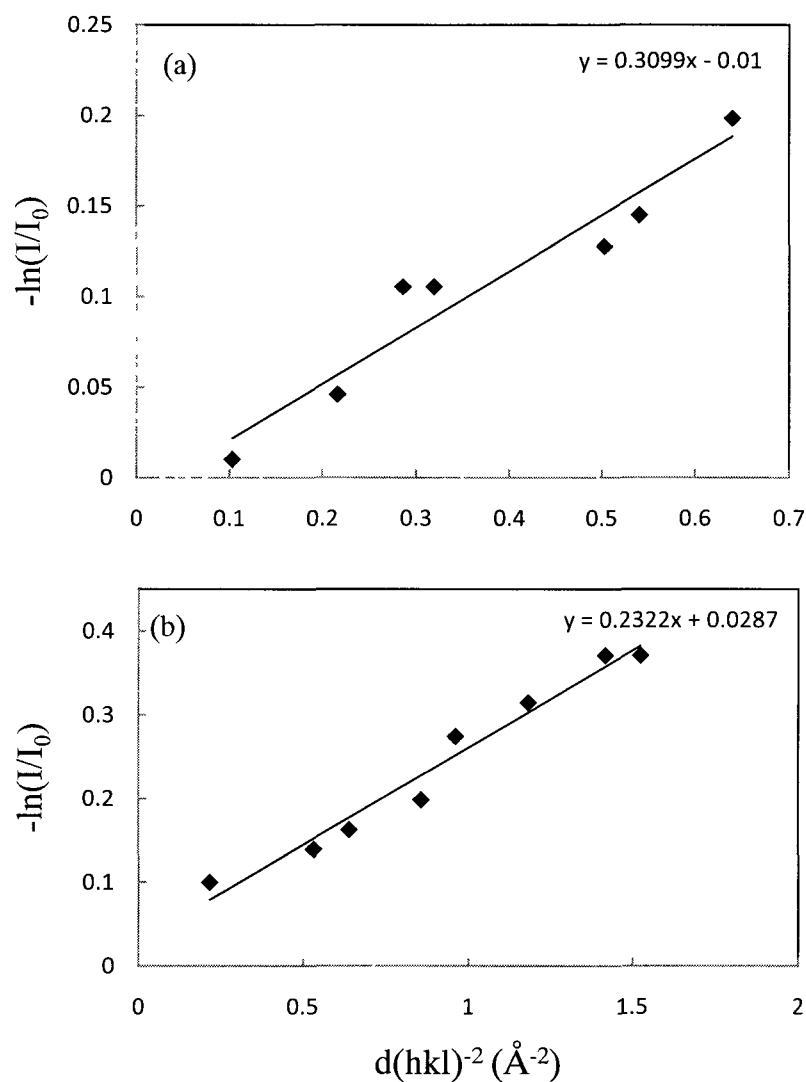


FIG. 4.38 The diffraction intensity of time-resolved scan of the 50 \AA effective thickness nanoparticles. (a) corresponds to Fig 4.35, and 200 \AA film (b) corresponds to Fig. 4.36. The fit indicates Debye-Waller effect. The normalized intensity is the average taken after minimum is reached.

Using the slopes from Fig. 4.38, the calculated Debye temperature of 150.2 K for the nanoparticles, and 174.4 K for the thin film, we get a temperature rise of 148 K for the nanoparticles, while that of the thin film is 150 K. The laser fluence was 3.6 mJ/cm^2 for both.

Eq. 4.3 can be rewritten as:

$$I_{asy}/I_0 = \exp\left(-\left(\frac{4\pi^2}{3}\right)(\langle u^2 \rangle - \langle u^2 \rangle_{RT})/d_{hkl}^2\right),$$

(4.6)

where $\langle u^2 \rangle$ and $\langle u^2 \rangle_{RT}$ are the mean square atomic displacement amplitudes at a given elevated temperature and at room temperature, respectively. Applying the slopes from Fig. 4.38, we get $(\langle u^2 \rangle - \langle u^2 \rangle_{RT}) = 0.0235 \text{ \AA}^2$ for the nanoparticles and 0.0176 \AA^2 for the thin film case.

IV.4.7. Inhomogeneous lattice spacing

Inhomogeneous lattice spacing reveals itself in a diffraction pattern image as a broadening of diffraction peaks.

What could cause this inhomogeneity is either reduction in the nanocrystals size, which is not the case due to reversibility with temperature (in this case we have a film, though) or the propagation of a sound wave, which is not the case either since we only have Coulomb heating, or lastly internal lattice strain. Fig. 4.39 shows the laser-induced broadening of multiple diffraction peaks for the 20 nm. The broadening effect for the (300) peak of the 34 nm film is shown in Fig. 4.40 at 20 ps after the zero-time delay.

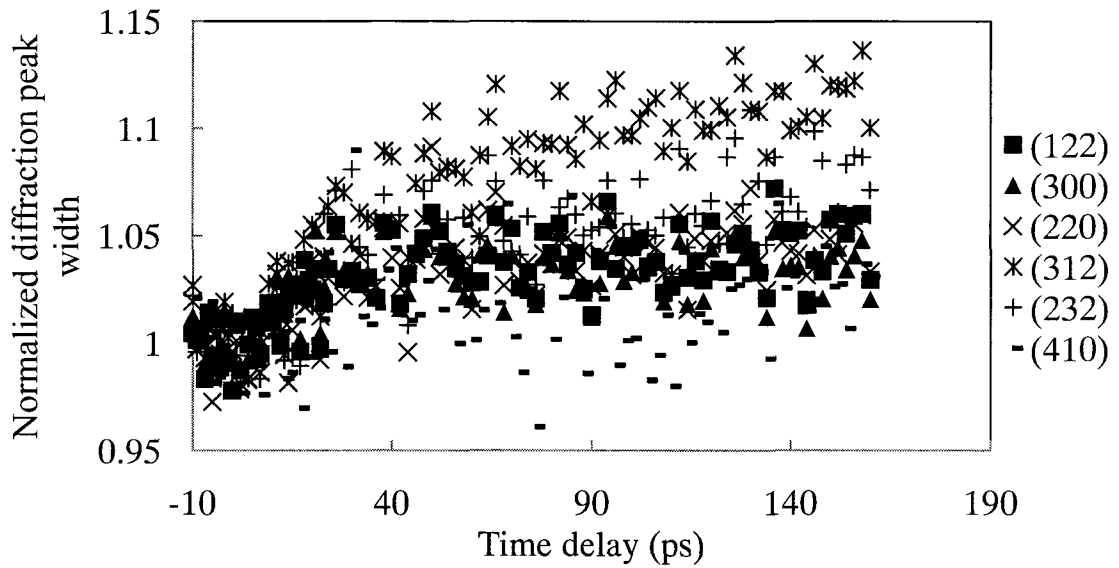


FIG. 4.39 Time-resolved scan of the 20 nm film. There is an obvious increase in the ring width, which indicates inhomogeneous lattice spacing.

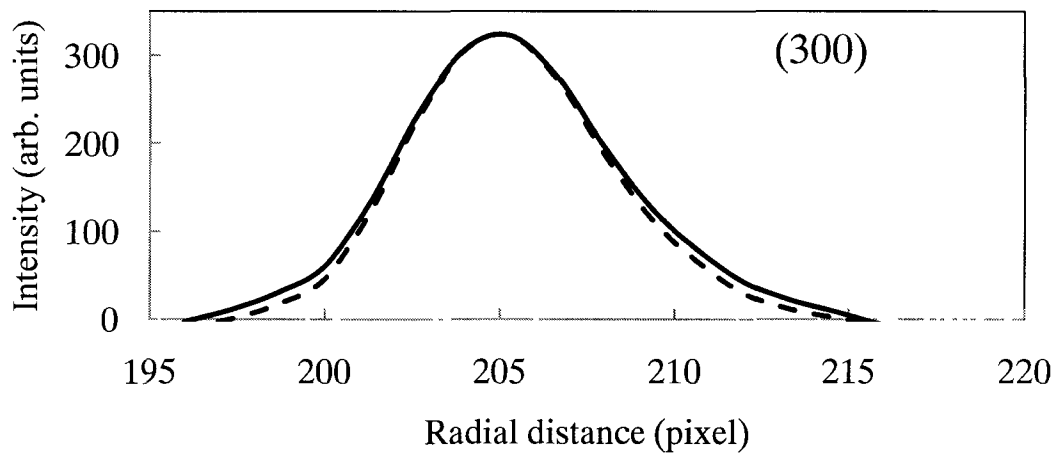


FIG. 4.40 Diffraction ring (300) of the 20 nm film. The continuous line represents the case with pump on and the dashed line represents the case with pump off. There is an obvious increase in the line width due to the application of laser pump.

IV.4.8. Harmonic lattice oscillations

The pump pulse triggers a stress wave which propagates with the speed of sound and is reflected between boundaries, forming a standing wave that can be seen in Fig 4.41. The standing wave with 20 ps period is fitted to a film thickness 34 nm instead of 20 nm indicated by the crystal thickness monitor.

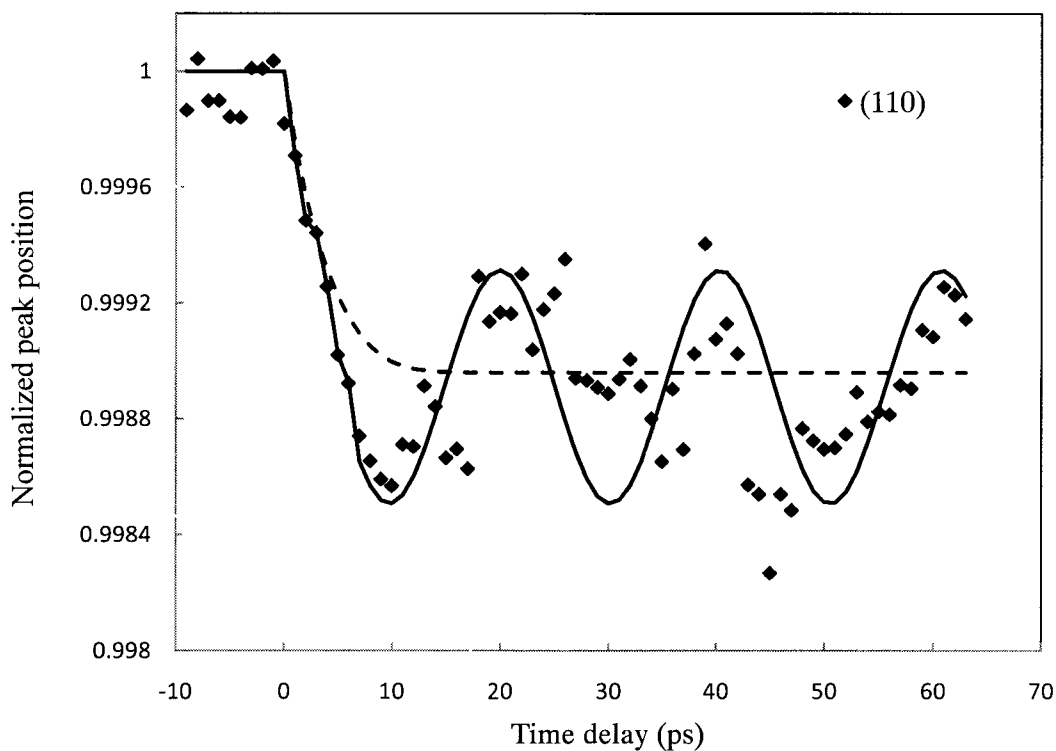


FIG. 4.41 Time-resolved scan of the 20 nm film. The (110) Bragg peak position shows lattice expansion that is fit exponentially with a decay time 3 ps. The lattice oscillates about the new equilibrium position with 20 ps period. Using the speed of sound in antimony (3420 m/s) reveals the film thickness to be 34 nm instead of 20 nm.

The propagation of the acoustic wave is further observed through the plot of the diffraction peak broadening in Fig. 4.42. The oscillation in the peak width is superimposed on an elevated background; the oscillation period is similar to that of the diffraction peak position one.

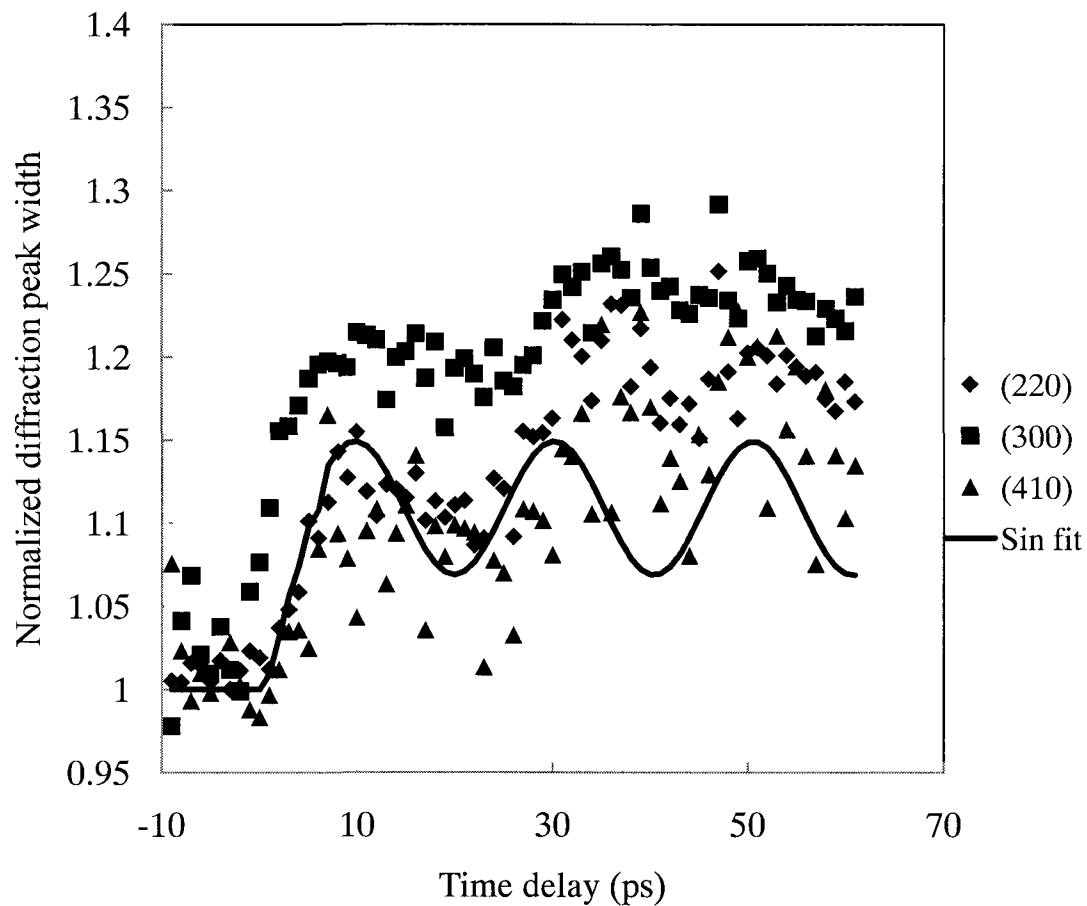


FIG. 4.42 Time-resolved scan of the 20 nm film. The Bragg peaks width shows inhomogeneous lattice expansion. The lattice oscillates about the new equilibrium position; and during the oscillation, the degree of homogeneity varies periodically with the same frequency as the lattice oscillation.

CHAPTER V

SUMMARY

The present work demonstrated the potential and limitations of using pulsed-electron diffraction to probe the lattice dynamics following the application of a femtosecond laser pulse. The sample of choice was antimony, which belongs to group V semimetals. Antimony has the advantage of forming well-isolated nanoparticles and optical phonons with interesting properties, as well as disadvantages, such as its extremely high vapor pressure that limited the ability to raise the temperature of the sample. The samples consisted of 20 nm thin films and 5 nm films that actually gave nanoparticles. Thermal studies showed that the Debye's temperature of the 20 nm film is 174 K and for the nanoparticles is 150 K, while that of the bulk is 200 K. The thermal expansion of the nanoparticles was used to show that the coefficient of thermal expansion is a good match to the bulk's value.

The Debye's temperature from the thermal studies was used to find the temperature increase of the lattice following the application of the laser-pump pulse assuming that thermal equilibrium will occur in several picoseconds. The resolution of our diffraction system is ~ 1.7 ps, which was determined from a time-resolved scan on an Al film. The exponential decay time constant was found generally to be in the range of 2 \sim 4 ps. We investigated the dependence of the decay constant on the laser pump fluence in the pumping range below sample damage and repeated the experiment three times for two levels of laser fluence and found no correlation between the decay constant and laser fluence. Such a study was needed since it was performed only for higher pumping

fluence where the excited electrons reached a critical threshold that could lead to enhanced electron-phonon coupling and non-thermal melting.

At relatively high fluence, we noticed a large delay (6 ps) between the onset of the diffraction intensity drop and the onset of the diffraction ring-size drop. This gap may be due to the propagation of a stress pulse into the film. When the speed of sound is implemented, we find that the 6 ps time delay corresponds to the actual thickness of our sample of 20 nm.

BIBLIOGRAPHY

1. M. Nisoli, S. De Silvestri, A. Cavalleri, A. M. Malvezzi, A. Stella, G. Lanzani, P. Cheyssac, and R. Kofman, "Coherent acoustic oscillations in metallic nanoparticles generated with femtosecond optical pulses," *Phys. Rev. B* **55**, R13424-R13427 (1997).
3. L. D. Sun, G. H. Takaoka, J. Matsuo, and I. Yamada, "Electron diffraction study of vaporized-metal clusters produced by a nozzle source," *Mater. Sci. Eng. A* **217-218**, 15-18 (1996).
4. M. Kaufmann, A. Wurl, J. G. Partridge, and S. A. Brown, "Structure of unsupported antimony nanoclusters," *Eur. Phys. J. D* **34**, 29-34 (2005).
5. M. Nisoli, S. De Silvestri, A. Cavalleri, A. M. Malvezzi, A. Stella, G. Lanzani, P. Cheyssac, and R. Kofman, "Coherent acoustic oscillations in metallic nanoparticles generated with femtosecond optical pulses," *Phys. Rev. B* **55**, pp. R13424-R13427, (1997).
6. A. A. Shvartsburg and M. F. Jarrold, "Solid clusters above the bulk melting point," *Phys. Rev. Lett.* **85**, pp. 2530-2532, (2000).
7. B. J. Siwick, J. R. Dwyer, R. E. Jordan, and R. J. D. Miller, "Ultrafast electron optics: Propagation dynamics of femtosecond electron packets," *J. App. Phys.* **92**, pp. 1643-1648, (2002).
8. L. Jiang, and H.-L. Tsai, "Improved two-temperature model and its application in ultrashort laser heating of metal films," *J. Heat Transfer* **127**, pp. 1167-1173, (2005).

9. J. S. Lannin, J. M. Calleja, and M. Cardona, "Second-order Raman scattering in the group-V_b semimetals: Bi, Sb, and As," *Phys. Rev. B* **12**, pp. 585-593, (1975).
10. M. L. Bansal, and A. P. Roy, "Raman study of phonons and intraband electronic excitations in antimony," *Phys. Rev. B* **33**, pp. 1526-1528, (1986).
11. S. Suckewer, C. H. Skinner, D. Kim, E. Valeo, D. Voorhees, and A. Wouters, "Divergence measurements of soft-x-ray laser beam," *Phys. Rev. Lett.* **57**, pp. 1004-1007, (1986).
12. T. K. Cheng, L. H. Acioli, J. Vidal, H. J. Zeiger, G. Dresselhaus, M. S. Dresselhaus, and E. P. Ippen, "Modulation of a semiconductor-to-semimetal transition at 7 THz via coherent lattice vibrations," *Appl. Phys. Lett.* **62**, pp. 1901-1903, (1993).
13. H. J. Zeiger, J. Vidal, T. K. Cheng, E. P. Ippen, G. Dresselhaus, and M. S. Dresselhaus, "Theory for displacive excitation of coherent phonons," *Phys. Rev. B* **45**, pp. 768-778, (1992).
14. M. Hase, K. Mizoguchi, H. Harima, S. Nakashima, M. Tani, K. Sakai, and M. Hangyo, "Optical control of coherent optical phonons in bismuth films," *Appl. Phys. Lett.* **69**, pp. 2474-2476, (1996).
15. T. E. Stevens, J. Kuhl, R. Merlin, "Coherent phonon generation and the two stimulated tensors," *Phys. Rev. B* **65**, pp. 144304-144307, (2002).
16. T. Dekorsy, H. Auer, H. J. Bakker, C. Waschke, H. G. Roskos, H. Kurz, W. Wagner, and P. Grosse, "Emission of submillimeter electromagnetic waves by coherent phonons," *Phys. Rev. Lett.* **74**, pp. 738-741, (1995).

17. G. A. Garrett, T. F. Albrecht, J. F. Whitaker, and R. Merlin, "Coherent THz phonons driven by light pulses and the Sb problem: What is the mechanism?" *Phys. Rev. Lett.* **77**, pp. 3661-3664, (1996).
18. K. Sokolowski-Tinten, C. Blome, J. Blums, A. Cavalleri, C. Dietrich, A. Tarasevitch, I. Uschmann, E. Förster, M. Kammler, M. Horn-von-Hoegen, and D. von der Linde, "Femtosecond x-ray measurement of coherent lattice vibrations near the Lindemann stability limit," *Nature* **422**, pp. 287-289, (2003).
19. S. Fahy and D. A. Reis, "Coherent phonons: Electronic softening or anharmonicity?," *Phys. Rev. Lett.* **93**, pp. 109701-109701, (2004).
20. M. Hase, M. Kitajima, S. Nakashima, and K.-I. Mizoguchi, "Coherent phonons: Electronic softening or anharmonicity? Hase et al. reply," *Phys. Rev. Lett.* **93**, pp. 109702-109702, (2004).
21. E. D. Murray, D. M. Fritz, J. K. Wahlstrand, S. Fahy, and D. A. Reis, "Effect of lattice anharmonicity on high-amplitude phonon dynamics in photoexcited bismuth," *Phys. Rev. B* **72**, pp. 060301-060304, (2005).
22. S. L. Johnson, P. Beaud, C. J. Milne, F. S. Krasniqi, E. S. Zijlstra, M. E. Garcia, M. Kaiser, D. Grolimund, R. Abela, and G. Ingold, "Nanoscale depth-resolved coherent femtosecond motion in laser-excited bismuth," *Phys. Rev. Lett.* **100**, pp. 155501-155504, (2008).
23. G. Sciaini, M. Harb, S. G. Kruglik, T. Payer, C. T. Hebeisen, F.-J. Meyer zu Heringdorf, M. Yamaguchi, M. Horn-von Hoegen, R. Ernstorfer, and R. J. D. Miller, "Electronic acceleration of atomic motions and disordering in bismuth," *Nature* **458**, pp. 56-59, (2009).

24. R. I. Sharp, and E. Warming, "The lattice dynamics of antimony," *J. Phys. F: Metal Phys.* **1**, pp. 570-587, (1971).
25. D. R. Lide, "CRC handbook of chemistry and physics," pp. 6-59, (2006).
26. E. S. Zijlstra, L. L. Tatarinova, and M. E. Garcia, "Laser-induced phonon-phonon interactions in bismuth," *Phys. Rev. B* **74**, pp. 220301-220305, (2006).
27. D. Shakhvorostov, R. A. Nistor, L. Krusin-Elbaum, G. J. Martyna, D. M. Newns, B. G. Elmegreen, Xiao-hu Liu, Z. E. Hughes, S. Paul, C. Cabral, S. Raoux, D. B. Shrekenhamer, D. N. Basov, Y. Song, and M. H. Müser, "Evidence for electric gap-driven metal-semiconductor transition in phase-change materials," *Proc. Nat. Acad. Sci. (PNAS)* **106**, pp. 10907-10911, (2009).
28. C. W. Siders, A. Cavalleri, K. Sokolowski-Tinten, Cs. Toth, T. Guo, M. Kammler, M. Horn-von-Hoegen, K. R. Wilson, D. von der Linde, and C. P. J. Barty "Detection of nonthermal melting by ultrafast x-ray diffraction," *Science* **286**, pp. 1340-1342, (1999).
29. A. Rousse, C. Rischel, and J. Gauthier, "Femtosecond x-ray crystallography," *Rev. Mod. Phys.* **73**, pp. 17-31, (2001).
30. B. Qian, H. and Elsayed-Ali, "Comment on 'Ultrafast electron optics: Propagation dynamics of femtosecond electron packets,'" *J. Appl. Phys.* **94**, pp. 803-806, (2003).
31. S. -S. Wellershoff, J. Hohlfeld, J. Güdde and E. Matthias, "The role of electron-phonon coupling in femtosecond laser damage of metals," *Appl. Phys. A* **69**, pp. S99-S107, (1999).

32. A. Kanavin, I. Isakov, Y. Afanasiev, B. Chickov, B. Wellegehausen, S. Nolte, C. Momma, and A. Tuennermann, "Heat transport in media irradiated by ultrashort laser pulses," *Phys. Rev. B* **57**, pp.14698-14703, (1998).
33. D. A. Arms, R. S. Shah, and R. O. Simmons, "X-ray Debye-Waller factor measurements of solid ^3He and ^4He ," *Phys. Rev. B* **67**, pp. 094303-1-094303-11, (2003).
34. H. E. Elsayed-Ali, "Surface Debye temperature measurement with reflection high-energy electron diffraction," *J. Appl. Phys.* **79**, pp. 6853-6857, (1996).
35. A. A. Shvartsburg and M. F. Jarrold, "Solid clusters above the bulk melting point," *Phys. Rev. Lett.* **85**, pp. 2530-2532, (2000).
36. L. Jiang, and H.-L. Tsai, "Improved two-temperature model and its application in ultrashort laser heating of metal films," *J. Heat Transfer* **127**, pp. 1167-1173, 2005.
37. W. Ibrahim, *Ph.D. Dissertation*, Old Dominion University, (2002).
38. C. Suarez, W. E. Bron, and T. Juhasz, "Dynamics and transport of electronic carriers in thin gold films," *Phys. Rev. Lett.* **75**, pp. 4536-4539, (1995).
39. B. J. Siwick, J. R. Dwyer, R. E. Jordan, and R. J. D. Miller, "Ultrafast electron optics: Propagation dynamics of femtosecond electron packets," *J. App. Phys.* **92**, pp. 1643-1648, (2002).
40. P. B. Allen, "Theory of thermal relaxation of electrons in metals," *Phys. Rev. Lett.* **59**, pp. 1460-1463, (1987).
41. P. Fischer, I. Sosnowska and M. Szymanski, "Debye-Waller factor and thermal expansion of arsenic, antimony and bismuth," *J. Phys. C* **11**, 1043-1051 (1973).

42. A. Matsumuro, M. Kobayashi, T. Kikegawa, and M. Senoo, "X-ray determination of the Debye temperature at high pressure using high-energy synchrotron radiation," *J. Appl. Phys.* **68**, 2719-2722 (1990).
43. B. G. Childs, "The thermal expansion of anisotropic metals," *Rev. Mod. Phys.* **25**, 665-670 (1953).
44. B.-L. Qian and H. E. Elsayed-Ali, "Electron pulse broadening due to space charge effects in a photoelectron gun for electron diffraction and streak camera systems," *J. Appl. Phys.* **91**, 462-468 (2002).
45. B. J. Siwick, J. R. Dwyer, R. E. Jordan, and R. J. D. Miller, "Ultrafast electron optics: Propagation dynamics of femtosecond electron packets," *J. Appl. Phys.* **92**, 1643-1648 (2002).
46. H. Park, X. Wang, S. Nie, R. Clinite, and J. Cao, "Mechanism of coherent acoustic phonon generation under nonequilibrium conditions," *Phys. Rev. B.* **72**, 100301-100304 (2005).
47. C. Rose-Petruck, R. Jimenez, T. Guo, A. Cavalleri, C.W. Siders, F. Raksi, J.A. Squier, B.C. Walker, K.R. Wilson, and C.P.J. Barty, "Picosecond-milliangstrom lattice dynamics measured by ultrafast x-ray diffraction," *Nature* **398**, 310-312 (1999).
48. A.H. Chin, R.W. Schoenlein, T.E. Glover, P. Balling, W.P. Leemans, and C.V. Shank, "Ultrafast structural dynamics in InSb probed by time-resolved x-ray diffraction," *Phys. Rev. Lett.* **83**, 336-339 (1999).

49. F. Vigliotti, S. Chen, C.Y. Ruan, V.A. Lobastov, A.H. Zewail, "Ultrafast electron crystallography of surface structural dynamics with atomic-scale resolution," *Angewandte Chemie International Edition* **43**, 20, 2705 (2004).
50. J. H. Hodak, A. Henglein, and G. V. Hartland, "Electron-phonon coupling dynamics in very small (between 2 and 8 nm diameter) Au nanoparticles," *J. Chem. Phys.* **112**, 5942-5947 (2000).
51. A. M. Lindenberg, J. Larsson, K. Sokolowski-Tinten, K. J. Gaffney, C. Blome, O. Synnergren, J. Sheppard, C. Caleman, A. G. MacPhee, D. Weinstein, D. P. Lowney, T. K. Allison, T. Matthews, R. W. Falcone, A. L. Cavalieri, D. M. Fritz, S. H. Lee, P. H. Bucksbaum, D. A. Reis, J. Rudati, P. H. Fuoss, C. C. Kao, D. P. Siddons, R. Pahl, J. Als-Nielsen, S. Duesterer, R. Ischebeck, H. Schlarb, H. Schulte-Schrepping, Th. Tschentscher, J. Schneider, D. von der Linde, O. Hignette, F. Sette, H. N. Chapman, R. W. Lee, T. N. Hansen, S. Techert, J. S. Wark, M. Bergh, G. Huldt, D. van der Spoel, N. Timneanu, J. Hajdu, R. A. Akre, E. Bong, P. Krejcik, J. Arthur, S. Brennan, K. Luening, and J. B. Hastings, "Atomic scale visualization of inertial dynamics," *Science* **308**, 392-395 (2005).
52. A. Rouse, C. Rischel, S. Fourmaux, I. Uschmann, S. Sebban, G. Grillon, Ph. Balcou, E. Förster, J.P. Geindre, P. Audebert, J.C. Gauthier, and D. Hulin, "Non-thermal melting in semiconductors measured at femtosecond resolution," *Nature* **410**, 65-68 (2001).
53. K. Andrews, D. J. Dyson and S. Keown, *Interpretation of Electron Diffraction Patterns*, 2nd Ed. Plenum Press, NY (1971).
54. G. Thomas, *Transmission Electron Microscopy of Metals*, Wiley, NY, (1962).

55. D. Schiferl and C. S. Barrett, "The crystal structure of arsenic at 4.2, 78 and 299°K,"
J. App. Cryst. **2**, 30-36 (1969).

APPENDICES

Appendix A: All figures with experimental results

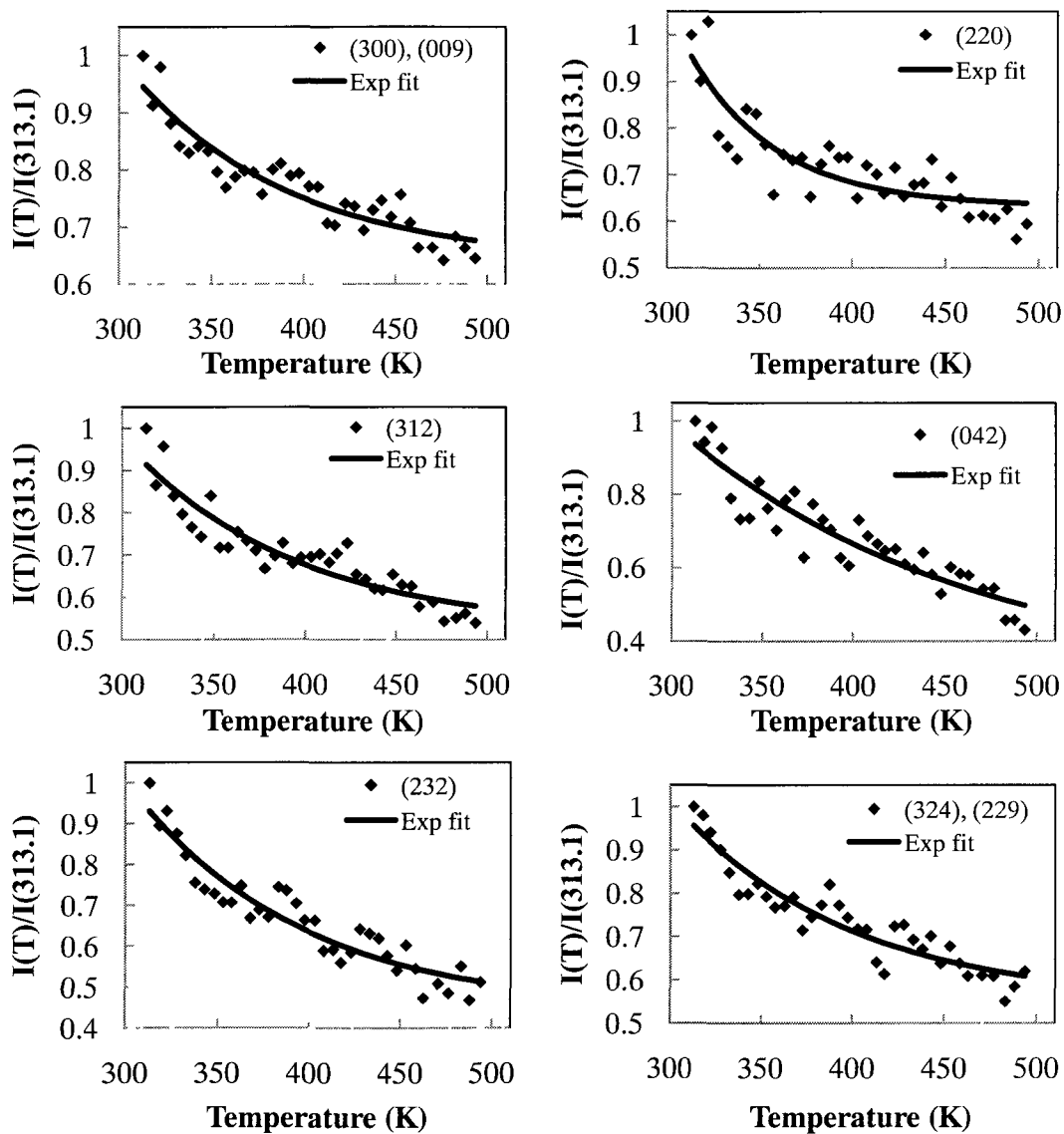


FIG. A-1. The diffraction intensity amplitude of Sb film of thickness 200 Å that is directly heated through the heating stage. The measured values are normalized to that taken at 313 K. Debye temperature calculated as 174 K.

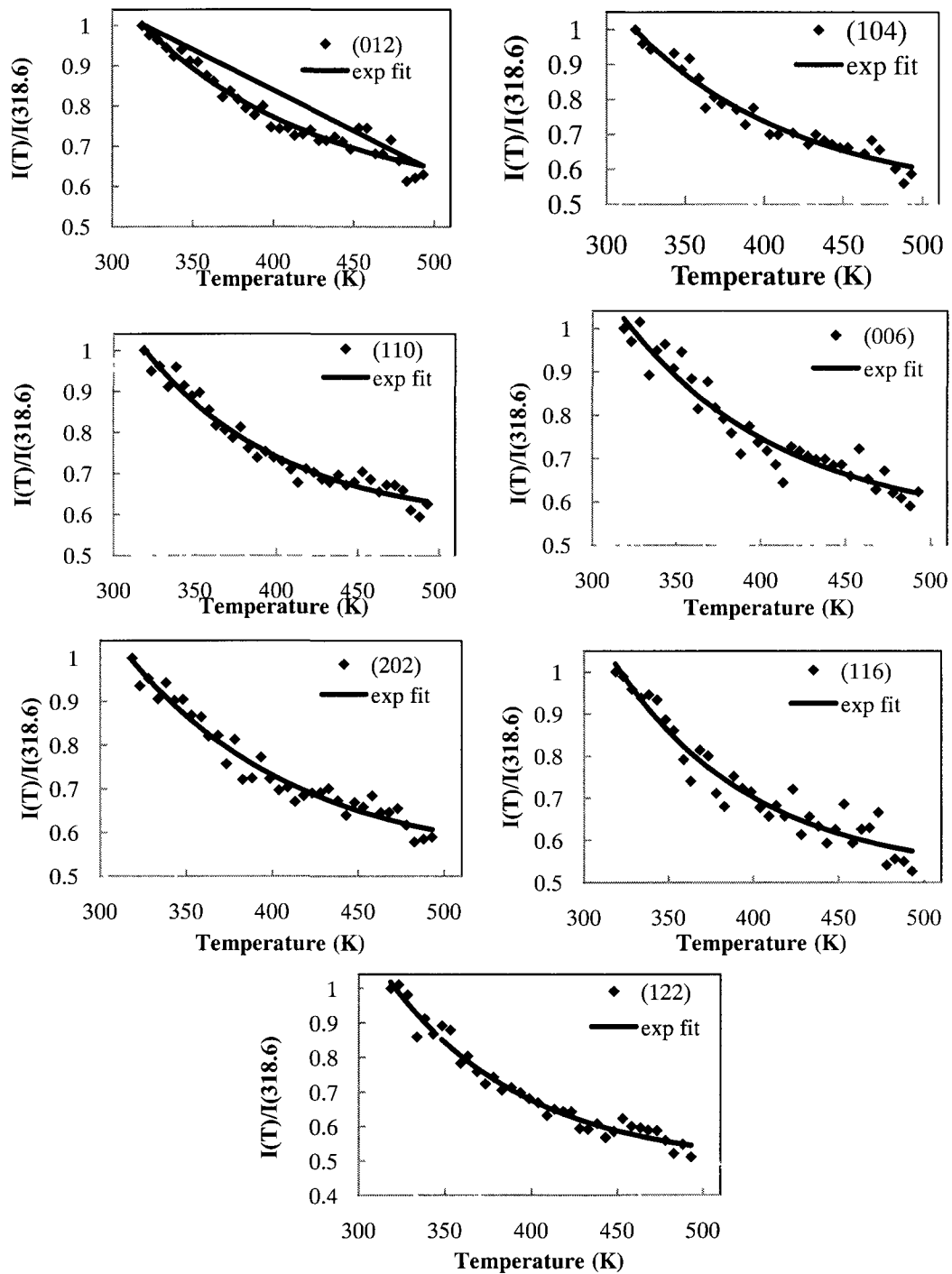


FIG. A-2. The diffraction intensity amplitude of Sb nanoparticles of film thickness 50 Å that is directly heated through the heating stage. The measured values are normalized to that taken at 313 K. Debye temperature calculated as 150 K.

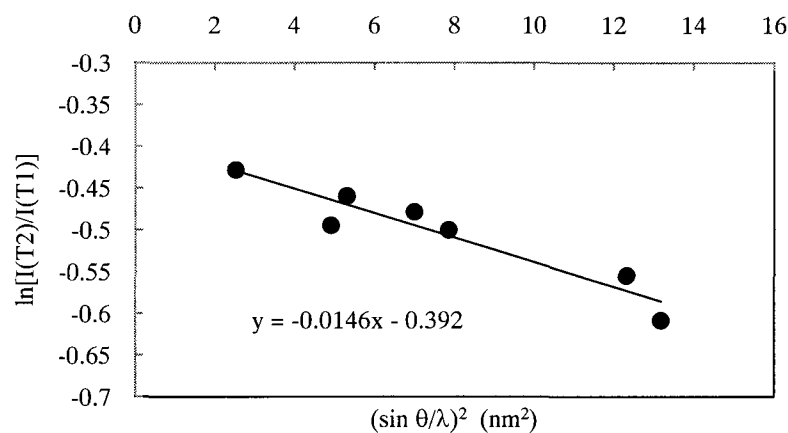


FIG. A-3. Natural logarithm of the intensity ratio of antimony nanoparticles as a function of $(\sin \theta/\lambda)^2$. The straight line slope gives $\Delta B = 0.0079 \text{ nm}^{-2}$ with $\Delta T = 174 \pm 2 \text{ K}$. The Debye temperature is found to be $150 \pm 2 \text{ K}$. The corresponding diffraction rings are: (012), (104), (110), (006), (202), (116), and (122), respectively.

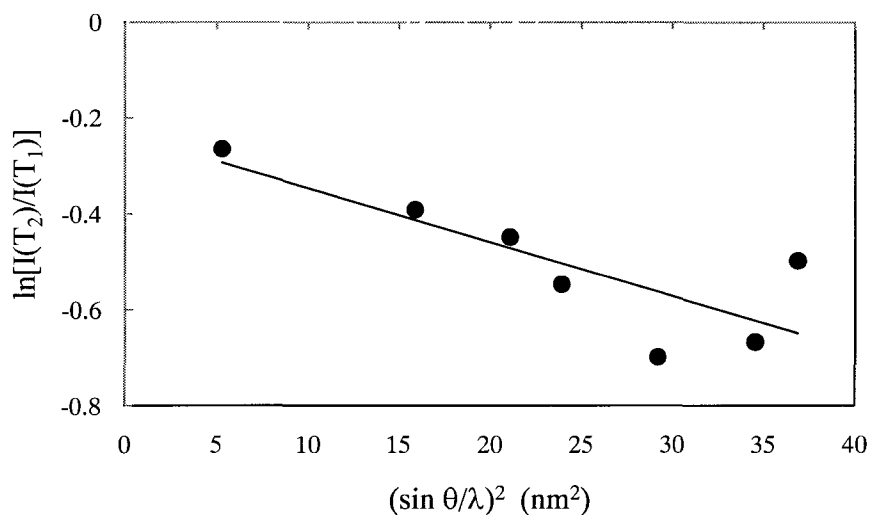


FIG. A-4. Natural logarithm of the intensity ratio of antimony 20 nm thin film as a function of $(\sin \theta/\lambda)^2$. The straight line slope gives $\Delta B = 0.0056 \text{ nm}^{-2}$ with $\Delta T = 180 \pm 2 \text{ K}$. The Debye temperature is found to be $174 \pm 2 \text{ K}$. The corresponding diffraction rings are: (110), (300), (220), (312), (042), (232), and $\{(324), (229)\}$, respectively.

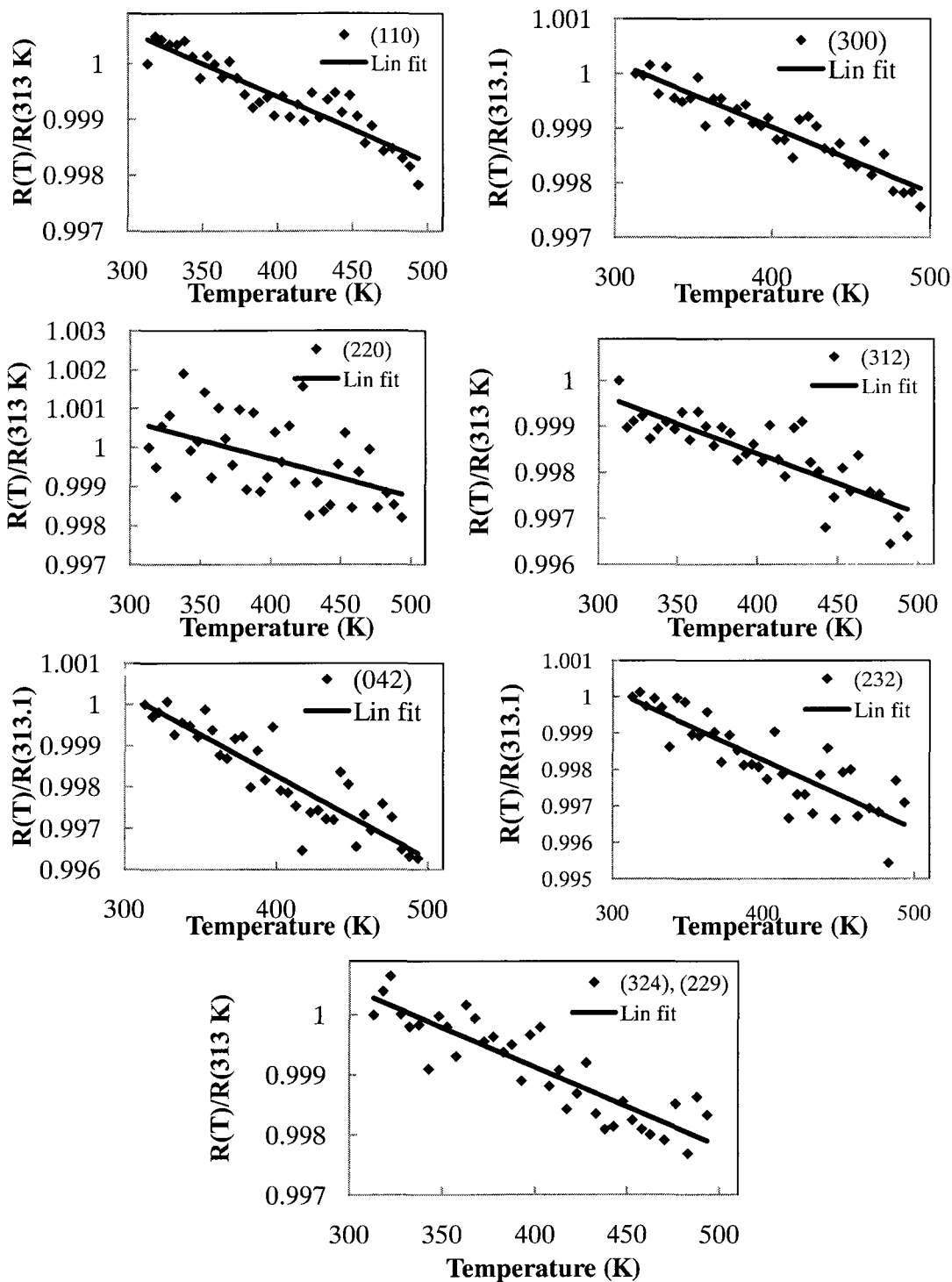


FIG. A-5. The diffraction ring radius of a 20 nm Sb thin film that is directly heated through the heating stage. The plotted values are normalized to that taken at 313 K. The slope gives the expansion coefficient for each lattice direction, the values range between $9\text{-}20 \times 10^{-6} \text{ K}^{-1}$. This is within the measured values for α_{\perp} and α_{\parallel} .

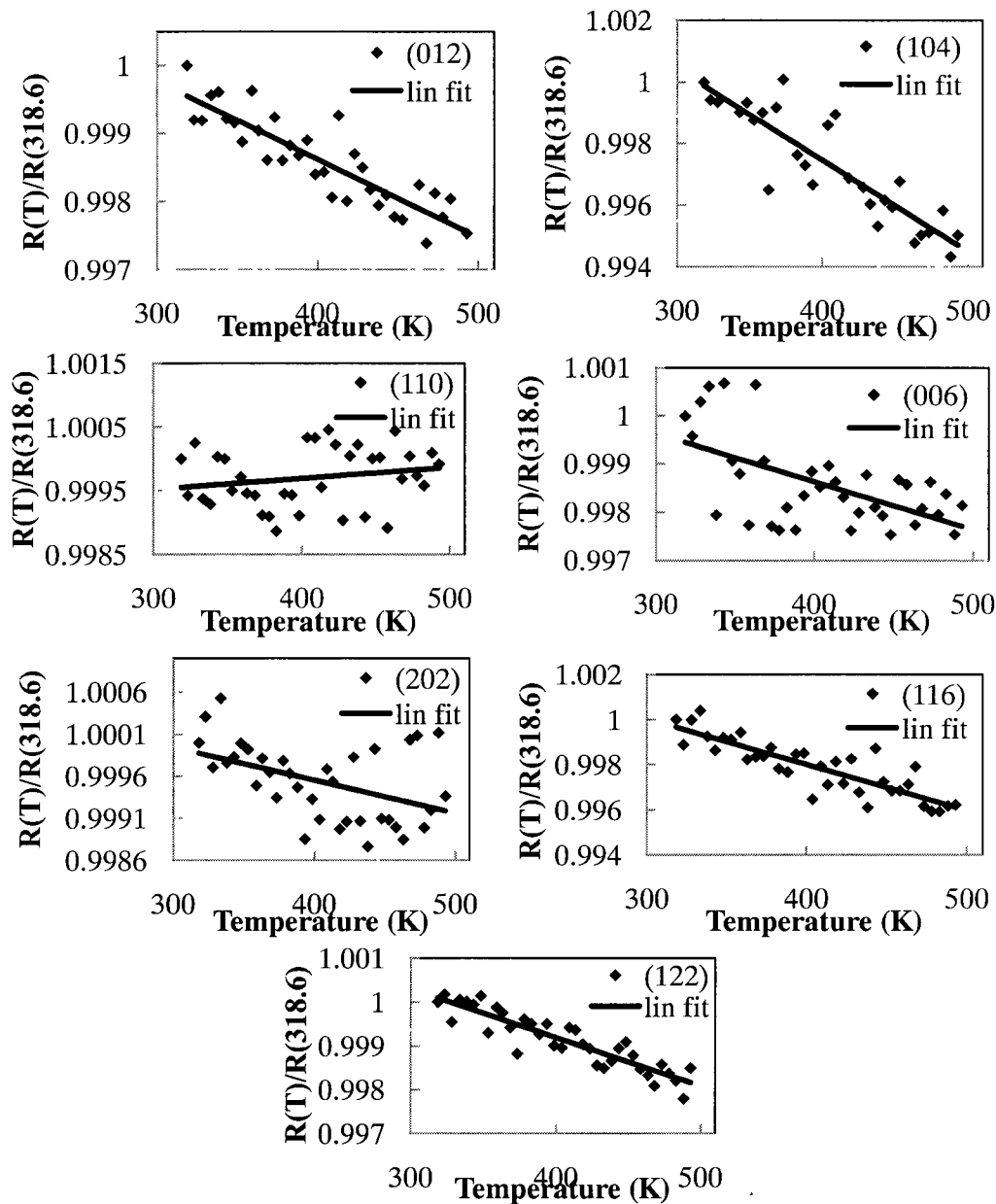


FIG. A-6. The diffraction ring radius of Sb nanoparticles that is directly heated through the heating stage. The plotted values are normalized to that taken at 313 K. The slope gives the expansion coefficient for each lattice direction, the values are 11, 30, -2, 10, 4, 20, and $11 \times 10^{-6} \text{ K}^{-1}$ for the planes (012), (104), (110), (006), (202), (116), and (122) respectively.

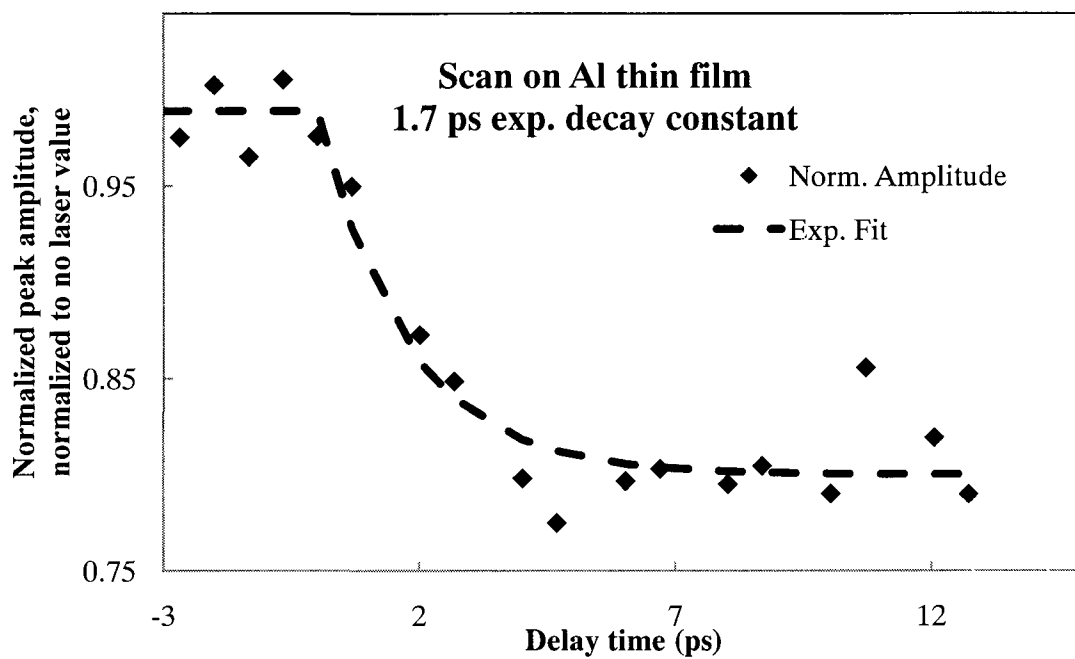


FIG. A-7 Al thin film diffraction has a decay constant of 1.72 ps. Since Al is known to be faster than this time, we can estimate the temporal resolution of our system to equal this characteristic time.

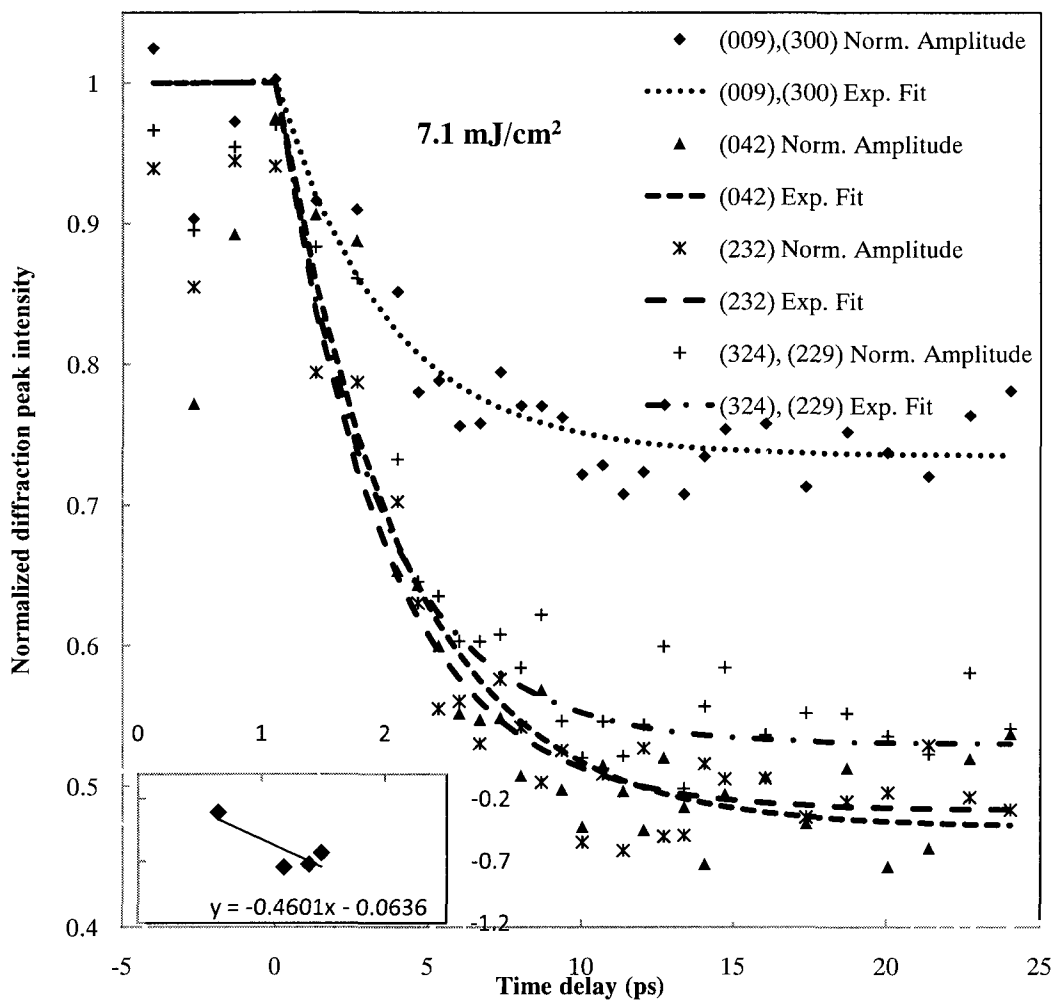


FIG. A-8 Diffraction intensity of the 20 nm thin film under a fluence of 5.3 mJ/cm^2 . The decay time constants for the four diffraction rings are 3.69, 4.67, 3.86, and 3.78 ps, respectively. The mean value for the decay constant is 4 ps. This intensity drop corresponds to a temperature increase 228 K, calculated using the previously calculated Debye temperature 174 K. The inset is a plot of $\ln[I(T)/I(t_0)]$ vs d^2 .

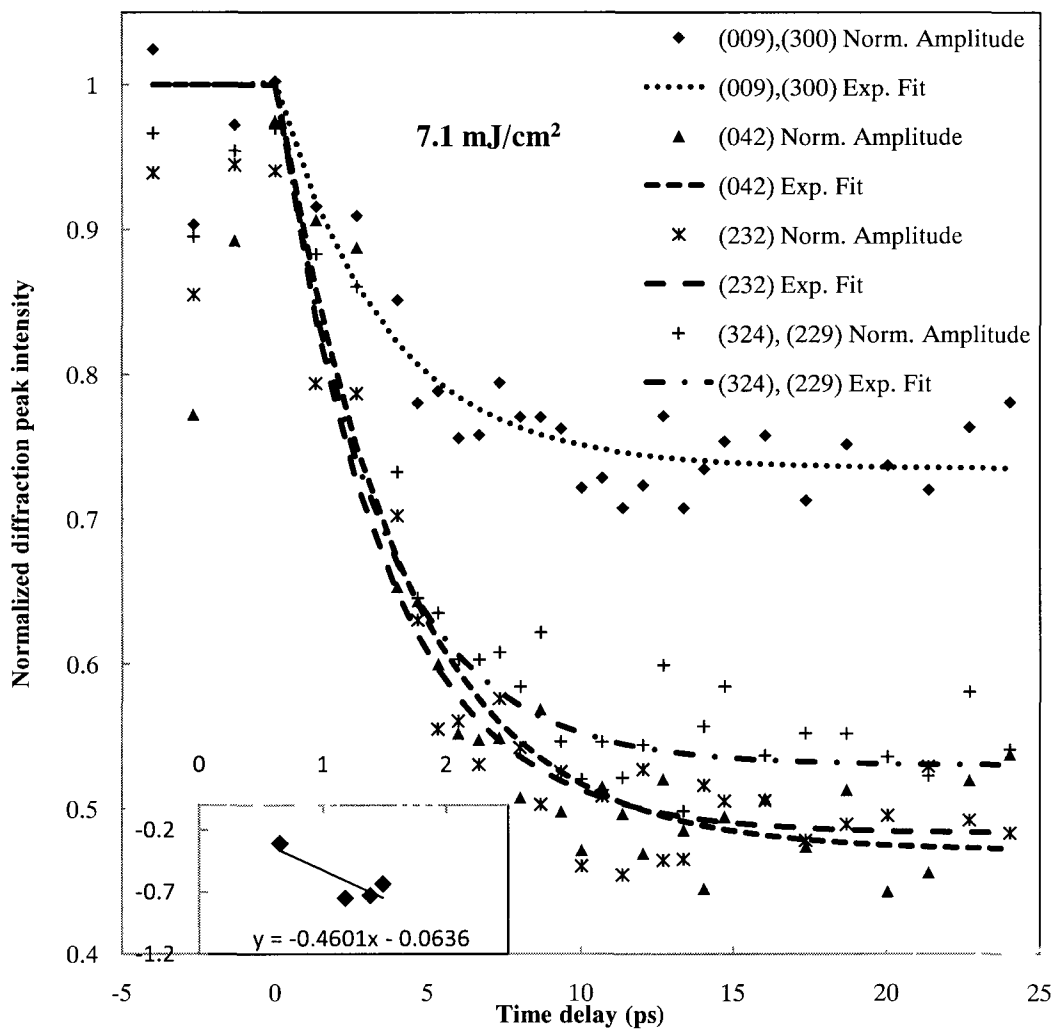


FIG. A-9 Diffraction intensity of the 20 nm thin film under a fluence of 7.3 mJ/cm^2 . The decay time constants for the four diffraction rings are 3.57, 4.09, 3.52, and 3.3 ps, respectively. The mean value for the decay constant is 3.62 ps. This intensity drop corresponds to a temperature increase of 296 K, calculated using the previously calculated Debye temperature 174 K. The inset is a plot of $\ln[I(T)/I(t_0)]$ vs d^{-2} .

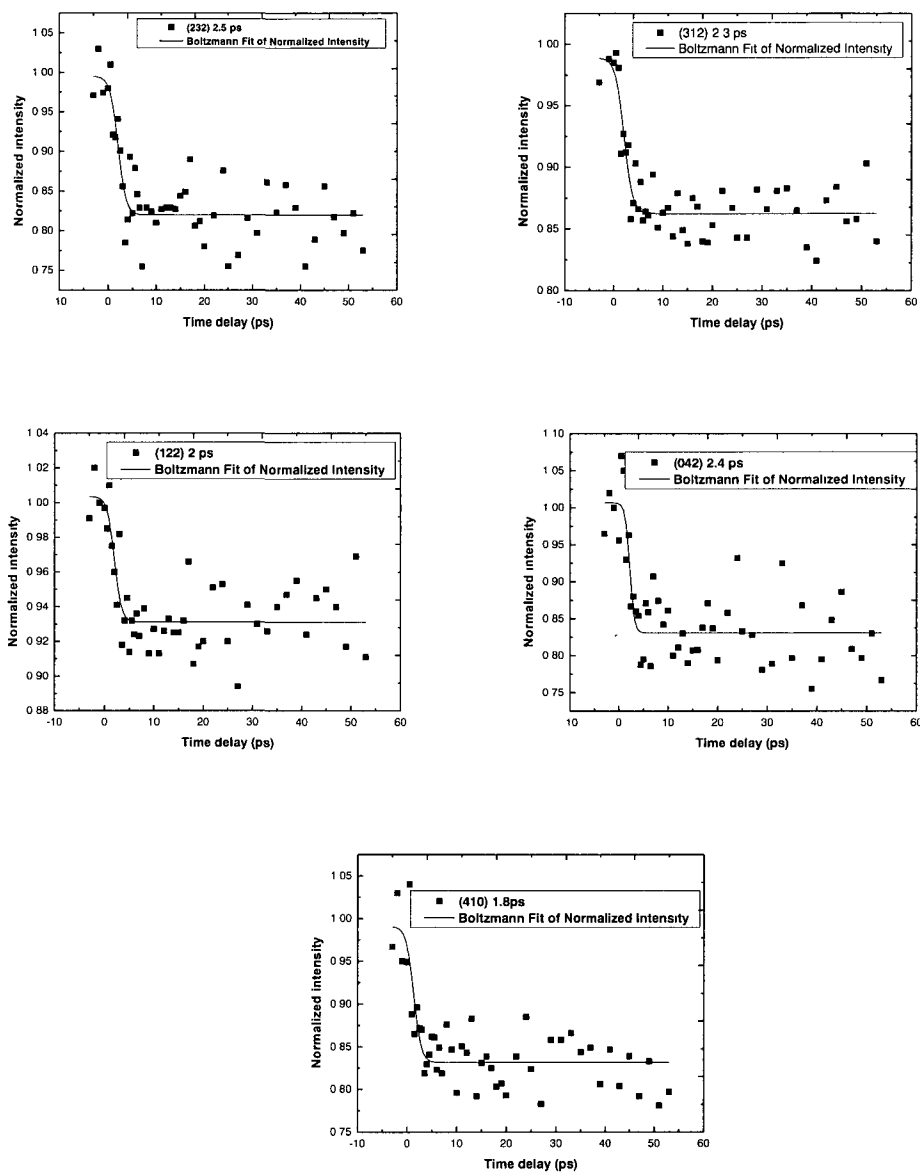


FIG. A-10 Diffraction rings (232), (312), (122), (042), (410) of the 20 nm thin film under laser fluence 2.9 mJ/cm^2 . The decay time constants for the five rings are 2.5, 2.3, 2.0, 2.4 and 1.8 ps, respectively.

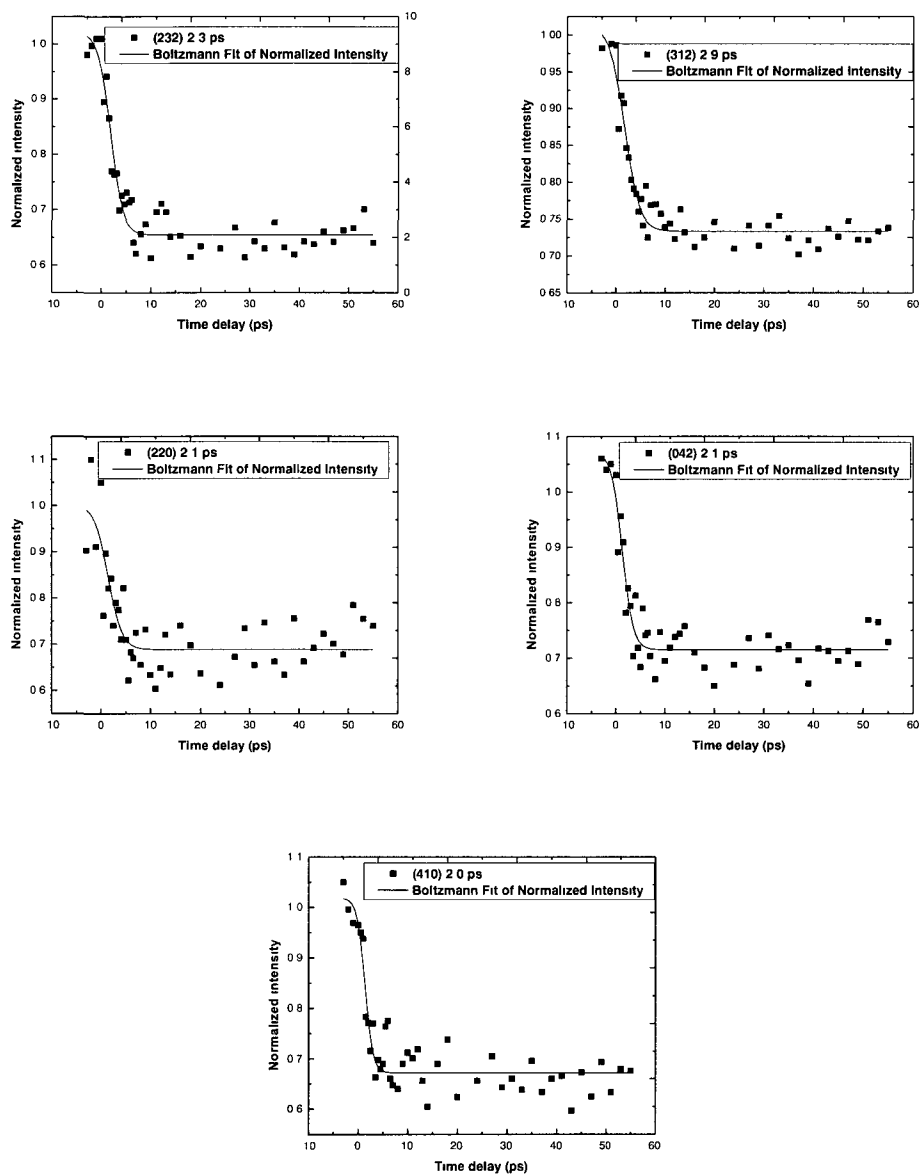


FIG. A-11 Diffraction rings (232), (312), (122), (042), (410) of the 20 nm thin film under laser fluence 6.0 mJ/cm^2 . The decay time constants for the five rings are 2.3, 2.9, 2.1, 2.1 and 2.0 ps, respectively.

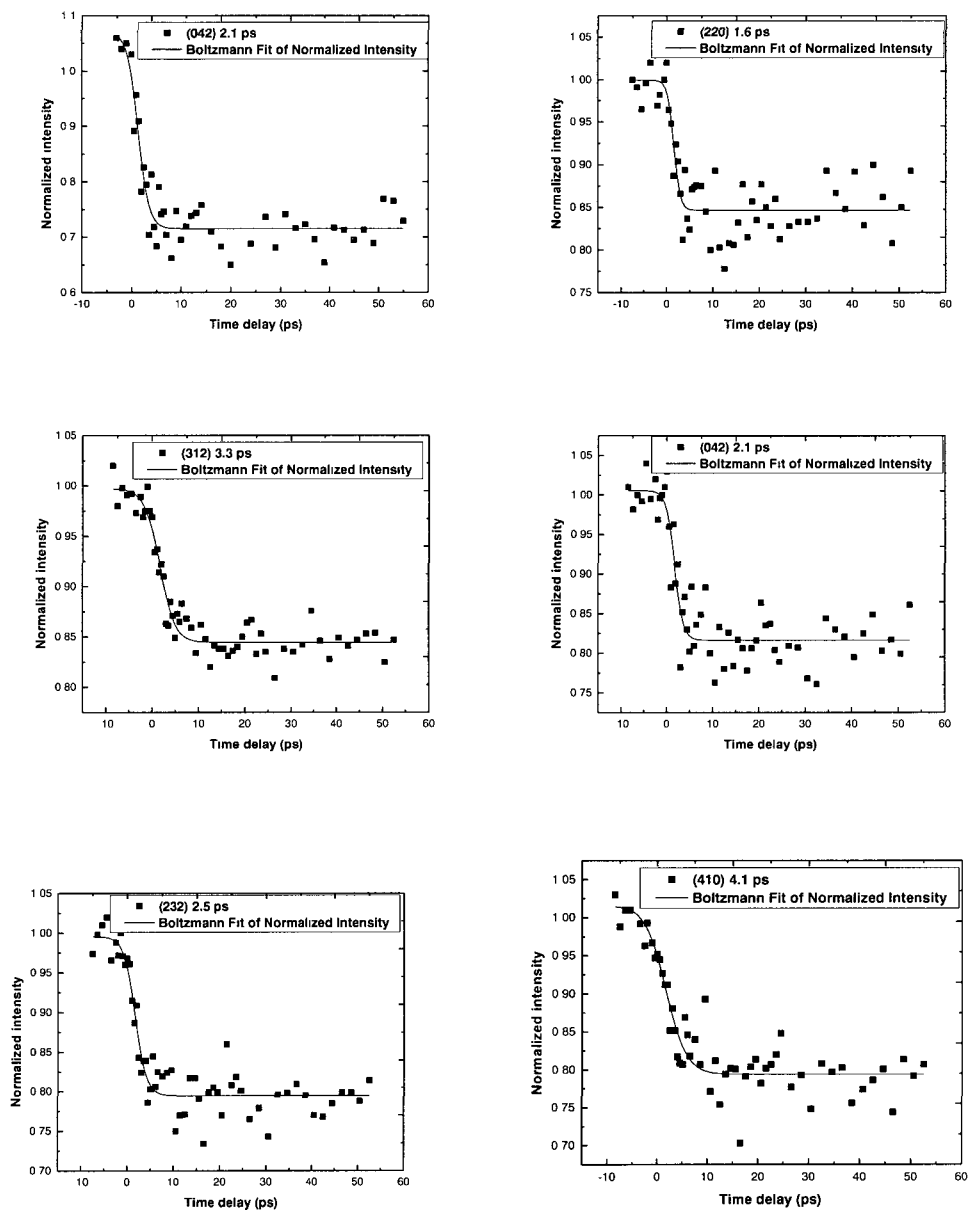


FIG. A-12 Diffraction rings (300), (220), (312), (042), (232), and (410) of the 20 nm thin film under laser fluence 3.3 mJ/cm^2 . The decay time constants for the six rings are 1.9, 1.6, 3.3, 2.1, 2.5 and 4.1 ps, respectively.

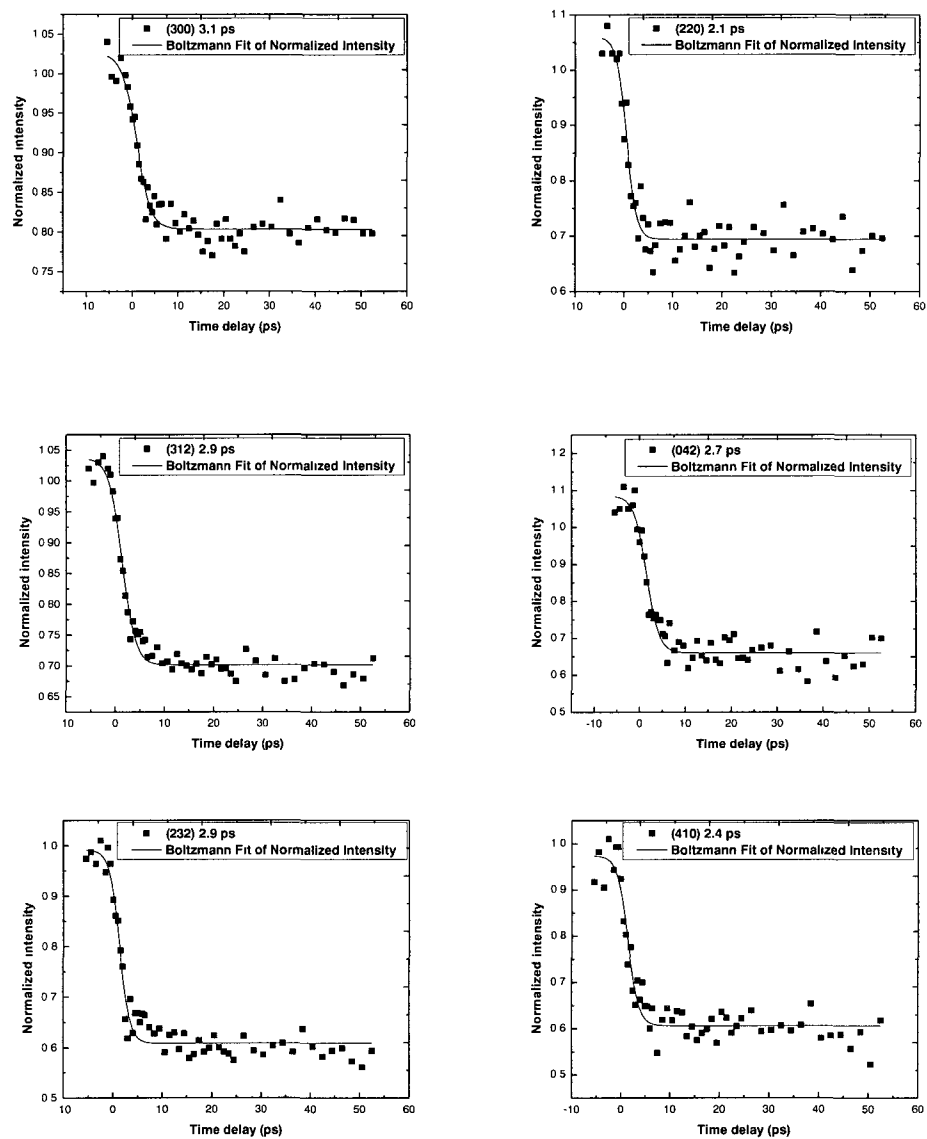


FIG. A-13 Diffraction rings (300), (220), (312), (042), (232), and (410) of the 20 nm thin film under laser fluence 7.3 mJ/cm^2 . The decay time constants for the six rings are 3.1, 2.1, 2.9, 2.7, 2.9 and 2.4 ps, respectively.

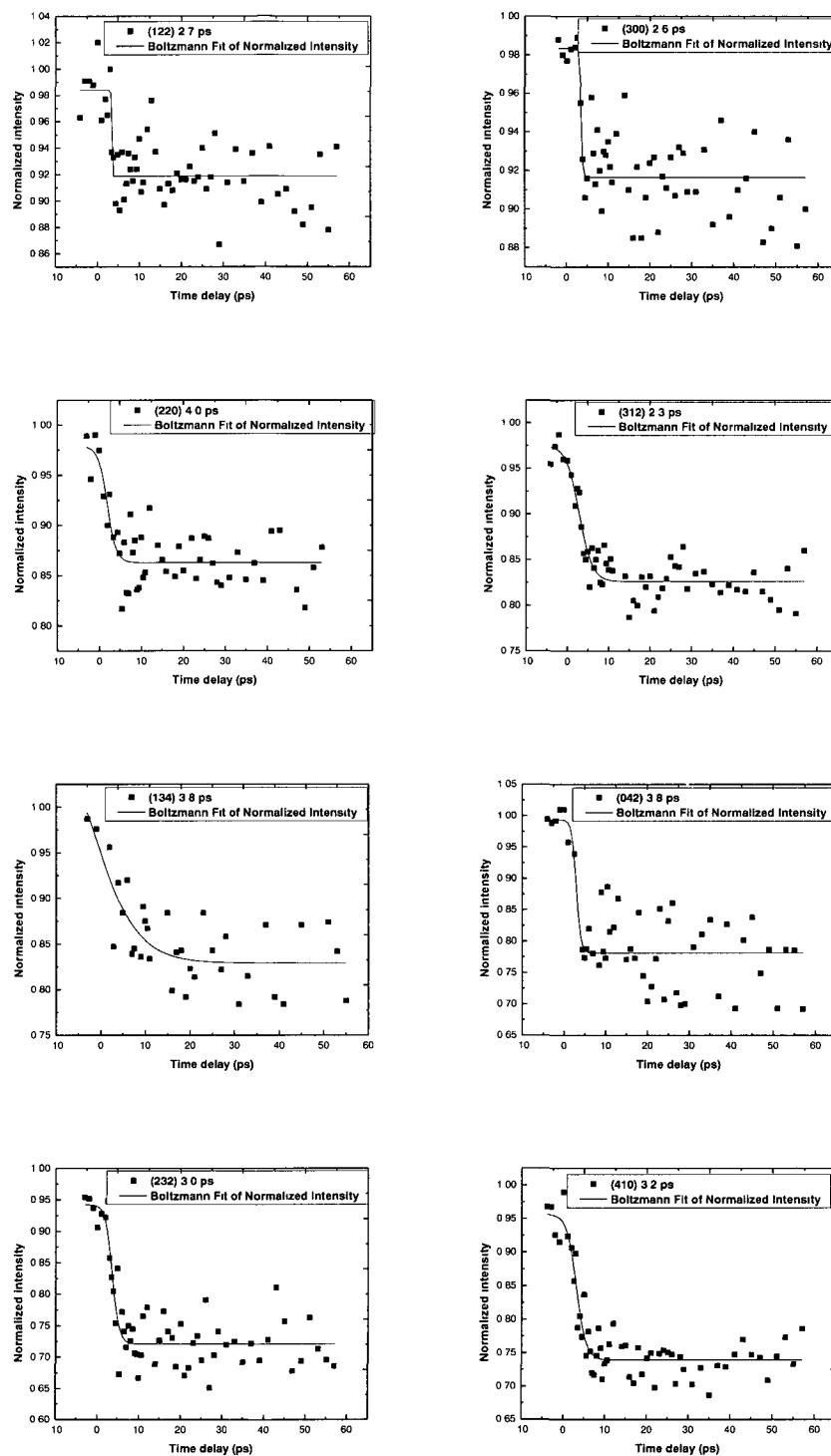


FIG. A-14 Diffraction rings (112), (300), (220), (312), (134), (042), (232), and (410) of the 20 nm thin film under laser fluence 2.7 mJ/cm^2 . The decay time constants for the eight rings are 2.7, 2.6, 4.0, 2.3, 3.8, 3.8, 3.0 and 3.2 ps, respectively.

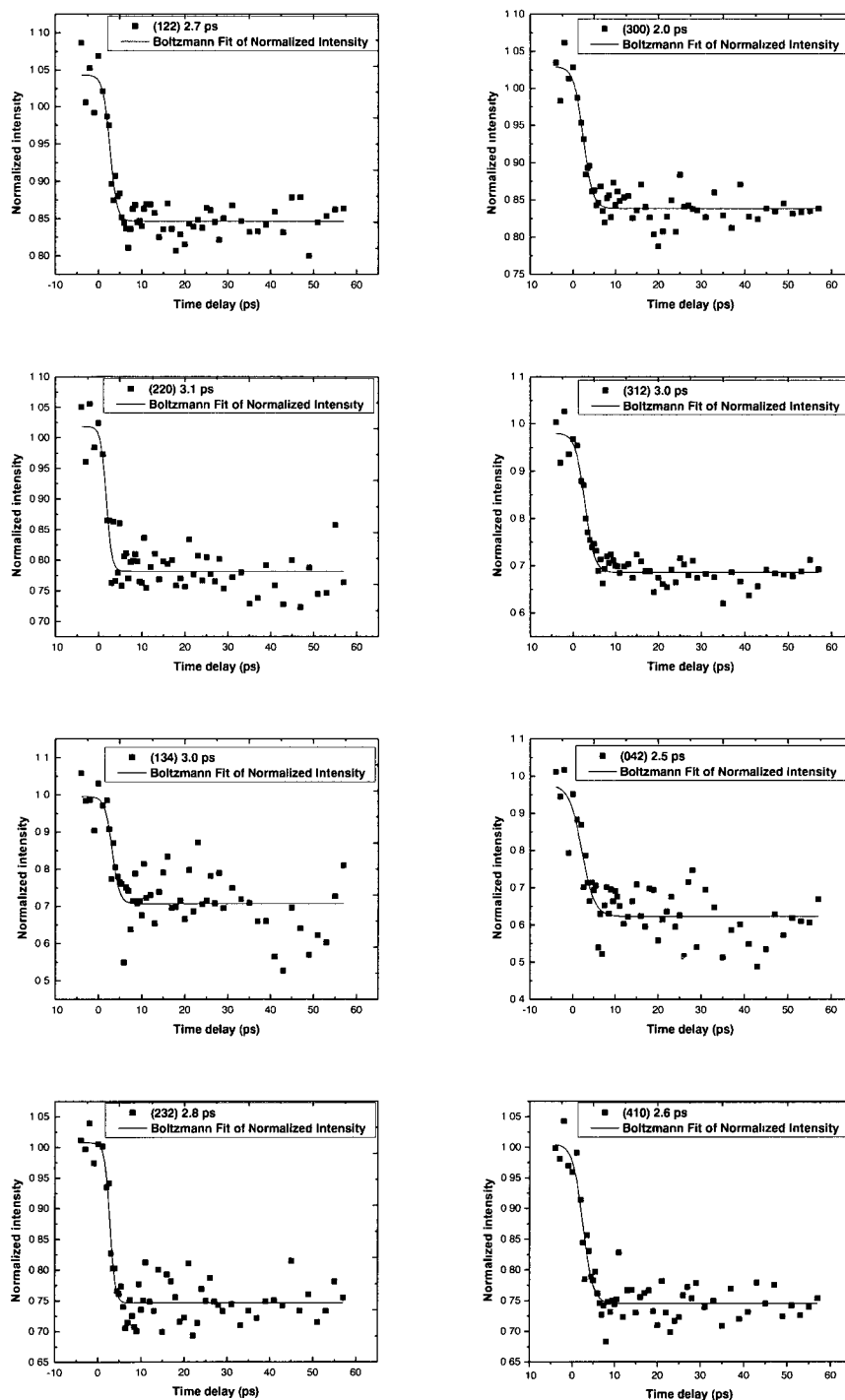


FIG. A-15 Diffraction rings (112), (300), (220), (312), (134), (042), (232), and (410) of the 20 nm thin film under laser fluence 5.3 mJ/cm^2 . The decay time constants for the eight rings are 2.0, 2.7, 2.0, 3.1, 3.0, 3.0, 2.5 and 2.8 ps, respectively.

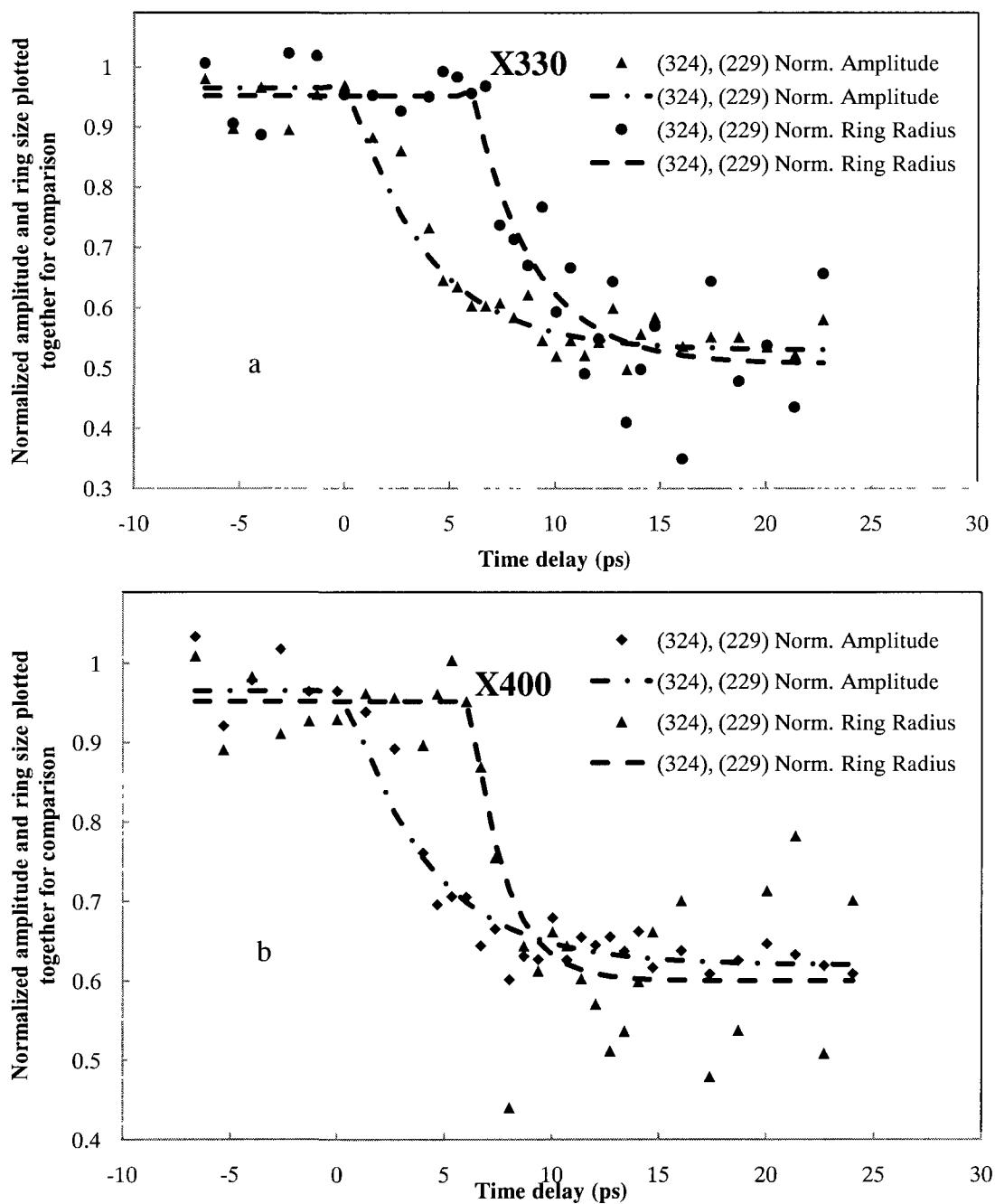


FIG. A-16 The intensity drop is plotted with the diffraction ring size in the same scale ($\times 330$). The 20 nm Sb film is under a laser fluence 7.1 (a) and 5.3 (b) mJ/cm². There is time delay 6 ps between the initial drop in intensity and the lattice expansion. This time delay corresponds to the propagation of the stress wave inside the film before the stress is relieved through lattice expansion. The propagation time with the speed of sound gives a film thickness 20.5 nm, which corresponds to the film thickness.

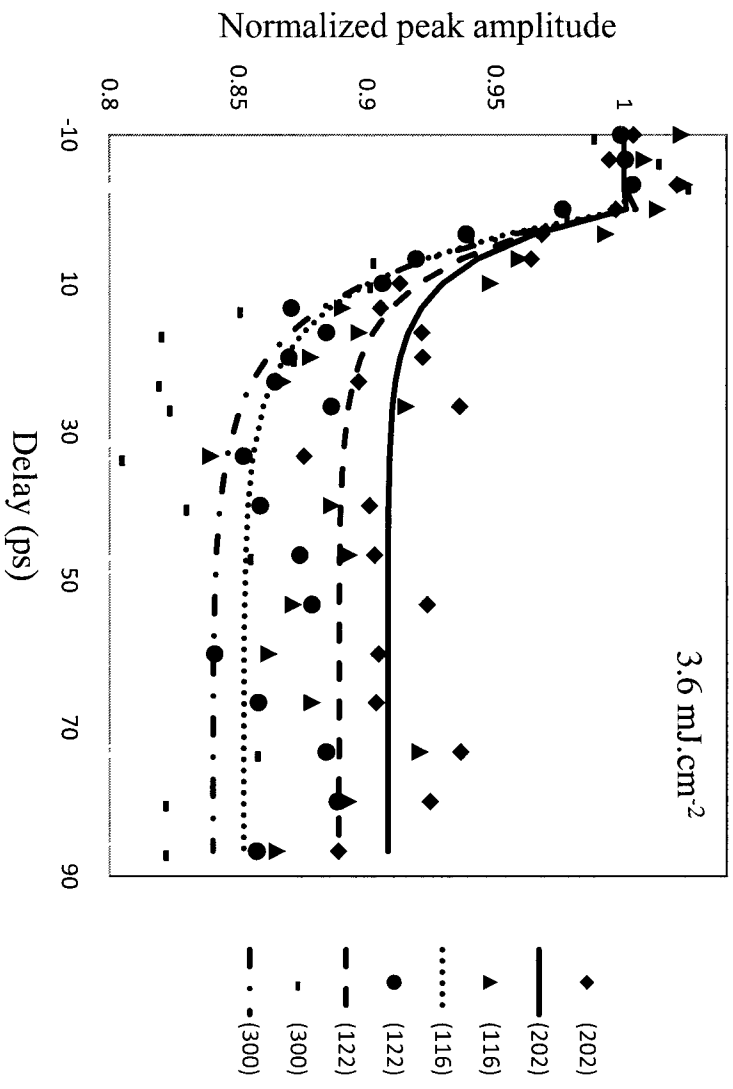


FIG. A-17 Time-resolved scan of the 50 Å effective thickness nanoparticles. Data is fit to an exponential decay function. The exponential decay constant is 8.3 ± 0.65 ps.

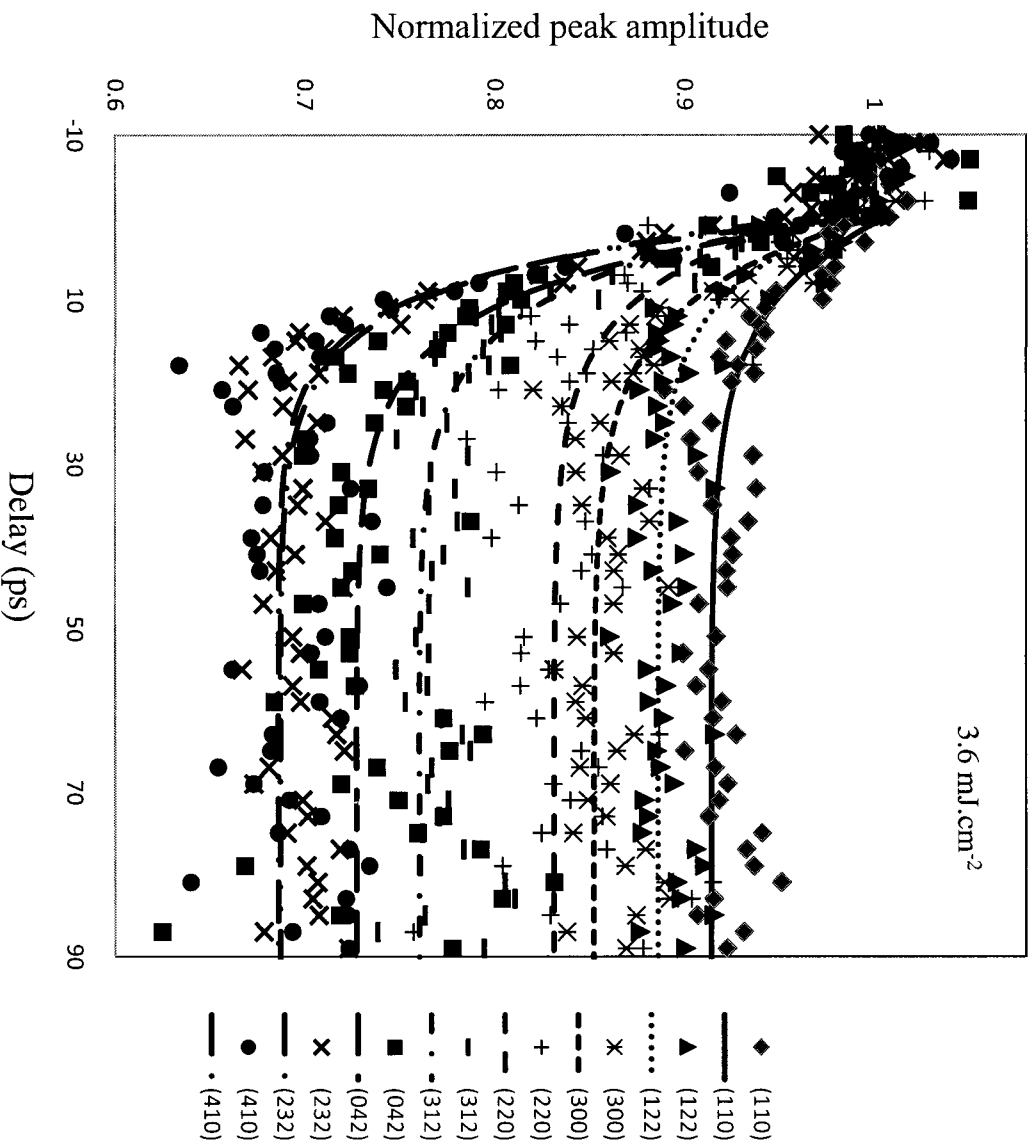


FIG. A-18 Time-resolved scan of the 300 Å film. Data is fit to an exponential decay function. The exponential decay constant is 8.45 ± 0.38 ps.

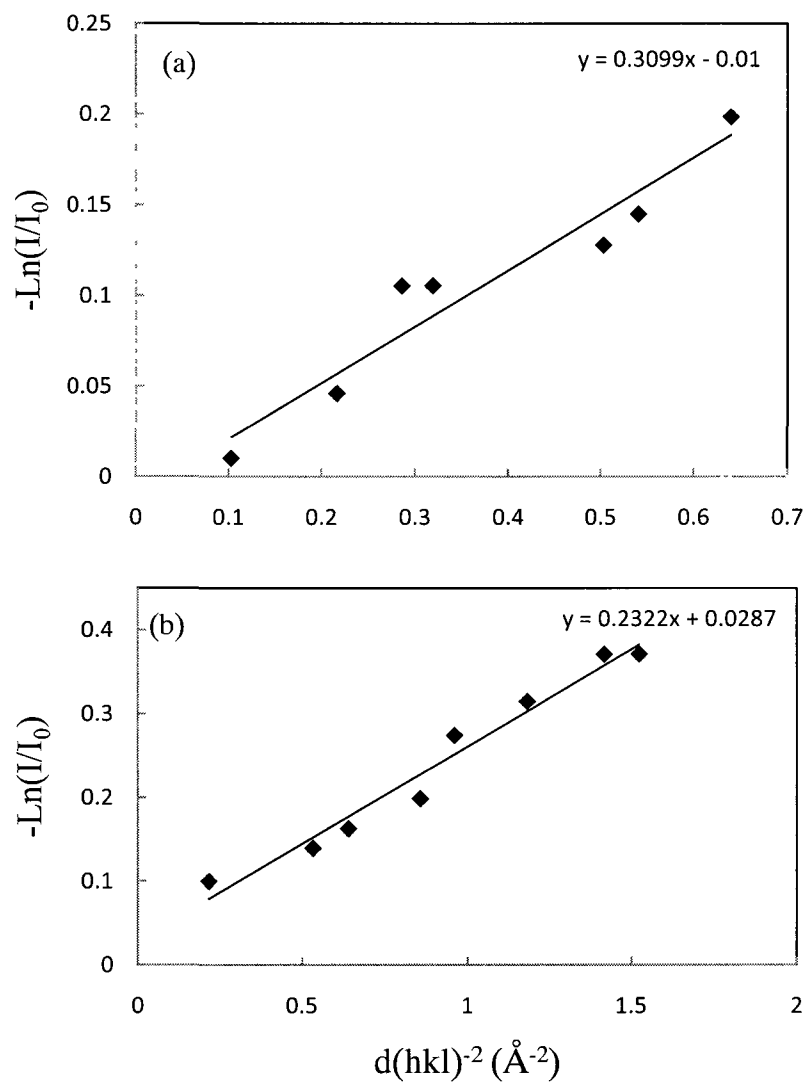


FIG. A-19 The diffraction intensity of time-resolved scan of the 50 \AA effective thickness nanoparticles. (a) corresponds to Fig 4.32, and 200 \AA film (b) corresponds to Fig. 4.33. The fit indicates Debye-Waller effect. The normalized intensity is the average taken after minimum is reached.

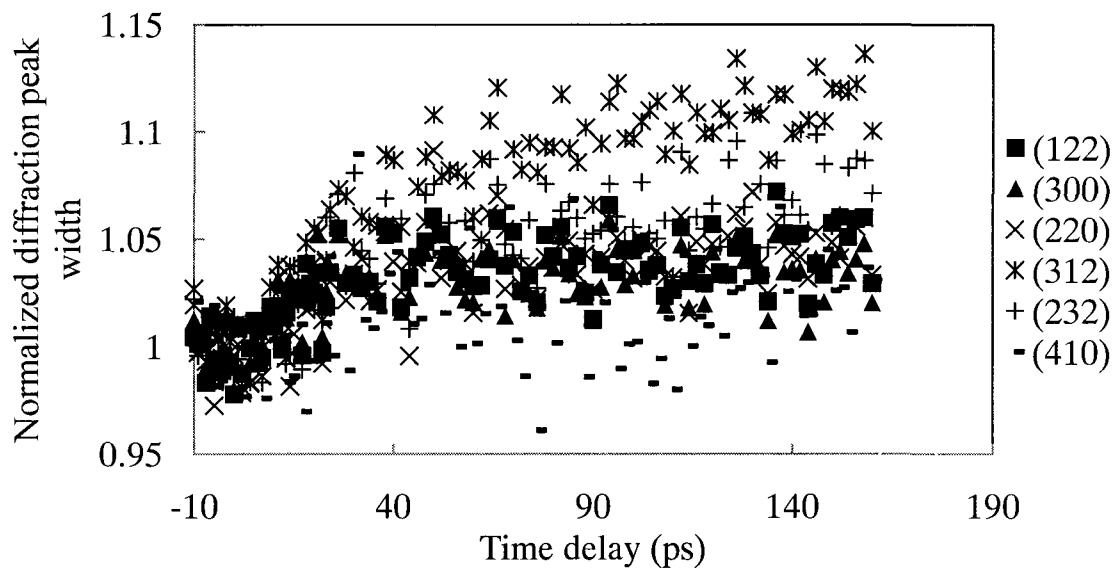


FIG. A-20 Time-resolved scan of the 20 nm film. There is an obvious increase in the ring width that indicates inhomogeneous lattice spacing.

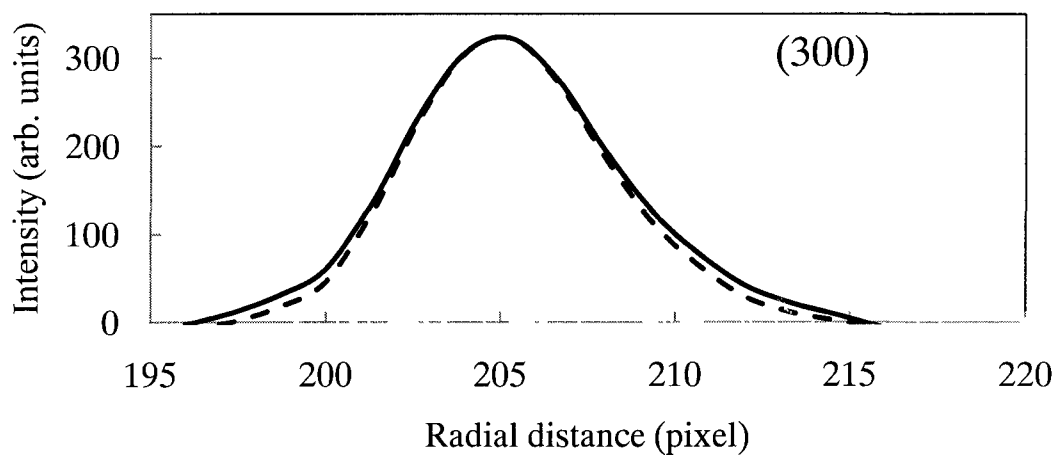


FIG. A-21 Diffraction ring (300) of the 34 nm film. The continuous line represents the case with pump on and the dashed line represents the case with pump off. There is an obvious increase in the line width due to the application of laser pump.

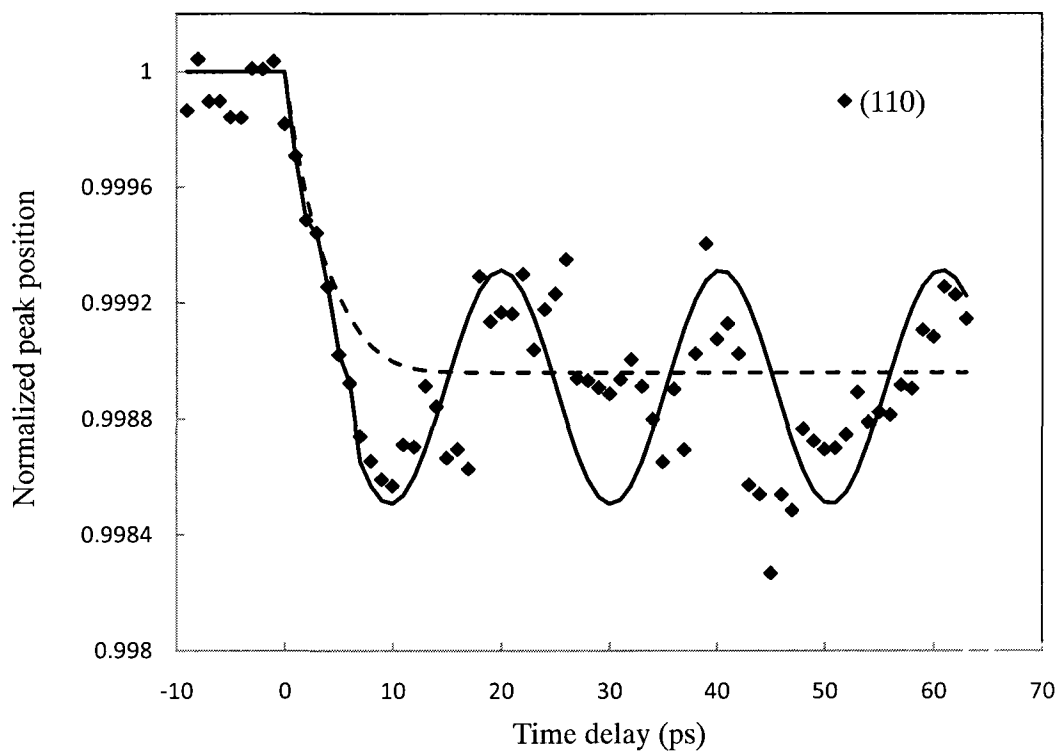


FIG. A-22 Time-resolved scan of the 23 nm film. The (110) Bragg peak position shows lattice expansion that is fit exponentially with a decay time 3 ps. The lattice oscillates about the new equilibrium position with 20 ps period. Using the speed of sound in antimony (3420 m/s) reveals the film thickness to be 34 nm instead of 23 nm.

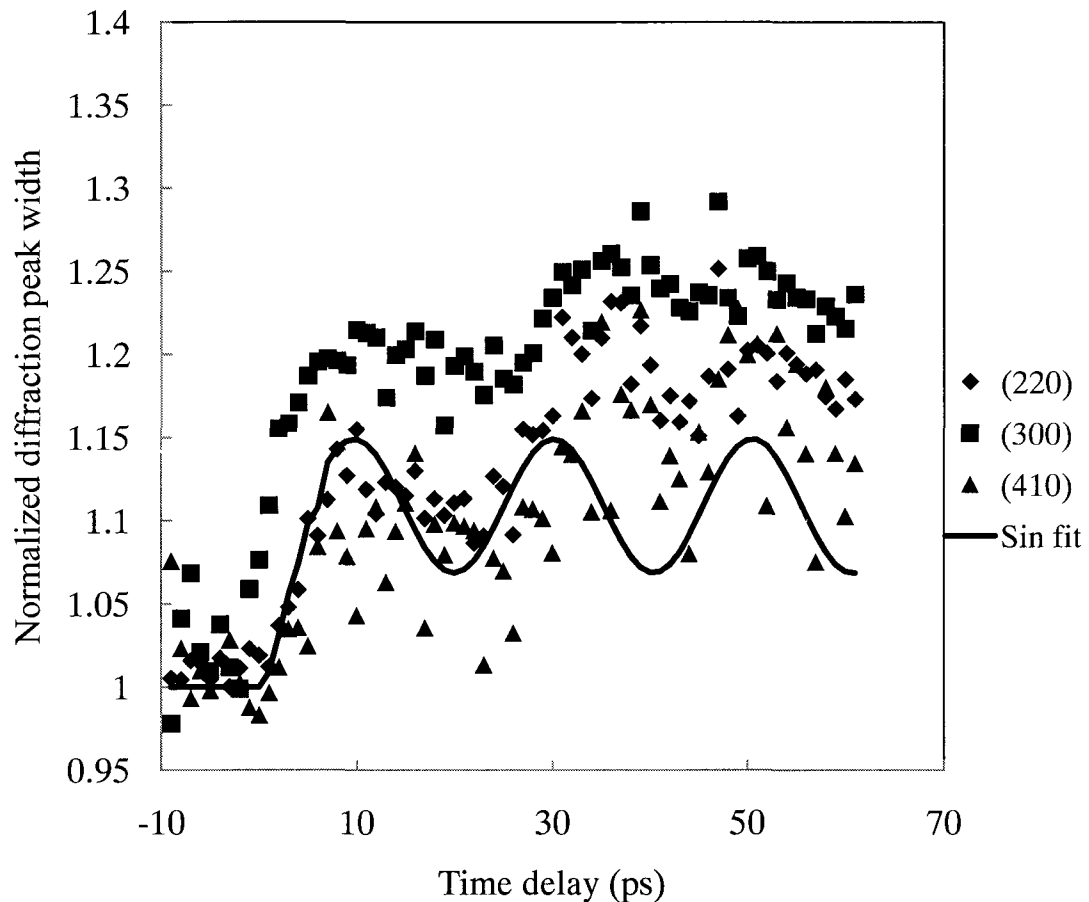


FIG. A-23 Time-resolved scan of the 20 nm film. The Bragg peaks width shows inhomogeneous lattice expansion. The lattice oscillates about the new equilibrium position; and during the oscillation, the degree of homogeneity varies periodically with the same frequency as the lattice oscillation.

Appendix B: Vacuum chamber procedure

- 1- Copper gaskets must be replaced with new ones every time a flange is removed.
- 2- The samples are loaded from the top 6" flange where the x-y-z manipulator is located.
- 3- Using half the number of bolts was found to be sufficient for high vacuum.
- 4- To pump down, open the valve and press the "start" button on the pumping station control panel. After at least one hour of pumping down close the valve, start the ion pump, and stop the turbo pump by pressing the start-stop button.

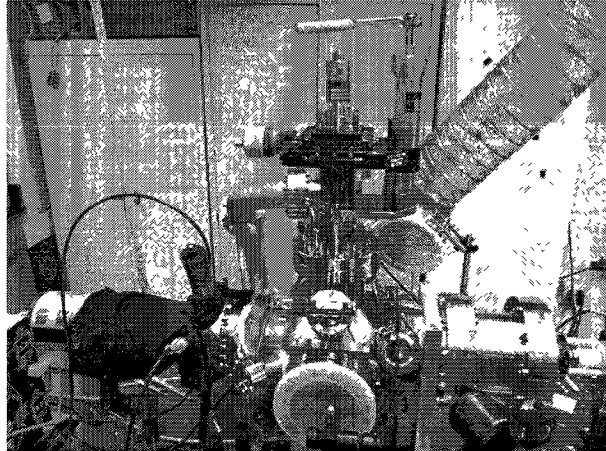


FIG. B-1 The diffraction chamber

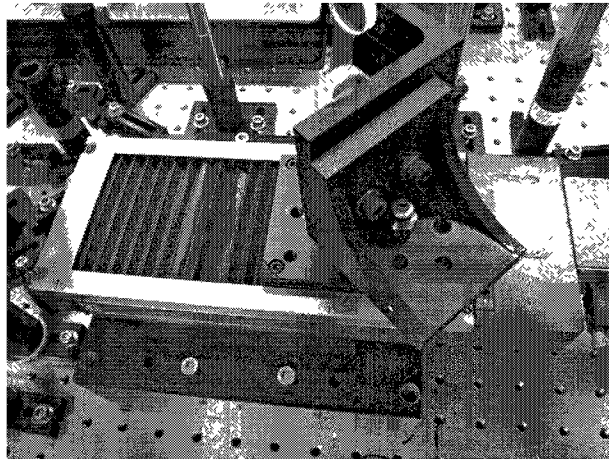


FIG. B-2 The delay stage



FIG. B-3 The ion pump power supply

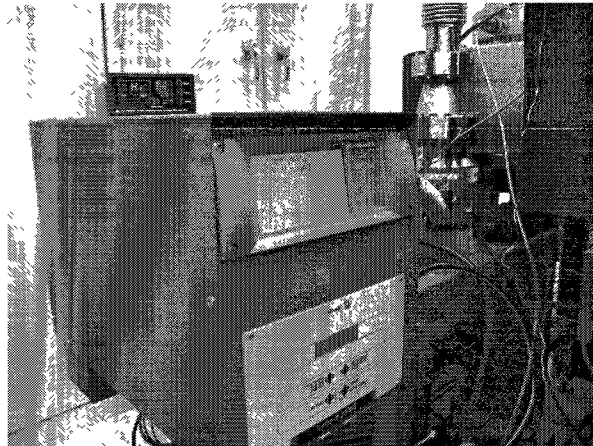


FIG. B-4 The mechanical and turbo pumping station

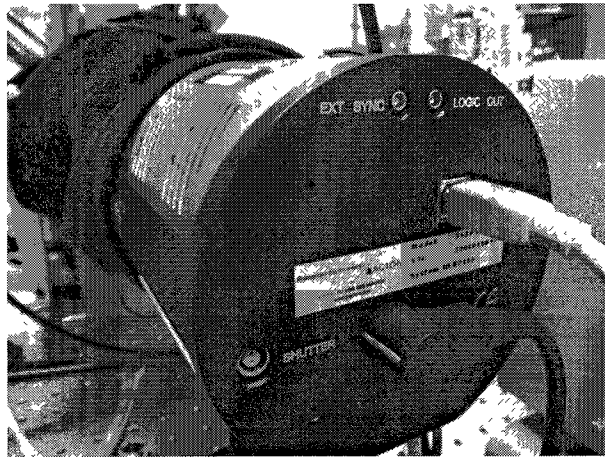


FIG. B-5 The imaging camera

Appendix C: Electron gun operation and construction

- 1- Make sure the high voltage contact is secured with the transparent plastic cover in place.
- 2- Press the on/off switch.
- 3- Make sure the voltage knob is all the way to zero.
- 4- The current knob should be one or two dashes on.
- 5- Press the high voltage enable button.
- 6- Turn the voltage knob slowly until you reach 35 kV.
- 7- While increasing the voltage, make sure the current on the ion pump controller stays unchanged.

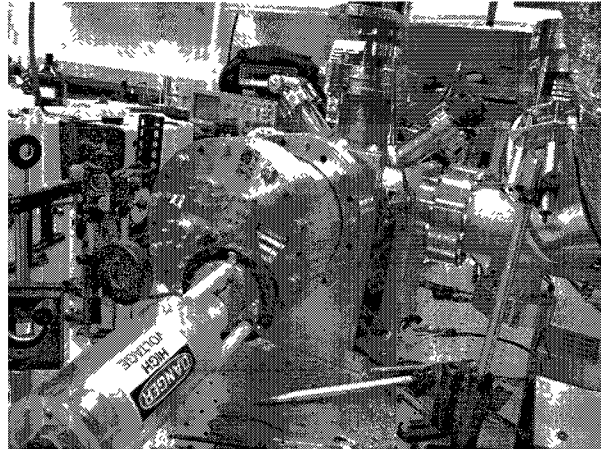


FIG. C-1 The electron gun side

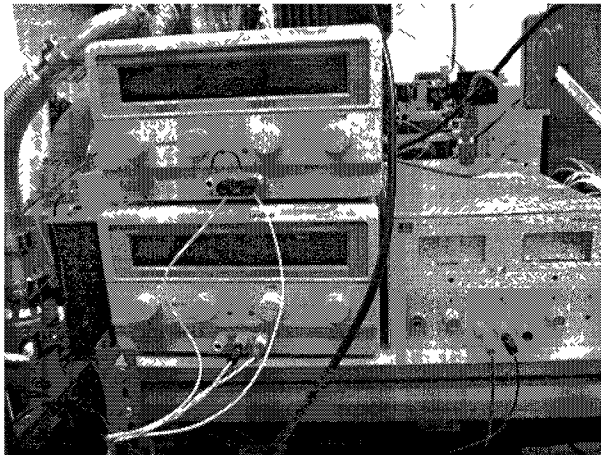


FIG. C-2 The electron beam focusing and deflection control

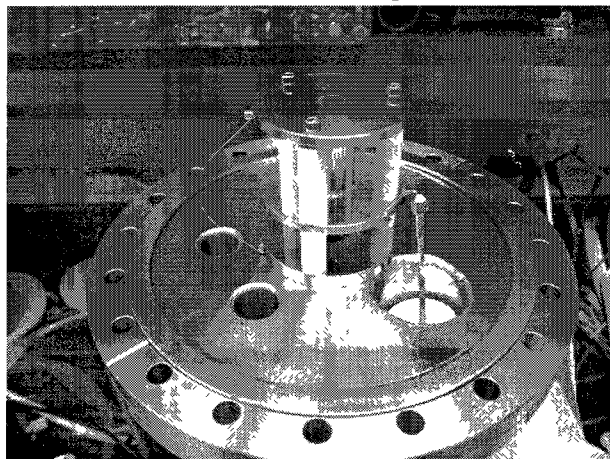


FIG. C-3 The electron gun

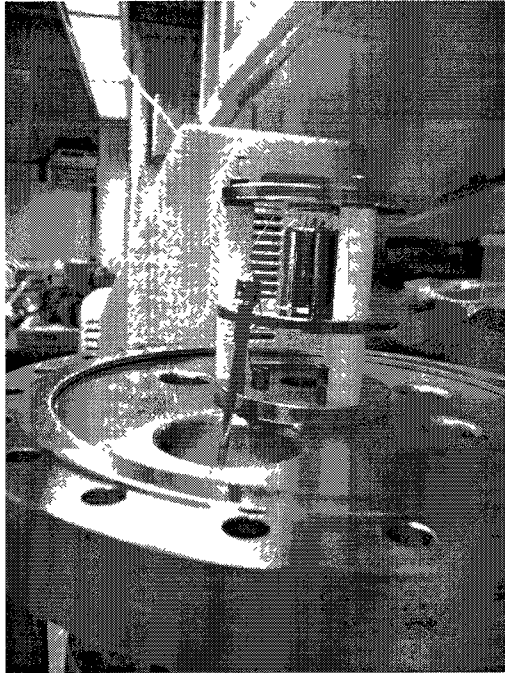


FIG. C-4 The electron gun

Appendix D: Laser operation

- 1- Check the water level in the chiller.
- 2- Start the Millennia pump laser by holding the power button for a few seconds.

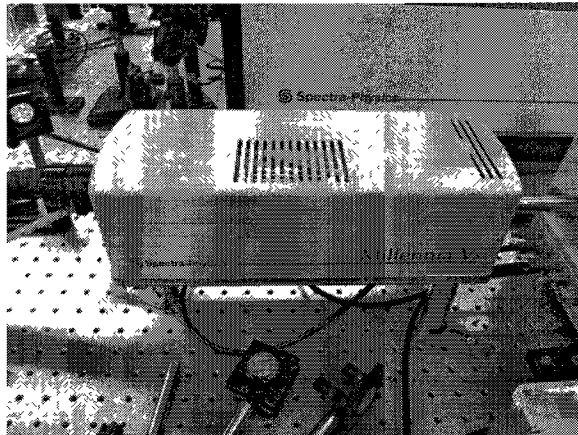


FIG. D-1 The DSS Millennia Vs laser

- 3- When the laser reaches the set value (4.75 W) open the shutter, the two LEDs on the face of the Spitfire amplifier should light indicating the Tsunami oscillator is mode locked.



FIG. D-2 The fs oscillator Tsunami

- 4- Make sure the mode locking trigger is enabled.
- 5- If the two LEDs of the Spitfire do not turn on knock gently on the table. If the two LEDs are not both on try to turn the two knobs on top of the oscillator back and forth to their original positions or very near to them. It may be necessary to move the two diodes up or down to overlap the laser with the diodes. Check the spectrum of the Tsunami oscillator using the spectrometer and the attached laptop.

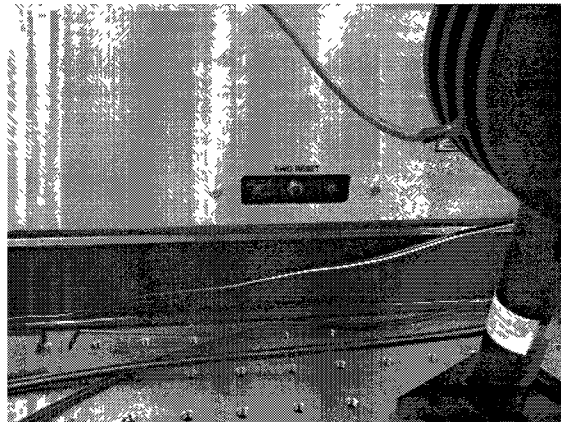


FIG. D-3 The mode-locking sensing diodes and the activation button

- 6- The output power of the Tsunami should be ~ 250 mW going into the Spitfire.
- 7- Start the Darwin laser by turning the key.



FIG. D-4 The DSS Quantronix Darwin pump for the regen

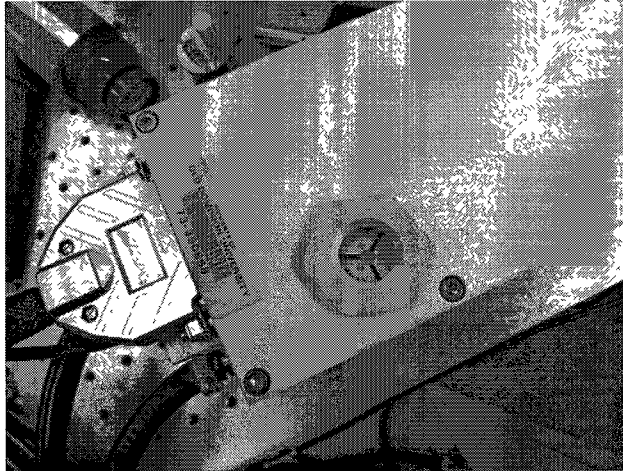


FIG. D-5 The Darwin desiccant monitor

- 8- Press the Select button and wait for start-up.
- 9- Start the three pieces of equipment on top of the Darwin (SDG, oscilloscope, and delay generator).
- 10- Go back to the Darwin laser and press Mode then Settings then Temperature and change temperature to 22.2 °C.
- 11- Back to settings and choose external mode. Open shutter and increase current to 30 A.
- 12- Press the button between the two LEDs on the Spitfire output side. Flip the enable switch on the SDG.

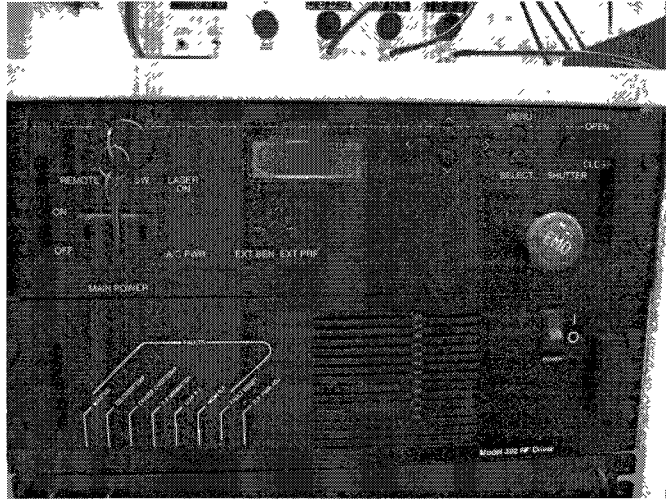


FIG. D-6 The Darwin laser control unit

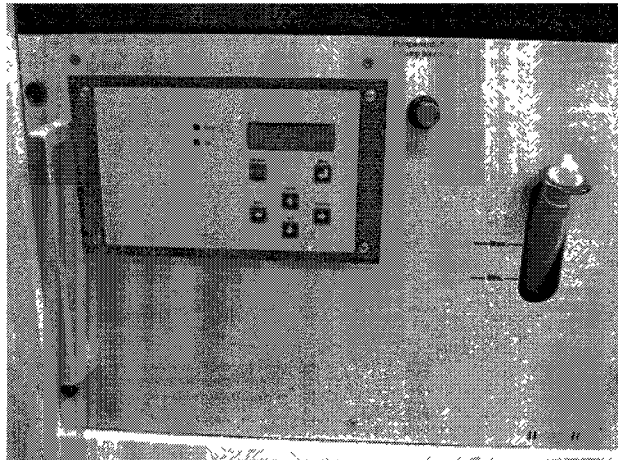


FIG. D-7 The Darwin laser chiller

13- The laser pulse is now visible on the oscilloscope.

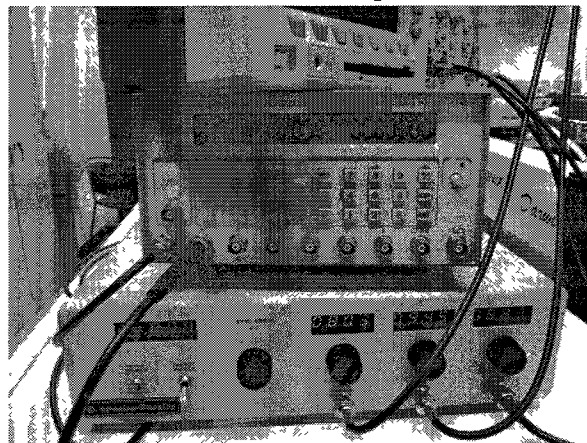


FIG. D-8 The SDG controller of the Spitfire (bottom), delay generator (middle), and oscilloscope (top)

14- Wait for laser to stabilize for about 20 minutes.

15- Never open the shutter at external trigger setting if the delay generator is not running.

Appendix E: MCP

- 1- Inner surface of MCP is either grounded or biased up to -100 V.
- 2- Outer surface of MCP is biased between +1.4 kV to +1.6 kV.
- 3- Phosphorus screen is biased between +4.1 kV to +4.5 kV.
- 4- Start by turning on the power supply that is connected to the inner side of the MCP.
- 5- Increase the phosphorus screen voltage to +2 kV slowly.
- 6- Increase the outer side of the MCP power supply to 500 V.
- 7- Increase the voltage on both power supplies until the operational values are reached. Make sure to go 100 V at a time.
- 8- Never allow the voltage at the MCP to be higher than that of the phosphorus screen, otherwise, the MCP will be damaged through discharge.**

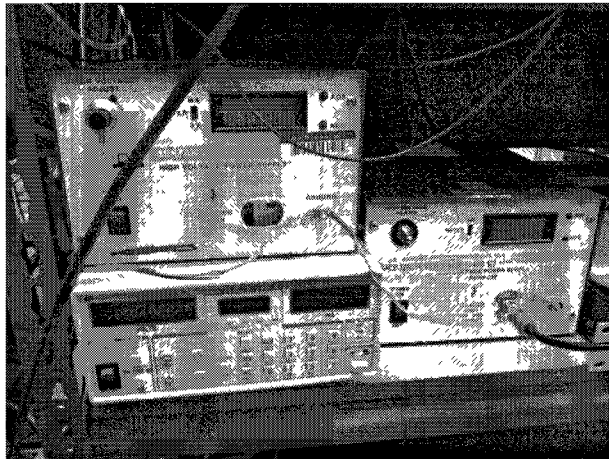


FIG. E-1 The MCP and phosphorus screen power supplies

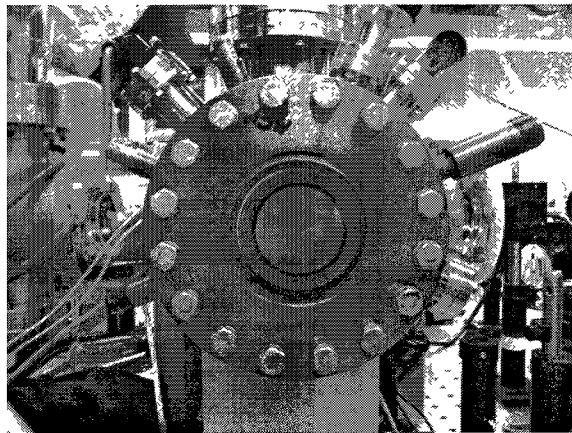


FIG. E-2 The external side of the MCP

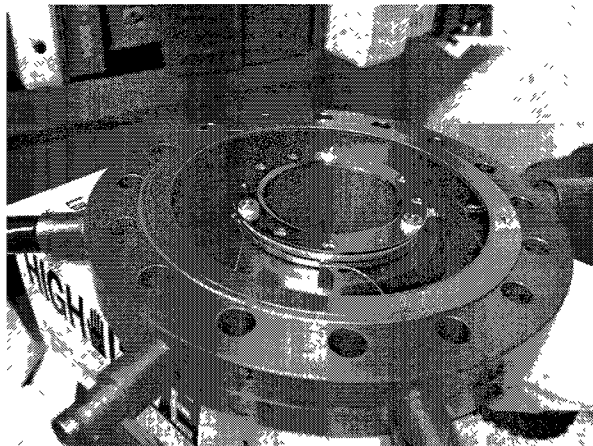


FIG. E-3 The MCP from the inside

Appendix F: Data analysis

- 1- Data are acquired in the .spe format from the WinView software that controls the camera.
- 2- The images are opened with ImageJ using the open spe plugin.
- 3- Use the radial integration plugin to match the diffraction rings, copy the data and paste into Excel.
- 4- Copy the data range of interest and paste into Peakfit, subtract the background and perform peak separation; then copy the data back into Excel under the proper delay reference.
- 5- Using the data from pump and no-pump images, perform the plots that you need.

Appendix G: Peak identification and calibration

- 1- Start with a 20 nm gold film.
- 2- Get a nice and strong diffraction pattern.
- 3- The strongest diffraction peaks will correspond to (111), (200), (220), and (311), respectively.
- 4- Calculate the $d(hkl)$ for each of these planes.
- 5- Calculate the wave length of the electron beam that corresponds to its energy.
- 6- Take a picture of the surface of the phosphorus screen of a known distance and have a pixel/mm calibration. You can just use the distances in the images in pixels if the camera is not to be changed. Never move the camera from its position or the calibration will be invalid.
- 7- Substitute the previous three values in the equation $[R(hkl)d(hkl) = \lambda L]$ which is derived from Bragg's equation to get the camera length (L).
- 8- Using the past equation find the (d) for any diffraction pattern of a known substance.

- 9- Use the X-ray powder diffraction data as a reference to find the most probable interpretation.

Appendix H: Electron pulse

- 1- The third harmonic 266 nm energy is kept at 50 nJ.
- 2- The number of electrons is measured by using a piece of copper gasket as a Faraday cup.
- 3- Connect the copper target to a bnc feedthrough.
- 4- Measure the current with the direct function of lock-in amplifier.
- 5- Divide by the electron charge to get an electron count per pulse.
- 6- To find the diffraction system temporal resolution run a time-resolved scan on an Al film.

Appendix I: Beam profile

- 1- Direct the pump beam away from the chamber and place a knife-edge that is mounted on a micrometer at a target equivalent distance.
- 2- Place a power meter behind the knife-edge.
- 3- Move the knife-edge using the micrometer to scan the beam profile making sure to get about 20 points across the beam.
- 4- The distance between 10% and 90% energy corresponds to the beam size for Gaussian beams.

Appendix J: Thin film fabrication

- 1- Load a piece of material in a fresh tungsten filament.
- 2- Stick a number of carbon support TEM grids to a glass slide from one edge with a tiny drop of colloidal silver.
- 3- Fit the glass slide on the top flange next to the crystal thickness monitor and close the vacuum chamber.
- 4- Pump the vacuum system down for 1 - 2 hours.
- 5- Open the water valve to cool the thickness monitor's crystal. Keep a weak flow and wait 10 minutes.
- 6- Increase the voltage on the variac very slowly until evaporation begins.
- 7- When the desired thickness is reached turn off the voltage and the water.
- 8- Wait 30 minutes and turn off the vacuum pump and open the vacuum chamber.
- 9- Carefully take off the samples and load them into the electron diffraction chamber.

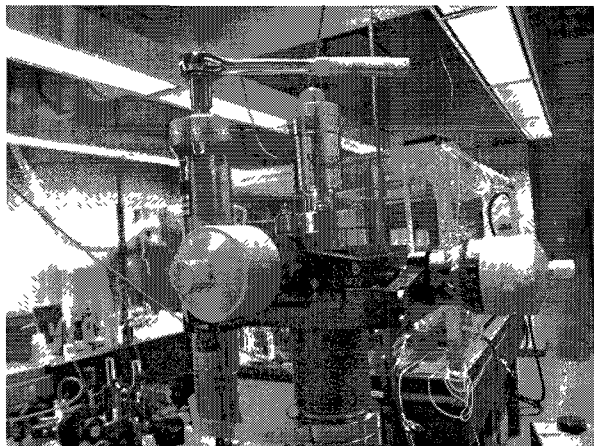


FIG. J-1 The x-y-z-rotation sample manipulator

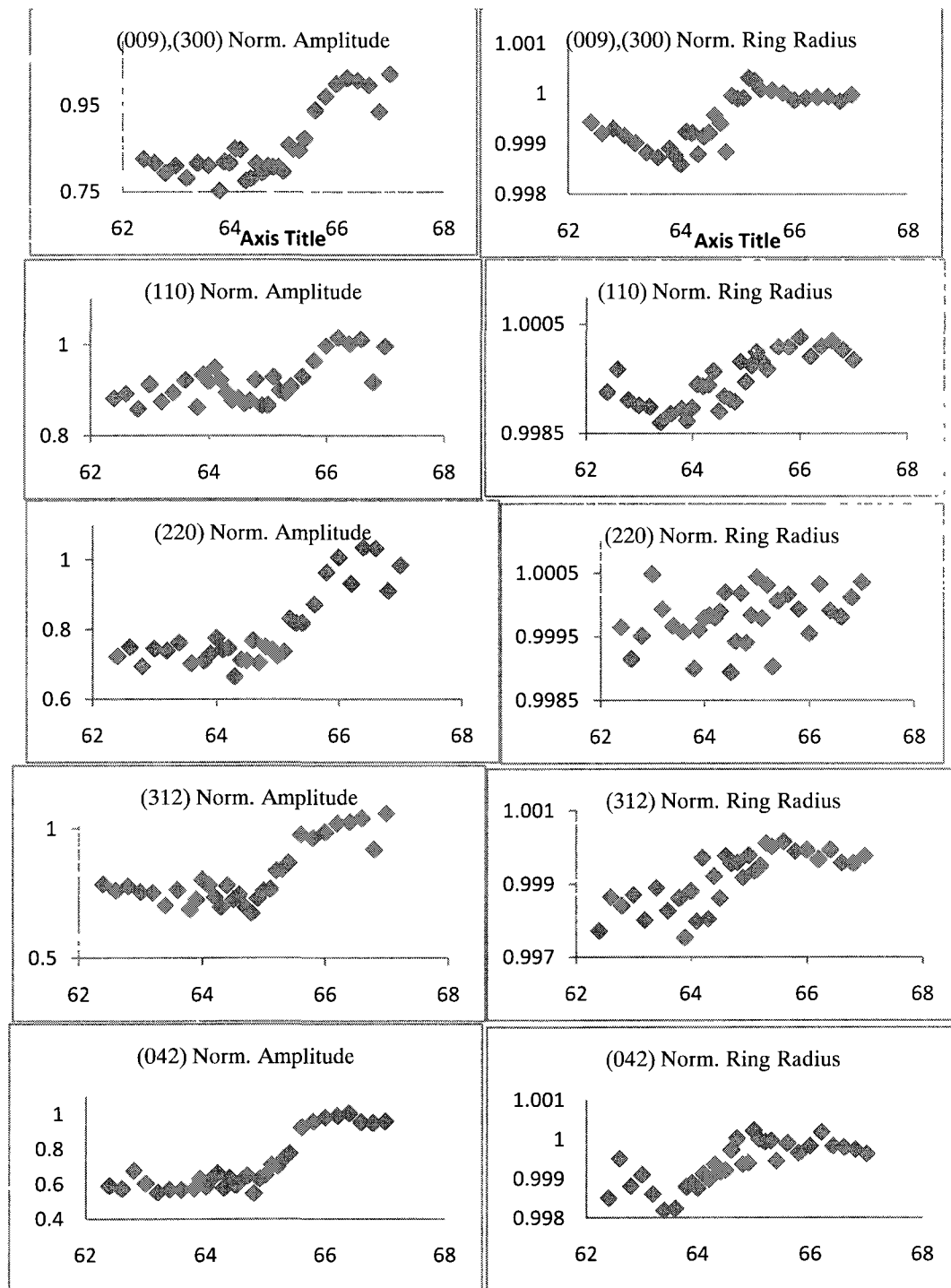
Appendix K: Supplies

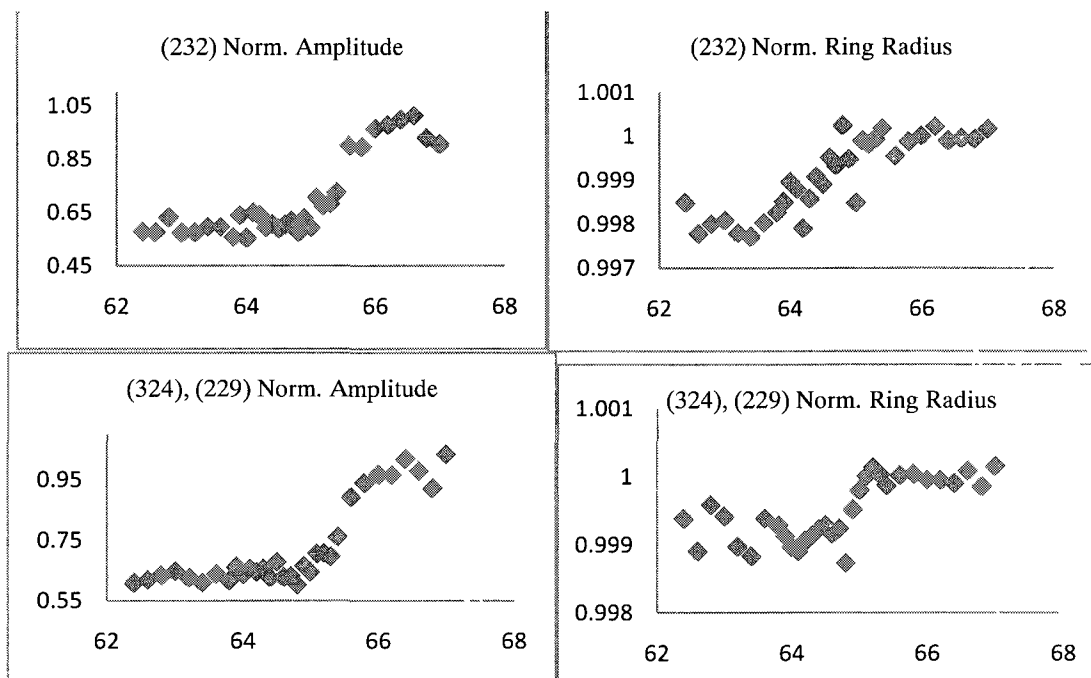
List of vendors for our experimental supplies

Unit description	Part number	Vendor
6 way high grade stainless steel vacuum chamber.	407008	http://www.mdcvacuum.com
UHV valve	313037	
70 l/s Turbo molecular pump	TG70FCND	http://www.osakavacuum.co.jp/en/
Mechanical pump	RV3	http://www.edwardsvacuum.com/
Evaporation filaments	-B5-0.04W -F12-3X0.030W	http://www.rdmthis.com/
TEM grids	Cu-400CN	http://www.grid-tech.com/
Inficon deposition monitor	XTM/2	http://www.inficonthinfilmdposition.com/en/index.html
Darwin 30 W pump laser	DARWIN-527-30-M	http://www.quantronixlasers.com/
Tsunami Ultrafast Ti:sapphire Laser	3941-M1S USP	http://www.newport.com/
Regenerative Amplifier	SPITFIRE	
Ultrafast laser mirrors	TLM1-800-45P-	http://cvimellesgriot.com/

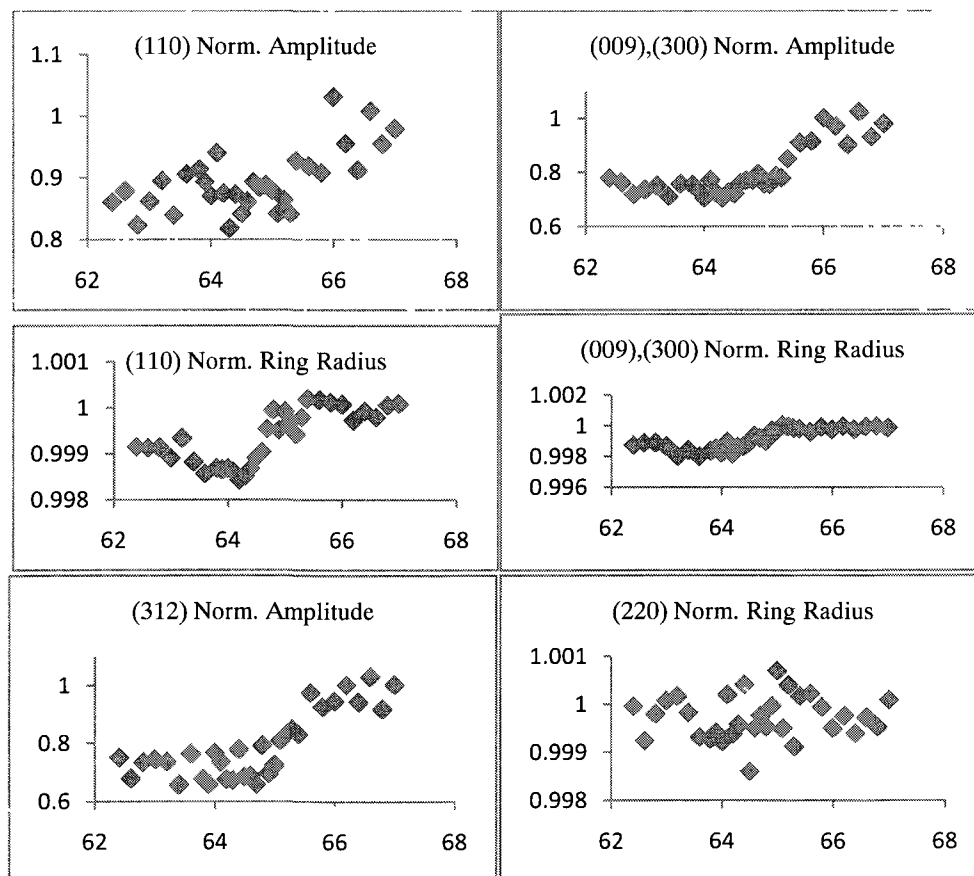
	1025	Products/Products.aspx
Ultrafast beam splitter	BS1-800-30-1012-45UNP	
Delay stage	UTM100-PE.1	http://www.newport.com/Optical-Delay-Line-Kit/396220/1033/catalog.aspx
CCD camera, Pixis1024	7520-0001	http://www.princetoninstruments.com/?gclid=CMmA2v7gqKUCFeYD5QodqxYV7A
Custom made high grade stainless steel vacuum chamber	---	http://www.lesker.com
Rotational manipulator	HTBRM-275-12	www.mdcvacuum.com
XYZ manipulator	PSM-1502	
Perkin-Elmer ion pump, 220 l/s	---	http://www.duniway.com/html/cs-ip-section.htm
Turbo-Molecular pump, 300 l/s	V300-HT	http://www.varianinc.com
Mechanical pump	949-9315	
MCP/phosphorous screen assembly	---	http://www.burle.com/mcp_pmts.htm
High voltage power supply (screen)	PS350/5000V-25W	http://www.thinksrs.com/
High voltage power supply (MCP)	05R	
E-gun high voltage power supply	FC50N2.4	http://www.glassmanhv.com/glassman_tech.shtml

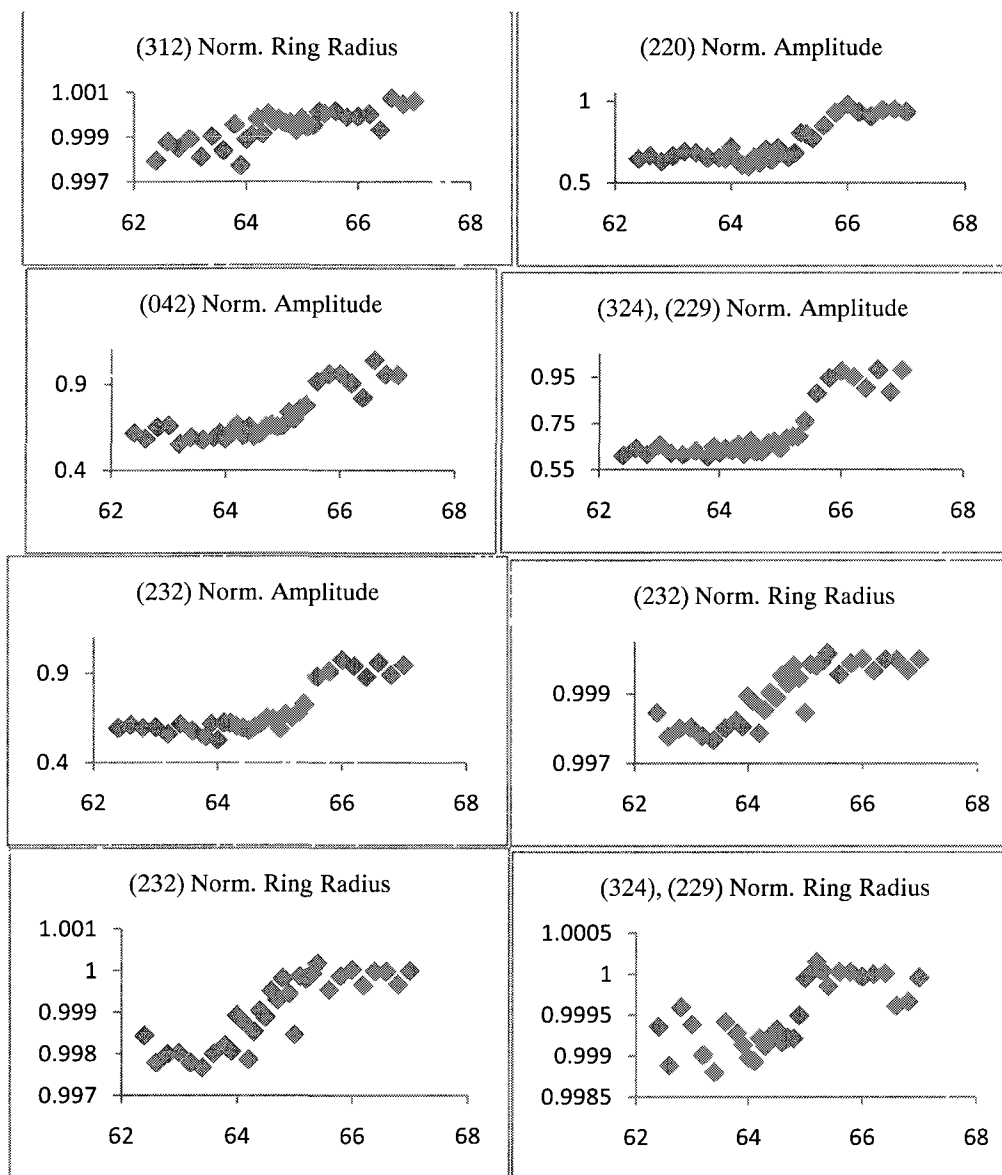
Appendix L: Raw data



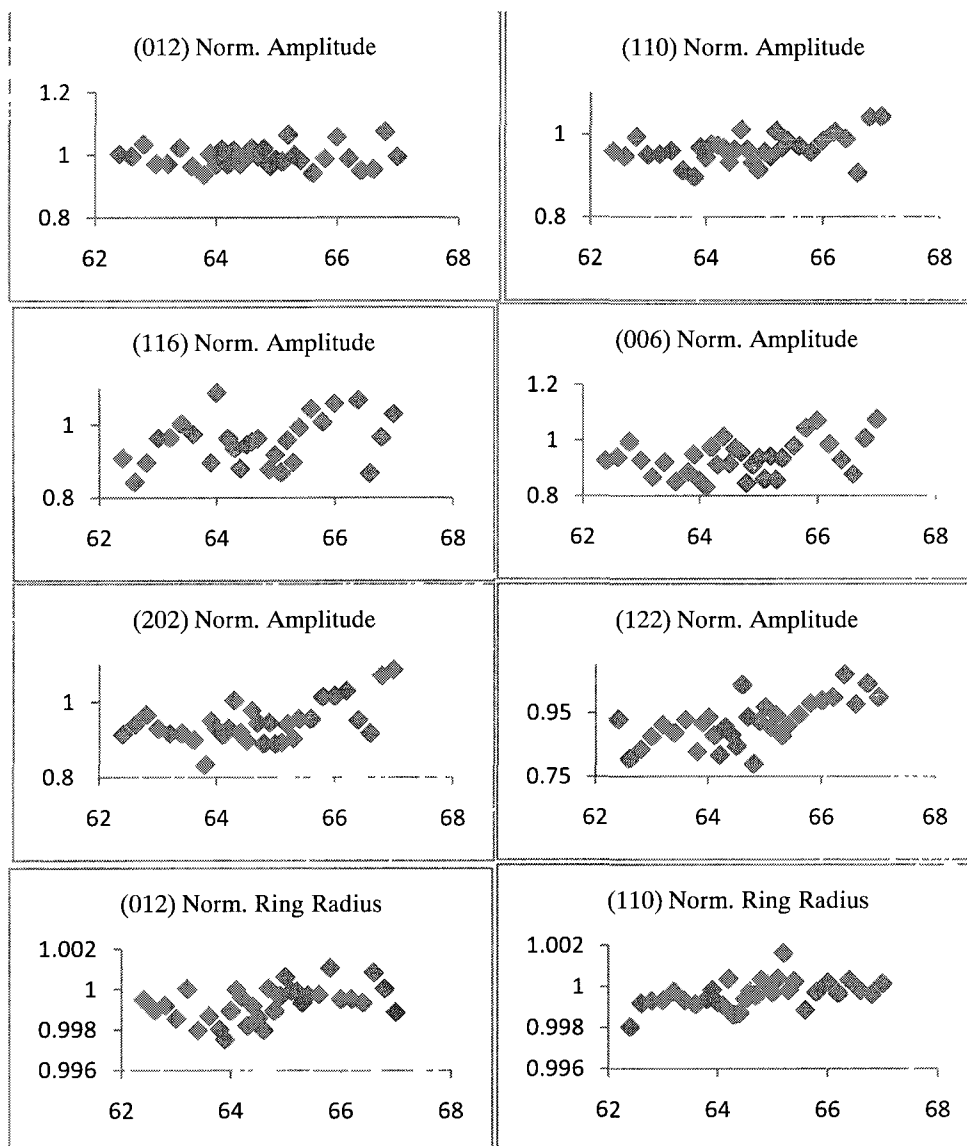


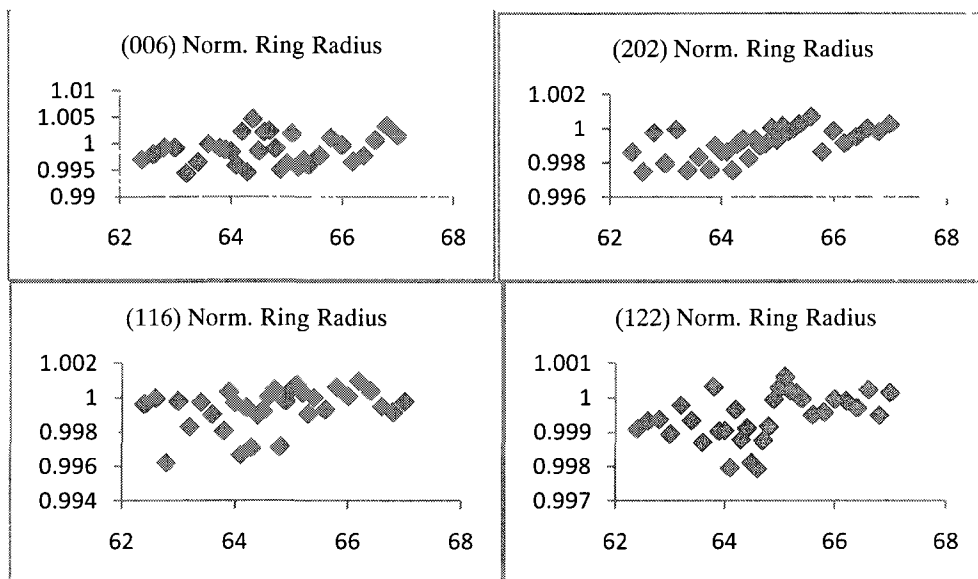
20nm-150 mJ, 9-23-2010



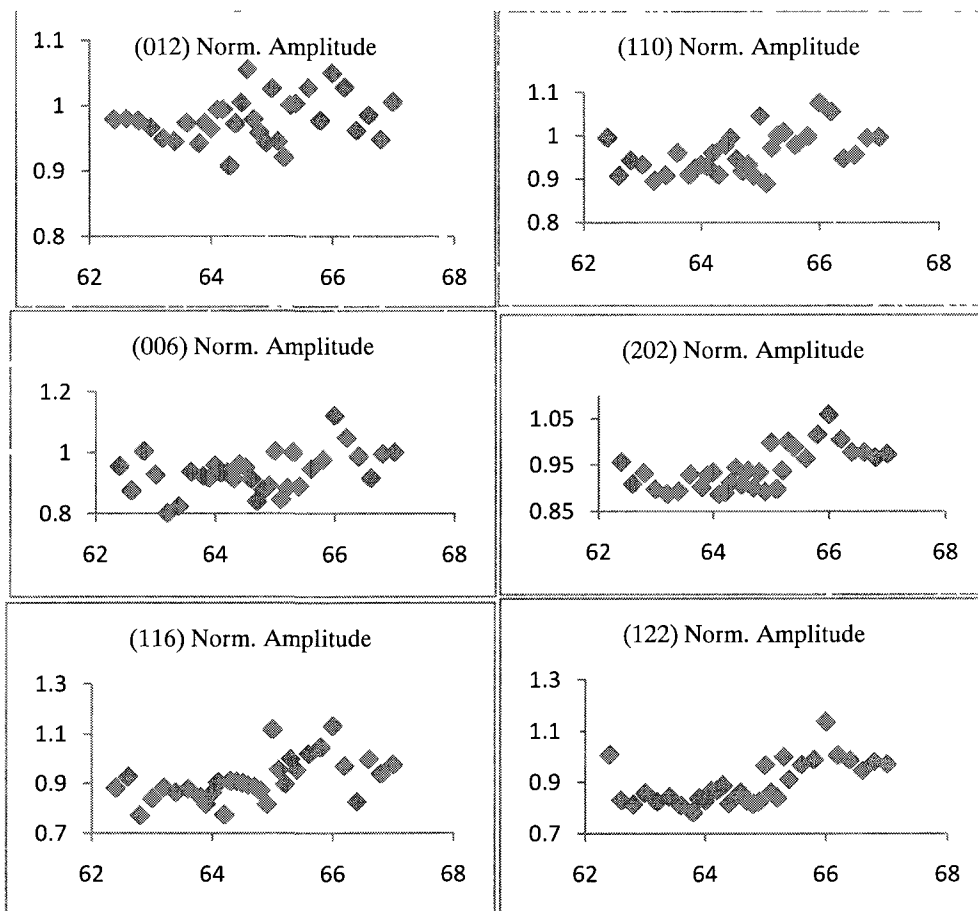


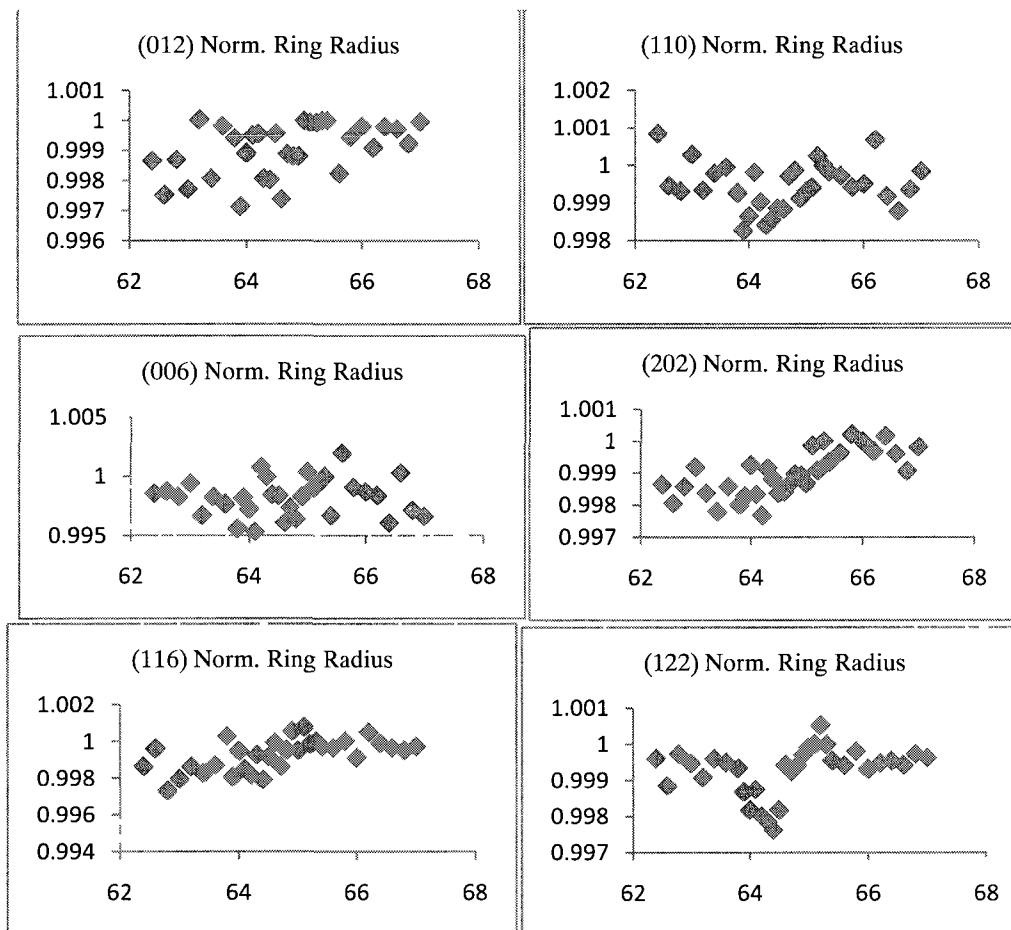
20nm, 200 mJ, 9-23-2010



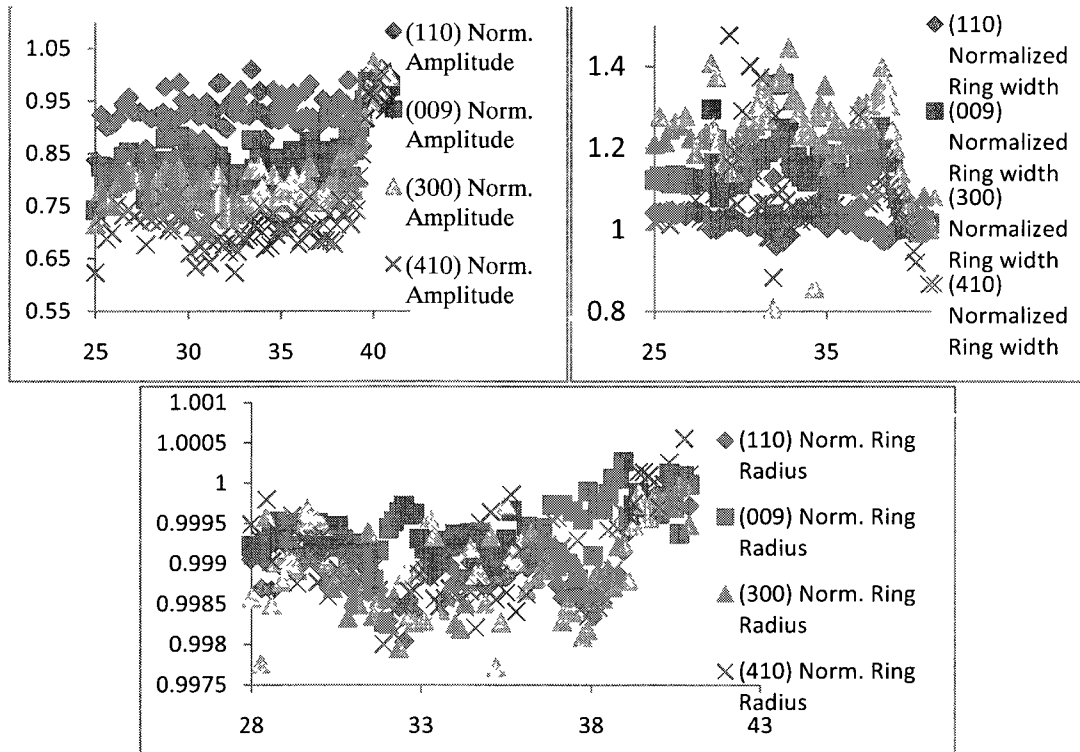


Np, 110 mJ, 9-23-2010

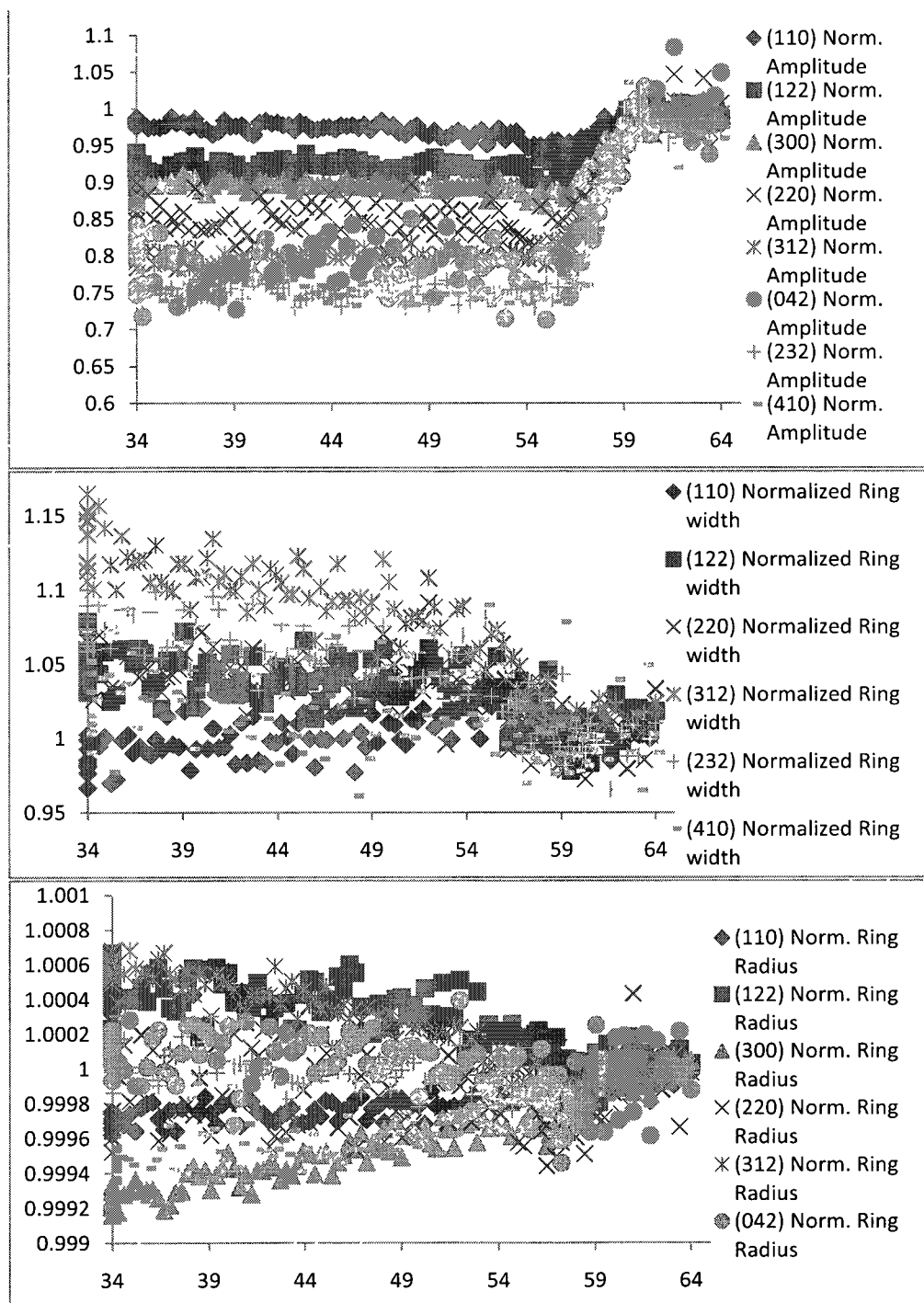




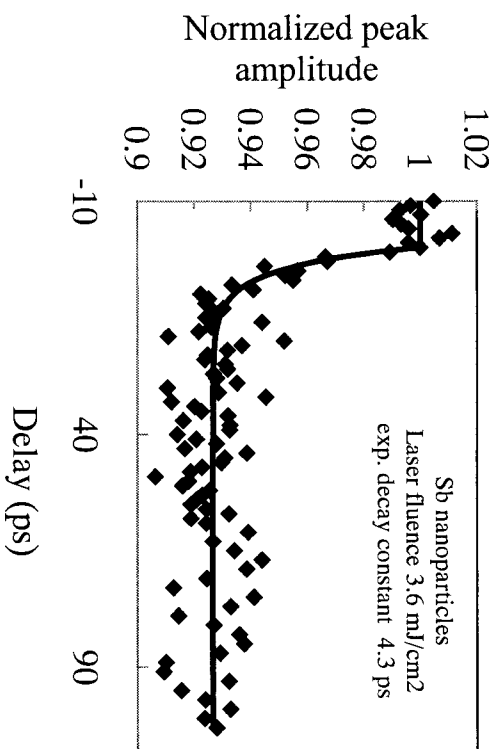
Np, 150 mJ 9-23-2010



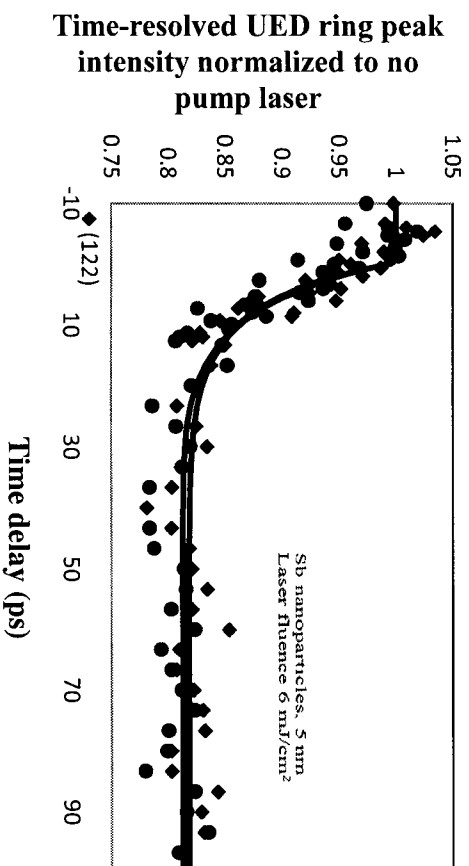
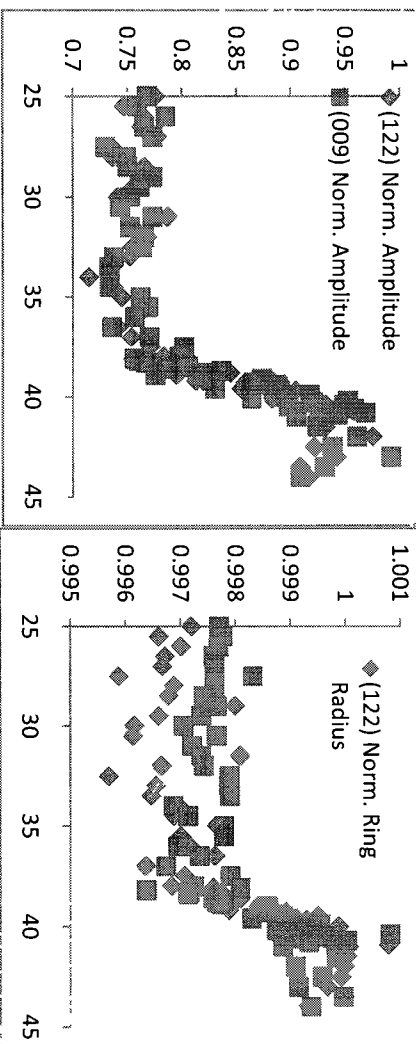
20nm, 5-13-2009



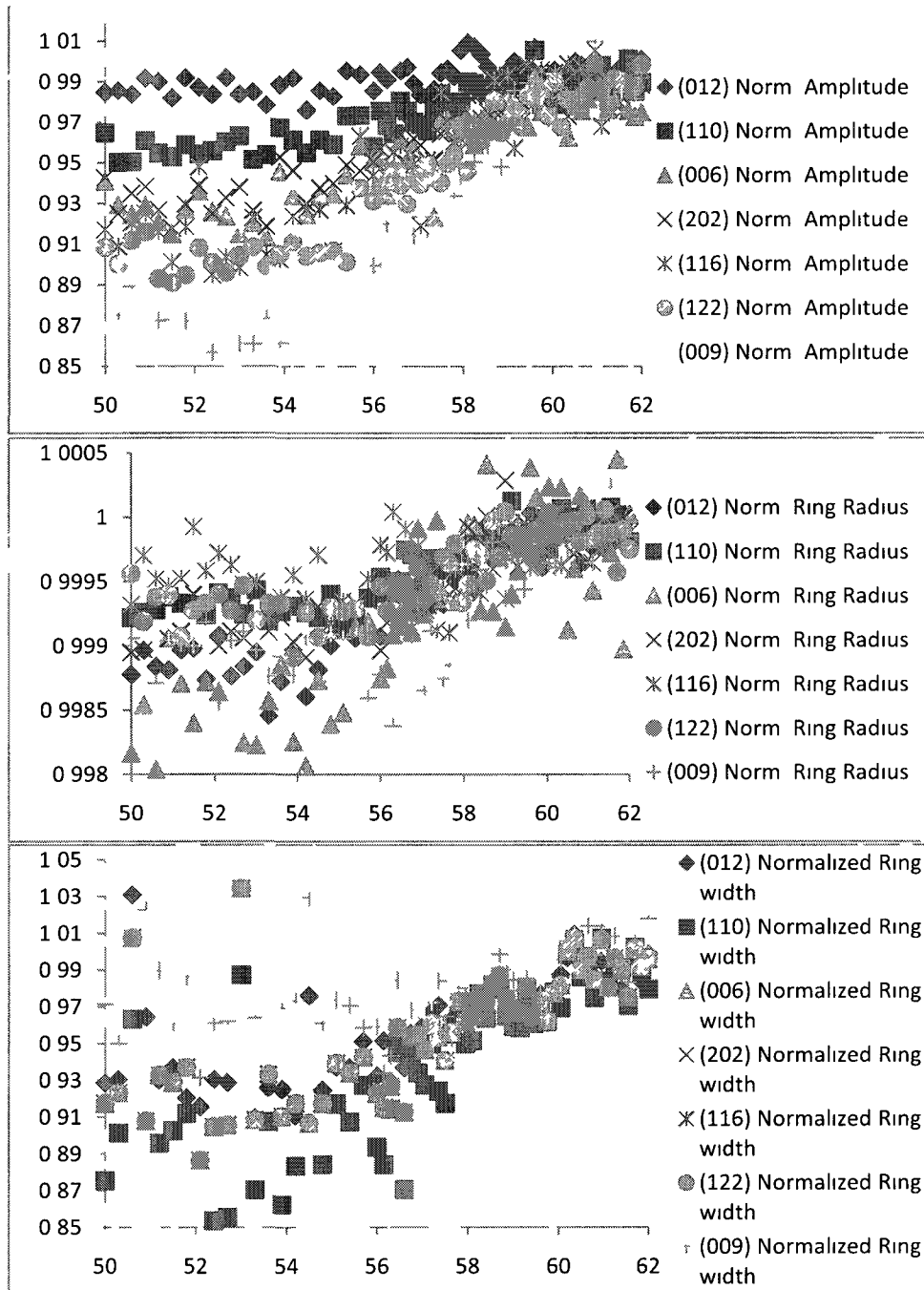
20nm, 1-20-2010



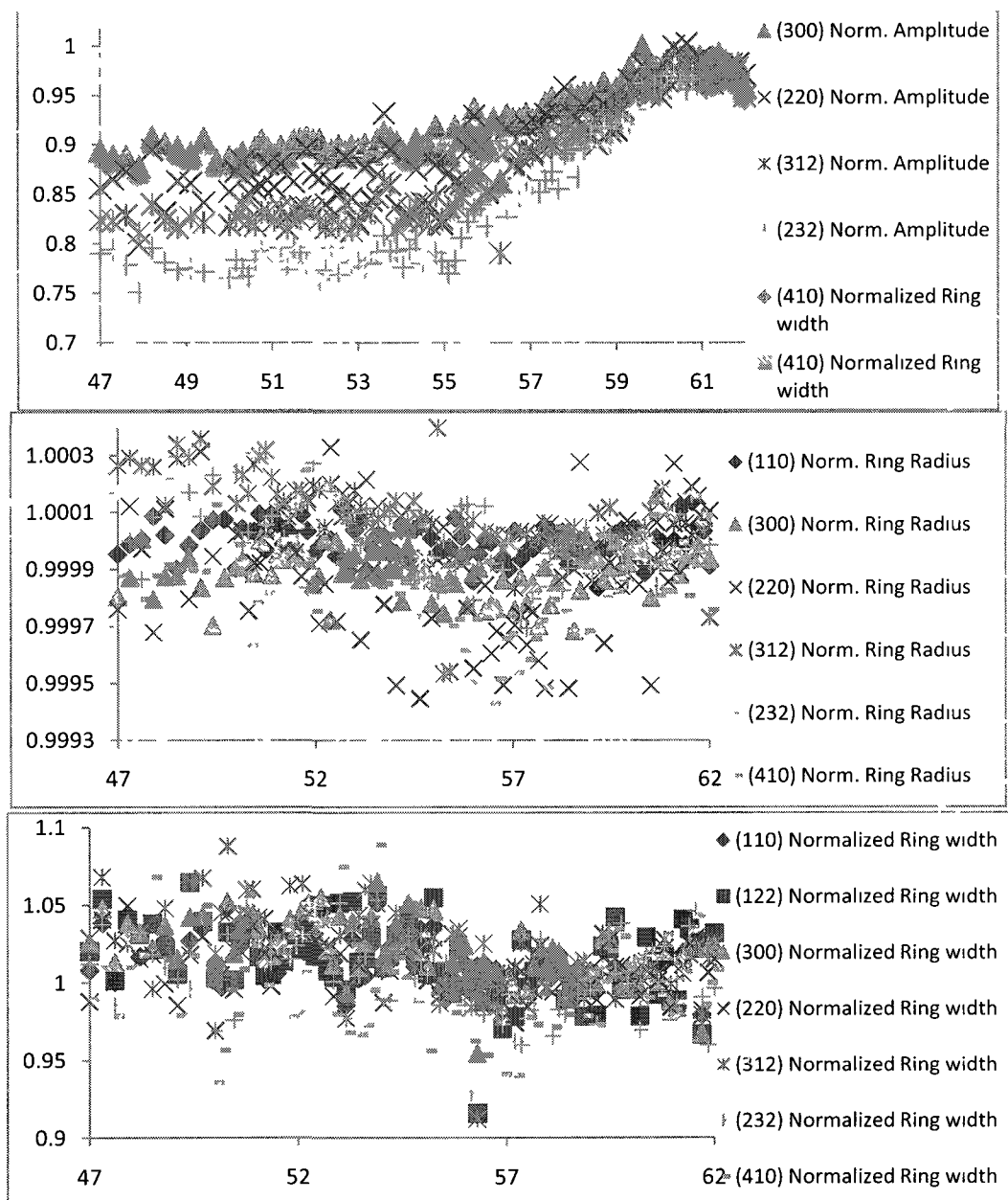
Np, 6-9-2009



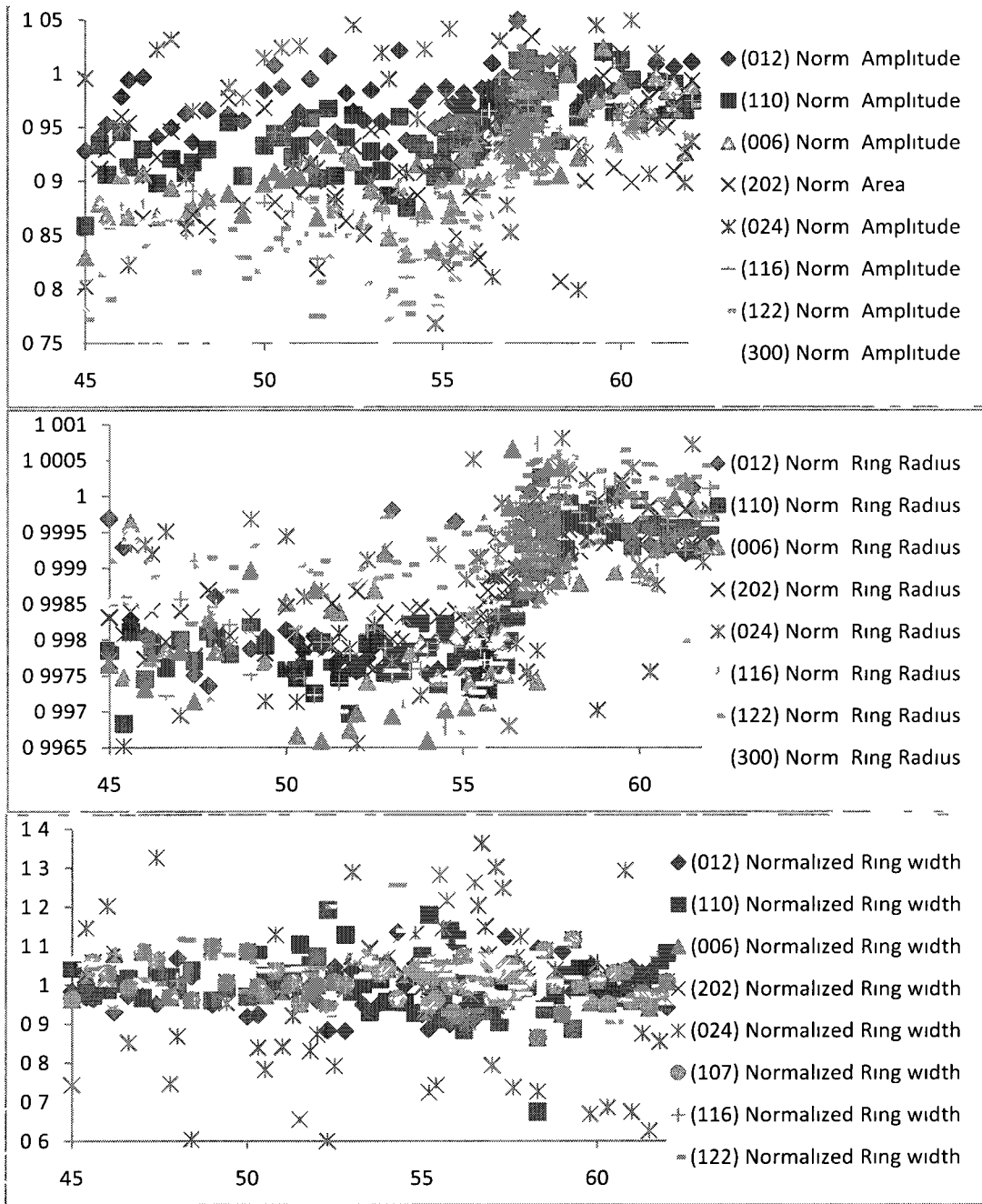
Np, 8-27-2009



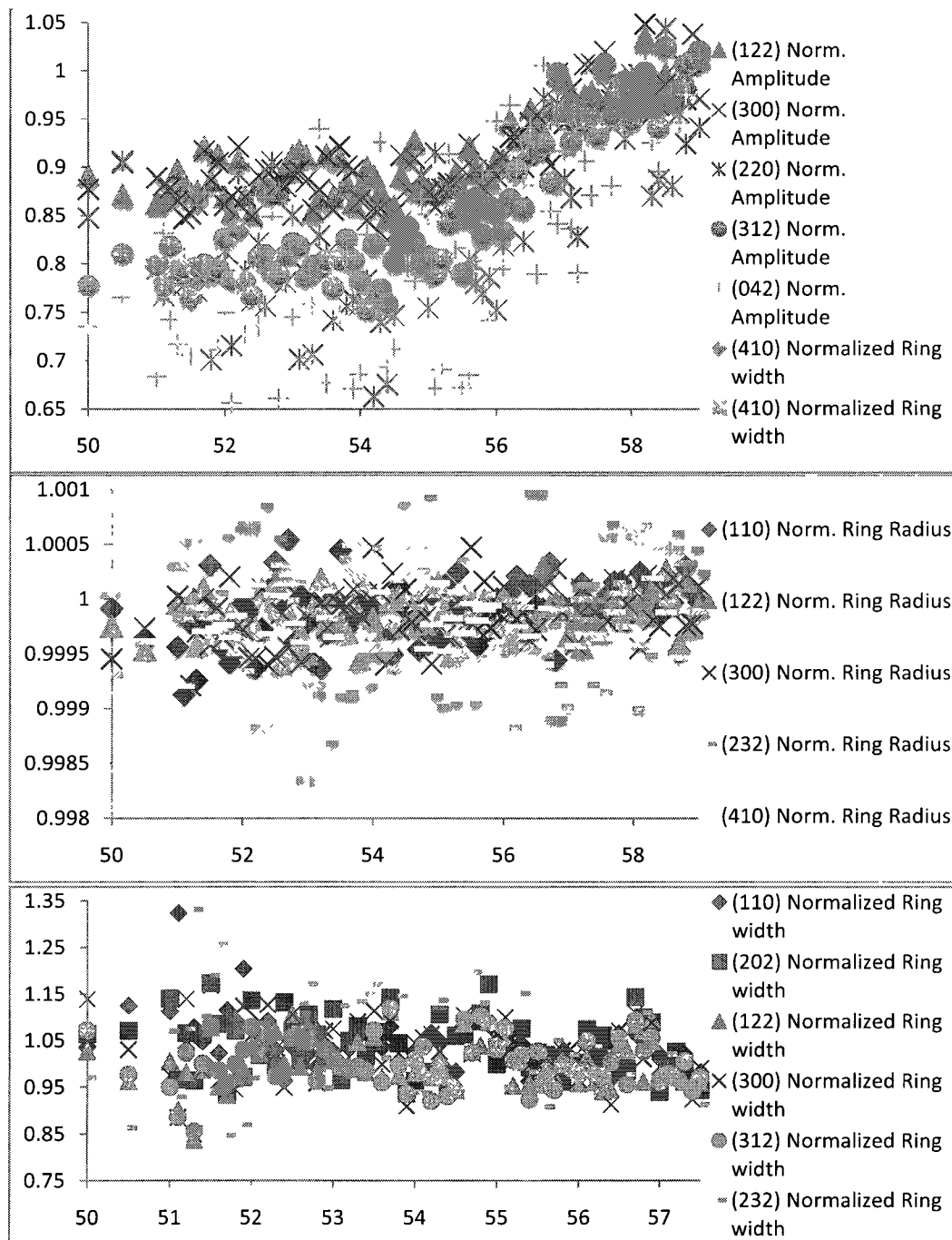
Np, 01-11-2010



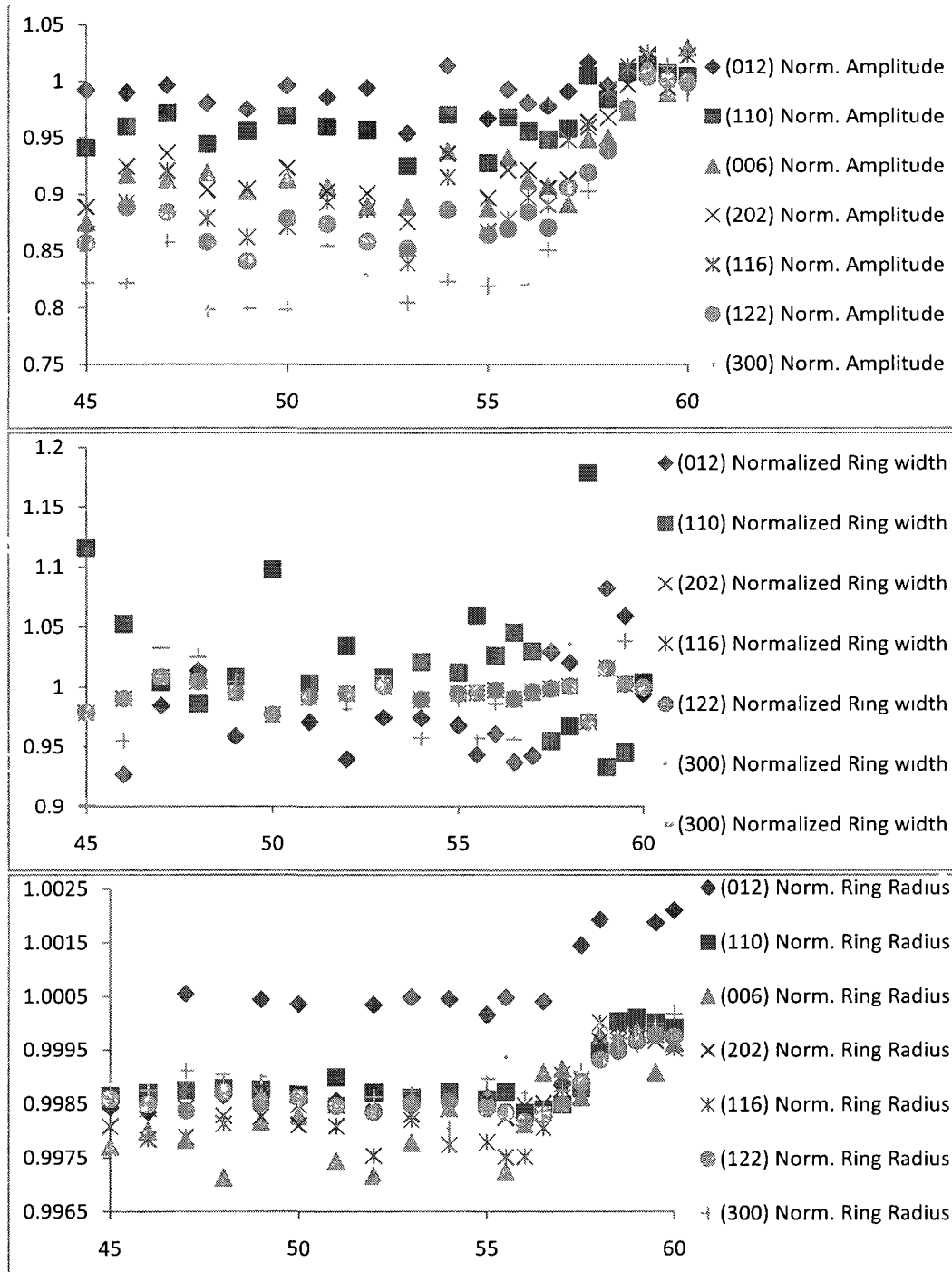
20 nm, 01-11-2010

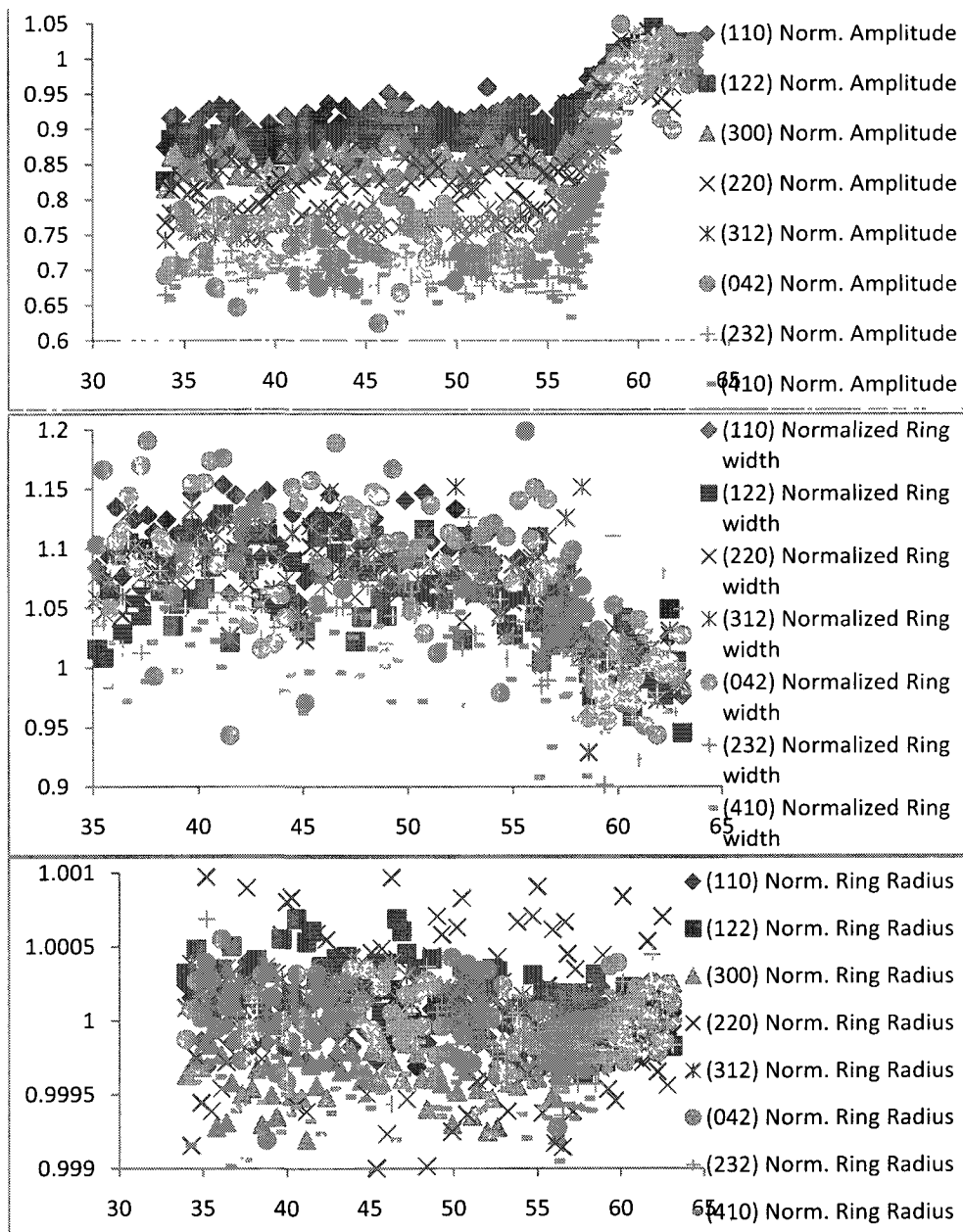


Np, 12-11-2009

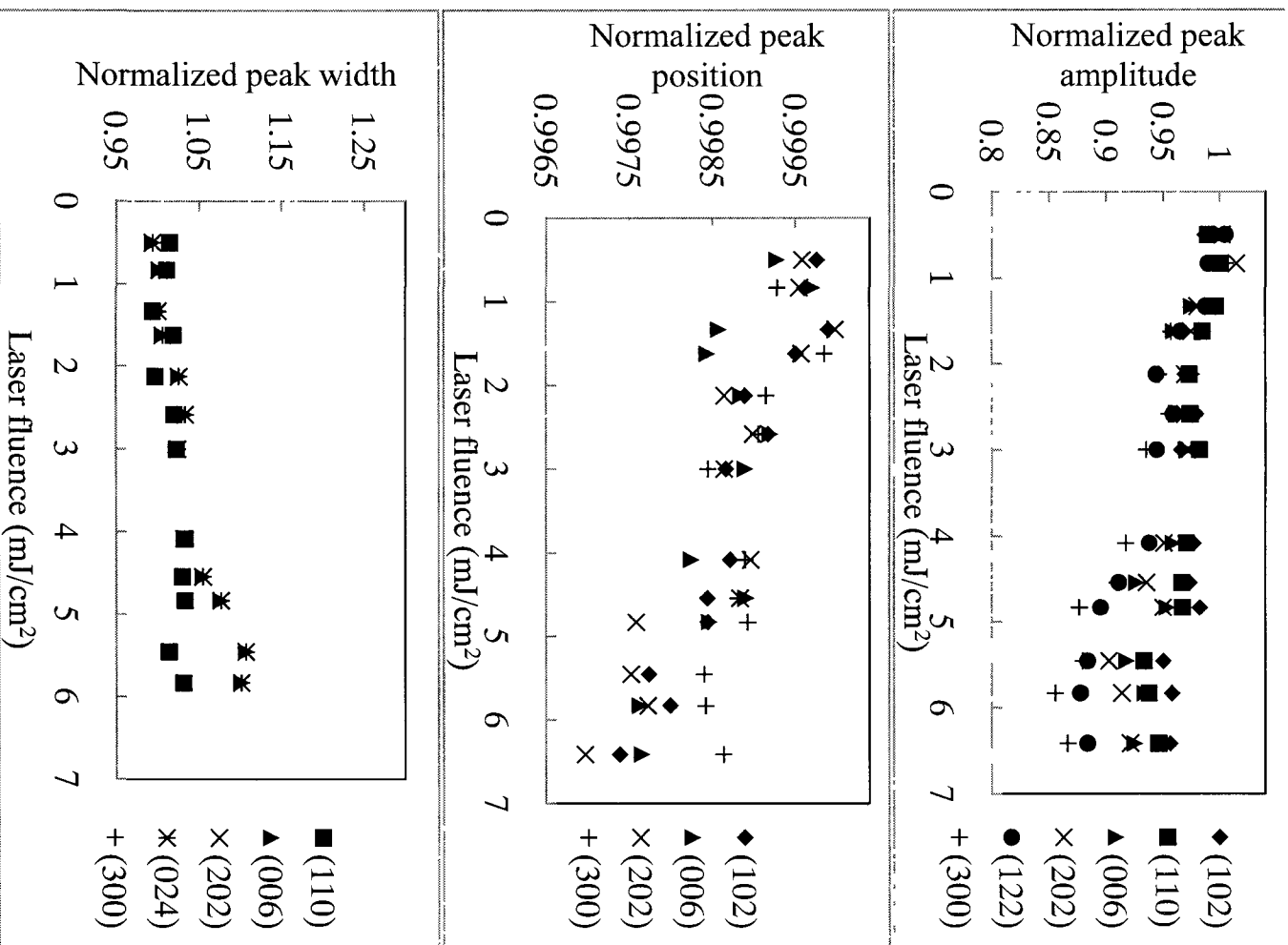


20 nm, 12-11-2009

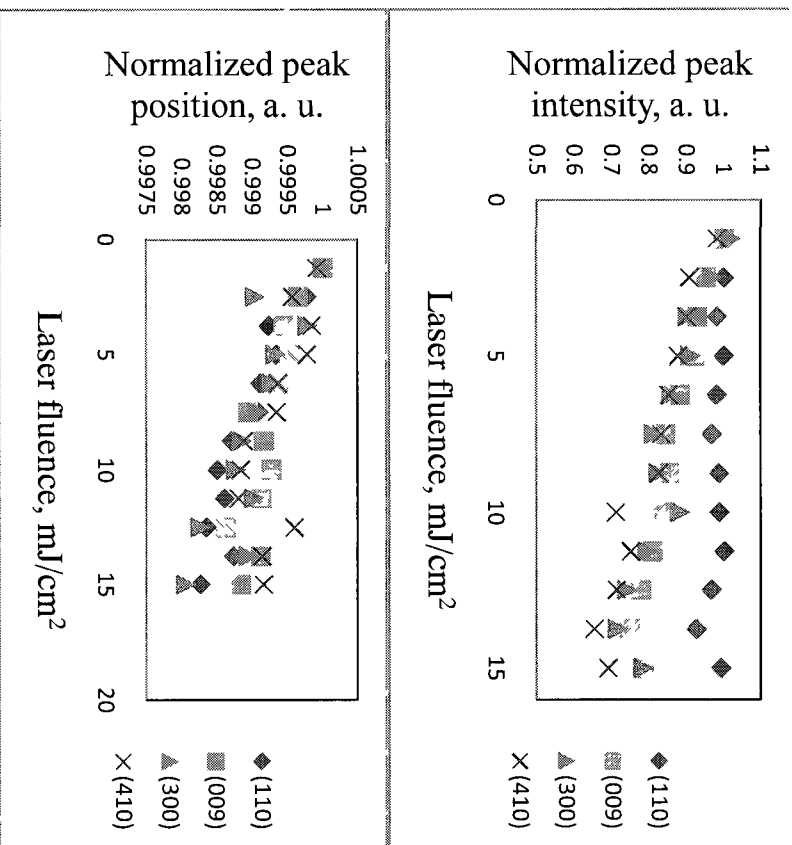




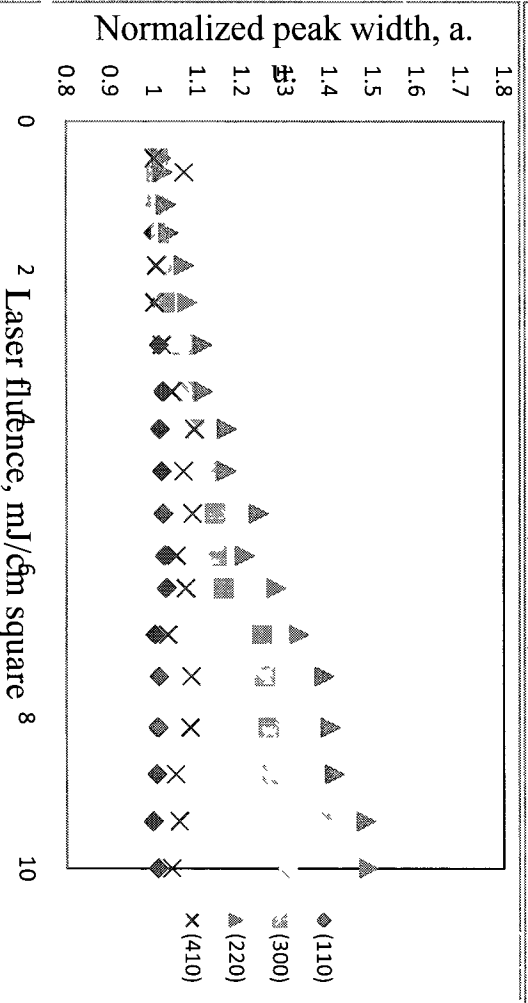
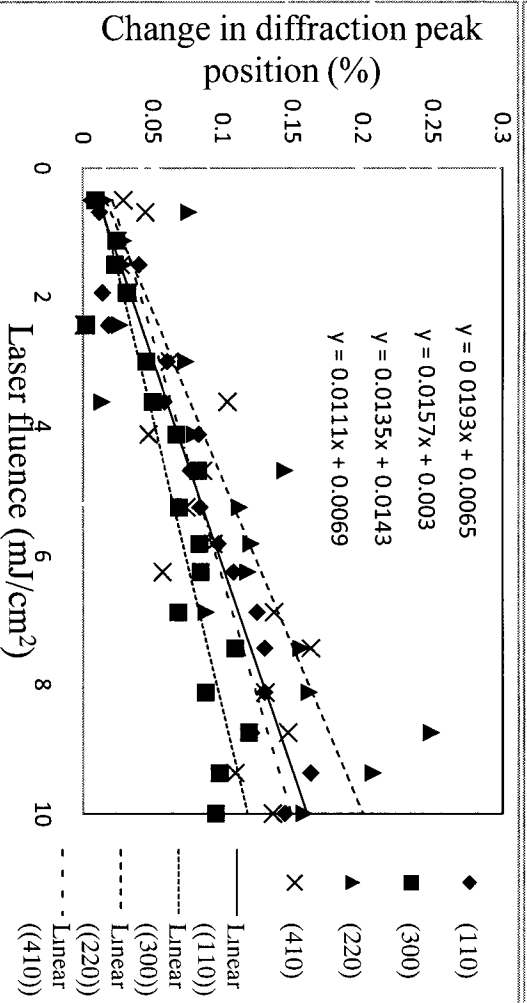
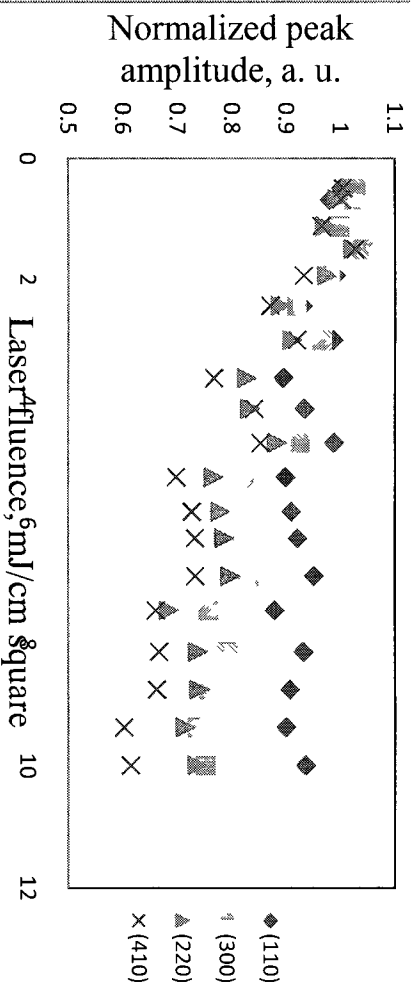
20 nm, 01-21-2010



05-28-2009



20 nm, 05-11-2009



20 nm, 05-14-2009

Appendix M: Licenses for figures' reprint

Fig. 1.4, 1.6

SPRINGER LICENSE TERMS AND CONDITIONS

Mar 13, 2011

This is a License Agreement between Mahmoud H Abdel ("You") and Springer ("Springer") provided by Copyright Clearance Center ("CCC"). The license consists of your order details, the terms and conditions provided by Springer, and the payment terms and conditions.

All payments must be made in full to CCC. For payment instructions, please see information listed at the bottom of this form.

License Number 2627310123532

License date Mar 13, 2011

Licensed content publisher Springer

Licensed content publication The European Physical Journal D - Atomic, Molecular, Optical and Plasma Physics

Licensed content title Structure of unsupported antimony nanoclusters

Licensed content author M. Kaufmann

Licensed content date Jul 1, 2005

Volume number 34

Issue number 1

Type of Use Thesis/Dissertation

Portion Figures

Author of this Springer

article

No

Order reference number

Title of your thesis /
dissertation

Ultrafast electron diffraction study of the dynamics of antimony thin
films and nanoparticles

Expected completion date Apr 2011

Estimated size(pages) 180

Total 0.00 USD

Terms and Conditions

Introduction

The publisher for this copyrighted material is Springer Science + Business Media. By clicking "accept" in connection with completing this licensing transaction, you agree that the following terms and conditions apply to this transaction (along with the Billing and Payment terms and conditions established by Copyright Clearance Center, Inc. ("CCC"), at the time that you opened your Rightslink account and that are available at any time at <http://myaccount.copyright.com>).

Limited License

With reference to your request to reprint in your thesis material on which Springer Science and Business Media control the copyright, permission is granted, free of charge, for the use Rightslink Printable License Page 1 of 3

<https://s100.copyright.com/App/PrintableLicenseFrame.jsp?publisherID=62&licenseID=2...> 3/13/2011 indicated in your enquiry. Licenses are for one-time use only with a maximum distribution equal to the number that you identified in the licensing process.

This License includes use in an electronic form, provided it is password protected or on the university's intranet, destined to microfilming by UMI and University repository. For any other electronic use, please contact Springer at (permissions.dordrecht@springer.com or permissions.heidelberg@springer.com) The material can only be used for the purpose of defending your thesis, and with a maximum of 100 extra copies in paper. Although Springer holds copyright to the material and is entitled to negotiate on rights, this license is only valid, provided permission is also obtained from the (co) author (address is given with the article/chapter) and provided it concerns original material which does not carry references to other sources (if material in question appears with credit to another source, authorization from that source is required as well). Permission free of charge on this occasion does not prejudice any rights we might have to charge for reproduction of our copyrighted material in the future. **Altering/Modifying Material: Not Permitted** However figures and illustrations may be altered minimally to serve your work. Any other abbreviations, additions, deletions and/or any other alterations shall be made only with prior written authorization of the author(s) and/or Springer Science + Business Media. (Please contact Springer at permissions.dordrecht@springer.com or permissions.heidelberg@springer.com)

Reservation of Rights

Springer Science + Business Media reserves all rights not specifically granted in the combination of (i) the license details provided by you and accepted in the course of this licensing transaction, (ii) these terms and conditions and (iii) CCC's Billing and Payment terms and conditions.

Copyright Notice:

Please include the following copyright citation referencing the publication in which the material was originally published. Where wording is within brackets, please include verbatim.

"With kind permission from Springer Science+Business Media: <book/journal title, chapter/article title, volume, year of publication, page, name(s) of author(s), figure number (s), and any original (first) copyright notice displayed with material>."

Warranties: Springer Science + Business Media makes no representations or warranties with respect to the licensed material.

Indemnity

You hereby indemnify and agree to hold harmless Springer Science + Business Media and CCC, and their respective officers, directors, employees and agents, from and against any and all claims arising out of your use of the licensed material other than as specifically authorized pursuant to this license.

No Transfer of License

Rightslink Printable License Page 2 of 3

<https://s100.copyright.com/App/PrintableLicenseFrame.jsp?publisherID=62&licenseID=2...> 3/13/2011

This license is personal to you and may not be sublicensed, assigned, or transferred by you to any other person without Springer Science + Business Media's written permission.

No Amendment Except in Writing

This license may not be amended except in a writing signed by both parties (or, in the case of Springer Science + Business Media, by CCC on Springer Science + Business Media's behalf).

Objection to Contrary Terms

Springer Science + Business Media hereby objects to any terms contained in any purchase order, acknowledgment, check endorsement or other writing prepared by you, which terms are inconsistent with these terms and conditions or CCC's Billing and Payment terms and conditions. These terms and conditions, together with CCC's Billing and Payment terms and conditions (which are incorporated herein), comprise the entire agreement between you and Springer Science + Business Media (and CCC) concerning this licensing transaction. In the event of any conflict between your obligations established by these terms and conditions and those established by CCC's Billing and Payment terms and conditions, these terms and conditions shall control.

Jurisdiction All disputes that may arise in connection with this present License, or the breach thereof, shall be settled exclusively by the country's law in which the work was originally published.

Other terms and conditions:

v1.2

Gratis licenses (referencing \$0 in the Total field) are free. Please retain this printable license for your reference. No payment is required.

If you would like to pay for this license now, please remit this license along with your payment made payable to "COPYRIGHT CLEARANCE CENTER" otherwise you will be invoiced within 48 hours of the license date. Payment should be in the form of a check or money order referencing your account number and this invoice number RLNK10948633.

Once you receive your invoice for this order, you may pay your invoice by credit card.

Please follow instructions provided at that time.

Make Payment To:

Copyright Clearance Center

Dept 001

P.O. Box 843006

Boston, MA 02284-3006

For suggestions or comments regarding this order, contact Rightslink Customer Support: customercare@copyright.com or +1-877-622-5543 (toll free in the US) or +1-

978-646-2777.

Rightslink Printable License Page 3 of 3

<https://s100.copyright.com/App/PrintableLicenseFrame.jsp?publisherID=62&licenseID=2...> 3/13/2011

Fig1.5

ELSEVIER LICENSE TERMS AND CONDITIONS

Mar 13, 2011

This is a License Agreement between Mahmoud H Abdel ("You") and Elsevier ("Elsevier") provided by Copyright Clearance Center ("CCC"). The license consists of your order details, the terms and conditions provided by Elsevier, and the payment terms and conditions.

All payments must be made in full to CCC. For payment instructions, please see information listed at the bottom of this form.

Supplier Elsevier Limited

The Boulevard, Langford Lane

Kidlington, Oxford, OX5 1GB, UK

Registered Company
 Number
 1982084
 Customer name Mahmoud H Abdel-Fattah
 Customer address 435 Harvard st, apt. 2
 Norfolk, VA 23505
 License number 2627301328280
 License date Mar 13, 2011
 Licensed content publisher Elsevier
 Licensed content publication Materials Science and Engineering: A
 Licensed content title Electron diffraction study of vaporized-metal clusters produced by a
 nozzle source
 Licensed content author L.D. Sun, G.H. Takaoka, J. Matsuo, I. Yamada
 Licensed content date 30 October 1996
 Licensed content volume
 number
 217-218
 Licensed content issue
 number
 Number of pages 4
 Start Page 15
 End Page 18
 Type of Use reuse in a thesis/dissertation
 Intended publisher of new
 work
 other
 Portion figures/tables/illustrations
 Number of
 figures/tables/illustrations
 1
 Format *both print and electronic*
 Are you the author of this
 Elsevier article?
 No
 Rightslink Printable License Page 1 of 6
[https://s100.copyright.com/App/PrintableLicenseFrame.jsp?publisherID=70&licenseID=](https://s100.copyright.com/App/PrintableLicenseFrame.jsp?publisherID=70&licenseID=2...)
 2... 3/13/2011
 Will you be translating? No
 Order reference number 1-2
 Title of your
 thesis/dissertation
 Ultrafast electron diffraction study of the dynamics of antimony thin
 films and nanoparticles
 Expected completion date Apr 2011
 Estimated size (number of
 pages)
 180
 Elsevier VAT number GB 494 6272 12
 Permissions price 0.00 USD
 VAT/Local Sales Tax 0.0 USD / 0.0 GBP
 Total 0.00 USD
 Terms and Conditions

INTRODUCTION

1. The publisher for this copyrighted material is Elsevier. By clicking "accept" in connection with completing this licensing transaction, you agree that the following terms and conditions apply to this transaction (along with the Billing and Payment terms and conditions established by Copyright Clearance Center, Inc. ("CCC"), at the time that you

opened your Rightslink account and that are available at any time at <http://myaccount.copyright.com>).

GENERAL TERMS

2. Elsevier hereby grants you permission to reproduce the aforementioned material subject to the terms and conditions indicated.

3. Acknowledgement: If any part of the material to be used (for example, figures) has appeared in our publication with credit or acknowledgement to another source, permission must also be sought from that source. If such permission is not obtained then that material may not be included in your publication/copies. Suitable acknowledgement to the source must be made, either as a footnote or in a reference list at the end of your publication, as follows:

“Reprinted from Publication title, Vol /edition number, Author(s), Title of article / title of chapter, Pages No., Copyright (Year), with permission from Elsevier [OR APPLICABLE SOCIETY COPYRIGHT OWNER].” Also Lancet special credit - “Reprinted from The Lancet, Vol. number, Author(s), Title of article, Pages No., Copyright (Year), with permission from Elsevier.”

4. Reproduction of this material is confined to the purpose and/or media for which permission is hereby given.

5. Altering/Modifying Material: Not Permitted. However figures and illustrations may be altered/adapted minimally to serve your work. Any other abbreviations, additions, deletions and/or any other alterations shall be made only with prior written authorization of Elsevier Ltd. (Please contact Elsevier at permissions@elsevier.com)

Rightslink Printable License Page 2 of 6

<https://s100.copyright.com/App/PrintableLicenseFrame.jsp?publisherID=70&licenseID=2...> 3/13/2011

6. If the permission fee for the requested use of our material is waived in this instance, please be advised that your future requests for Elsevier materials may attract a fee.

7. Reservation of Rights: Publisher reserves all rights not specifically granted in the combination of (i) the license details provided by you and accepted in the course of this licensing transaction, (ii) these terms and conditions and (iii) CCC's Billing and Payment terms and conditions.

8. License Contingent Upon Payment: While you may exercise the rights licensed immediately upon issuance of the license at the end of the licensing process for the transaction, provided that you have disclosed complete and accurate details of your proposed use, no license is finally effective unless and until full payment is received from you (either by publisher or by CCC) as provided in CCC's Billing and Payment terms and conditions. If full payment is not received on a timely basis, then any license preliminarily granted shall be deemed automatically revoked and shall be void as if never granted. Further, in the event that you breach any of these terms and conditions or any of CCC's Billing and Payment terms and conditions, the license is automatically revoked and shall be void as if never granted. Use of materials as described in a revoked license, as well as any use of the materials beyond the scope of an unrevoked license, may constitute copyright infringement and publisher reserves the right to take any and all action to protect its copyright in the materials.

9. Warranties: Publisher makes no representations or warranties with respect to the licensed material.

10. **Indemnity:** You hereby indemnify and agree to hold harmless publisher and CCC, and their respective officers, directors, employees and agents, from and against any and all claims arising out of your use of the licensed material other than as specifically authorized pursuant to this license.

11. **No Transfer of License:** This license is personal to you and may not be sublicensed, assigned, or transferred by you to any other person without publisher's written permission.

12. **No Amendment Except in Writing:** This license may not be amended except in a writing signed by both parties (or, in the case of publisher, by CCC on publisher's behalf).

13. **Objection to Contrary Terms:** Publisher hereby objects to any terms contained in any purchase order, acknowledgment, check endorsement or other writing prepared by you, which terms are inconsistent with these terms and conditions or CCC's Billing and Payment terms and conditions. These terms and conditions, together with CCC's Billing and Payment terms and conditions (which are incorporated herein), comprise the entire agreement between you and publisher (and CCC) concerning this licensing transaction. In the event of any conflict between your obligations established by these terms and conditions and those established by CCC's Billing and Payment terms and conditions, these terms and conditions shall control.

14. **Revocation:** Elsevier or Copyright Clearance Center may deny the permissions described in this License at their sole discretion, for any reason or no reason, with a full refund payable to you. Notice of such denial will be made using the contact information provided by you.

Failure to receive such notice will not alter or invalidate the denial. In no event will Elsevier Rightslink Printable License Page 3 of 6

<https://s100.copyright.com/App/PrintableLicenseFrame.jsp?publisherID=70&licenseID=2...> 3/13/2011 or Copyright Clearance Center be responsible or liable for any costs, expenses or damage incurred by you as a result of a denial of your permission request, other than a refund of the amount(s) paid by you to Elsevier and/or Copyright Clearance Center for denied permissions.

LIMITED LICENSE

The following terms and conditions apply only to specific license types:

15. **Translation:** This permission is granted for non-exclusive world **English** rights only unless your license was granted for translation rights. If you licensed translation rights you may only translate this content into the languages you requested. A professional translator must perform all translations and reproduce the content word for word preserving the integrity of the article. If this license is to re-use 1 or 2 figures then permission is granted for non-exclusive world rights in all languages.

16. **Website:** The following terms and conditions apply to electronic reserve and author websites:

Electronic reserve: If licensed material is to be posted to website, the web site is to be password-protected and made available only to bona fide students registered on a relevant course if:

This license was made in connection with a course,

This permission is granted for 1 year only. You may obtain a license for future website posting,

All content posted to the web site must maintain the copyright information line on the bottom of each image,

A hyper-text must be included to the Homepage of the journal from which you are licensing at <http://www.sciencedirect.com/science/journal/xxxxx> or the Elsevier homepage for books at <http://www.elsevier.com> , and Central Storage: This license does not include permission for a scanned version of the material to be stored in a central repository such as that provided by Heron/XanEdu.

17. **Author website** for journals with the following additional clauses:

All content posted to the web site must maintain the copyright information line on the bottom of each image, and the permission granted is limited to the personal version of your paper. You are not allowed to download and post the published electronic version of your article (whether PDF or HTML, proof or final version), nor may you scan the printed edition to create an electronic version,

A hyper-text must be included to the Homepage of the journal from which you are licensing at <http://www.sciencedirect.com/science/journal/xxxxx> , As part of our normal production process, you will receive an e-mail notice when your article appears on Elsevier's online service ScienceDirect (www.sciencedirect.com). That e-mail will include the article's

Digital Object Identifier (DOI). This number provides the electronic link to the published article and should be included in the posting of your personal version. We ask that you wait until you receive this e-mail and have the DOI to do any posting.

Central Storage: This license does not include permission for a scanned version of the material to be stored in a central repository such as that provided by Heron/XanEdu.

Rightslink Printable License Page 4 of 6

<https://s100.copyright.com/App/PrintableLicenseFrame.jsp?publisherID=70&licenseID=2...> 3/13/2011

18. **Author website** for books with the following additional clauses:

Authors are permitted to place a brief summary of their work online only.

A hyper-text must be included to the Elsevier homepage at <http://www.elsevier.com>

All content posted to the web site must maintain the copyright information line on the bottom of each image

You are not allowed to download and post the published electronic version of your chapter, nor may you scan the printed edition to create an electronic version.

Central Storage: This license does not include permission for a scanned version of the material to be stored in a central repository such as that provided by Heron/XanEdu.

19. **Website** (regular and for author): A hyper-text must be included to the Homepage of the journal from which you are licensing at

<http://www.sciencedirect.com/science/journal/xxxxx>. or for books to the Elsevier homepage at <http://www.elsevier.com>

20. **Thesis/Dissertation**: If your license is for use in a thesis/dissertation your thesis may be submitted to your institution in either print or electronic form. Should your thesis be published commercially, please reapply for permission. These requirements include permission for the Library and Archives of Canada to supply single copies, on demand, of the complete thesis and include permission for UMI to supply single copies, on demand, of the complete thesis. Should your thesis be published commercially, please reapply for permission.

21. Other Conditions:

v1.6

Gratis licenses (referencing \$0 in the Total field) are free. Please retain this printable license for your reference. No payment is required.

If you would like to pay for this license now, please remit this license along with your payment made payable to "COPYRIGHT CLEARANCE CENTER" otherwise you will be invoiced within 48 hours of the license date. Payment should be in the form of a check or money order referencing your account number and this invoice number RLNK10948631.

Once you receive your invoice for this order, you may pay your invoice by credit card.

Please follow instructions provided at that time.

Make Payment To:

Copyright Clearance Center

Dept 001

P.O. Box 843006

Boston, MA 02284-3006

For suggestions or comments regarding this order, contact Rightslink Customer Support: customercare@copyright.com or +1-877-622-5543 (toll free in the US) or +1-978-646-2777.

Rightslink Printable License Page 5 of 6

<https://s100.copyright.com/App/PrintableLicenseFrame.jsp?publisherID=70&licenseID=2...> 3/13/2011

Rightslink Printable License Page 6 of 6

<https://s100.copyright.com/App/PrintableLicenseFrame.jsp?publisherID=70&licenseID=2...> 3/13/2011

Fig. 2.3

SPRINGER LICENSE TERMS AND CONDITIONS

Mar 13, 2011

This is a License Agreement between Mahmoud H Abdel ("You") and Springer ("Springer") provided by Copyright Clearance Center ("CCC"). The license consists of your order details, the terms and conditions provided by Springer, and the payment terms and conditions.

All payments must be made in full to CCC. For payment instructions, please see information listed at the bottom of this form.

License Number 2627300051868

License date Mar 13, 2011

Licensed content publisher Springer

Licensed content publication Applied Physics A

Licensed content title The role of electron-phonon coupling in femtosecond laser damage of metals

Licensed content author S.-S. Wellershoff

Licensed content date Dec 1, 1999

Volume number 69

Issue number 7

Type of Use Thesis/Dissertation

Portion Figures

Author of this Springer

article

No

Order reference number 2-2

Title of your thesis /

dissertation
 Ultrafast electron diffraction study of the dynamics of antimony thin
 films and nanoparticles
 Expected completion date Apr 2011
 Estimated size(pages) 180
 Total 0.00 USD
 Terms and Conditions

Introduction

The publisher for this copyrighted material is Springer Science + Business Media. By clicking "accept" in connection with completing this licensing transaction, you agree that the following terms and conditions apply to this transaction (along with the Billing and Payment terms and conditions established by Copyright Clearance Center, Inc. ("CCC"), at the time that you opened your Rightslink account and that are available at any time at <http://myaccount.copyright.com>).

Limited License

With reference to your request to reprint in your thesis material on which Springer Science and Business Media control the copyright, permission is granted, free of charge, for the use Rightslink Printable License Page 1 of 3 <https://s100.copyright.com/App/PrintableLicenseFrame.jsp?publisherID=62&licenseID=2...> 3/13/2011 indicated in your enquiry. Licenses are for one-time use only with a maximum distribution equal to the number that you identified in the licensing process. This License includes use in an electronic form, provided it is password protected or on the university's intranet, destined to microfilming by UMI and University repository. For any other electronic use, please contact Springer at (permissions.dordrecht@springer.com or permissions.heidelberg@springer.com)

The material can only be used for the purpose of defending your thesis, and with a maximum of 100 extra copies in paper.

Although Springer holds copyright to the material and is entitled to negotiate on rights, this license is only valid, provided permission is also obtained from the (co) author (address is given with the article/chapter) and provided it concerns original material which does not carry references to other sources (if material in question appears with credit to another source, authorization from that source is required as well). Permission free of charge on this occasion does not prejudice any rights we might have to charge for reproduction of our copyrighted material in the future.

Altering/Modifying Material: Not Permitted

However figures and illustrations may be altered minimally to serve your work. Any other abbreviations, additions, deletions and/or any other alterations shall be made only with prior written authorization of the author(s) and/or Springer Science + Business Media. (Please contact Springer at permissions.dordrecht@springer.com or permissions.heidelberg@springer.com)

Reservation of Rights

Springer Science + Business Media reserves all rights not specifically granted in the combination of (i) the license details provided by you and accepted in the course of this licensing transaction, (ii) these terms and conditions and (iii) CCC's Billing and Payment terms and conditions.

Copyright Notice:

Please include the following copyright citation referencing the publication in which the material was originally published. Where wording is within brackets, please include

verbatim.

"With kind permission from Springer Science+Business Media: <book/journal title, chapter/article title, volume, year of publication, page, name(s) of author(s), figure number (s), and any original (first) copyright notice displayed with material>."

Warranties: Springer Science + Business Media makes no representations or warranties with respect to the licensed material.

Indemnity

You hereby indemnify and agree to hold harmless Springer Science + Business Media and CCC, and their respective officers, directors, employees and agents, from and against any and all claims arising out of your use of the licensed material other than as specifically authorized pursuant to this license.

No Transfer of License

Rightslink Printable License Page 2 of 3

<https://s100.copyright.com/App/PrintableLicenseFrame.jsp?publisherID=62&licenseID=2...> 3/13/2011

This license is personal to you and may not be sublicensed, assigned, or transferred by you to any other person without Springer Science + Business Media's written permission.

No Amendment Except in Writing

This license may not be amended except in a writing signed by both parties (or, in the case of Springer Science + Business Media, by CCC on Springer Science + Business Media's behalf).

Objection to Contrary Terms

Springer Science + Business Media hereby objects to any terms contained in any purchase order, acknowledgment, check endorsement or other writing prepared by you, which terms are inconsistent with these terms and conditions or CCC's Billing and Payment terms and conditions. These terms and conditions, together with CCC's Billing and Payment terms and conditions (which are incorporated herein), comprise the entire agreement between you and Springer Science + Business Media (and CCC) concerning this licensing transaction. In the event of any conflict between your obligations established by these terms and conditions and those established by CCC's Billing and Payment terms and conditions, these terms and conditions shall control.

Jurisdiction All disputes that may arise in connection with this present License, or the breach thereof, shall be settled exclusively by the country's law in which the work was originally published.

Other terms and conditions:

v1.2

Gratis licenses (referencing \$0 in the Total field) are free. Please retain this printable

license for your reference. No payment is required.

If you would like to pay for this license now, please remit this license along with your payment made payable to "COPYRIGHT CLEARANCE CENTER" otherwise you will be invoiced within 48 hours of the license date. Payment should be in the form of a check or money order referencing your account number and this invoice number RLNK10948625.

Once you receive your invoice for this order, you may pay your invoice by credit card.

Please follow instructions provided at that time.

Make Payment To:

Copyright Clearance Center

Dept 001

P.O. Box 843006

Boston, MA 02284-3006

For suggestions or comments regarding this order, contact Rightslink Customer Support: customercare@copyright.com or +1-877-622-5543 (toll free in the US) or +1-

978-646-2777.

Rightslink Printable License Page 3 of 3

<https://s100.copyright.com/App/PrintableLicenseFrame.jsp?publisherID=62&licenseID=2...> 3/13/2011

VITA

Mahmoud ABDEL-FATTAH

Department of Electrical and Computer Engineering

Old Dominion University, Norfolk, VA 23529

Email: mabde001@odu.edu Phone: (757) 816-0129

Mahmoud Abdel-Fattah received his B.Sc. from the physics department Cairo University in 1991. In 1998 he received his M.Sc. from the same department. The subject of the master's study was laser induced breakdown in gases, spectral analysis was used to study the produced laser plasma. The author is expected to receive his Ph.D. in electrical engineering from Old Dominion University in the field of surface science. During the Ph.D. research the author used femtosecond laser, ultrahigh vacuum technology, time resolved techniques, electron diffraction, thin film growth, and image processing to study the ultrafast phenomena in thin films and nanoparticles following the application of an ultrafast laser pulse.